

Rivastigmine-Loaded Nanocarriers for Improved Nose-to-Brain Delivery: Design, Development and Pharmacokinetic Evaluation

THESIS

Submitted in partial fulfillment
of the requirements for the degree of
DOCTOR OF PHILOSOPHY

by

Nikita Subhash Hinge

2018PHXF0041P

Under the Supervision of
Prof. Murali Monohar Pandey



**BIRLA INSTITUTE OF TECHNOLOGY AND SCIENCE
PILANI (RAJASTHAN) 2024**

CERTIFICATE

This is to certify that the thesis entitled “**Rivastigmine-Loaded Nanocarriers for Improved Nose-to-Brain Delivery: Design, Development and Pharmacokinetic Evaluation**” submitted by **Ms. Nikita Subhash Hinge**, ID No. **2018PHXF0041P** for the award of Ph.D. Degree of the Institute, embodies the original work done by her under my supervision.

Supervisor

Prof. Murali Monohar Pandey

Associate Professor,

Department of Pharmacy

BITS-Pilani, Pilani Campus

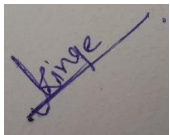
Date:

Place:

Declaration

I hereby declare that the work carried out in this thesis titled **“Rivastigmine-Loaded Nanocarriers for Improved Nose-to-Brain Delivery: Design, Development and Pharmacokinetic Evaluation”** is an original piece of research work carried out under the guidance of Prof. Murali Monohar Pandey at BITS-Pilani, Pilani Campus, Pilani, India. This thesis has not been submitted by me for the award of any other degree of any other University/Institute.

Name: Nikita Subhash Hinge

A small, square image showing a handwritten signature in blue ink. The signature appears to be 'N. Hinge' written diagonally across a horizontal line.

Signature

Date: 19.06.2024

Table of Content

<i>Acknowledgment</i>	<i>i</i>
<i>List of Abbreviations</i>	<i>iv</i>
<i>List of Tables</i>	<i>viii</i>
<i>List of Figures</i>	<i>x</i>
<i>Abstract</i>	<i>xix</i>
Chapter 1	1
1. Introduction	1
1.1 Alzheimer’s disease	2
1.2 Pathophysiology	4
1.3 USFDA-approved drugs for treatment and their drawbacks	6
1.4 Physical barriers in brain targeting	8
1.5 Approaches for brain targeting	10
1.6 Nose-to-Brain delivery	11
1.6.1 Ion-pair complexes	13
1.6.2 Nasal anatomy	14
1.6.3 Nose-to-brain transport pathways	15
1.6.3.1 Olfactory pathway	15
1.6.3.2 Trigeminal nerve pathway	16
1.6.3.3 Cellular transport in nose-to-brain delivery	16
1.7 Formulation approaches for nose-to-brain delivery	18

1.7.1	<i>In-situ</i> hydrogel-based nose-to-brain delivery	18
1.7.1.1	Thermoresponsive gel	18
1.7.1.2	pH-responsive gel	19
1.7.2	Nanocarrier-based nose-to-brain delivery.....	20
1.7.2.1	Polymeric nanoparticles.....	20
1.7.2.2	Lipidic nanocarriers	22
1.7.2.2.1	Microemulsion	22
1.7.2.2.2	Liposomes	22
1.7.2.2.3	Solid lipid nanocarriers and nanostructured lipid carriers	23
1.7.3	Surface-engineered nanocarriers for nose-to-brain delivery.....	25
1.8	Gap in existing research	27
1.9	Outline of the work	29
1.10	Objective of research work	31
	References	33
	Chapter 2.....	60
	2. Drug profile.....	60
2.1	Physicochemical properties of rivastigmine hydrogen tartrate	61
2.1.1	Description.....	61
2.1.2	Solubility.....	61
2.1.3	Polymorphism.....	62

2.1.4	Stability and storage	63
2.2	Clinical pharmacology	64
2.2.1	Mechanism of action.....	64
2.2.2	Absorption.....	64
2.2.3	Distribution	64
2.2.4	Metabolism	64
2.2.5	Excretion.....	65
2.2.6	Adverse effects.....	65
2.3	Marketed formulation.....	65
2.3.1	Exelon®	65
2.4	Drawbacks of currently available therapy.....	65
2.5	Conclusion.....	66
	References	67
Chapter 3.....		69
3. Analytical and bioanalytical method development and validation for estimation of RIV-HT		
.....		69
3.1	Analytical and bioanalytical method development and validation	70
3.1.1	Introduction.....	72
3.1.2	Materials and method.....	73
3.1.2.1	Materials	73

3.1.2.2	Instrumentation	73
3.1.2.3	Preparation of standard solutions	73
3.1.2.4	Method validation	74
3.1.2.4.1	Specificity	74
3.1.2.4.2	Calibration curve, linearity, and range	74
3.1.2.4.3	Accuracy	74
3.1.2.4.4	Precision	74
3.1.2.4.5	Robustness	75
3.1.2.4.6	Limit of detection and limit of quantification	75
3.1.2.4.7	Stability study	75
3.1.3	Result and discussion	75
3.1.3.1	Method development	75
3.1.3.2	Method validation	76
3.1.3.2.1	Calibration curve, linearity, and range	76
3.1.3.2.2	Specificity	78
3.1.3.2.3	Accuracy	78
3.1.3.2.4	Precision	79
3.1.3.2.5	Limit of detection and limit of quantification	79
3.1.3.2.6	Robustness	80
3.1.3.2.7	Stability	80
3.1.4	Conclusion	81

3.2	Method II: HPLC-based analytical method for quantification of RIV	82
3.2.1	Introduction	82
3.2.2	Material and method.....	83
3.2.2.1	Material	83
3.2.2.2	Instrumentation	83
3.2.2.3	Chromatographic conditions.....	84
3.2.2.4	Preparation of standard solutions.....	84
3.2.2.5	Method validation	84
3.2.2.5.1	Specificity	85
3.2.2.5.2	Calibration curve, linearity, and range.....	86
3.2.2.5.3	Accuracy	86
3.2.2.5.4	Precision.....	86
3.2.2.5.5	Robustness	87
3.2.2.5.6	Limit of detection and limit of quantification.....	87
3.2.2.5.7	Stability study	87
3.2.3	Result and discussion	88
3.2.3.1	Method development	88
3.2.3.2	Method validation	90
3.2.3.2.1	Specificity	91
3.2.3.2.2	Calibration curve, linearity, and range.....	94
3.2.3.2.3	Accuracy	94

3.2.3.2.4	Precision.....	96
3.2.3.2.5	Limit of detection and limit of quantification.....	96
3.2.3.2.6	Robustness	96
3.2.3.2.7	Stability.....	97
3.2.4	Conclusion.....	98
3.3	Method III: Bioanalytical method for quantification of RIV in plasma and brain samples	99
3.3.1	Introduction	99
3.3.2	Material and method.....	100
3.3.2.1	Material.....	100
3.3.2.2	Instrumentation	100
3.3.2.3	Collection of blood and brain from rats.....	101
3.3.2.4	Sample extraction technique	101
3.3.2.5	Chromatographic conditions.....	102
3.3.2.6	Preparation of standard solutions.....	102
3.3.2.7	Method validation	103
3.3.2.7.1	Selectivity	103
3.3.2.7.2	Linearity, range, and calibration curve	103
3.3.2.7.3	Limit of detection and limit of quantification.....	103
3.3.2.7.4	Accuracy	103
3.3.2.7.5	Precision.....	103

3.3.2.7.6	Stability study	104
3.3.2.7.7	Dilution integrity.....	104
3.3.3	Result and discussion	104
3.3.3.1	Method validation	104
3.3.3.1.1	Selectivity	104
3.3.3.1.2	Calibration curve, linearity, and range.....	106
3.3.3.1.3	Limit of detection and limit of quantification.....	107
3.3.3.1.4	Accuracy	107
3.3.3.1.5	Precision.....	108
3.3.3.1.6	Recovery	108
3.3.3.1.7	Stability	109
3.3.4	Conclusion.....	111
	References	112
Chapter 4.....		118
4. Rivastigmine-DHA ion-pair complex improved loading in hybrid nanoparticles for better amyloid inhibition and nose-to-brain targeting in Alzheimer's.....		118
4.1	Introduction.....	119
4.2	Material and method	122
4.2.1	Material	122
4.2.2	RIV:DHA preparation for loading in LPH nanoparticles	123

4.2.3	RIV:DHA characterization	124
4.2.3.1	Percent complexation efficiency	124
4.2.3.2	Water/octanol partition coefficient	124
4.2.3.3	Particle size, zeta potential and viscosity measurements.....	124
4.2.3.4	Proton nuclear magnetic resonance spectroscopy (¹ H NMR).....	125
4.2.3.5	Fourier transform infrared spectroscopy (FTIR)	125
4.2.3.6	Molecular modeling	125
4.2.3.7	Differential scanning calorimetry (DSC) and powdered X-ray diffraction (PXRD).....	126
4.2.4	Preliminary screening of ingredients for LPH nanoparticles.....	126
4.2.5	LPH nanoparticles preparation loaded with RIV:DHA	128
4.2.6	In-vitro amyloid aggregation inhibition using LPH nanoparticles	130
4.2.6.1	ThT fluorescence Assay.....	130
4.2.6.2	Particle size and zeta potential measurements	131
4.2.6.3	ATR-FTIR spectroscopy and microscopy	131
4.2.7	Preparation of hydrogel embedded with LPH nanoparticles	131
4.2.8	Hydrogel rheological characterization	132
4.2.8.1	Scanning electron microscopy	132
4.2.9	Stability study	133
4.2.10	<i>In-vitro</i> drug release of RIV from LPH hydrogel	133
4.2.11	<i>Ex-vivo</i> permeation of RIV from hydrogel	134

4.2.12	<i>In-vivo</i> study in rats.....	134
4.2.12.1	Mucociliary clearance time.....	135
4.2.12.2	Pharmacokinetic study in rats	135
4.2.13	Histopathological study	136
4.2.14	Statistical analysis.....	137
4.3	Result and discussion.....	137
4.3.1	RIV:DHA complex preparation for loading in LPH nanoparticles	137
4.3.2	RIV:DHA characterisation.....	138
4.3.2.1	Complexation efficiency	138
4.3.2.2	Proton nuclear magnetic resonance spectroscopy.....	139
4.3.2.3	Fourier transform infrared spectroscopy.....	141
4.3.2.4	Particle size, zeta potential, and viscosity measurement	142
4.3.2.5	Differential scanning calorimetry and powder X-ray powder diffraction .	142
4.3.3	Preliminary screening of ingredients for LPH nanoparticle	143
4.3.4	LPH nanoparticles preparation loaded with RIV:DHA.....	144
4.3.5	<i>In-vitro</i> amyloid aggregation inhibition using LPH nanoparticles	151
4.3.6	Preparation of hydrogel loaded with LPH nanoparticles.....	157
4.3.7	Hydrogel rheological characterization.....	158
4.3.7.1	Scanning electron microscopy	159
4.3.7.2	Fourier transform infra-red analysis	161
4.3.8	Stability study	163

4.3.9	<i>In-vitro</i> drug release of RIV from hydrogel.....	163
4.3.10	<i>Ex-vivo</i> nasal permeation of RIV from hydrogel.....	165
4.3.11	<i>In-vivo</i> study in rats.....	166
4.3.11.1	Mucociliary clearance time.....	166
4.3.11.2	Pharmacokinetic study in rats	167
4.3.12	Histopathological study	173
4.4	Conclusion	174
	References	175
Chapter 5	189
5.	Rivastigmine-DHA ion-pair complex-based nanodispersion for improved nose-to-brain targeting in Alzheimer's disease	189
5.1	Introduction	190
5.2	Material and method.....	191
5.2.1	Material.....	191
5.2.2	Preparation and characterization of of RIV:DHA	192
5.2.3	Preliminary screening of surfactant for preparation of RIV:DHA ND.....	192
5.2.4	Preparation of RIV:DHA ND	192
5.2.5	Preparation of hydrogel loaded with RIV:DHA formulations.....	193
5.2.6	Hydrogel rheological characterisation	194
5.2.6.1	Scanning electron microscopy	194

5.2.6.2	Stability study	194
5.2.7	<i>In-vitro</i> drug release	195
5.2.8	<i>Ex-vivo</i> nasal permeation	195
5.2.9	<i>In-vivo</i> study in rats.....	196
5.2.9.1	Mucociliary clearance time.....	196
5.2.9.2	Pharmacokinetic study in rats	197
5.2.10	Histopathological study	198
5.2.11	Statistical analysis.....	198
5.3	Result.....	199
5.3.1	Preparation and characterization of RIV:DHA.....	199
5.3.2	Preliminary screening of surfactant for preparation of RIV:DHA ND.....	199
5.3.3	Preparation of RIV:DHA ND	199
5.3.4	Hydrogel rheological characterization.....	200
5.3.4.1	Scanning electron microscopy	201
5.3.4.2	Stability study	202
5.3.5	<i>In vitro</i> drug release study.....	203
5.3.6	<i>Ex-vivo</i> nasal permeation	204
5.3.7	Pharmacokinetic study in rats	205
5.3.7.1	Mucociliary drug clearance.....	205
5.3.7.2	Pharmacokinetic study in rats	205
5.3.8	Histopathological study	208

5.4	Conclusion.....	209
	References.....	210
Chapter 6.....		215
6.	Chitosan-coated liposomes embedded into <i>in-situ</i> gel system improved nose-to-brain targeting of rivastigmine in Alzheimer’s disease.....	215
6.1	Introduction	216
6.2	Material and method.....	218
6.2.1	Material.....	218
6.2.2	Preparation of RIV-HT Liposome and CHT@RIV-HT Liposome	219
6.2.3	<i>In-vitro</i> characterisation	221
6.2.3.1	Particle size, polydispersity index, zeta potential and percent encapsulation efficiency.....	221
6.2.3.2	Transmission electron microscopy	221
6.2.4	Preparation of <i>in-situ</i> gel loaded with RIV-HT Liposome and CHT@RIV-HT Liposome	222
6.2.5	Rheological characterization of <i>in-situ</i> gel	222
6.2.6	Stability studies.....	223
6.2.7	<i>In-vitro</i> drug release	223
6.2.8	<i>Ex-vivo</i> nasal drug permeation.....	223
6.2.9	Pharmacokinetic study in rats	224

6.2.9.1	Intranasal dosing	225
6.2.9.2	Mucociliary clearance time.....	225
6.2.9.3	Brain distribution and plasma pharmacokinetic study in rats.....	225
6.2.10	Histopathological examination.....	226
6.2.11	Statistical analysis	227
6.3	Result and discussion	227
6.3.1	Preparation of RIV-HT Liposome and CHT@RIV-HT Liposome	227
6.3.2	<i>In-vitro</i> Characterization	230
6.3.2.1	Particle size, PDI, zeta potential, percent encapsulation efficiency	230
6.3.2.2	Transmission electron microscopy	232
6.3.3	Preparation of <i>in-situ gel</i> loaded with RIV-HT Liposome and CHT@RIV-HT Liposome.....	233
6.3.4	Rheological characterization of <i>in-situ gel</i>	234
6.3.5	Stability study.....	236
6.3.6	<i>In-vitro</i> drug release	237
6.3.7	<i>Ex-vivo</i> nasal drug permeation	239
6.3.8	<i>In-vivo</i> study in rats	241
6.3.8.1	Mucociliary clearance time.....	241
6.3.8.2	Brain distribution and plasma pharmacokinetic study in rats.....	241
6.3.9	Histopathological examination.....	246
6.4	Conclusion	247

References	249
Chapter 7	256
7. Future Scope of work.....	256
<i>Appendix 1</i>	<i>A1</i>
<i>Appendix 2</i>	<i>A2</i>

Acknowledgment

I take this opportunity to thank each and every person who has made this research work possible. Foremost I would like to thank my research supervisor, **Prof. Murali Monohar Pandey** for giving me constant support, guidance, and motivation throughout my Ph.D. tenure. His mentorship helped me throughout my Ph.D. and without his effort this work would have not been possible. His sheer dedication and perseverance towards research have immensely helped me in completing my research work. His teachings are not restricted to research but are beneficial in the professional world too. I will cherish the experience that I have gained under his supervision throughout my life.

I would express my gratitude towards **Prof. Gautam Singhvi** (Doctoral Advisory Committee Member), for his valuable guidance and input in my research work. His guidance and support have strongly benefited me in all aspects from my research work to the development of my personality.

I would like to especially thank **Prof. Deepak Chitkara** (Doctoral Advisory Committee member) for his valuable teaching and for providing insight into the research work. I would also thank him for providing a research facility at times.

I would like to express my heartfelt thanks to our collaborator **Dr. Himanshu Kathuria** for his constant support and recommendation. His prodigious assistance throughout my Ph.D. tenure through his valuable research ideas and suggestions has benefitted me in improvising my writing work.

I sincerely thank **Prof. V. Ramgopal Rao** (Vice-Chancellor), **Prof. A.K. Sarkar** (Ex. Director, BITS-Pilani, Pilani Campus), **Prof. Sudhir Kumar Barai** (Director, BITS-Pilani, Pilani Campus), **Col. Soumyabrata Chakraborty** (Registrar, BITS Pilani), **Prof. Venkata Vamsi Krishna Venuganti** (Dean, AGSRD, BITS Pilani), **Prof. Anil Gaikwad** (Head, Department

of Pharmacy, BITS-Pilani, Pilani Campus), **Prof. Shamik Chakraborty** (Associate Dean, AGSRD, BITS-Pilani, Pilani Campus) for providing all resources to complete my research work. I would thank external examiners Prof. Gaurav Kumar Jain and Prof. Brahmeshwar Mishra for reviewing the thesis.

I would like to extend my thanks to all faculties of Department of Pharmacy BITS Pilani for their immense cooperation and support for making my Ph.D journey a prolific experience. I thank **Prof. R. Mahesh, Prof. Hemant Jadhav, Prof. S. Murugesan, Prof. Atish T. Paul, Prof. Rajeev Taliyan, Dr. Sunil Kumar Dubey, Prof. Gautam Singhvi, Prof. Anupama Mittal, Prof Anil Jindal, Prof. Sandeep Sundriyal, Dr. Richa Shrivastava** for their cooperation during my research program. I would like to extend my gratitude towards **Dr. Sushil Yadav** (Senior veterinarian in-charge, Animal house facility) for his teachings of animal handling practices and authority guidelines. I would also like to thank BITS Pilani for giving me this opportunity to perceive my Ph.D and for providing advanced research facility that has immensely enhanced the quality of my research work. I would also like to thank BITS Pilani for providing institutional fellowship throughout my research. I would also thank DBT for providing research fellowship.

This acknowledgement would be partial without acknowledging the names of my beloved family members, my mother, (Mrs. Vanita Hinge and Dr. Sunanda Pukale), father (Mr. Sudesh Pukale), sister (Ms. Ankita Hinge) and my brother (Mr. Prathamesh Hinge) for always guiding me and strongly standing behind me at tough times. Their unconditional love and affection are pillar of my life.

I express my heartfelt gratitude towards my Ph.D. labmates Mrs. Paramita Saha whose research expertise has contributed me in my research work. A very heartfelt thanks to my Ph.D. lab mate Miss. Shivangi Nema and Mr. Yash Patidar for sharing their new ideas and experiences. A good

time with them will always be cherished. I would also like to thank master's thesis students Mr. Souradeep Bose, Miss. Anjana, Miss Kalpashree for their valuable assistance. Apart from this I would like to thank my lab mates Dr. Saurabh Sharma, Dr. K.V. Krishna, Dr. Kishan Italiya, Dr. Dhanashree Surve, Dr. Pracheta Sengupta, Dr. Vamshi Krishna for their expertise and timely help. I would like to extend my thanks to my friends, Somya Agarwal, Arihant Singh, Moumita Basak, Rajesh Pradhan, Prabhjeet Singh, Kavyashree, Vidyashree, Shwetha, Swati Sharma, Shikha.

Atlas this acknowledgement would be incomplete without thanking people very close to my heart, Mr. Subhash Hinge and Dr. Sudeep Pukale. Thank you for always inspiring me to keep up the good work. Your motivation has always swayed me through my tough times. This work would have really not been possible without your immense faith in me and it's difficult to thank you in any possible way.

Above all, I would like to thank ALMIGHTY GOD for making me lucky to experience this good time.

“Alone we can do little; together we can do so much”.....Helen Keller

(Nikita Hinge)

List of Abbreviations

AD	Alzheimer's disease
AB ₁₋₄₂	Amyloid beta ₁₋₄₂
NFT	Neurofibrillary tangles
AChEI	Acetylcholinesterase inhibitor
RIV-HT	Rivastigmine hydrogen tartrate
BBB	Blood-brain barrier
CNS	Central nervous system
ICH	International Council for Harmonization
HPLC	High performance liquid chromatographic
LOD	Limit of detection
LOQ	Limit of quantification
CHT	Chitosan
DTE	Drug transport efficiency
DTP	Drug transport permeation
PK	Pharmacokinetic
IPC	Ion-pair complex
ND	Nanodispersion
LPH	lipid polymer hybrid
C _{max}	Maximum concentration
MRT	Mean residence time
AUC	Area under curve
CTF	C-terminus fragment
APP	Amyloid precursor protein

CSF	Cerebrospinal fluid
IAEC	Institutional Animal Ethics Committee
N2B	Nose-to-brain
SLN	Solid lipid nanoparticles
NLC	Nanostructure lipid carriers
PLGA	Poly(lactic-co-glycolic) acid
IN	Intranasal
NP	Nanoparticle
PDI	Polydispersity index
LLQC	Lower limit of quantification
LQC	Low quality control
MQC	Medium quality control
HQC	High quality control
RSD	Relative standard deviation
QC	Quality control
LC-MS-MS	Liquid chromatography-tandem mass spectrometry
IS	Internal standard
VEL	Venlafaxine hydrochloride
PBS	Phosphate buffer saline
TEM	Transmission electron microscopy
FESEM	Field emission scanning electron microscopy
DHA	Docosahexaenoic acid
GMS	Glyceryl monostearate
ThT	Thioflavin-T
DLS	Dynamic light scattering

LVER	Linear viscoelastic range
ANOVA	Analysis of variance
FTIR	Fourier transform infra-red analysis
NMR	Nuclear magnetic resonance
~	Equivalent
>	More than
<	Less than
o C	Degree centigrade
%	Percentage
mg	Milligram
gm	Gram
µg	Microgram
ng	Nanogram
cm	Centimeter
min	Minute
h	Hour
s	Second
nm	Nanometer
±	Plus or minus
=	Equal to
mL	Millilitre
L	Litre
rpm	Rotations per minute
mV	Millivolt
G'	Storage modulus

G''	Loss modulus
mPa	Millipascal
Pa	Pascal
Cp	Centipoise
PEG	Polyethylene glycol
t _{1/2}	Half-life
R ²	Regression coefficient
EDTA	Ethylene diamine tetra acetic acid
CAN	Acetonitrile
IPA	Iso-propyl alcohol
<i>p</i> value	Significance level in statistical tests

List of Tables

Table 1.1. List of nanotherapeutics for N2B delivery of Alzheimer’s disease.....	24
Table 2.1. Physicochemical properties of RIV-HT	63
Table 3.1. Analytical parameters of RIV-HT-based fluorescence method.....	76
Table 3.2. Specificity data for pure drug and drug-loaded formulation components. Standard concentration of 0.1 µg/mL was utilized for analysis (n = 5).....	78
Table 3.3. Accuracy data at different quality control levels (n = 3)	78
Table 3.4. Precision data at different quality control levels	79
Table 3.5. Robustness data at different pH conditions	80
Table 3.6. Stability data at different storage conditions	81
Table 3.7. Optimization of mobile phase using 100 ng/mL RIV-HT solution (n = 3)	89
Table 3.8. Chromatographic condition representing system suitability parameters	90
Table 3.9. Assay of RIV-HT solution in presence of varying stress conditions using 500 ng/mL RIV-HT solution (n = 3)	93
Table 3.10. Accuracy data at different quality control levels (n = 3)	95
Table 3.11. Precision data at different quality control levels	96
Table 3.12. Robustness data at different chromatographic conditions	97
Table 3.13. Stability data at different storage conditions	97
Table 3.14. Accuracy data at different quality control levels (n = 3)	107
Table 3.15. Precision data at different quality control levels	108
Table 3.16. Stability data at different storage conditions	110
Table 4.1 Effect of formulation parameters on characteristics of RIV:DHA LPH(+ve).....	146
Table 4.2. Effect of formulation parameters on characteristics of RIV:DHA LPH(-ve).....	148
Table 4.3. Characteristics of RIV:DHA LPH nanoparticles. Data is presented as mean ± SD (n = 3).....	151

Table 4.4. RIV:DHA LPH loaded gels representing viscosity, storage modulus and $\tan \delta$ at different oscillatory frequencies	
Viscosity of RIV:DHA LPH loaded gels (at 20 °C and 33 °C) and storage modulus at 33 °C	159
Table 4.5. Kinetic parameters of RIV release from RIV:DHA based nanoformulations	165
Table 4.6. Permeation kinetics of RIV:DHA LPH loaded hydrogel.	166
Table 4.7 Brain and plasma PK parameters after intranasal administration of RIV-HT gel, RIV:DHA LPH(+ve) gel and RIV:DHA LPH(-ve) gel	172
Table 5.1. Brain and plasma P.K. parameters after intranasal administration of RIV-HT gel, RIV:DHA ND gel formulation.....	207
Table 6.1. Effect of formulation parameters on characteristics properties of rivastigmine formulations (n = 3)	230
Table 6.2. Formulation characteristics of RIV-HT Liposome and CHT@RIV-HT Liposome formulation.....	232
Table 6.3. RIV-HT Liposome and CHT@RIV-HT Liposome loaded gels representing viscosity, storage modulus and $\tan \delta$ values at different oscillatory frequencies	235
Table 6.4 . R^2 values for different <i>in-vitro</i> drug release models of rivastigmine formulations	239
Table 6.5. Permeation kinetics of RIV-HT Liposome gel and CHT@RIV-HT Liposome gel formulation.....	240
Table 6.6. Brain and plasma PK parameters after intranasal administration of RIV-HT gel, RIV-HT Liposome gel and CHT@RIV-HT Liposome gel	245

List of Figures

Fig. 1.1. Pathophysiology of Alzheimer's disease. It shows amyloid- β monomers form oligomers and aggregates to form plaques, damaging neurons and accumulation of $A\beta_{1-42}$ in blood vessels.	6
Fig. 1.2. Schematic representation showing intranasal nanocarriers absorption pathways to the brain. It shows the nasal respiratory epithelium pathway, olfactory pathway, and trigeminal nerve pathway. The cellular endocytic uptake mechanism is also shown.	17
Fig. 2.1. Chemical structure of rivastigmine hydrogen tartrate	61
Fig. 2.2. (A) SEM of RIV-HT shows the presence of plate-like structure, (B) DSC, (C) X-ray diffraction graph exhibit polymorphic Form I and (D) represents FTIR spectra of RIV-HT, Form I shows carbamate absorption at 1720 cm^{-1}	62
Fig. 3.1. Overlay spectra of calibration curve concentrations	77
Fig. 3.2. Graph represents calibration curve of concentration vs fluorescence intensity graph.	77
Fig. 3.3. Chromatogram of (A) RIV-HT standard solution (500 ng/mL) and forced degradation study demonstrating the specificity of the drug in presence of (B) acid, (C) base, (D) water, (E) H_2O_2 , (F) temperature and (G) UV light. (H) Represents chromatogram of blank formulation matrix, (I) RIV-HT loaded formulation matrix, and specificity of the drug in presence of (J) <i>in-vitro</i> release medium and (K) <i>ex-vivo</i> permeation medium.....	92
Fig. 3.4. Calibration curve of RIV-HT representing linearity range within 25-600 ng/mL	94
Fig. 3.5. Representative overlay of blank and RIV-HT at LQC (30 ng/mL), MQC (300 ng/mL) and HQC (500 ng/mL) concentrations.....	95
Fig. 3.6. Overlay of Blank, LLQOC, LQC, MQC and HQC sample of (A) brain and (B) plasma matrices representing selectivity of the method with presence of no interfering peak at the retention time of RIV-HT and internal standard.....	105

Fig. 3.7. Graph represents calibration curve of (A) brain and (B) plasma matrices.....	106
Fig. 4.1. Schematic showing the preparation of RIV:DHA ion pair complex. The alkalized RIV-HT mixed with equal parts of DHA gave ion pair complex (RIV:DHA), which was purified and concentrated to get a semisolid mass. Aq.: Aqueous; DHA: docosahexaenoic acid RIV-HT: Rivastigmine hydrogen tartrate; RIV: Rivastigmine.....	123
Fig. 4.2. Image represents screening of lipids, oils, surfactant, and composition of RIV:DHA LPH(+ve) and RIV:DHA LPH(-ve) based formulation	127
Fig. 4.3. Schematic showing (A) loading of RIV using RIV-DHA to prepare RIV:DHA LPH(+ve) and RIV:DHA LPH(+ve) gel (B) loading of RIV using RIV-DHA to prepare RIV:DHA LPH(-ve) and RIV:DHA LPH(-ve) gel. DHA: docosahexaenoic acid; DCM: dichloromethane; GMS: glyceryl monostearate; PEG: polyethylene glycol; LPH: Lipid polymer hybrid nanoparticles; PLGA: Poly (lactic-co-glycolic acid); RIV: Rivastigmine, RIV:DHA: RIV and DHA ion pair complex.	129
Fig. 4.4. Chemical structure of (A) RIV-HT, (B) DHA, (C) RIV and (D) RIV:DHA (1:1 molar ratio).....	138
Fig. 4.5. (A) Proton NMR of RIV-HT, DHA and RIV:DHA demonstrate the formation of complex at 1:1 molar ratio. (B) FTIR spectra representing the formation of RIV:DHA. (C) DSC thermogram of RIV-HT, physical mixture and RIV:DHA showed conversion into amorphous form after formation of IPC, (D) X-ray diffraction studies of RIV-HT, physical mixture and RIV:DHA (1:1 ratio) demonstrate amorphous form of IPC. DHA: docosahexaenoic acid; RIV: Rivastigmine; RIV-HT: Rivastigmine hydrogen tartrate, RIV:DHA: RIV and DHA ion pair complex.....	140
Fig. 4.6. Solubility studies of RIV:DHA in (A) 0.5% w/v surfactants, (B) solid lipids and (C) liquid lipids/oils. DHA: docosahexaenoic acid; RIV: Rivastigmine; RIV:DHA: RIV and DHA ion pair complex	143

Fig. 4.7. Photographic image represents physical appearance of (A) RIV:DHA LPH(-ve), (B) RIV:DHA LPH(+ve). (C) and (D) represent particle size distribution and zeta potential of RIV:DHA LPH(-ve) and RIV:DHA LPH(+ve) formulation. DHA: docosahexaenoic acid; RIV: Rivastigmine; RIV:DHA: RIV and DHA ion pair complex, LPH: Lipid polymer hybrid nanoparticles 149

Fig. 4.8. Schematic representation, A) sample preparation of amyloid β_{1-42} treated with drug equivalent varying concentrations (50, 100, 200, 400 ng/mL) of RIV:DHA LPH(+ve) and RIV:DHA LPH(-ve). (B) Represents *in-vitro* amyloid inhibition, evaluating particle size and ThT fluorescence intensity of cationic and anionic LPH nanoparticles at different concentrations (50, 100, 200, 400 ng/mL). C) Demonstrate the concentration of RIV:DHA LPH(+ve) and RIV:DHA LPH(-ve) with maximum amyloid inhibition was characterized for ATR-FTIR analysis and microscopic observation at 6, 12, 24 and 48 h. The zeta-potential and ThT fluorescence intensity of (D) RIV:DHA LPH(+ve) and (E) RIV:DHA LPH(-ve) at 50, 100, 200 and 400 ng/mL concentration. DHA: docosahexaenoic acid; RIV: Rivastigmine; RIV:DHA: RIV and DHA ion pair complex, LPH: Lipid polymer hybrid nanoparticles..... 152

Fig. 4.9. (A) Fluorescent microscopic images of *in-vitro* $A\beta_{1-42}$ aggregation inhibition in presence and absence of RIV:DHA LPH(+ve) and RIV:DHA LPH(-ve), at various intervals. RIV:DHA LPH(+ve) (400 ng/mL) showed enhanced inhibition in comparison to RIV:DHA LPH(-ve) (50 ng/mL), demonstrating the presence of insoluble amyloid fibrils at 6 h, while that was reduced at 12 h. At 24 and 48 h, it showed the presence of soluble fibrils and soluble amyloid oligomers. Whereas RIV:DHA LPH(-ve) had insoluble amyloid fibrils and oligomer at all intervals of 6, 12, 24, and 48 h, exhibiting lesser and slower inhibition than RIV:DHA LPH(+ve) (magnification: 40x, scale bar: 50 μ m). B) and C) represents ATR FTIR spectra of RIV:DHA LPH(+ve) and RIV:DHA LPH(-ve) treated $A\beta_{1-42}$ exhibiting decreased absorbance at different intervals. RIV:DHA LPH(+ve) showed comparatively reduced $A\beta_{1-42}$ fibrils and

A β ₁₋₄₂ oligomers in comparison to RIV:DHA LPH(-ve) at respective interval. DHA: docosahexaenoic acid; RIV: Rivastigmine; RIV:DHA: RIV and DHA ion pair complex, LPH: Lipid polymer hybrid nanoparticles..... 154

Fig. 4.10. Bright field microscopic images of *in-vitro* amyloid beta inhibition in presence and absence LPH, representing phosphate buffer as control (without LPH) at various time intervals. RIV:DHA LPH(+ve) (400 ng/mL) showed enhanced inhibition in comparison to RIV:DHA LPH(-ve) (50 ng/mL) demonstrating presence of insoluble amyloid fibrils at 6 h, while that has been observed to be significantly reduced at 12 h. At 24 and 48 h, it showed presence of soluble fibrils and soluble amyloid oligomers. Whereas RIV:DHA LPH(-ve) represents presence of insoluble amyloid fibrils and oligomer at all time intervals of 6, 12, 24 and 48 h exhibiting comparatively lesser and slower inhibition in comparison to RIV:DHA LPH(+ve) (magnification: 40x, scale bar: 50 μ m). 156

Fig. 4.11. Image (A) represents preliminary testing of sol-to-gel conversion with inversion tube test, (B) Temperature vs viscosity of, RIV:DHA LPH(-ve) gel and RIV:DHA LPH(+ve) gel representing viscosity at 33 $^{\circ}$ C. Storage modulus and loss modulus of RIV:DHA LPH(-ve) gel and RIV:DHA LPH(+ve) gel representing hydrogel behaviour at different (C) temperature and (D) angular frequency 157

Fig. 4.12. FE-SEM micrograph of (A) RIV-HT (Magnification: 30000X, scale bar: 2 μ m), (B) RIV:DHA (1:1 molar ratio) (C) RIV:DHA LPH(-ve) (D) RIV:DHA LPH(-ve) gel, (E) RIV:DHA LPH(+ve) and (F) RIV:DHA LPH(+ve) gel (Magnification: 100000X, scale bar: 500nm 160

Fig. 4.13. FTIR spectra of RIV:DHA (1:1molar ratio), blank LPH(-ve), blank LPH(-ve) gel, RIV:DHA LPH(-ve) and RIV:DHA LPH(-ve) gel to evaluate encapsulation of RIV:DHA into LPH based nanoformulation 161

Fig. 4.14. FTIR spectra of RIV:DHA (1:1 molar ratio), blank LPH(+ve), blank LPH(+ve) gel, RIV:DHA LPH(+ve) and RIV:DHA LPH(+ve) gel to evaluate encapsulation of RIV:DHA into LPH based nanoformulation 162

Fig. 4.15. Image represents stability indicating graph of (A) RIV:DHA LPH(-ve) gel and (B) RIV:DHA LPH(+ve) gel evaluated on particle size (nm), PDI, zeta potential (mV) vs time (days). The graph represented no significant increase in particle size, PDI, of nanoparticles upto 180 days, representing stability of formulation upto 6 months. 163

Fig. 4.16. (A) *In-vitro* cumulative drug release representing sustained RIV release from RIV:DHA LPH gel upto 72 h. (B) *Ex-vivo* permeation study representing improved drug permeation efficiency of RIV:DHA LPH across nasal epithelium. (C) Steady-state flux of RIV:DHA LPH gels and RIV-HT gel. (D) Schematic showing mechanism for improved drug permeation of LPH nanoparticle across the nasal epithelium..... 164

Fig. 4.17. *In-vivo* studies of RIV:DHA LPH(-ve) gel, RIV:DHA LPH(+ve) gel and RIV-HT gel (2 mg/kg) showed (A) significantly increased mucociliary clearance time of RIV:DHA LPH(+ve) gel (* signify $p < 0.05$, ** represents $p < 0.005$). (B) Brain profile of RIV formulations demonstrate significantly improved brain concentrations and mean residence time of RIV in RIV:DHA LPH(+ve) gel. (C) Represents plasma profile of RIV formulations in which RIV gel showed distinctly higher plasma concentrations, while RIV:DHA LPH(-ve) gel and RIV:DHA LPH(+ve) gel showed comparatively reduced plasma concentration of RIV. ‘^’ show data points which were analysed but could not be quantified as these were below quantifiable limit..... 168

Fig. 4.18. *In-vivo* study demonstrate comparative evaluation of RIV formulations in brain at 0.75, 2, 6, 12 and 24 h. RIV:DHA LPH(+ve) gel demonstrated distinctly improved brain concentrations at all time points as compared to RIV:DHA LPH(-ve) gel and RIV-HT gel (*

signify $p < 0.05$, ** represents $p < 0.005$, *** represents $p < 0.001$, **** represents $p < 0.0001$ and NS signify no significant difference..... 170

Fig. 4.19 Hematoxylin and eosin stained histopathological specimen of rat brain and nasal epithelium upon intranasal administration of RIV:DHA LPH(-ve) gel and RIV:DHA LPH(+ve) gel (2 mg/kg). Microscopic observation of brain tissue showed normal morphological structures with no alterations in brain. The nasal epithelium also showed an intact, normal structure of pseudostratified ciliated columnar cells compared to the control group. 5x, 20x and 40x shows magnification of objective lens, where eyepiece lens magnification was 10x. Black arrow: Cerebral cortex, Yellow arrow: Hippocampus, Red arrow: Ciliated columnar cells.. 173

Fig. 5.1. Schematic representation for preparation of RIV:DHA ND and RIV:DHA ND gel. RIV:DHA was dissolved in DCM and organic phase was dropwise added to 0.5% w/v tween 80 solution, and reduced using probe sonication. DCM was evaporated and resultant RIV:DHA ND was loaded into poloxamer-based hydrogel. DCM: Dichloromethane, RIV:DHA: RIV, DHA ion pair complex, Aq: Aqueous, rpm: Rotation per minute, P407: Poloxamer 407, P188: Poloxamer 188. 193

Fig. 5.2. Image represents (A) particle size and (B) zeta potential of RIV:DHA ND.....200

Fig. 5.3. (A) Graph of temperature vs viscosity of RIV:DHA ND gel representing viscosity at 33° C. Graph demonstrates storage modulus and loss modulus of RIV:DHA ND gel representing hydrogel behavior at different (B) temperature and (C) angular frequency.201

Fig. 5.4. SEM micrographs of (A) RIV-HT (Magnification: 5000X, scale bar: 2µm), (B) RIV:DHA (1:1 molar ratio), (C) RIV:DHA ND and (D) RIV:DHA ND gel (Magnification: 100000X, scale bar: 500nm).202

Fig. 5.5. Image represents stability study of RIV:DHA ND gel at refrigerated condition. The graph represented no significant increase in particle size, PDI of nanodispersion gel up to 90 days, representing stability of formulation upto 3 months.203

Fig. 5.6. *In-vitro* drug release profile from (A) RIV:DHA ND gel and (B) *ex-vivo* nasal permeation study showing the amount of drug permeated in case of RIV:DHA ND gel. (C) Represents improved steady-state flux of RIV:DHA ND gel as compared to RIV-HT gel..204

Fig. 5.7. (A) significantly increased mucociliary clearance time of RIV:DHA ND gel formulation (* signify $p < 0.05$ and N.S. signify no significant difference). (B) Brain profile of RIV-HT formulations demonstrate significantly improved brain concentrations and mean residence time of RIV in RIV:DHA ND gel formulation. (C) Represents plasma profile of RIV-HT formulations in which RIV-HT gel showed higher plasma concentrations and RIV:DHA ND gel showed comparatively reduced plasma concentration of RIV-HT.206

Fig. 5.8. Histopathological evaluation of nasal and brain tissue after intranasal administration of RIV:DHA ND gel were compared with control group. The microscopic images of brain showed no signs of damage/toxicity in cerebral cortex and hippocampus. Nasal tissue also showed intact morphological structure of pseudostratified ciliated columnar cells of RIV:DHA ND gel formulation as that of control group.....208

Fig. 6.1. Schematic representation for preparation of RIV-Liposome gel and CHT@RIV-Liposome gel formulation. The lipid thin film constituting S100:cholesterol was hydrated with drug solution, and reduced to form RIV-Liposome. Subsequent chitosan-coating of RIV-Liposome were loaded into thermoresponsive gel.RIV-Liposome: Rivastigmine liposome; CHT@RIV-Liposome: Chitosan coated rivastigmine liposome; Sol.: Solution220

Fig. 6.2. (A) and (B) represents particle size and zeta potential of RIV-HT Liposome and CHT@RIV-HT Liposome formulation. (C) Represents physical appearance and TEM images of RIV-HT Liposome and CHT@RIV-HT Liposome demonstrating surface morphology, particle size and chitosan coating in case of CHT@RIV-HT Liposome.231

Fig. 6.3. (A) Represents physical appearance and transition of sol-to-gel state at 33° C. (B) Demonstrate temperature-dependent viscosity of RIV-HT Liposome and CHT@RIV-HT

Liposome based gel formulations. (C) Represents temperature and (D) frequency dependent storage and loss modulus for liposome loaded gel formulations.233

Fig. 6.4. Represents (A) stability of CHT@RIV-HT Liposome for 90 days. (B) Shows increased particle size, PDI and zeta potential of RIV-HT Liposome gel at 30 days, thus demonstrating the stability of formulation upto 20 days. (C) SEM images represent particle size and spherical shape of CHT@RIV-HT Liposome (D) exhibiting no aggregation after loading into *in-situ* gel based system.237

Fig. 6.5. Represents comparative evaluation of (A) *in-vitro* drug release, (B) amount of drug permeated across nasal mucosa and (C) steady-state flux of RIV-HT Liposome gel, CHT@RIV-HT Liposome gel and RIV-HT gel formulation. (D) represents a mechanistic approach for improved drug nasal permeation of CHT@RIV-HT Liposome gel formulation.238

Fig. 6.6. (A) demonstrates significantly increased mucociliary clearance time of CHT@RIV-Liposome gel formulation (* signify $p < 0.05$ and NS signify no significant difference). (B) Brain profile of RIV formulations demonstrate significantly improved brain concentrations and mean residence time of RIV in CHR@RIV-Liposome gel formulation. (C) Represents plasma profile of RIV formulations in which RIV gel showed higher plasma concentrations and RIV-Liposome gel and CHT@RIV-Liposome gel formulations showed comparatively reduced plasma concentration of RIV. ‘^’ represents data points that were analyzed but are present below the quantifiable limit.244

Fig. 6.7. Histopathological evaluation of nasal and brain tissue after intranasal administration of RIV-HT Liposome gel and CHT@RIV-HT Liposome gel formulations were compared with control group. The microscopic images of brain showed no signs of damage/toxicity in cerebral cortex and hippocampus. Nasal tissue also showed the intact morphological structure of

pseudostratified ciliated columnar cells of RIV-HT Liposome gel and CHT@RIV-HT
Liposome gel formulation as that of control group.246

Abstract

Alzheimer's disease (AD) is a complex, multifactorial neurodegenerative disorder prevalent in older adults above age 65 years. In recent years, this number is also growing in young adults aged 40-50 years, termed early-onset AD. It is usually characterized by early signs of mild dementia and impaired cognition with a gradual decline in memory, thinking, and decision-making, progressively culminating into abnormal behavior and social skills. Sometimes, it also leads to psychiatric symptoms such as apathy and depression. The condition progressively worsens, affecting daily activities and relationships with the overall decline in mental and behavioral functions. In severe stages, neurodegeneration leads to inability of the patient to perform routine activities such as thinking, decision-making, walking, speaking, swallowing etc. At the end-stage, the patient eventually becomes bedridden. The increasing population of Alzheimer's patients and the economic toll on several countries have made Alzheimer's a major global concern. It accounts for a global economic burden of around 1 trillion US dollars and is estimated to increase twice by 2030.

Alzheimer's disease hallmarks lesions, senile plaques constituting extracellular deposition of amyloid beta plaques ($A\beta_{1-42}$) and neurofibrillary tangles (NFT) formed by abnormal accumulation of tau proteins. The progressive accumulation of $A\beta_{1-42}$ and NFT hamper neurochemical transmission resulting in neurotoxicity and neurodegeneration. It is well-known that cholinergic synapses are particularly affected in AD. So, treatment involves drugs that particularly target the cholinergic pathway. The approved acetylcholinesterase inhibitor (AChEI) includes rivastigmine, donepezil, and galantamine. They are usually prescribed for the treatment of mild to moderate AD. Another class of drug under NMDA receptor antagonist includes memantine preferred for treating moderate to severe AD. Amongst all classes of drugs, rivastigmine hydrogen tartrate (RIV-HT) is the only dual-acting AChE inhibitor widely used

in the treatment of Alzheimer's. Its cholinergic action delays the degradation of acetylcholine, facilitating cholinergic transmission. Its marketed formulation is available as oral capsule and solution. However, marketed formulations have limited brain access due to restrictions imposed by the blood-brain barrier (BBB), enforcing a significant challenge in achieving therapeutic efficacy. Hydrophilic RIV-HT hinders drug passage across BBB, resulting in lesser drug concentration in the brain. RIV-HT exhibits shorter half-life due to extensive first-pass metabolism. The low oral bioavailability (36%) also results in limited drug concentration in the brain. Therefore, oral therapy with RIV-HT necessitates frequent dosing, which in turn leads to intra-individual variability, and requires repetitive dose administration. Frequent dose administration often leads to gastrointestinal tract-mediated side effects and hepatotoxicity in some cases. Therefore, suitable delivery systems are needed to efficiently deliver the drugs into central nervous system (CNS), with minimal drug exposure to peripheral organs. Several studies have acclaimed the benefits of the intranasal drug delivery route. It has an unrivalled ability to overcome the drawbacks of current therapies and encompasses the vast potential to achieve effective intranasal brain targeting of actives. It offers enormous therapeutic opportunities in ameliorating AD with rapid onset of action, improved patient compliance, enhanced therapeutic efficacy, and avoidance of pre-systemic metabolism. However, nasal delivery does have a few shortcomings. It includes distribution of drugs in systemic circulation due to limited permeability through the nasal cavity, lack of site-specific targeting to CNS areas, enzymatic degradation of actives, insufficient CNS bioavailability, restrictions due to nasal anatomy, dose limitation, etc. Nose-to-brain delivery has been revolutionized with nanotechnology-based drug delivery systems that can overcome these problems. It offers protection to drugs from enzymatic degradation. In addition, it comprises advantages such as targeted therapy, sufficient brain bioavailability, extended therapeutic action, lesser systemic absorption of actives etc.

The research work disclosed in the present thesis entitled “**Rivastigmine-Loaded Nanocarriers for Improved Nose-to-Brain Delivery: Design, Development and Pharmacokinetic Evaluation**”. The research work includes fabrication and optimization of nanocarrier systems and further *in-vivo* evaluation of pharmacokinetic profile and parameters in brain and plasma of Wistar rats. Various analytical methods were developed for the analysis of the designed formulation. A fluorescence-based analytical method was developed and validated as per protocol specified by the International Council for Harmonization (ICH). The linearity and range of the validated method was observed within 0.1-20 µg/mL in pH 6.4 phosphate buffer solution. The next stage of formulation development demanded a sensitive high-performance liquid chromatographic (HPLC) method for estimating drug in stability samples, *in-vitro* release and *ex-vivo* permeation samples. The developed method demonstrated linearity within 0.25-600 ng/mL with a limit of detection (LOD) and limit of quantification (LOQ) values as 7.32 and 24.15 ng/mL. The forced degradation study of RIV-HT also ensured the specificity of the proposed HPLC method. Furthermore, bioanalytical method was developed in plasma and brain matrices for pre-clinical pharmacokinetic evaluation of RIV-HT formulations. The mobile phase consisted of A: acetonitrile constituting 0.05% (v/v) triethylamine, B: pH 6 phosphate buffer (10 mM), and C: iso-propyl alcohol with the composition of 36:60:4 (%A:%B:%C) at a flow rate of 0.8 mL/min. For brain and plasma samples, the method was linear within 50-1000 ng/mL with LOD, and LOQ values as 15.47 and 46.90 ng/mL in brain matrices and 15.03 and 45.56 ng/mL in plasma.

The initial formulation approach describes the development of hydrophobic ion-pair complex (IPC) of RIV-HT to improve encapsulation efficiency of lipid polymer hybrid (LPH) nanoparticles. The IPC was developed using varying molar ratios of docosahexaenoic acid (DHA). The micron-sized RIV:DHA IPC (RIV:DHA) was reduced to RIV:DHA-based nanodispersion (RIV:DHA ND) for improved drug permeation efficiency. Furthermore,

RIV:DHA was loaded into hybrid-based nanoparticle system for further improvement in permeation efficiency, *in-vitro* drug release and *in-vivo* brain pharmacokinetic profile. Hybrid nanoparticles comprising opposite charges, *viz.* cationic (RIV:DHA LPH(+ve)) and anionic LPH (RIV:DHA LPH(-ve)) were developed. The study investigated the effect of LPH surface charge on *in-vitro* amyloid inhibition, *in-vivo* brain drug concentrations and nose-to-brain targeting efficiency. LPH nanoparticles showed concentration-dependent amyloid inhibition. Wherein, RIV:DHA LPH (+ve) demonstrated relatively enhanced A β ₁₋₄₂ peptide inhibition. Furthermore, RIV:DHA ND and LPH nanoparticles were embedded into a thermoresponsive gel (RIV:DHA ND gel, RIV:DHA LPH (+ve) gel and RIV:DHA LPH (-ve) gel) which enabled improved drug retention time in the nasal cavity. *In-vitro* evaluation of RIV:DHA ND gel showed sustained drug release upto 24 h. Further encapsulation of RIV:DHA into LPH nanoparticle gel demonstrated slow, sustained drug release upto 3 days with 3.18 and 4.07-fold increased nasal *ex-vivo* permeation efficiency of RIV:DHA LPH(-ve) gel and RIV:DHA LPH(+ve) gel. *In-vivo* determination of RIV:DHA ND gel demonstrated 2.18, 4.27 and 3.24 fold improved C_{max}, mean residence time and area under curve (AUC_{0-t}) in brain as compared to RIV-HT gel. *In-vivo* evaluation of LPH nanoparticles displayed significantly improved pharmacokinetic parameters as compared to RIV-HT gel formulation. Amongst LPH nanoparticles, RIV:DHA LPH(+ve) gel exhibited 1.19, 2.13, 1.48-fold improved C_{max}, t_{1/2} and AUC_{0-t} brain concentrations than RIV:DHA LPH(-ve) gel. The intranasally administered LPH nanoparticles were safe and could efficiently improve nose-to-brain targeting in managing brain disorders.

Another formulation approach describes the development of chitosan-coated liposomes for improved formulation stability and nose-to-brain targeting. RIV-HT loaded liposomes (RIV-HT Liposome) were prepared using combination of S100[®] (soya phosphatidylcholine) and cholesterol employing thin film hydration method. The optimized chitosan-coated liposome

(CHT@ RIV-HT Liposome) exhibited particle size (PDI) of 188.9 ± 1.1 nm (0.485 ± 0.028) and improved formulation stability for at least 3 months. The uniform coating of chitosan over RIV-Liposome was observed under transmission electron microscopy. Further, the CHT@RIV-Liposome was dispersed into poloxamer-based *in-situ* gel (CHT@RIV-Liposome gel) that reduced mucociliary drug clearance upon intranasal administration in rats. The *ex-vivo* studies confirmed the improved nasal drug permeation efficiency with CHT@RIV-Liposome gel. The brain pharmacokinetic profiles also demonstrated direct nose-to-brain drug transport with drug transport efficiency (DTE %) and drug transport permeation (DTP %) values as 651.44 % and 84.64 %, respectively. CHT@RIV-Liposome gel showed 1.64, 2.38 and 2.14-fold improved C_{max} , AUC_{0-t} and MRT concentrations in brain, demonstrating improved therapeutic effect compared to RIV-HT Liposome gel.

Finally, it can be concluded that the developed nanocarriers significantly improved RIV targeting to the brain through nose-to-brain pathways. The prepared nanocarriers were also found to effectively address the issues associated with the drug.

CHAPTER 1

INTRODUCTION

1.1 Alzheimer's disease

Alzheimer's disease (AD) is a complex, multifactorial neurodegenerative disorder that occurs in older adults above age of 65 years. It is generally characterized by early signs of mild dementia and impaired cognition with a gradual decline in memory, thinking, and decision-making that culminates into abnormal behavioral and social skills [1]. Sometimes, it may also lead to psychiatric symptoms such as apathy and depression [2]. The condition progressively worsens, affecting daily activities and relationships [3] with the overall decline in mental and behavioral functions [4]. In severe stages, neurodegeneration leads to the inability of the patient to perform routine activities such as thinking, decision-making, walking, speaking, swallowing, etc. At the end stage, the patient may eventually become bedridden [5]. AD symptoms appear lately, but disease initiation starts around 20 years before the occurrence of symptoms [6,7].

The long duration of illness leads to social, and economic burdens as the condition progressively increases the level of dependency on medical attention and caregiver support. The lifetime cost of caregivers for an Alzheimer's patient is estimated to be 41757 dollars in 2022 [8]. It accounts for a global economic burden of around 1 trillion US dollars and is estimated to increase twice by 2030 [9,10]. The increasing population of Alzheimer's patients and the economic toll on several countries have made Alzheimer's a major global concern. In recent years, the number is also growing in young adults aged 40-50 years, termed early onset AD [11]. It is the fifth leading cause of death globally, accounting for 60–80 % of dementia cases [12,13]. As per a 2018 report, around 50 million people across the globe have Alzheimer's and related dementias, and it may cross 152 million by 2050 [10]. Every 3 s, a new dementia case is reported worldwide. As per Alzheimer's association statistics, nearly 6.7 million Americans are living with Alzheimer-related dementia [14]. In India,

approximately 8.8 million people have dementia, and the prevalence is 7.4 % for adults above age 60 years [15]. Since 2019, the COVID pandemic has surged the possibility of Alzheimer's and related dementias. Several reports suggest that infection with COVID-19 leads to leakage in small blood vessels and different areas of the CNS, accelerating the risk of developing Alzheimer's and other dementia [16]. Usually, patients with Alzheimer's and related dementia are more prone to contracting COVID-19 [17,18]. Moreover, patients with dementia are three times at higher risk of developing severe COVID-19 symptoms than normal individuals [19].

Several factors are associated with the initiation of AD, such as age, gender [20], lifestyle, and food [21] are also linked with AD. Usually, women are at higher risk of developing Alzheimer's than men [22]. People with diabetes and heart disease are also at higher risk [23]. In addition, the risk of developing AD is increased by stress-induced lifestyle [24], cerebral hypoperfusion [25], and lousy food habits. Some studies have found vitamin deficiencies in AD patients [24,25]. Several clinical trials suggested that regular intake of natural dietary supplements [26] mitigates oxidative stress, neurodegeneration, and AD-related memory impairment [27].

The neuropathological autopsies of the human brain hallmark the presence of lesions and senile plaques that comprise extracellular deposition of AB₁₋₄₂ and NFT formed by abnormal accumulation of tau proteins [28]. The senile plaques usually affect cerebral cortex, hippocampus and then progress slowly into the neocortex. The progressive accumulation of AB₁₋₄₂ and NFT hamper neurochemical transmission, resulting in neurotoxicity and neurodegeneration. It is well-known that cholinergic synapses are particularly affected in AD [2]. It leads to neuronal transmission deficit, impaired cognition, and memory function [29]. The impaired transmission of several signaling pathways further increases the complexity of

the disease [2]. Understanding basic biology is essential for the treatment of AD. It requires a detailed understanding of Alzheimer's pathophysiology as discussed in further/upcoming section.

1.2 Pathophysiology

The primary causative factor and effective treatment strategies for Alzheimer's remain elusive, despite the disease's sufficient understanding of basic biology and clinical neuropathology [30]. The probability of developing Alzheimer's depends on genetic, non-genetic, and causative factors [31]. Genomic studies have explored crucial loci responsible for AD's development, but it is difficult to establish a causal relationship between them [32,33]. The histopathological studies revealed that amyloid plaques consist of $A\beta_{1-42}$ peptides (**Fig.1.1**) [34]. Further $A\beta_{1-42}$ accumulation leads to hyperphosphorylation of tau proteins resulting in intracellular, misfolded NFT. The assembly of $A\beta_{1-42}$ peptides and NFTs causes synaptic deficit, neuronal death, and grey matter loss [35]. These are particularly found in the frontal cortex and hippocampal regions, causing severe loss of cognitive abilities and memory functions [36]. $A\beta_{1-42}$ consists of 39–43 hydrophobic peptide residues, majorly constituting $A\beta_{1-42}$ and $A\beta_{1-40}$ accumulation, resulting in loss of synaptic transmission, neurodegeneration, and cognitive decline [37]. In normal conditions, amyloid precursor protein (APP) is cleaved by α -secretase to generate APP- α and C-terminus fragment- α (CTF). APP- α is further cleaved by γ -secretase (a membrane-bound enzyme complex) to produce soluble APP peptides. In Alzheimer's, APP is cleaved by β -secretase and subsequently by γ -secretase to form $A\beta$ peptides [38]. Cleavage by β -secretase produces APP- β and C-terminus fragments, which are eventually cleaved by γ -secretase to produce $A\beta$ peptides of varying lengths. These $A\beta$ peptides aggregate to form a self-assembled structure with characteristic secondary β -sheet and super secondary structures called "protofibrils"

[39]. These soluble protofibrils mature to form insoluble plaques, disturbing the typical architecture of the affected area [40]. The tau hypothesis postulates that alteration in tau proteins is responsible for the initiation of AD [41]. Tau proteins are composed of 350–440 amino acids, microtubule-associated proteins in neurons, responsible for essential functions such as cell signaling, synaptic plasticity, and regulation of genomic stability [42]. The intrinsic biological reactions are usually accountable for changes in tau proteins. Several biological reactions, such as phosphorylation, acetylation, ubiquitination, and glycosylation, mainly cause alteration in tau proteins. However, phosphorylation is primarily responsible for the changes in tau proteins [41]. These are hydrophilic, unfolded microtubule-binding proteins in the neurons [43]. Cellular kinases, di-sulfide dependant, and di-sulfide independent dimerization of tau proteins result in the intracellular conversion of soluble aggregates into insoluble helical aggregates. It forms a misfolded NFT, disrupting the microtubule structure [44]. Another hypothesis states that dysfunction or enlargement in perivascular spaces is associated with several neuropathological conditions like dementia, Alzheimer's, and cerebral amyloid angiopathy [45,46]. Perivascular spaces have a role in clearing metabolic CNS waste that connects to the glymphatic system [47]. It is also referred to as intramural periarterial drainage. The densely packed aquaporin-4 channels ensheath perivascular spaces. Cerebrospinal fluid (CSF) from these perivascular spaces flows into the brain interstitium and mixes with interstitial fluid [48]. Impaired CSF-interstitial fluid exchange postulates initiation and progression of Alzheimer's due to compromised clearance, and drainage of A β into interstitium and blood [49]. The accumulation of A β_{40} , A β_{42} , and NFT promotes mitochondrial dysfunction. Mitochondrial dysfunction along with A β_{1-42} accumulation, subsequently leads to Ca²⁺ imbalance and activation of adenosine monophosphate-activated kinase protein, resulting in synaptic loss and memory decline [50]. Hence, there are several hypotheses postulated for initiation and increasing the severity of

Alzheimer's, the present research primarily focuses on targeting $A\beta_{1-42}$ and tau proteins for effective treatment of the disease.

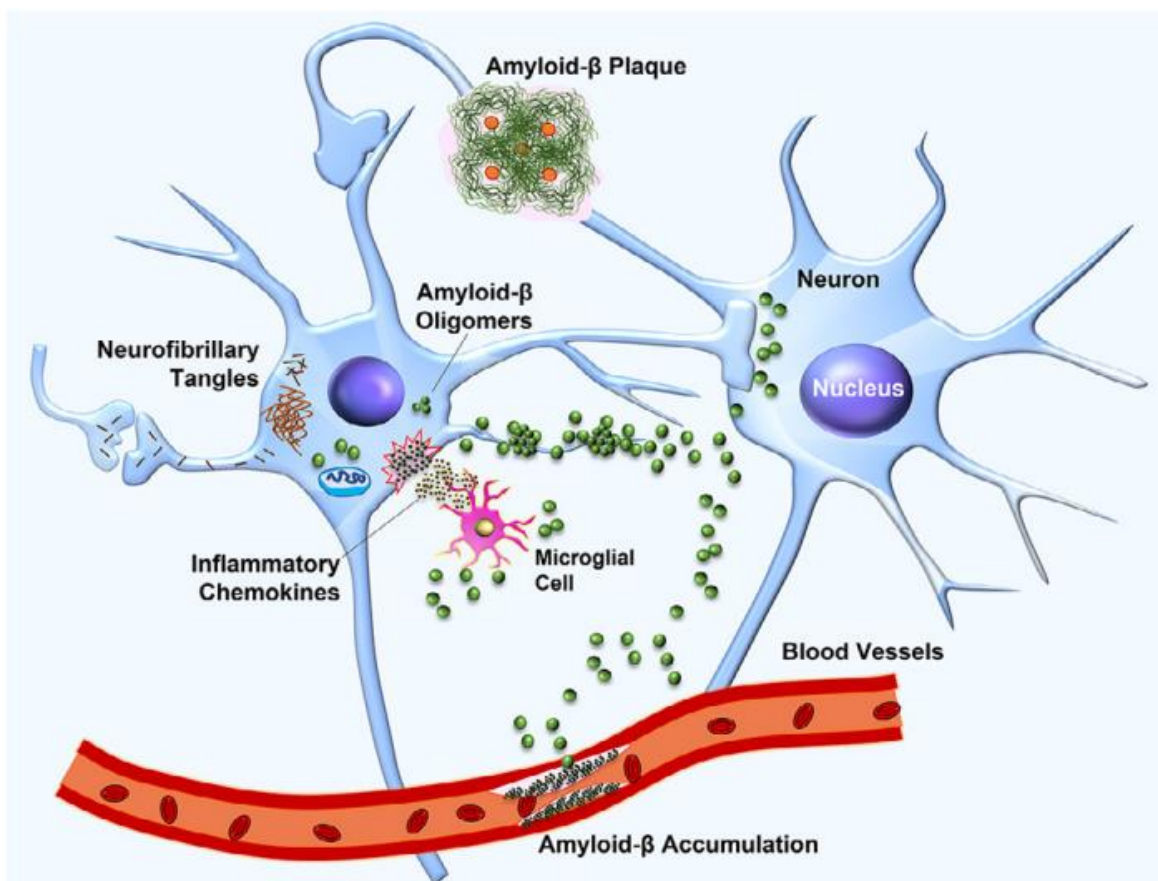


Fig. 1.1. Pathophysiology of Alzheimer's disease. It shows amyloid- β monomers form oligomers and aggregates to form plaques, damaging neurons and accumulation of $A\beta_{1-42}$ in blood vessels.

1.3 USFDA-approved drugs for treatment and their drawbacks

Currently, available therapeutic modalities primarily emphasize decreasing the disease's progression rather than a complete cure [51]. There are four prescription drugs approved by the United States Food and Drug Administration (USFDA): Three AChEI and one N-methyl-d-aspartate (NMDA) receptor antagonist [52]. In June 2021, USFDA approved Aducanumab (marketed as AduhelmTM), an amyloid- β directed antibody [53]. The approved AChE inhibitors include RIV-HT, donepezil, and galantamine. These drugs provide symptomatic

relief in mild to moderate Alzheimer's [6,54,55]. The AChE causes the degradation of acetylcholine. Whereas AChE inhibitor delays the degradation of acetylcholine, increasing cholinergic transmission [56]. NMDA antagonist class of drug exhibit potent activity to detoxify the brain, acting on free radicals. It demonstrates neuroprotective action, restoring neuronal cells around A β ₁₋₄₂ oligomer and improving AD symptoms. Memantine is the only NMDA receptor antagonist class of drug approved for treating moderate to severe AD [57]. Both classes (NMDA antagonist and AChE inhibitor) of approved drugs have limited brain access due to restrictions imposed by the blood-brain barrier (BBB), enforcing a significant challenge in achieving therapeutic efficacy. The presence of drug efflux transporters (P-glycoproteins) in BBB imposes an additional challenge in achieving therapeutic levels [58]. The saturation of carriers present on the surface of BBB can result in lesser drug concentration in the brain [59]. For example, memantine exhibits limited CNS concentrations despite excellent oral bioavailability [60]. The possible reason is due to the saturation of influx transporters, *i.e.*, organic cationic transporters (OCTN 1–3) on BBB [61]. Likewise, donepezil [62] and galantamine show lesser concentration in the brain, despite high oral bioavailability [63]. Rivastigmine hydrogen tartrate (RIV-HT) is associated with the problem of a shorter half-life due to extensive first-pass metabolism [64]. In humans, only 40% of RIV-HT is absorbed in the CNS after intravenous (IV) administration owing to its hydrophilic nature [65]. All four molecules are generally prescribed in AD, but their poor brain permeation hinders their therapeutic effectiveness. Additionally, these drugs are associated with hepatotoxicity [66,67], nephrotoxicity [68,69], and gastrointestinal-mediated side effects [70]. These side effects often lead to the cessation of therapy in chronic conditions. Therefore, a suitable delivery system is needed to efficiently deliver the drugs into CNS, with minimal drug exposure to peripheral organs.

1.4 Physical barriers in brain targeting

The human brain is protected from external stimuli, toxins, antigens, and foreign materials and is separated from peripheral system through physiological barriers. These barriers are selectively permeable that regulate homeostasis and allow passage of nutrients to the CNS. BBB is the major physiological barrier in drug targeting to the CNS [71,72].

BBB is a highly selective, semi-permeable barrier composed of several types of cells, such as brain capillary endothelial cells, pericytes, astrocytes, and neuronal cells. The tight junctions within BBB result in extremely high trans-endothelial electrical resistance between the blood and brain, restricting paracellular transport. It allows entry of only small, low-molecular weight, non-polar molecules (<400Da) to the brain [73]. It comprises several transporters and carriers/receptors for the passage of nutrients and metabolites across CNS [71,73]. Many receptors and carriers are overexpressed on BBB could transport specific ligands into the brain. The negatively charged BBB, shows higher affinity towards cationic molecules/nanoparticles, triggering cellular internalization [58]. Some of the brain-targeting approaches across BBB are discussed in this section. Surface functionalization of nanoparticles with corresponding ligands could promote binding with these receptors and trigger cellular internalization. Several receptors such as transferrin receptor, insulin-receptor, acetylcholine receptor, nicotinic receptor, low-density lipoprotein and insulin-like growth factor receptors are commonly explored ligands for improved drug uptake across BBB [74]. Most essential ions, sugars, and amino acids pass intracellularly through various transporters. Amino acid transporters are categorized into two major types based on their physiological role, i.e., neurotransmitter transporters [75] and nutrient amino acid transporters [76]. Transporters such as mannose, glucose, hexose, and amino-acid transporters are highly expressed on the surface of BBB and bear potential for utilization in brain targeting [74]. For example,

intravenous administration of glutathione-modified liposomes demonstrated a 4-fold improvement in brain concentration compared to unmodified liposomes [77]. Another approach involves adsorptive-mediated drug transport for targeting actives across BBB. Adsorptive-mediated brain targeting is based on nanocarriers' electrostatic interaction with oppositely charged cell membrane domains [78]. Various polysaccharides and proteins have been extensively studied in nanocarrier development due to the role of their surface charge in adsorptive-mediated brain targeting [79,80]. For example, cationic bovine serum albumin conjugated nanoparticles demonstrated improved nanocarrier uptake and permeation efficiency across *in-vitro* BBB model. *In-vivo* studies demonstrated 1.6-fold higher brain accumulation than unmodified nanoparticles [81]. Cell-penetrating peptides (CPP) are established to deliver both small molecules and macromolecules into the cell [82]. Cationic CPP consists of a short sequence of amino acids (arginine, lysine, and histidine) that interacts with the plasma membrane's anionic moieties [83]. The distinct advantage of CPP is their ability to translocate through cell membranes at lower concentrations through endocytic uptake mechanism [84]. For example, transactivator of transcription (TAT) modified liposomes exhibited 2.52-fold increased brain accumulation as compared to unmodified liposomes [85]. Several reports suggest adsorptive-mediated, carrier-mediated and CPP-mediated approaches for brain targeting. Despite several successful studies, the applicability of these delivery systems is limited due to carrier-induced toxicity, biocompatibility issues, uncontrolled drug release, and related side effects. Alternatively, nose-to-brain delivery has shown positive outcomes in several clinical studies. It has ability to transport actives directly to the brain, negating drug's passage through BBB [72]. So, it could be a potential drug delivery strategy for brain targeting.

1.5 Approaches for brain targeting

Strategies employed for brain drug delivery are broadly categorized into invasive and non-invasive drug delivery approaches. Invasive approaches involve drug delivery to the brain *via*. intracerebral implants or intracerebral injections [74]. The non-invasive approach involves the passage of drug across BBB or bypassing BBB using nose-to-brain delivery [74].

The invasive approach involves intracerebral administration of actives to the brain either by direct administration or by using an intracerebral implant to directly deliver actives into the brain parenchyma [71]. Intracerebral devices or implants are used in the ailment of neurological disorders, brain cancer and for administering opioids in pain management. For example, interstitial wafer or polymeric implants are generally in practice for glioblastoma treatment [86,87]. However, intracerebral dose administration is restricted to implant size and lesser drug penetration into deeper layers due to high intracerebral pressure are some of the associated drawbacks. Moreover, it is also associated with a higher probability of causing local toxicity, trauma, and infection to the brain and spinal cord. Intracerebral administration is usually unsuitable for long-term therapies such as Alzheimer's, as it is associated with relatively high cost, frequent follow-ups, critical care, monitoring, and decreased patient compliance [71]. Another invasive approach for brain targeting involves deep brain stimulation. It is preferred to stimulate neurochemical transmission and is usually employed to treat Parkinson's disease. It involves connection of a neurostimulator to an implanted electrode. Often, it is associated with a risk of brain damage thereby it has limited applications. Overall, non-invasive approaches are unreliable and have limited applications in brain drug delivery [87].

BBB is a major hurdle for effectively delivering drugs to the CNS. An obvious non-invasive approach involves increasing BBB permeability by transiently increasing permeation using hyperosmotic agents [71]. It usually includes compounds such as urea, lactamide, mannitol saline solution, etc. However, BBB opening by hyperosmotic agents is non-selective and allows uncontrolled entry for several low and high-molecular-weight compounds [87]. It often leads to increased brain fluid accumulation, neurological toxicity, aphasia and hemiparesis [1].

Nose-to-brain (N2B) delivery is another non-invasive approach for delivering actives to the brain bypassing BBB. Several studies have acclaimed the benefits of the intranasal drug delivery route in targeting actives directly to the CNS. The understanding of nasal physiology, anatomy, and formulation approaches for efficient nose-to-brain delivery has been discussed in upcoming sections.

1.6 Nose-to-brain delivery

N2B delivery has enormous potential in targeting actives to the CNS [86]. It has ability to bypass BBB to help deliver actives directly to the brain [88]. It offers enormous therapeutic opportunities with several advantages such as rapid onset of action, improved patient compliance, enhanced therapeutic efficacy, and avoidance of pre-systemic metabolism [89]. It also provides an opportunity to deliver various small and macromolecules directly to the brain [90]. N2B delivery has an unrivaled ability to overcome the drawbacks of current oral therapy and encompasses the vast potential to achieve effective brain targeting [91]. For example, N2B delivery of cerebrolysin improved cognition and amyloid- β clearance efficiency in Alzheimer's induced mice model [92,93]. However, intranasal delivery does have a few shortcomings [94]. It includes lack of site-specific targeting (to CNS areas), enzymatic degradation, insufficient CNS bioavailability, restrictions imposed due to nasal

anatomy, limited surface area, dose limitation, etc. [95][96]. N2B delivery has been revolutionized with nanotechnology-based drug delivery systems that have potential to overcome these problems [97]. It prevents the drug from enzymatic degradation [98], and leads to increased drug targeting, brain bioavailability, extended therapeutic action, lesser systemic absorption, etc. [99]. For example, thiolated chitosan NP (loaded with galantamine) demonstrated decreased cholinesterase activity in mice than in nasal solution [100]. Hanafy *et al.*, developed galantamine/chitosan complex NP that also demonstrated decreased AChE levels compared to oral formulations [101,102]. In another study, donepezil solid lipid nanoparticles (SLN) demonstrated improved brain pharmacokinetics parameters than intranasal and IV solutions [103]. But delivery of hydrophilic drugs through nanocarrier-based delivery systems may come across certain disadvantages as follows:

- Lesser drug loading and encapsulation efficiency
- Faster drug release profiles with an inability to achieve sustained drug release
- Faster drug release can cause dose dumping, resulting drug-induced toxicity
- Compromised targeting efficiency and sustained therapeutic action

So, there is a need to increase lipophilicity of drug molecules to overcome above mentioned drawbacks. There are mainly two approaches involved in modulating the hydrophobicity of drug molecules. Primarily it includes lipid-drug conjugate, which employs covalent conjugation of charged hydrophilic drugs with lipidic molecules. It also includes drug-antibody conjugate, and drug-drug conjugate [104]. Moreover, the conjugation of lipids or hydrophobic linkers increases drug lipophilicity. However, this approach has limited applicability due to irreversible changes in the physicochemical properties of the active molecule [105]. Another extensively utilized approach for increasing drug lipophilicity involves the development of hydrophobic ion-pair complexes. Hydrophobic ion pairing has

become helpful in making charged hydrophilic molecules into hydrophobic drug complexes [106]. It involves improved drug lipophilicity without altering the chemical structure, with the advantage of achieving reversible aqueous solubility of a hydrophilic drug [107].

1.6.1 Ion-pair complexes

Hydrophobic ion pairing forms ionic interaction within charged hydrophilic molecules and oppositely charged hydrophobic counterion forming uncharged complexes, with limited aqueous solubility. The counterion consists of hydrophobic domains such as aromatic rings or alkyl tails. The increased hydrophobicity with ion-pair complexes (IPC) involves two mechanisms. Firstly, the hydrophilic moiety's actual charge is masked, mitigating solubility in polar solvents. Secondly, the hydrophobic domain of counterion coats the hydrophilic molecule and repels water. The non-polar groups of counterion exclude water from solvating ionic-ionic interactions owing to a lesser dielectric constant. The magnitude of increased lipophilicity depends upon, hydrophobicity or log P value of a counterion molecule [107]. Hang *et al.*, developed doxorubicin-cholesteryl hemisuccinate IPC to increase the encapsulation efficiency of doxorubicin hydrochloride. The complex-loaded liposome demonstrated approximately 99 % encapsulation efficiency with sustained drug release up to 24 h, while pure doxorubicin exhibited complete drug release within 4 h [108]. In another report, IPC was developed using N-deoxycholy-l-lysyl-methylester to improve pemetrexed anti-cancer activity and oral bioavailability [109]. Torky *et al.*, explored berberine-sodium oleate IPC to evaluate topical skin penetration efficiency. The developed complex exhibited 251-fold increased saturation solubility in n-octanol with superior skin penetration and deposition compared to free berberine [110]. Ren *et al.*, developed Azithromycin-cholesteryl hemisuccinate IPC-based liposome for the treatment of dry eyes. The developed IPC distinctly improved encapsulation efficiency from 9.2 % to 95.6 % [111]. The IPC has ability

to provide sustained drug release profiles due to increased drug hydrophobicity. In one such study lycobetain solution exhibited 42.6 % drug release within 1 h, whereas upon development of lycobetain-oleic acid IPC, it showed only 18.9 % drug release at similar time intervals [112]. In another study, Zhang *et al.*, developed vincristine-oleic acid IPC-based microemulsion to reduce the *in-vitro* burst release and associated toxicity of vincristine solution. In case of vincristine solution, it exhibited 63.96 % drug release in 6 h. Whereas, vincristine-oleic acid IPC showed lesser burst effect with only 35 % drug release in 6 h [113]. In one such study, IPC of RIV-HT was fabricated using salicylic acid for development of a controlled, long-acting transdermal RIV-HT-adhesive patch. The developed patch exhibited 2.8-fold increased drug permeation efficiency, significantly enhanced *in-vivo* plasma concentration with sustained drug release upto 3 days [114]. There are no reports available for IPC-based N2B delivery for anti-Alzheimer drugs. However, it has been well-utilized in drug delivery for other routes of administration.

The role and advantages of nanocarrier-based N2B delivery in brain targeting has been discussed in previous sections. This upcoming section provides an understanding of nasal anatomy for drug/nanocarrier transport. It also emphasizes several drug/nanocarrier transport pathways, including a mechanistic approach for the cellular uptake of nanocarriers through N2B delivery.

1.6.2 Nasal anatomy

The nasal cavity is divided by the nasal septum into two sections and further differentiated into 3 subsections: vestibule, respiratory and olfactory region. The frontal portion is called the vestibule, lined by squamous epithelium, sweat, and sebaceous gland [115]. This portion of the nasal cavity is of less interest in drug transport. The respiratory region is generally the area of great interest for drug targeting owing to its high surface area, vasculature, and

permeability. This region consists of inferior, middle, and superior turbinates, lined by respiratory epithelium, also known as ciliated pseudostratified columnar epithelium. It comprises basal, goblet, ciliated and non-ciliated columnar cells. The lamina propria situated above respiratory epithelium constitutes blood vessels, capillaries and neuronal innervations. This region consists of ophthalmic and maxillary branches of trigeminal nerve, representing a direct connection to the CNS [116]. It also constitutes olfactory axon bundles, lymphatic vessels and mucus-secreting gland. The olfactory region is situated in the upper portion of the nasal cavity, above superior nasal turbinate and below cribriform plates. This region directly connects nasal cavity to the CNS. The olfactory epithelium comprises of three cell types: basal, supporting and olfactory receptor neurons. The cribriform plate is a bony, little porous structure constituting neuronal bundles that facilitate passage from olfactory region to the CNS [86].

1.6.3 Nose-to-brain transport pathways

The first and fifth cranial nerves, *viz.* olfactory and trigeminal nerves, play an essential role for drugs to pass to the CNS from deeper nose areas. This is the transport mechanism of nanocarrier from nasal cavity to the CNS. Olfactory nerve fibers and axons in the upper posterior segments reach directly to the olfactory bulb in the limbic section of the brain. The intranasal route gives a direct entry from environment to the brain without any peripheral sensory receptor relay. This pathway is usually called N2B transport [117,118]. The direct N2B delivery of nanocarriers majorly follows trigeminal and olfactory pathways.

1.6.3.1 Olfactory pathway

The olfactory epithelium is the only CNS region exposed directly to the environment. So this pathway contributes a substantial role in the transport of drugs directly to the brain upon intranasal administration [94]. This region comprises the olfactory epithelium, lamina

propria, and olfactory bulb. The olfactory epithelium consists of olfactory receptor neurons. This neuronal pathway is considered as the determining drug transport mechanism directly to the brain. The olfactory neuronal pathway helps the drug enter into CSF directly, *via* intranasal route [119]. In this pathway, drugs, *via* olfactory axon crosses cribriform plate and reaches olfactory bulb, as an opening to various parts of the brain like amygdale, piriform cortex, and hypothalamus (**Fig.1.2**) [87,94]. It takes only few minutes to deliver the drugs directly into the brain by transporting them from CSF to the brain's interstitial fluid [94].

1.6.3.2 Trigeminal nerve pathway

The trigeminal nerve is the largest and fifth cranial nerve, comprising three branches, ophthalmic, maxillary, and mandibular. The trigeminal nerve pathway joins to the end part of the brain, such as spinal cord, medulla, and pons [94]. N2B delivery uses trigeminal pathway as a channel to carry actives from the nose to the brainstem opening. Further, actives enter *via* pons and then get transferred to the rest of the hindbrain [120]. Ophthalmic and maxillary branches of the trigeminal nerve have a crucial role in direct N2B delivery of drugs. These two branches of the trigeminal nerve directly pass through the nasal mucosa to the forebrain and supply innervation to the different parts of the nasal mucosa and anterior section of the nose [121–123].

1.6.3.3 Cellular transport in nose-to-brain delivery

Nanoparticles need to cross the nasal epithelium to translocate to the brain *via* olfactory and trigeminal nerve pathways [124]. Endocytosis is required for the permeation of nanocarriers across epithelial cells [125]. Paracellular transport occurs for small molecules and nanoparticles with a particle size of less than 20 nm. It has quick access to the CNS (within 2 h) [126]. Transcellular is the major pathway for the translocation of molecules across epithelial cells. It involves two major processes: phagocytosis (cell eating) and pinocytosis

(cell drinking). Phagocytosis involves uptake of bacteria and solid particles (> 250 nm) forming large vesicles called phagosomes. In contrast, pinocytosis involves four different mechanisms: macropinocytosis, clathrin-mediated endocytosis,

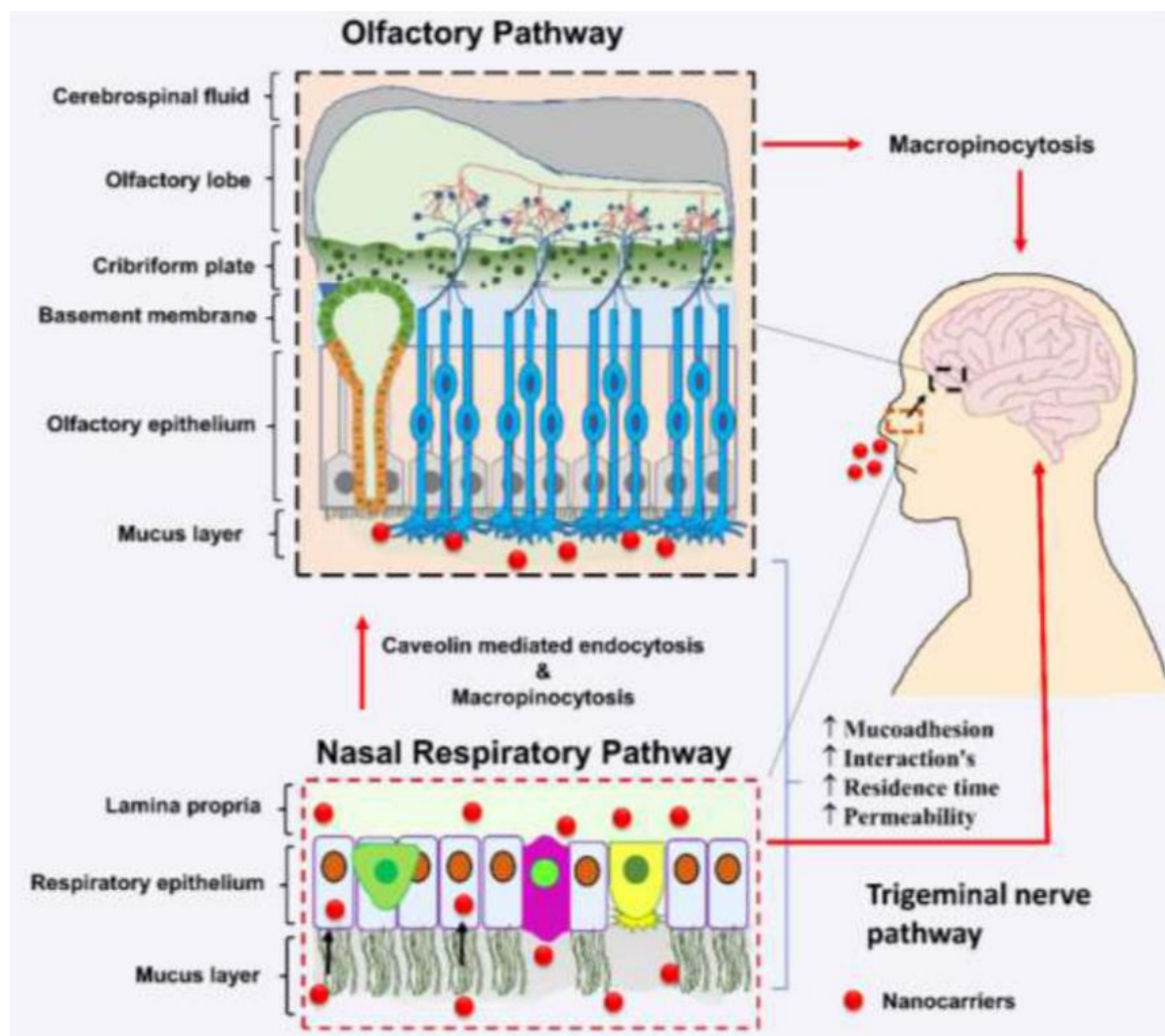


Fig. 1.2. Schematic representation showing intranasal nanocarriers absorption pathways to the brain. It shows the nasal respiratory epithelium pathway, olfactory pathway, and trigeminal nerve pathway. The cellular endocytic uptake mechanism is also shown.

caveolae-dependent endocytosis, and clathrin/caveolae-independent endocytosis. Macropinocytosis involves uptake of cellular debris, bacteria, viruses with the formation of actin-mediated vesicles [127]. While clathrin, a group of internal proteins, involves receptor-mediated transport associated with vesicle formation (~120 nm). Caveolae, another group of

internal proteins, form a small flask-shaped cell membrane structure (60–80 nm) for nanocarrier uptake [128]. However, clathrin/caveolae-independent endocytosis is associated with NP having a diameter of 90–120 nm [129]. Nanocarrier size and surface charge significantly impact cellular uptake across epithelial cells [130].

1.7 Formulation approaches for nose-to-brain delivery

This section primarily emphasizes two approaches for N2B drug delivery. It involves *in-situ* hydrogel and nanocarrier-based delivery systems. Each approach can be used alone or in combination for enhanced drug targeting. *In-situ* hydrogel-based N2B delivery resists mucociliary drug clearance. The presence of gel-loaded formulation improves drug residence time in the nasal cavity, thereby increasing drug absorption and targeting the brain. Nanocarrier-based N2B delivery improves drug transport through targeting pathways, offers slow drug release from nanocarriers, avoids dose dumping, and provides sustained therapeutic efficacy.

1.7.1 *In-situ* hydrogel-based nose-to-brain delivery

Hydrogels are hydrophilic molecules that can absorb large amounts of water and form a three-dimensional network upon cross-linking. *In-situ* gelling system has emerged as an interesting N2B drug delivery strategy because of several advantages such as increased drug retention time, bioavailability, protection from enzymatic degradation, reduced mucociliary clearance, etc. The conversion of sol-gel transitioning is based on external stimuli such as pH, temperature and ionic modulation.

1.7.1.1 Thermoresponsive gel

Thermoresponsive hydrogels exhibit sol-to-gel transition above a particular temperature (27° C) to ensure accurate dose administration without any drug loss. Amongst thermoresponsive polymers, poloxamer 407 and 188 are frequently used as gelling agents to achieve gelation

within the desired temperature range. Poloxamer is a triblock polymer constituting one polyoxypropylene unit and two polyoxyethylene units that undergo sol-to-gel transition driven by supramolecular entanglements of micelle and consequent dehydration of the polyoxypropylene units [131]. Abouhusein *et al.*, developed RIV-HT-loaded thermoresponsive gel to evaluate improved brain bioavailability *via* intranasal route. They used pluronic F127 (poloxamer 407) in combination with mucoadhesive polymers such as HPMC, chitosan, carbopol 934, and sodium CMC. The gel formulation was evaluated for sol-gel transition temperature, consistency, gel strength, mucoadhesion and time required for 50 % drug release. *In-vivo* pharmacokinetics and biodistribution studies of optimized gel showed 84 % transnasal permeation and improved brain distribution compared to RIV-HT intranasal and intravenous solution [132]. Cunha *et al.*, developed RIV-HT loaded nanoemulsion and RIV-HT loaded nanostructured lipid carriers (NLC) to evaluate the potential of thermoresponsive gel in N2B delivery. The hydrogel prepared using a combination of poloxamer 407 (17 % w/v) and HPMC (0.3 % w/v) showed gelation within the temperature range 31-35° C. Nasal deposition study demonstrated 4 % drug deposition for RIV-HT NLC and RIV-HT nanoemulsion, while it was observed to 8% in case both hydrogel loaded formulations. Thus following results demonstrated the potential of thermoresponsive *in-situ* gel in increasing drug deposition in N2B delivery [133–135]. Similarly, donepezil-loaded ethosomal thermoresponsive gel was prepared using a combination of poloxamer 407 (18 % w/v), 188 (6 % w/v) and Carbopol 934 (0.4 % w/v) as mucoadhesive polymers showed effective brain concentrations due to improved residence time in the nasal cavity. [136].

1.7.1.2 pH-responsive gel

The hydrogel contains weakly acidic or basic functional groups within the polymer network that are capable of swelling at pH above or below the pKa. Wavikar *et al.*, developed RIV-

HT NLC loaded, dual pH and thermoresponsive *in-situ* gel using poloxamer 407 (20 % w/v) and screened with a combination of mucoadhesive polymers *viz.*, chitosan (1 % w/v), gellan gum (0.8 % w/v) and carbopol 924 (1 % w/v). The hydrogel prepared using a combination of carbopol 924 led to the formation of a very stiff gel at basic pH and a lower viscosity gel at acidic pH of the nasal cavity (pH 6.3). Thereby the optimized gel formulation was prepared using gellan gum that showed effective gelation within the desired temperature range [64]. There are no reports available suggesting the development of pH-responsive gels for N2B delivery of Alzheimer's drugs.

1.7.2 Nanocarrier-based nose-to-brain delivery

Nanocarrier-based intranasal delivery has been revolutionized owing to their efficient brain targeting ability compared to conventional formulations (intranasal drug solution). Nanocarrier-based systems include both lipidic (vesicular systems, microemulsions or nanoemulsion, SLN, NLC etc.) and polymeric nanocarriers (nanoparticles, micelles, nanoconjugate, dendrimers etc.). N2B delivery with nanocarrier-based systems helps overcome the drawbacks of conventional systems, such as lack of site-specific targeting, protection of drug from enzymatic degradation, restrictions offered owing to nasal anatomy and limited brain concentrations due to limited drug permeability. Importantly, nanocarrier-based intranasal delivery particularly leads to targeted therapy, improved brain bioavailability, and extended therapeutic action with reduced systemic absorption of drugs. Some of the preclinical studies demonstrated the advantages of nanocarrier-based intranasal delivery systems for treating Alzheimer's has been discussed below.

1.7.2.1 Polymeric nanoparticles

They have attracted significant attention as potential delivery systems for N2B delivery to the CNS. They offer the advantage of delivering a wide range of actives with the advantages of

offering controlled drug release with improved brain targeting. Polymeric NPs are widely utilized in N2B delivery due to its ability to deliver hydrophilic and hydrophobic drugs. The literature demonstrates the development of polymeric NP using poly(lactic-co-glycolic) acid (PLGA) and chitosan are extensively studied for N2B delivery. These polymeric NPs are biocompatible, biodegradable and GRAS-approved. Fazil *et al.*, developed RIV-HT loaded chitosan nanoparticles using ionic gelation technique to improve brain targeting through N2B delivery. Amongst all formulations, chitosan NP demonstrated maximum direct brain transport efficiency with a greater brain/blood ratio of 1.72. On the contrary, the brain/blood ratio was comparatively lesser in case of RIV-HT_{IV sol} and RIV-HT_{IN sol} with 0.23 and 0.79 respectively. The higher drug transport efficiency ($355 \pm 13.52\%$) and direct transport percentage ($71.80 \pm 6.71\%$) demonstrated enhanced brain targeting efficiency with chitosan nanoparticles (**Table 1.1**) [137]. In another study galantamine-chitosan complex-loaded nanoparticle was developed to evaluate their therapeutic efficacy in AD. Intranasal administration of the developed formulation for 12 consecutive days showed significantly decreased AChE levels compared to oral and intranasal administration of free galantamine solution. The developed nanoformulation was observed to be pharmacologically effective and safe, and serves to be a promising drug delivery approach for Alzheimer's therapeutics [138]. Salatin *et al.*, developed RIV-HT, *in-situ* gel-loaded PLGA NP using nanoprecipitation, solvent displacement method. The optimized formulation resulted in dose and time-dependent drug uptake by A549 cells. Comparatively, PLGA NP exhibited improved *ex-vivo* permeation profile as compared to the free RIV-HT solution. [134]. In another study, Salatin *et al.*, developed RIV-HT-loaded Eudragit NP using nanoprecipitation method. The mucus penetration efficiency of RIV-HT is influenced by mucoadhesive property of Eudragit. The developed formulation showed comparatively improved *ex-vivo*

permeation efficiency (34×10^{-4} mg/cm².min) in comparison to free RIV-HT solution (24×10^{-4} mg/cm².min) [135].

1.7.2.2 Lipidic nanocarriers

1.7.2.2.1 Microemulsion

Amongst colloidal drug delivery systems, microemulsions have gained special interest due to their ability to deliver a wide range of drugs with hydrophilic and hydrophobic characteristics. Shah *et al.*, developed RIV-HT-microemulsion and RIV-HT loaded mucoadhesive microemulsion using chitosan to evaluate brain targeting efficiency, *via*. intranasal route. *In-vivo* studies demonstrated 2.6 and 1.6 fold-higher brain AUC₀₋₂₄₀ concentrations in mucoadhesive microemulsion and microemulsion formulation as compared to free RIV-HT solution (**Table 1.1**). Moreover, mucoadhesive microemulsion resulted in 1.7-fold increased brain AUC concentration than plain microemulsion formulation. The presence of chitosan in mucoadhesive microemulsion resulted in increased residence time and drug absorption from the nasal cavity [139]. In another study, Khunt *et al.*, developed microemulsion using fish oil and butter oil to evaluate the drug-targeting efficiency of both formulations through intranasal delivery. Pharmacokinetic studies conducted for fish oil and butter oil microemulsion demonstrated 4.15 and 3.98-fold improved brain bioavailability compared to plain RIV-HT solution. Thus microemulsion enriched with essential fatty acids has potential to improve drug concentration in CNS [140,141]. Similarly, donepezil-loaded fish oil and butter oil microemulsions improved drug permeation efficiency across BBB and demonstrated improved efficacy against lipopolysaccharide-induced oxidative stress [142].

1.7.2.2.2 Liposomes

Liposomes are lipid-bilayered vesicles having the ability to encapsulate hydrophilic and hydrophobic drugs. They are biocompatible, biodegradable, and extend sustained *in-vitro*

drug release. Rajput *et al.*, developed liposome-loaded *in-situ* gel for intranasal delivery of donepezil. The *in-vitro* release study showed complete drug release within 8 h, while *in-situ* liposome formulation showed only 10 % cumulative drug release at similar time intervals. *In-vivo* study demonstrated that drug transport majorly occurred through olfactory and trigeminal nerve pathway with drug targeting efficiency observed to be 314.29 % in case of *in-situ* gel-loaded liposomal formulation (**Table 1.1**) [143]. Kumar *et al.*, developed rivastigmine liposomes and rivastigmine-loaded PLGA nanoparticles for comparative evaluation of the pharmacokinetic profile of both formulations. The plasma AUC of intranasally administered rivastigmine liposome was greater than PLGA nanoparticles. Also, the liposomal formulation's drug clearance rate was lesser than PLGA nanoparticles and pure drug formulation [144]. In another study, the pharmacokinetic profile of intranasally administered rivastigmine liposomes showed enhanced brain concentrations and improved half-life as compared to pure drug. Thus it can be concluded that liposome-based formulations are effective in brain targeting and might be a potential drug delivery approach for the treatment of AD [145]. As per our knowledge, an effort was made to cover all literature reports, but very few articles were published for intranasal delivery of liposomes in Alzheimer's therapeutics.

1.7.2.2.3 Solid lipid nanocarriers and nanostructured lipid carriers

Lipidic nanoparticles are described as aqueous dispersion of solid lipid particles stabilized using emulsifiers alone or in combination. There are mainly two types of lipidic NP, *viz.* SLN and NLC. SLNs are composed of single lipids with highly organized inner structure, while NLCs are constituted of a mixture of lipids resulting in disorganised inner structure. The disoriented assembly of lipids thereby results in higher encapsulation efficiency, improved stability, and lesser drug expulsion upon storage [146]. Cunha *et al.*, developed RIV-HT-

nanoemulsion and RIV-HT-NLC formulation. The formulations were further loaded into *in-situ* thermoresponsive gel to evaluate nasal drug deposition efficiency using nasal cast. The particle size of RIV-HT-NLC and RIV-HT-nanoemulsion were observed to be 114.0 ± 1.9 nm and 135.8 ± 0.5 nm, respectively. The percentage of drug deposition in case of RIV-HT-nanoemulsion gel and RIV-HT-NLC gel was observed to be 8 % (**Table 1.1**). In contrast, it was found to be 4% for RIV-HT-nanoemulsion and RIV-HT-NLC formulation and 0.8% for RIV-HT drug solution [133]. In another study, Cunha *et al.*, developed RIV-HT loaded NLC using different size reduction techniques *viz.*, high-pressure homogenizer and ultrasonicator. The particle size (PDI) of nanoformulation with these size reduction techniques were observed to be 109.0 ± 0.9 nm (0.196 ± 0.007) and 114.0 ± 1.9 nm (0.221 ± 0.003) respectively [147]. In another study, Wavikar *et al.* developed *in-situ* RIV-HT loaded cationic NLC formulation to evaluate N2B drug transport efficiency compared to intravenous administration. The pharmacokinetic study showed a sustained drug release with 4.6 and 5.3-fold enhanced brain AUC_{0-t} concentrations followed by intranasal and intravenous NLC administration. Pharmacodynamic studies showed faster regain of memory loss in amnesic rats with 5-fold decreased escape latency in intranasal NLC formulation compared to intranasal free drug solution (**Table 1.1**) [64].

Table 1.1. List of nanotherapeutics for N2B delivery of Alzheimer's disease

Carrier	Therapeutic agent	Benefits	Ref
Polymeric nanoparticle			
Chitosan NP	Rivastigmine	Enhanced brain targeting efficiency	[137]
Galantamine-chitosan complex	Galantamine	Decreased AChE levels in the brain	[138]
PLGA NP	Rivastigmine	Improved ex-vivo permeation profiles	[134]
Eudragit-RL NP	Rivastigmine	Improved ex-vivo permeation efficiency	[135]
Lipidic nanocarrier			

Carrier	Therapeutic agent	Benefits	Ref
Microemulsion	Rivastigmine	1.6 fold enhanced brain AUC levels	[139]
Microemulsion	Rivastigmine	4.15 fold improved brain bioavailability	[140]
Microemulsion	Donepezil	Improved lipopolysaccharide induced oxidative stress	[142]
Nanoemulsion	Memantine	Improved anti-oxidative effect	[141]
Liposome	Donepezil	Improved brain C _{max} and drug targeting efficiency	[143]
NLC	Rivastigmine	Improved nasal drug deposition	[133]
NLC	Rivastigmine	Improved ex-vivo permeation efficiency	[147]
Cationic NLC	Rivastigmine	5.3 fold improved brain AUC concentration	[64]

NP: Nanoparticles, PLGA: Poly(lactic-co-glycolic) acid, NLC: Nanostructured lipid carriers, AUC: Area under curve, C_{max}: Maximum concentration.

1.7.3 Surface-engineered nanocarriers for nose-to-brain delivery

Surface modification appears to be the key strategy for drug delivery from the nasal cavity to the CNS. Nanocarrier attributes such as surface charge, mucoadhesive polymers, or chemical moieties targeting nasal epithelium has been extensively explored for N2B delivery. Surface-engineered nanocarriers help to offer following advantages in comparison to conventional nanocarriers for N2B delivery:

- Improved cellular uptake and mucosal permeation
- Improved site-specific targeting
- Reduced drug distribution at non-targeted sites with minimal systemic exposure
- Improved residence time at the site of absorption

Gajbhiye *et al.*, developed ascorbic acid grafted PLGA-b-PEG NP of galantamine to improve brain transport efficiency of the developed formulation. Ascorbic acid grafted PLGA-b-PEG NP showed significantly increased cellular uptake within NIH/3T3 cells in comparison to PLGA and PLGA-b-mPEG NP. It also showed improved brain distribution and PK

parameters compared to other formulations. *In-vivo* pharmacodynamic study evaluated using Morris water maze, radial arm maze, and AChE activity determination demonstrated higher therapeutic efficacy with ascorbic acid grafted PLGA nanoparticles compared to other formulations [148]. Several cell-penetrating peptides have emerged to mediate enhanced drug permeation and brain targeting due to their affinity towards particular cells [149]. For example, TET-1 peptide (consisting of 12 amino acids) shows retrograde transport through nerve cells due to its higher affinity and interaction with neurons [150,151]. Thus, delivering drugs using permeation enhancers that selectively bind with nerve cells leads to an increase in brain targeting and overall therapeutic efficiency [152]. Yang *et al.*, developed RIV-HT-loaded liposomes and RIV-HT-Loaded cell-penetrating peptide-modified liposomes to evaluate brain distribution and pharmacodynamics by intranasal administration. *In-vitro* cell culture studies revealed that liposome formulation especially modified liposomes showed significantly enhanced permeability across BBB in murine brain microvascular endothelial cells. *In-vivo* studies of modified liposomes showed significantly improved brain distribution and adequate drug retention in the brain, particularly in the hippocampus and cortex (affected peculiarly in AD) compared to plain liposome_{IN, IV} [153]. One of the major challenges associated with liposomal formulation development involves its stability. Steric stabilization of liposomes with surface coating with long bulky molecules such as polyethylene glycol develop steric hindrance. It is the most extensively used stabilizer in pharmaceutical applications due to its biodegradability, water solubility, water binding capacity, high flexibility in polymer chains, and lesser uptake cellular uptake by reticuloendothelial system. Moreover, PEGylated liposomes show enhanced pharmacokinetic parameters such as improved half-life, decreased plasma clearance, decreased distribution volume, favored accumulation in the target organ, and prevent drug leakage. The particle size of stealth liposome was observed to be 478 ± 4.9 nm with -8 ± 0.2 mV zeta potential. *Ex-vivo* study in

sheep nasal mucosa showed 48.6 % and 28.7 % drug permeation in stealth liposome and free drug solution respectively. *In-vivo* pharmacokinetic studies showed 424.2 % and 486 % relative bioavailability in plasma and brain compared to RIV-HT intranasal solution [154]. Yasir *et al.*, developed donepezil-loaded chitosan-coated NLC. Chitosan coating provides mucoadhesion, increased drug retention and absorption from the nasal cavity. The brain availability with intranasal and intravenously administered chitosan-coated formulation was observed to be 2.02 and 2.41-fold greater than intranasal RIV-HT solution. Also, the efficient brain targeting and drug targeting potential was observed to be much higher *viz.* 321.21% and 74.55% in comparison to IN solution [155]. Thus, chitosan-coated NLC displayed enhanced brain concentration and greater brain-targeting potential when administered as intranasal and intravenous formulations. Overall, it can be concluded that surface-engineered nanocarriers improve brain concentrations and brain-targeting efficiency of drugs in nose-to-brain delivery. As per our knowledge, there are very few articles published for small molecules-based surface-engineered nanocarriers for N2B delivery of Alzheimer's therapeutics. Still, there is a wider scope for exploration of surface-functionalized nanocarriers for nose-to-brain delivery.

1.8 Gap in existing research

Alzheimer's disease (AD) is a complex, multifactorial neurodegenerative disorder that is commonly observed in older adults above 65 years of age. In recent years this number is also growing in young adults aged 40-50 years termed as early onset AD [1]. The symptoms appear lately, but disease initiation starts around 20 years before the occurrence of symptoms [7,156]. The life expectancy of an AD patient averages nine years after diagnosis [28]. The increasing population of Alzheimer's patients is a major global concern, contributing as the fifth leading cause of death. It also accounts for 60–80% of total dementia cases [5,6]. An

estimated 50 million people suffered from Alzheimer's and other dementias in 2018, and it may cross 152 million by 2050. Every 3 s, a new dementia case is reported somewhere in the world. It accounts for a global economic burden of around 1 trillion US dollars, and it is estimated to increase twice by 2030 [7]. There are four USFDA-approved drugs (memantine hydrochloride, galantamine hydrobromide, rivastigmine hydrogen tartrate and donepezil hydrochloride) for the treatment of Alzheimer's. Amongst them, RIV-HT is a widely used drug in Alzheimer's therapeutics. It is a dual-acting cholinesterase used to treat mild to moderate Alzheimer's and related dementias. However, orally administered RIV-HT exhibits very low bioavailability (36%), extensive first-pass metabolism [157], shorter half-life (90 min), intra-individual variability, requires repetitive dose administration and is associated with severe cholinergic gastro-intestinal mediated side-effects [158]. Furthermore, the hydrophilic RIV-HT represents a lesser concentration in CNS due to limited permeability across the blood-brain barrier. Therefore, the current oral therapy of RIV-HT necessitates the development of an alternative approach to improve brain targeting and therapeutic action.

N2B delivery has emerged as a potential, non-invasive strategy for brain targeting. It facilitates the direct transport of drugs to the CNS, devoiding BBB, and first-pass metabolism, with minimal systemic exposure and associated peripheral side effects [159]. However, intranasal delivery of RIV as free drug is associated with limitations such as limited permeability, rapid mucociliary clearance, enzymatic degradation, and inability to transport actives, *via.* olfactory and trigeminal nerve-mediated pathways [110,160]. These limitations of intranasal delivery could be overcome with nanocarrier-based delivery systems [160]. However, encapsulation of hydrophilic RIV-HT into a nanoparticle-based delivery system eventually leads to lower encapsulation efficiency, and faster drug release that in turn

lacks targeting and sustained therapeutic action [161]. Also, dose dumping occurs due to faster drug release resulting in drug-induced toxicity.

Nanocarrier-based delivery systems include both lipidic (vesicular systems, microemulsions or nanoemulsion SLN, NLC etc.) and polymeric nano-carriers (nanoparticles, micelles, dendrimers etc.). Generally, liposome-based delivery systems for hydrophilic drugs are associated with relatively faster drug release due to bilayer fluidity. It is often linked with fewer shortcomings such as compromised colloidal stability, prone to lipid oxidation [162], and drug leakage upon storage [19]. Lipidic nanoparticles display constraints in terms of their high polydispersity index (PDI), stability and burst release of the drug [163]. However, polymer-based nanocarriers are associated with certain disadvantages, such as limited drug loading capacity and involvement of several critical preparation steps [164]. So, there's an unmet need for a carrier system to overcome these drawbacks. A suitable nanocarrier delivery system is necessary to provide higher stability, permeation efficiency and sustained drug release. The developed formulations should have the ability to enhance brain concentrations and drug-targeting efficiency to the brain.

1.9 Outline of the work

We explored three different formulation approaches for delivering RIV-HT *via* N2B delivery. In the first approach, we fabricated hydrophobic IPC of RIV-HT that offers several advantages such as improved drug saturation solubility (in non-polar solvents), % encapsulation efficiency, drug permeation efficiency with slow, controlled *in-vitro* drug release profile [106,111,165]. The micron-sized IPC was reduced to a nanodispersion-based formulation for improved brain targeting. Nanodispersion owing to reduced particle size and improved hydrophobicity exhibits enhanced drug permeation across physical barriers. The

hydrophobic characteristics of IPC-based nanodispersion demonstrated a slow and controlled drug release profile.

In the second formulation approach, IPC was further loaded into an advanced, efficient, multi-component lipid-polymer hybrid (LPH) nanoparticle-based system. LPHs are advanced, versatile delivery systems that have potential to overcome the drawbacks of lipidic and polymeric nanocarriers [15]. Additionally, it offers several other advantages, such as improved colloidal stability, biocompatibility, a more controlled drug release pattern, and improved cellular uptake efficiency. Furthermore, hybrid nanoparticles comprising opposite charges, *viz.* cationic and anionic LPH nanoparticles, were developed. Studies were conducted to investigate the effect of LPH surface charge on *in-vitro* amyloid inhibition, brain bioavailability and N2B drug targeting efficiency. There are several reports available on the development of microemulsion [166], lipidic (SLN, NLC and liposomes) [64,154,167] and polymeric nanocarrier systems for permeation enhancement of RIV-HT for N2B delivery. Nevertheless, advanced LPH-based systems have remained unexplored for N2B delivery of AD-approved drugs. Also, IPC has not been explored for intranasal delivery of Alzheimer's therapeutics. In one such study, IPC of RIV-HT was fabricated using salicylic acid for the development of a controlled, long-acting transdermal RIV-HT-adhesive patch. The developed patch demonstrated enhanced *in-vivo* plasma concentration with a 2.8-fold increase in drug permeation efficiency, and sustained drug release up to 3 days. Moreover, our study particularly emphasized *in-vitro* amyloid inhibition, brain, plasma PK parameters, and N2B drug targeting efficiency of LPH nanoparticles based on surface charge.

In the third formulation approach, we developed chitosan-coated liposomes (CHT@RIV-HT-Liposome) for improved formulation stability and nose-to-brain targeting. It was hypothesized that chitosan coating onto RIV-HT liposome may improve stability, *in-vitro*

drug release and permeation efficiency of hydrophilic RIV. The optimized CHT@RIV-Liposome was loaded into *in-situ* thermoresponsive gel (CHT@RIV-Liposome gel) to enable longer drug retention in the nasal cavity. *In-vivo* pharmacokinetic study was conducted to compare brain bioavailability and nose-to-brain targeting efficiency of developed chitosan-coated liposomes.

1.10 Objective of research work

The objectives of the present research work are as follows:

Objective 1: Design and optimization of suitable rivastigmine-loaded nanocarrier systems for intranasal administration

- I. Development and optimization of IPC-loaded anionic LPH nanoparticle gel
- II. Development and optimization of IPC-loaded cationic LPH nanoparticle gel
- III. Development and optimization of IPC-based nanodispersion gel
- IV. Development and optimization of chitosan-coated liposome gel

Objective 2: *In-vitro* characterization of optimized RIV-loaded nanoformulations

Objective 3: Comparative evaluation of *ex-vivo* nasal permeation efficiency of optimized nanoformulations as compared to pure drug gel formulation

Objective 4: *In vivo* brain and plasma pharmacokinetic studies of RIV-loaded intranasal nanocarriers using Wistar rats.

In the present research work, we developed chitosan-coated liposomes to improve formulation stability, permeation efficiency and nose-to-brain targeting of RIV-HT. Chitosan has mucoadhesive property, that in turn leads to improved cellular internalization. Chitosan-coated liposomes were embedded into *in-situ* thermoresponsive gel to improve drug retention and absorption upon intranasal administration. In another approach, the IPC of RIV-HT was

developed to provide sustained drug release and improved nasal permeation efficiency. The IPC was further developed into IPC-based nanodispersion. The micron sized IPC complex was reduced to nano-size dispersion to improve drug permeation efficiency. The developed IPC was loaded into cationic and anionic lipid polymer hybrid nanoparticles to improve drug permeation and further sustain the drug's release. The effect of nanoparticle surface charge in nose-to-brain delivery was extensively evaluated. All four developed nanoformulations (chitosan-coated liposome gel, IPC-based nanodispersion gel, Cationic LPH nanoparticle gel, anionic LPH nanoparticle gel) were characterized for particle size, zeta potential, percent encapsulation efficiency, *in-vitro drug* release and nasal *ex-vivo* drug permeation efficiency. Pharmacokinetic study evaluated brain concentration and brain targeting efficiency of respective gel-loaded formulations. Plasma and brain PK parameters were elucidated for comparative evaluation of respective gel formulation with RIV-HT gel.

References

- [1] H. Mathys, J. Davila-Velderrain, Z. Peng, F. Gao, S. Mohammadi, J.Z. Young, M. Menon, L. He, F. Abdurrob, X. Jiang, A.J. Martorell, R.M. Ransohoff, B.P. Hafler, D.A. Bennett, M. Kellis, L.H. Tsai, Single-cell transcriptomic analysis of Alzheimer's disease, *Nature*. 570 (2019) 332–337. <https://doi.org/10.1038/s41586-019-1195-2>.
- [2] M.E. Hasselmo, M. Sarter, Modes and models of forebrain cholinergic neuromodulation of cognition, *Neuropsychopharmacology*. 36 (2011) 52–73. <https://doi.org/10.1038/npp.2010.104>.
- [3] Y. Duan, L. Lu, J. Chen, C. Wu, J. Liang, Y. Zheng, J. Wu, Psychosocial interventions for Alzheimer's disease cognitive symptoms: A Bayesian network meta-analysis, (2018) 1–11. <https://doi.org/10.1186/s12877-018-0864-6>.
- [4] A. Kumar, A. Singh, Ekavali, A review on Alzheimer's disease pathophysiology and its management: an update, *Pharmacol. Rep.* 67 (2015) 195–203. <https://doi.org/10.1016/J.PHAREP.2014.09.004>.
- [5] 2020 Alzheimer's disease facts and figures, *Alzheimer's Dement.* 16 (2020) 391–460. <https://doi.org/10.1002/alz.12068>.
- [6] Y.H. Yang, R. Liscic, J. Dominguez, Framework of treating Alzheimer's dementia, *Brain Sci. Adv.* 5 (2020) 82–93. <https://doi.org/10.1177/2096595820902580>.
- [7] C.L. Masters, R. Bateman, K. Blennow, C.C. Rowe, R.A. Sperling, J.L. Cummings, Alzheimer's disease, *Nat. Rev. Dis. Prim.* 1 (2015). <https://doi.org/10.1038/NRDP.2015.56>.
- [8] A.P. Skaria, The Economic and Societal Burden of Alzheimer Disease: Managed Care Considerations, *Am. J. Manag. Care.* 28 (2022) S188–S196.

<https://doi.org/10.37765/AJMC.2022.89236>.

- [9] A.D. International, C. Patterson, World Alzheimer Report 2018: The state of the art of dementia research: New frontiers, (2018). <https://www.alzint.org/resource/world-alzheimer-report-2018/> (accessed October 8, 2021).
- [10] Z. Breijyeh, R. Karaman, D. Muñoz-Torrero, R. Dembinski, Comprehensive Review on Alzheimer's Disease: Causes and Treatment, Mol. 2020, Vol. 25, Page 5789. 25 (2020) 5789. <https://doi.org/10.3390/MOLECULES25245789>.
- [11] Early-Onset Alzheimer's Disease | Johns Hopkins Medicine. <https://www.hopkinsmedicine.org/health/conditions-and-diseases/alzheimers-disease/earlyonset-alzheimer-disease> (accessed April 12, 2023).
- [12] Alzheimer's Association, Alzheimer's Association 2020 Facts and Figures Report, Alzheimer's Assoc. (2020) 1.
- [13] The top 10 causes of death, World Heal. Organ. (2020). <https://www.who.int/news-room/fact-sheets/detail/the-top-10-causes-of-death> (accessed November 23, 2020).
- [14] Alzheimer's Facts and Figures Report | Alzheimer's Association. <https://www.alz.org/alzheimers-dementia/facts-figures> (accessed April 12, 2023).
- [15] J. Lee, E. Meijer, K.M. Langa, M. Ganguli, M. Varghese, J. Banerjee, P. Khobragade, M. Angrisani, R. Kurup, S.S. Chakrabarti, I.S. Gambhir, P.A. Koul, D. Goswami, A. Talukdar, R.R. Mohanty, R.S. Yadati, M. Padmaja, L. Sankhe, C. Rajguru, M. Gupta, G. Kumar, M. Dhar, P. Chatterjee, S. Singhal, R. Bansal, S. Bajpai, G. Desai, A.R. Rao, P.T. Sivakumar, K.P. Muliya, S. Bhatankar, A. Chattopadhyay, D. Govil, S. Pedgaonkar, T. V. Sekher, D.E. Bloom, E.M. Crimmins, A.B. Dey, Prevalence of dementia in India: National and state estimates from a nationwide study, Alzheimer's

- Dement. (2023). <https://doi.org/10.1002/ALZ.12928>.
- [16] X. Xia, Y. Wang, J. Zheng, COVID-19 and Alzheimer's disease: how one crisis worsens the other., *Transl. Neurodegener.* 10 (2021) 15. <https://doi.org/10.1186/s40035-021-00237-2>.
- [17] A. Tsugawa, S. Sakurai, Y. Inagawa, D. Hirose, Y. Kaneko, Y. Ogawa, S. Serisawa, N. Takenoshita, H. Sakurai, H. Kanetaka, K. Hirao, S. Shimizu, Awareness of the COVID-19 outbreak and resultant depressive tendencies in patients with severe Alzheimer's disease, *J. Alzheimer's Dis.* 77 (2020) 539–541. <https://doi.org/10.3233/JAD-200832>.
- [18] S. Alonso-lana, M. Marquié, A. Ruiz, M. Boada, Cognitive and Neuropsychiatric Manifestations of COVID-19 and Effects on Elderly Individuals With Dementia, 12 (2020). <https://doi.org/10.3389/fnagi.2020.588872>.
- [19] K. Numbers, H. Brodaty, The effects of the COVID-19 pandemic on people with dementia, *Nat. Rev. Neurol.* 17 (2021) 69–70. <https://doi.org/10.1038/s41582-020-00450-z>.
- [20] B. Williams, R. Jalilianhasanpour, N. Matin, G.L. Fricchione, J. Sepulcre, M.S. Keshavan, W.C. LaFrance, B.C. Dickerson, D.L. Perez, Individual differences in corticolimbic structural profiles linked to insecure attachment and coping styles in motor functional neurological disorders, *J. Psychiatr. Res.* 102 (2018) 230–237. <https://doi.org/10.1016/J.JPSYCHIRES.2018.04.006>.
- [21] R. Deth, A. Clarke, J. Ni, M. Trivedi, Clinical evaluation of glutathione concentrations after consumption of milk containing different subtypes of β -casein: Results from a randomized, cross-over clinical trial, *Nutr. J.* 15 (2016) 1–6.

<https://doi.org/10.1186/s12937-016-0201-x>.

- [22] 2019 Alzheimer's Statistics, Alzheimer's Stat. (2019). <https://www.alzheimers.net/resources/alzheimers-statistics> (accessed November 23, 2020).
- [23] M. Kivipelto, F. Mangialasche, T. Ngandu, Lifestyle interventions to prevent cognitive impairment, dementia and Alzheimer disease, *Nat. Rev. Neurol.* 14 (2018) 653–666. <https://doi.org/10.1038/s41582-018-0070-3>.
- [24] K.N. Nam, A. Mounier, M.W. Cody, N.F. Fitz, A.Y. Carter, E.L. Castranio, H.I. Kamboh, V.L. Reeves, J. Wang, X. Han, J. Schug, I. Lefterov, R. Koldamova, Effect of high fat diet on phenotype , brain transcriptome and lipidome in Alzheimer's model mice, (2017) 1–13. <https://doi.org/10.1038/s41598-017-04412-2>.
- [25] T. Ali, T. Kim, S.U. Rehman, M.S. Khan, F.U. Amin, M. Khan, M. Ikram, M.O. Kim, Effect of high fat diet on phenotype, brain transcriptome and lipidome in Alzheimer's model mice, *Sci. Rep.* 7 (2017) 6076. <https://doi.org/10.1038/s41598-017-04412-2>.
- [26] S.G. Jeon, M. Cha, J. Kim, T.W. Hwang, K.A. Kim, T.H. Kim, K.C. Song, J. Kim, M. Moon, Vitamin D-binding protein-loaded PLGA nanoparticles suppress Alzheimer ' s disease-related pathology in 5XFAD mice, *Nanomedicine Nanotechnology, Biol. Med.* 17 (2019) 297–307. <https://doi.org/10.1016/j.nano.2019.02.004>.
- [27] X. Zhou, Y. Wang, S. Sohn, T.M. Therneau, H. Liu, D.S. Knopman, Automatic extraction and assessment of lifestyle exposures for Alzheimer's disease using natural language processing, *Int. J. Med. Inform.* 130 (2019). <https://doi.org/10.1016/j.ijmedinf.2019.08.003>.
- [28] M. Citron, Alzheimer's disease: strategies for disease modification, *Nat. Rev. Drug*

- Discov. 9 (2010) 387–398. <https://doi.org/10.1038/NRD2896>.
- [29] T. H. Ferreira-Vieira, I. M. Guimaraes, F. R. Silva, F. M. Ribeiro, Alzheimer's disease: Targeting the Cholinergic System, *Curr. Neuropharmacol.* 14 (2016) 101–115. <https://doi.org/10.2174/1570159x13666150716165726>.
- [30] T. Guo, D. Zhang, Y. Zeng, T.Y. Huang, H. Xu, Y. Zhao, Molecular and cellular mechanisms underlying the pathogenesis of Alzheimer's disease, *Mol. Neurodegener.* 15 (2020) 1–37. <https://doi.org/10.1186/s13024-020-00391-7>.
- [31] V.K. Sharma, V. Mehta, T.G. Singh, Alzheimer's Disorder: Epigenetic Connection and Associated Risk Factors, *Curr. Neuropharmacol.* 18 (2020) 740–753. <https://doi.org/10.2174/1570159x18666200128125641>.
- [32] J. V. Sanchez-Mut, H. Heyn, B.A. Silva, L. Dixsaut, P. Garcia-Esparcia, E. Vidal, S. Sayols, L. Glauser, A. Monteagudo-Sánchez, J. Perez-Tur, I. Ferrer, D. Monk, B. Schneider, M. Esteller, J. Gräff, PM20D1 is a quantitative trait locus associated with Alzheimer's disease, *Nat. Med.* 24 (2018) 598–603. <https://doi.org/10.1038/s41591-018-0013-y>.
- [33] S. Mostafavi, C. Gaiteri, S.E. Sullivan, C.C. White, S. Tasaki, J. Xu, M. Taga, H.U. Klein, E. Patrick, V. Komashko, C. McCabe, R. Smith, E.M. Bradshaw, D.E. Root, A. Regev, L. Yu, L.B. Chibnik, J.A. Schneider, T.L. Young-Pearse, D.A. Bennett, P.L. De Jager, A molecular network of the aging human brain provides insights into the pathology and cognitive decline of Alzheimer's disease, *Nat. Neurosci.* 21 (2018) 811–819. <https://doi.org/10.1038/s41593-018-0154-9>.
- [34] K. Takeda, A. Uda, M. Mitsubori, S. Nagashima, H. Iwasaki, N. Ito, I. Shiiba, S. Ishido, M. Matsuoka, R. Inatome, S. Yanagi, Mitochondrial ubiquitin ligase alleviates

- Alzheimer's disease pathology via blocking the toxic amyloid- β oligomer generation, *Commun. Biol.* 4 (2021) 1–13. <https://doi.org/10.1038/s42003-021-01720-2>.
- [35] D. Holtzman, J. Ulrich, Senescent glia spell trouble in Alzheimer's disease, *Nat. Neurosci.* 22 (2019) 683–684. <https://doi.org/10.1038/s41593-019-0395-2>.
- [36] W.V. Graham, A. Bonito-Oliva, T.P. Sakmar, Update on Alzheimer's disease therapy and prevention strategies, *Annu. Rev. Med.* 68 (2017) 413–430. <https://doi.org/10.1146/annurev-med-042915-103753>.
- [37] M.O. Quartey, J.N.K. Nyarko, J.M. Maley, J.R. Barnes, M.A.C. Bolanos, R.M. Heistad, K.J. Knudsen, P.R. Pennington, J. Buttigieg, C.E. De Carvalho, S.C. Leary, M.P. Parsons, D.D. Mousseau, The A β (1–38) peptide is a negative regulator of the A β (1–42) peptide implicated in Alzheimer disease progression, *Sci. Rep.* 11 (2021) 1–17. <https://doi.org/10.1038/s41598-020-80164-w>.
- [38] G.F. Chen, T.H. Xu, Y. Yan, Y.R. Zhou, Y. Jiang, K. Melcher, H.E. Xu, Amyloid beta: Structure, biology and structure-based therapeutic development, *Acta Pharmacol. Sin.* 38 (2017) 1205–1235. <https://doi.org/10.1038/aps.2017.28>.
- [39] D. Röhr, B.D.C. Boon, M. Schuler, K. Kremer, J.J.M. Hoozemans, F.H. Bouwman, S.F. El-Mashtoly, A. Nabers, F. Großerueschkamp, A.J.M. Rozemuller, K. Gerwert, Label-free vibrational imaging of different A β plaque types in Alzheimer's disease reveals sequential events in plaque development, *Acta Neuropathol. Commun.* 8 (2020) 1–13. <https://doi.org/10.1186/s40478-020-01091-5>.
- [40] T.J. Esparza, N.C. Wildburger, H. Jiang, M. Gangolli, N.J. Cairns, R.J. Bateman, D.L. Brody, Soluble amyloid-beta aggregates from human Alzheimer's disease brains, *Sci. Rep.* 6 (2016) 1–16. <https://doi.org/10.1038/srep38187>.

-
- [41] M. Gassowska-Dobrowolska, A. Kolasa-Wołoskiuk, M. Cieślik, A. Dominiak, K. Friedland, A. Adamczyk, Alterations in tau protein level and phosphorylation state in the brain of the autistic-like rats induced by prenatal exposure to valproic acid, *Int. J. Mol. Sci.* 22 (2021) 1–33. <https://doi.org/10.3390/ijms22063209>.
- [42] A. Michalicova, P. Majerova, A. Kovac, Tau Protein and Its Role in Blood–Brain Barrier Dysfunction, *Front. Mol. Neurosci.* 13 (2020) 178. <https://doi.org/10.3389/FNMOL.2020.570045/BIBTEX>.
- [43] A. Sanabria-Castro, I. Alvarado-Echeverría, C. Monge-Bonilla, Molecular pathogenesis of alzheimer’s disease: An update, *Ann. Neurosci.* 24 (2017) 46–54. <https://doi.org/10.1159/000464422>.
- [44] B. Mroczko, M. Groblewska, A. Litman-Zawadzka, The role of protein misfolding and tau oligomers (TauOs) in Alzheimer’s disease (AD), *Int. J. Mol. Sci.* 20 (2019). <https://doi.org/10.3390/ijms20194661>.
- [45] B.A. Plog, M. Nedergaard, The glymphatic system in central nervous system health and disease: Past, present, and future, *Annu. Rev. Pathol.* 13 (2018) 379–394. <https://doi.org/10.1146/ANNUREV-PATHOL-051217-111018>.
- [46] K. Gouveia-Freitas, A.J. Bastos-Leite, Perivascular spaces and brain waste clearance systems: relevance for neurodegenerative and cerebrovascular pathology, *Neuroradiology.* 63 (2021) 1581. <https://doi.org/10.1007/S00234-021-02718-7>.
- [47] B.C. Reeves, J.K. Karimy, A.J. Kundishora, H. Mestre, H.M. Cerci, C. Matouk, S.L. Alper, I. Lundgaard, M. Nedergaard, K.T. Kahle, Glymphatic system Impairment in Alzheimer’s disease and idiopathic normal pressure hydrocephalus, *Trends Mol. Med.* 26 (2020) 285–295. <https://doi.org/10.1016/J.MOLMED.2019.11.008>.

-
- [48] E. Melin, P.K. Eide, G. Ringstad, In vivo assessment of cerebrospinal fluid efflux to nasal mucosa in humans, *Sci. Reports* 2020 101. 10 (2020) 1–10. <https://doi.org/10.1038/s41598-020-72031-5>.
- [49] Y. Cheng, D.Y. Tian, Y.J. Wang, Peripheral clearance of brain-derived A β in Alzheimer's disease: pathophysiology and therapeutic perspectives, *Transl. Neurodegener.* 2020 91. 9 (2020) 1–11. <https://doi.org/10.1186/S40035-020-00195-1>.
- [50] Y. Han, X. Chu, L. Cui, S. Fu, C. Gao, Y. Li, B. Sun, Neuronal mitochondria-targeted therapy for Alzheimer's disease by systemic delivery of resveratrol using dual-modified novel biomimetic nanosystems, *Drug Deliv.* 27 (2020) 502–518. <https://doi.org/10.1080/10717544.2020.1745328>.
- [51] J. Cao, J. Hou, J. Ping, D. Cai, Advances in developing novel therapeutic strategies for Alzheimer's disease, *Mol. Neurodegener.* 13 (2018) 1–20. <https://doi.org/10.1186/s13024-018-0299-8>.
- [52] S. Agatonovic-Kustrin, C. Kettle, D.W. Morton, A molecular approach in drug development for Alzheimer's disease, *Biomed. Pharmacother.* 106 (2018) 553–565. <https://doi.org/10.1016/j.biopha.2018.06.147>.
- [53] M. Esang, M. Gupta, Aducanumab as a novel treatment for Alzheimer's disease: A decade of hope, controversies, and the future, (2021). <https://doi.org/10.7759/cureus.17591>.
- [54] G.K. Wilcock, S. Lilienfeld, E. Gaens, Efficacy and safety of galantamine in patients with mild to moderate Alzheimer's disease: Multicentre randomised controlled trial, *Br. Med. J.* 321 (2000) 1445–1449. <https://doi.org/10.1136/bmj.321.7274.1445>.
- [55] N. Govind, Donepezil for dementia due to Alzheimer's disease, *Br. J. Community*

-
- Nurs. 25 (2020) 148–149. <https://doi.org/10.12968/bjcn.2020.25.3.148>.
- [56] M. Treinin, Y. Jin, Cholinergic transmission in *C. elegans*: Functions, diversity, and maturation of ACh-activated ion channels, *J. Neurochem.* (2020) 1–18. <https://doi.org/10.1111/jnc.15164>.
- [57] D. Lo, G.T. Grossberg, Use of memantine for the treatment of dementia, *Expert Rev. Neurother.* 11 (2011) 1359–1370. <https://doi.org/10.1586/ern.11.132>.
- [58] H. Gao, Progress and perspectives on targeting nanoparticles for brain drug delivery, *Acta Pharm. Sin. B.* 6 (2016) 268–286. <https://doi.org/10.1016/j.apsb.2016.05.013>.
- [59] S.G. Summerfield, Y. Zhang, H. Liu, Examining the uptake of central nervous system drugs and candidates across the blood-brain barrier, *J. Pharmacol. Exp. Ther.* 358 (2016) 294–305. <https://doi.org/10.1124/jpet.116.232447>.
- [60] M.G. Beconi, D. Howland, L. Park, K. Lyons, J. Giuliano, C. Dominguez, I. Munoz-Sanjuan, R. Pacifici, Pharmacokinetics of memantine in rats and mice, *PLoS Curr.* 3 (2012). <https://doi.org/10.1371/currents.RRN1291>.
- [61] D.C. Mehta, J.L. Short, J.A. Nicolazzo, Memantine transport across the mouse blood-brain barrier is mediated by a cationic influx H⁺ antiporter, *Mol. Pharm.* 10 (2013) 4491–4498. <https://doi.org/10.1021/mp400316e>.
- [62] S. Al Harthi, S.E. Alavi, M.A. Radwan, M.M. El Khatib, I.A. AlSarraf, Nasal delivery of donepezil HCl-loaded hydrogels for the treatment of Alzheimer’s disease, *Sci. Rep.* 9 (2019) 1–20. <https://doi.org/10.1038/s41598-019-46032-y>.
- [63] S. Misra, K. Chopra, V.R. Sinha, B. Medhi, Galantamine-loaded solid-lipid nanoparticles for enhanced brain delivery: preparation, characterization, in vitro and in

- vivo evaluations, *Drug Deliv.* 23 (2016) 1434–1443.
<https://doi.org/10.3109/10717544.2015.1089956>.
- [64] P. Wavikar, R. Pai, P. Vavia, Nose to brain delivery of rivastigmine by in situ gelling cationic nanostructured lipid carriers: Enhanced brain distribution and pharmacodynamics, *J. Pharm. Sci.* 106 (2017) 3613–3622.
<https://doi.org/10.1016/j.xphs.2017.08.024>.
- [65] F. Luis, G. Moncayo, EXELON (rivastigmine tartrate) Capsules, 2020.
https://www.accessdata.fda.gov/drugsatfda_docs/label/2000/208231bl.pdf.
- [66] H. Hirono, K. Watanabe, K. Hasegawa, K. Hiroyasu, K. Shibasaki, S. Ohkoshi, Anti-Dementia drugs and hepatotoxicity—report of two cases, *Int. J. Gerontol.* 12 (2018) 261–263. <https://doi.org/10.1016/j.ijge.2018.02.008>.
- [67] N. Ferrara, G. Corbi, A. Capuano, A. Filippelli, F. Rossi, Memantine-induced hepatitis with cholestasis in a very elderly patient, *Ann. Intern. Med.* 148 (2008) 631–632.
<https://doi.org/10.7326/0003-4819-148-8-200804150-00023>.
- [68] T. Tsukamoto, H. Yamada, N. Uchimura, Memantine-associated hyperkalaemia in a patient with Alzheimer’s disease, *Psychogeriatrics.* 13 (2013) 180–181.
<https://doi.org/10.1111/psyg.12022>.
- [69] N. Horikawa, H. Yamada, N. Uchimura, Memantine-associated renal impairment in a patient with Alzheimer’s disease, *Psychiatry Clin. Neurosci.* 67 (2013) 126.
<https://doi.org/10.1111/pcn.12020>.
- [70] A.K. Leonard, A.P. Sileno, G.C. Brandt, C.A. Foerder, S.C. Quay, H.R. Costantino, In vitro formulation optimization of intranasal galantamine leading to enhanced bioavailability and reduced emetic response in vivo, *Int. J. Pharm.* 335 (2007) 138–

146. <https://doi.org/10.1016/j.ijpharm.2006.11.013>.
- [71] Y. Sun, L. Du, M. Yang, Q. Li, X. Jia, Q. Li, L. Zhu, Y. Zhang, Y. Liu, S. Liu, Brain-targeted drug delivery assisted by physical techniques and its potential applications in traditional Chinese medicine, *J. Tradit. Chinese Med. Sci.* 8 (2021) 186–197. <https://doi.org/10.1016/J.JTCMS.2021.07.003>.
- [72] K. Vashi, Y.Y. Pathak, Challenges in targeting to brain and brain tumors, Nanocarriers for Drug-Targeting Brain Tumors. (2022) 51–68. <https://doi.org/10.1016/B978-0-323-90773-6.00009-9>.
- [73] A. Alexander, M. Agrawal, A. Uddin, S. Siddique, A.M. Shehata, M.A. Shaker, S. Ata, U. Rahman, M. Iqbal, M. Abdul, M.A. Shaker, Recent expansions of novel strategies towards the drug targeting into the brain, (2019). <https://doi.org/10.2147/IJN.S210876>.
- [74] H. Gao, Progress and perspectives on targeting nanoparticles for brain drug delivery, *Acta Pharm. Sin. B.* 6 (2016) 268–286. <https://doi.org/10.1016/J.APSB.2016.05.013>.
- [75] P.J. Focke, X. Wang, H.P. Larsson, Neurotransmitter transporters: Structure meets function, *Structure.* 21 (2013) 694–705. <https://doi.org/10.1016/j.str.2013.03.002>.
- [76] P. Kandasamy, G. Gyimesi, Y. Kanai, M.A. Hediger, Amino acid transporters revisited: New views in health and disease, *Trends Biochem. Sci.* 43 (2018) 752–789. <https://doi.org/10.1016/j.tibs.2018.05.003>.
- [77] J. Rip, L. Chen, R. Hartman, A. Van Den Heuvel, A. Reijerkerk, J. Van Kregten, B. Van Der Boom, C. Appeldoorn, M. De Boer, D. Maussang, E.C.M. De Lange, P.J. Gaillard, Glutathione PEGylated liposomes: Pharmacokinetics and delivery of cargo across the blood-brain barrier in rats, *J. Drug Target.* 22 (2014) 460–467.

- <https://doi.org/10.3109/1061186X.2014.888070>.
- [78] Y. Li, N. Gu, Thermodynamics of charged nanoparticle adsorption on charge-neutral membranes: A simulation study, *J. Phys. Chem. B.* 114 (2010) 2749–2754. <https://doi.org/10.1021/jp904550b>.
- [79] M. Zeeshan, M. Mukhtar, Q. Ul Ain, S. Khan, H. Ali, Nanopharmaceuticals: A Boon to the Brain-Targeted Drug Delivery, *Pharm. Formul. Des. - Recent Pract.* (2020). <https://doi.org/10.5772/intechopen.83040>.
- [80] K.M. Jaruszewski, S. Ramakrishnan, J.F. Poduslo, K.K. Kandimalla, Chitosan enhances the stability and targeting of immuno-nanovehicles to cerebro-vascular deposits of Alzheimer ' s disease amyloid protein, *Nanomedicine Nanotechnology, Biol. Med.* 8 (2012) 250–260. <https://doi.org/10.1016/j.nano.2011.06.008>.
- [81] F. Xu, W. Lu, H. Wu, L. Fan, X. Gao, X. Jiang, Brain delivery and systemic effect of cationic albumin conjugated PLGA nanoparticles, *J. Drug Target.* 17 (2009) 423–434. <https://doi.org/10.1080/10611860902963013>.
- [82] S. Aroui, A. Kenani, Cell-Penetrating Peptides: A Challenge for Drug Delivery, in: *Cheminformatics Its Appl., IntechOpen,* 2020. <https://doi.org/10.5772/intechopen.91684>.
- [83] T. Skotland, T.G. Iversen, M.L. Torgersen, K. Sandvig, Cell-penetrating peptides: Possibilities and challenges for drug delivery in vitro and in vivo, *Molecules.* 20 (2015) 13313–13323. <https://doi.org/10.3390/molecules200713313>.
- [84] A. Bolhassani, B.S. Jafarzade, G. Mardani, In vitro and in vivo delivery of therapeutic proteins using cell penetrating peptides, *Peptides.* 87 (2017) 50–63. <https://doi.org/10.1016/j.peptides.2016.11.011>.

-
- [85] Y. Qin, H. Chen, W. Yuan, R. Kuai, Q. Zhang, F. Xie, L. Zhang, Z. Zhang, J. Liu, Q. He, Liposome formulated with TAT-modified cholesterol for enhancing the brain delivery, *Int. J. Pharm.* 419 (2011) 85–95. <https://doi.org/10.1016/J.IJPHARM.2011.07.021>.
- [86] C.P. Costa, J.N. Moreira, J.M. Sousa Lobo, A.C. Silva, Intranasal delivery of nanostructured lipid carriers, solid lipid nanoparticles and nanoemulsions: A current overview of in vivo studies, *Acta Pharm. Sin. B.* 11 (2021) 925–940. <https://doi.org/10.1016/j.apsb.2021.02.012>.
- [87] A.R. Khan, M. Liu, M.W. Khan, G. Zhai, Progress in brain targeting drug delivery system by nasal route, *J. Control. Release.* 268 (2017) 364–389. <https://doi.org/10.1016/J.JCONREL.2017.09.001>.
- [88] F. Sonvico, A. Clementino, F. Buttini, G. Colombo, S. Pescina, S.S. Guterres, A.R. Pohlmann, S. Nicoli, Surface-modified nanocarriers for nose-to-brain delivery: From bioadhesion to targeting, *Pharmaceutics.* 10 (2018) 1–34. <https://doi.org/10.3390/pharmaceutics10010034>.
- [89] M. Agrawal, S. Saraf, S. Saraf, S.G. Antimisiaris, M.B. Chougule, S.A. Shoyele, A. Alexander, Nose-to-brain drug delivery: An update on clinical challenges and progress towards approval of anti-Alzheimer drugs, *J. Control. Release.* 281 (2018) 139–177. <https://doi.org/10.1016/j.jconrel.2018.05.011>.
- [90] V. Bourganis, O. Kammona, A. Alexopoulos, C. Kiparissides, Recent advances in carrier mediated nose-to-brain delivery of pharmaceuticals, *Eur. J. Pharm. Biopharm.* 128 (2018) 337–362. <https://doi.org/10.1016/j.ejpb.2018.05.009>.
- [91] T. Musumeci, R. Pellitteri, M. Spatuzza, G. Puglisi, Nose-to-Brain Delivery :

- evaluation of polymeric nanoparticles on olfactory ensheathing cells uptake, *J. Pharm. Sci.* 103 (2014) 628–635. <https://doi.org/10.1002/jps.23836>.
- [92] E. Pourmemar, A. Majdi, M. Haramshahi, M. Talebi, P. Karimi, S. Sadigh-Eteghad, Intranasal Cerebrolysin Attenuates Learning and Memory Impairments in D-galactose-Induced Senescence in Mice, *Exp. Gerontol.* 87 (2017) 16–22. <https://doi.org/10.1016/j.exger.2016.11.011>.
- [93] C. Humpel, Intranasal delivery of collagen-loaded neprilysin clears beta-amyloid plaques in a transgenic Alzheimer mouse model, 13 (2021) 1–11. <https://doi.org/10.3389/fnagi.2021.649646>.
- [94] K. Selvaraj, K. Gowthamarajan, V.V.S.R. Karri, Nose to brain transport pathways an overview: potential of nanostructured lipid carriers in nose to brain targeting, *Artif. Cells, Nanomedicine Biotechnol.* 46 (2018) 2088–2095. <https://doi.org/10.1080/21691401.2017.1420073>.
- [95] S. Md, S.K. Bhattmisra, F. Zeeshan, N. Shahzad, M.A. Mujtaba, V. Srikanth Meka, A. Radhakrishnan, P. Kesharwani, S. Baboota, J. Ali, Nano-carrier enabled drug delivery systems for nose to brain targeting for the treatment of neurodegenerative disorders, *J. Drug Deliv. Sci. Technol.* 43 (2018) 295–310. <https://doi.org/10.1016/j.jddst.2017.09.022>.
- [96] P. Kaur, T. Garg, G. Rath, A.K. Goyal, In situ nasal gel drug delivery: A novel approach for brain targeting through the mucosal membrane, *Artif. Cells, Nanomedicine Biotechnol.* 44 (2016) 1167–1176. <https://doi.org/10.3109/21691401.2015.1012260>.
- [97] A.S. Hanafy, R.M. Farid, S.S. Elgamal, Complexation as an approach to entrap

- cationic drugs into cationic nanoparticles administered intranasally for Alzheimer ' s disease management: preparation and detection in rat brain, 9045 (2015) 1–14. <https://doi.org/10.3109/03639045.2015.1062897>.
- [98] S. Bahadur, D.M. Pardhi, J. Rautio, J.M. Rosenholm, K. Pathak, Intranasal nanoemulsions for direct nose-to-brain delivery of actives for cns disorders, *Pharmaceutics*. 12 (2020) 1–27. <https://doi.org/10.3390/pharmaceutics12121230>.
- [99] H. Akel, R. Ismail, I. Csóka, Progress and perspectives of brain-targeting lipid-based nanosystems via the nasal route in Alzheimer's disease, *Eur. J. Pharm. Biopharm.* 148 (2020) 38–53. <https://doi.org/10.1016/j.ejpb.2019.12.014>.
- [100] Sunena, S.K. Singh, D.N. Mishra, Nose to Brain Delivery of Galantamine Loaded Nanoparticles: In-vivo Pharmacodynamic and Biochemical Study in Mice, *Curr. Drug Deliv.* 16 (2018) 51–58. <https://doi.org/10.2174/1567201815666181004094707>.
- [101] A.S. Hanafy, R.M. Farid, M.W. Helmy, S.S. Elgamal, A.S. Hanafy, R.M. Farid, M.W. Helmy, S.S. Elgamal, A.S. Hanafy, R.M. Farid, M.W. Helmy, S.S. Elgamal, Pharmacological , toxicological and neuronal localization assessment of galantamine / chitosan complex nanoparticles in rats : future potential contribution in Alzheimer ' s disease management Pharmacological , toxicological and neuronal localization asse, 7544 (2016). <https://doi.org/10.3109/10717544.2016.1153748>.
- [102] L.S. Kandil, R.M. Farid, S.S. Elgamal, A.S. Hanafy, Intranasal galantamine / chitosan complex nanoparticles elicit neuroprotection potentials in rat brains via antioxidant effect, *Drug Dev. Ind. Pharm.* 0 (2021) 1–6. <https://doi.org/10.1080/03639045.2021.1934861>.
- [103] M. Yasir, U.V.S. Sara, I. Chauhan, P.K. Gaur, A.P. Singh, D. Puri, A. Aameeduzzafar,

- Solid lipid nanoparticles for nose to brain delivery of donepezil: formulation, optimization by Box–Behnken design, in vitro and in vivo evaluation, *Artif. Cells, Nanomedicine Biotechnol.* 46 (2018) 1838–1851. <https://doi.org/10.1080/21691401.2017.1394872>.
- [104] Y. Wang, X. Wang, F. Deng, N. Zheng, Y. Liang, H. Zhang, B. He, W. Dai, X. Wang, Q. Zhang, The effect of linkers on the self-assembling and anti-tumor efficacy of disulfide-linked doxorubicin drug-drug conjugate nanoparticles, *J. Control. Release.* 279 (2018) 136–146. <https://doi.org/10.1016/J.JCONREL.2018.04.019>.
- [105] A. Beck, L. Goetsch, C. Dumontet, N. Corvaia, Strategies and challenges for the next generation of antibody–drug conjugates, *Nat. Rev. Drug Discov.* 16 (2017) 315–337. <https://doi.org/10.1038/nrd.2016.268>.
- [106] R.S. Kalhapure, C. Mocktar, D.R. Sikwal, S.J. Sonawane, M.K. Kathiravan, A. Skelton, T. Govender, Ion pairing with linoleic acid simultaneously enhances encapsulation efficiency and antibacterial activity of vancomycin in solid lipid nanoparticles, *Colloids Surfaces B Biointerfaces.* 117 (2014) 303–311. <https://doi.org/10.1016/j.colsurfb.2014.02.045>.
- [107] K.D. Ristroph, R.K. Prud'homme, Hydrophobic ion pairing: Encapsulating small molecules, peptides, and proteins into nanocarriers, *Nanoscale Adv.* 1 (2019) 4207–4237. <https://doi.org/10.1039/c9na00308h>.
- [108] H. Xu, L. Zhang, L. Li, Y. Liu, Y. Chao, X. Liu, Z. Jin, Y. Chen, X. Tang, H. He, Q. Kan, C. Cai, Membrane-Loaded doxorubicin liposomes based on ion-pairing technology with high drug loading and pH-responsive property, *AAPS PharmSciTech.* 18 (2017) 2120–2130. <https://doi.org/10.1208/s12249-016-0693-x>.

-
- [109] R. Pangeni, J.U. Choi, V.K. Panth, Y. Byun, J.W. Park, Enhanced oral absorption of pemetrexed by ion-pairing complex formation with deoxycholic acid derivative and multiple nanoemulsion formulations: Preparation, characterization, and in vivo oral bioavailability and anticancer effect, *Int. J. Nanomedicine*. 13 (2018) 3329–3351. <https://doi.org/10.2147/IJN.S167958>.
- [110] A.S. Torky, M.S. Freag, M.M.A. Nasra, O.Y. Abdallah, Novel skin penetrating berberine oleate complex capitalizing on hydrophobic ion pairing approach, *Int. J. Pharm.* 549 (2018) 76–86. <https://doi.org/10.1016/j.ijpharm.2018.07.051>.
- [111] T. Ren, X. Lin, Q. Zhang, D. You, X. Liu, X. Tao, J. Gou, Y. Zhang, T. Yin, H. He, X. Tang, Encapsulation of azithromycin ion pair in liposome for enhancing ocular delivery and therapeutic efficacy on dry eye, *Mol. Pharm.* 15 (2018) 4862–4871. <https://doi.org/10.1021/ACS.MOLPHARMACEUT.8B00516>.
- [112] H. Zhao, H. Lu, T. Gong, Z. Zhang, Nanoemulsion loaded with lycobetaine-oleic acid ionic complex: Physicochemical characteristics, in vitro, in vivo evaluation, and antitumor activity, *Int. J. Nanomedicine*. 8 (2013) 1959–1973. <https://doi.org/10.2147/IJN.S43892>.
- [113] T. Zhang, Y. Zheng, Q. Peng, X. Cao, T. Gong, Z. Zhang, A novel submicron emulsion system loaded with vincristine-oleic acid ion-pair complex with improved anticancer effect: in vitro and in vivo studies, *Int. J. Nanomedicine*. 8 (2013) 1185–1196. <https://doi.org/10.2147/IJN.S41775>.
- [114] Q. Jiang, J. Wang, P. Ma, C. Liu, M. Sun, Y. Sun, Z. He, Ion-pair formation combined with a penetration enhancer as a dual strategy to improve the transdermal delivery of meloxicam, *Drug Deliv. Transl. Res.* 8 (2018) 64–72. <https://doi.org/10.1007/s13346->

017-0434-z.

- [115] S. Gänger, K. Schindowski, Tailoring Formulations for Intranasal Nose-to-Brain Delivery: A Review on Architecture, Physico-Chemical Characteristics and Mucociliary Clearance of the Nasal Olfactory Mucosa, *Pharm.* 2018, Vol. 10, Page 116. 10 (2018) 116. <https://doi.org/10.3390/PHARMACEUTICS10030116>.
- [116] M. Agrawal, S. Saraf, S. Saraf, S.K. Dubey, A. Puri, U. Gupta, P. Kesharwani, V. Ravichandiran, P. Kumar, V.G.M. Naidu, U.S. Murty, Ajazuddin, A. Alexander, Stimuli-responsive In situ gelling system for nose-to-brain drug delivery, *J. Control. Release.* 327 (2020) 235–265. <https://doi.org/10.1016/J.JCONREL.2020.07.044>.
- [117] P.G. Djupesland, J.C. Messina, R.A. Mahmoud, The nasal approach to delivering treatment for brain diseases: an anatomic, physiologic, and delivery technology overview, *Ther. Deliv.* 5 (2014) 709–733. <https://doi.org/10.4155/tde.14.41>.
- [118] A. Paul, K.S. Yadav, Parkinson’s disease: Current drug therapy and unraveling the prospects of nanoparticles, *J. Drug Deliv. Sci. Technol.* 58 (2020) 101790. <https://doi.org/10.1016/j.jddst.2020.101790>.
- [119] S. V. Dhuria, L.R. Hanson, W.H. Frey, Novel vasoconstrictor formulation to enhance intranasal targeting of neuropeptide therapeutics to the central nervous system, *J. Pharmacol. Exp. Ther.* 328 (2009) 312–320. <https://doi.org/10.1124/JPET.108.145565>.
- [120] S. Kyrkanides, M. Yang, R.H. Tallents, J. nie H. Miller, S.M. Brouxhon, J.A. Olschowka, The trigeminal retrograde transfer pathway in the treatment of neurodegeneration, *J. Neuroimmunol.* 209 (2009) 139–142. <https://doi.org/10.1016/J.JNEUROIM.2009.02.006>.
- [121] R.G. Thorne, G.J. Pronk, V. Padmanabhan, W.H. Frey, Delivery of insulin-like growth

- factor-I to the rat brain and spinal cord along olfactory and trigeminal pathways following intranasal administration, *Neuroscience*. 2 (2004) 481–496. <https://doi.org/10.1016/J.NEUROSCIENCE.2004.05.029>.
- [122] S. V. Dhuria, L.R. Hanson, W.H. Frey, Intranasal delivery to the central nervous system: mechanisms and experimental considerations., *J. Pharm. Sci.* 99 (2010) 1654–1673. <https://doi.org/10.1002/JPS.21924>.
- [123] X.F. Liu, J.R. Fawcett, L.R. Hanson, W.H. Frey, The window of opportunity for treatment of focal cerebral ischemic damage with noninvasive intranasal insulin-like growth factor-I in rats, *J. Stroke Cerebrovasc. Dis.* 13 (2004) 16–23. <https://doi.org/10.1016/J.JSTROKECEREBROVASDIS.2004.01.005>.
- [124] M.C. Veronesi, M. Alhamami, S.B. Miedema, Y. Yun, M. Ruiz-Cardozo, M.W. Vannier, Imaging of intranasal drug delivery to the brain, *Am. J. Nucl. Med. Mol. Imaging*. 10 (2020) 1. [/pmc/articles/PMC7076302/](https://pubmed.ncbi.nlm.nih.gov/37076302/) (accessed January 3, 2023).
- [125] M.J. Mitchell, M.M. Billingsley, R.M. Haley, M.E. Wechsler, N.A. Peppas, R. Langer, Engineering precision nanoparticles for drug delivery, *Nat. Rev. Drug Discov.* 20 (2021) 101–124. <https://doi.org/10.1038/s41573-020-0090-8>.
- [126] M.S.A. Tan, H.S. Parekh, P. Pandey, D.J. Siskind, J.R. Falconer, Nose-to-brain delivery of antipsychotics using nanotechnology: a review, *Expert Opin. Drug Deliv.* 17 (2020) 839–853. <https://doi.org/10.1080/17425247.2020.1762563>.
- [127] M. Sousa De Almeida, E. Susnik, B. Drasler, P. Taladriz-Blanco, A. Petri-Fink Ab, B. Rothen-Rutishauser, Understanding nanoparticle endocytosis to improve targeting strategies in nanomedicine, *Chem. Soc. Rev.* 50 (2021) 5397. <https://doi.org/10.1039/d0cs01127d>.

-
- [128] A. El-Sayed, H. Harashima, Endocytosis of gene delivery vectors: From clathrin-dependent to lipid raft-mediated endocytosis, *Mol. Ther.* 21 (2013) 1118–1130. <https://doi.org/10.1038/mt.2013.54>.
- [129] D. Sinha, S. Roy, P. Saha, N. Chatterjee, A. Bishayee, Trends in research on exosomes in cancer progression and anticancer therapy, *Cancers (Basel)*. 13 (2021) 1–31. <https://doi.org/10.3390/cancers13020326>.
- [130] S. Behzadi, V. Serpooshan, W. Tao, M.A. Hamaly, Y. Mahmoud, E.C. Dreaden, D. Brown, A.M. Alkilany, C. Omid, M. Mahmoudi, M.G. Hospital, M.G. Hospital, S. Arabia, *HHS Public Access*, 46 (2018) 4218–4244. <https://doi.org/10.1039/c6cs00636a.Cellular>.
- [131] E. Giuliano, D. Paolino, M. Fresta, D. Cosco, Mucosal applications of poloxamer 407-based hydrogels: An overview, *Pharmaceutics*. 10 (2018) 159. <https://doi.org/10.3390/PHARMACEUTICS10030159>.
- [132] D.M.N. Abouhusein, A. Khattab, N.A. Bayoumi, A.F. Mahmoud, T.M. Sakr, Brain targeted rivastigmine mucoadhesive thermosensitive In situ gel: Optimization, in vitro evaluation, radiolabeling, in vivo pharmacokinetics and biodistribution, *J. Drug Deliv. Sci. Technol.* 43 (2018) 129–140. <https://doi.org/10.1016/J.JDDST.2017.09.021>.
- [133] S. Cunha, M. Swedrowska, Y. Bellahnid, Z. Xu, J.M. Sousa Lobo, B. Forbes, A.C. Silva, Thermosensitive in situ hydrogels of rivastigmine-loaded lipid-based nanosystems for nose-to-brain delivery: characterisation, biocompatibility, and drug deposition studies, *Int. J. Pharm.* 620 (2022) 121720. <https://doi.org/10.1016/J.IJPHARM.2022.121720>.
- [134] S. Salatin, J. Barar, M. Barzegar-Jalali, K. Adibkia, M. Jelvehgari, Thermosensitive in

- situ nanocomposite of rivastigmine hydrogen tartrate as an intranasal delivery system: Development, characterization, ex vivo permeation and cellular studies, *Colloids Surf. B. Biointerfaces*. 159 (2017) 629–638. <https://doi.org/10.1016/j.colsurfb.2017.08.031>.
- [135] S. Salatin, J. Barar, M. Barzegar-Jalali, K. Adibkia, M. Alami-Milani, M. Jelvehgari, Formulation and Evaluation of Eudragit RL-100 nanoparticles loaded in-situ forming gel for intranasal delivery of rivastigmine, *Adv. Pharm. Bull.* 10 (2020) 20–29. <https://doi.org/10.15171/APB.2020.003>.
- [136] A. Gangopadhyay, P.M. Dandagi, K.P. Sutar, Development and evaluation of thermoreversible ethosomal gel of donepezil hydrochloride for intranasal delivery, *J. Pharm. Innov.* (2022). <https://doi.org/10.1007/S12247-022-09636-Y>.
- [137] M. Fazil, S. Md, S. Haque, M. Kumar, S. Baboota, J.K. Sahni, J. Ali, Development and evaluation of rivastigmine loaded chitosan nanoparticles for brain targeting, *Eur. J. Pharm. Sci.* 47 (2012) 6–15. <https://doi.org/10.1016/j.ejps.2012.04.013>.
- [138] A.S. Hanafy, R.M. Farid, M.W. Helmy, S.S. ElGamal, Pharmacological, toxicological and neuronal localization assessment of galantamine/chitosan complex nanoparticles in rats: future potential contribution in Alzheimer's disease management, *Drug Deliv.* 23 (2016) 3111–3122. <https://doi.org/10.3109/10717544.2016.1153748>.
- [139] B. Shah, D. Khunt, M. Misra, H. Padh, Formulation and in-vivo pharmacokinetic consideration of intranasal microemulsion and mucoadhesive microemulsion of rivastigmine for brain targeting, *Pharm. Res.* 35 (2018) 1–10. <https://doi.org/10.1007/S11095-017-2279-Z/FIGURES/6>.
- [140] D. Khunt, S. Polaka, M. Shrivastava, M. Misra, Biodistribution and amyloid beta induced cell line toxicity study of intranasal Rivastigmine microemulsion enriched with Fish

-
- Oil and Butter oil, *J. Drug Deliv. Sci. Technol.* 57 (2020) 101661. <https://doi.org/10.1016/j.jddst.2020.101661>.
- [141] A. Kaur, K. Nigam, S. Srivastava, A. Tyagi, S. Dang, Memantine nanoemulsion: a new approach to treat Alzheimer's disease, *J. Microencapsul.* 37 (2020) 355–365. <https://doi.org/10.1080/02652048.2020.1756971>.
- [142] M.M. Aakash Katdare, Dignesh Khunt, Shreya Thakkar, Surya Narayana Polaka, Comparative evaluation of fish oil and butter oil in modulating delivery of galantamine hydrobromide to brain via intranasal route: pharmacokinetic and oxidative stress studies., *Drug Deliv. Transl. Res.* 10 (2020) 1136–1146. <https://doi.org/10.1007/S13346-020-00739-Y>.
- [143] A. Rajput, S. Butani, Donepezil Hcl liposomes: development, characterization, cytotoxicity, and pharmacokinetic study, *AAPS PharmSciTech.* 23 (2022) 74. <https://doi.org/10.1208/s12249-022-02209-9>.
- [144] S. Kumar, L.R. Karthik, A. Sree, L. Bojja, N. Kumar, C.M. Rao, Pharmacokinetic and pharmacodynamic evaluation of nasal liposome and nanoparticle based rivastigmine formulations in acute and chronic models of Alzheimer ' s disease, *Naunyn-Schmiedeberg's Arch. Pharmacol.* (2021). <https://doi.org/10.1007/s00210-021-02096-0>.
- [145] K. Arumugam, G.S. Subramanian, S.R. Mallayasamy, R.K. Averineni, M.S. Reddy, N. Udupa, A study of rivastigmine liposomes for delivery into the brain through intranasal route, *Acta Pharm.* 58 (2008) 287–297. <https://doi.org/10.2478/V10007-008-0014-3>.
- [146] S. Cunha, B. Forbes, J. Manuel, S. Lobo, A.C. Silva, Improving drug delivery for

- Alzheimer's disease through nose-to-brain delivery using nanoemulsions, nanostructured lipid carriers (NLC) and in situ hydrogels, *Int J Nanomedicine*. 29 (2021) 4373–4390. <https://doi.org/10.2147/IJN.S305851>.
- [147] S. Cunha, C.P. Costa, J.A. Loureiro, J. Alves, A.F. Peixoto, B. Forbes, J.M.S. Lobo, A.C. Silva, Double optimization of rivastigmine-loaded nanostructured lipid carriers (NLC) for nose-to-brain delivery using the quality by design (QbD) approach: Formulation variables and instrumental parameters, *Pharm.* 2020, Vol. 12, Page 599. 12 (2020) 599. <https://doi.org/10.3390/PHARMACEUTICS12070599>.
- [148] K.R. Gajbhiye, V. Gajbhiye, I.A. Siddiqui, S. Pilla, V. Soni, Ascorbic acid tethered polymeric nanoparticles enable efficient brain delivery of galantamine: An in vitro-in vivo study, *Sci. Rep.* 7 (2017). <https://doi.org/10.1038/S41598-017-11611-4>.
- [149] L. Yan, H. Wang, Y. Jiang, J. Liu, Z. Wang, Y. Yang, S. Huang, Y. Huang, Cell-penetrating peptide-modified PLGA nanoparticles for enhanced nose-to-brain macromolecular delivery, *Acta Biomater.* 21 (2013) 435–441. <https://doi.org/10.1007/s13233-013-1029-2>.
- [150] A. Mathew, T. Fukuda, Y. Nagaoka, T. Hasumura, H. Morimoto, Y. Yoshida, T. Maekawa, K. Venugopal, D.S. Kumar, Curcumin loaded-PLGA nanoparticles conjugated with Tet-1 peptide for potential use in Alzheimer's disease, *PLoS One*. 7 (2012). <https://doi.org/10.1371/journal.pone.0032616>.
- [151] P.C. Bhatt, A. Verma, F.A. Al-Abbasi, F. Anwar, V. Kumar, B.P. Panda, Development of surface-engineered PLGA nanoparticulate-delivery system of TET1-conjugated nattokinase enzyme for inhibition of A β 40 plaques in Alzheimer's disease, *Int. J. Nanomedicine*. 12 (2017) 8749–8768. <https://doi.org/10.2147/IJN.S144545>.

-
- [152] N. Kamei, T. Shingaki, Y. Kanayama, M. Tanaka, R. Zochi, K. Hasegawa, Y. Watanabe, M. Takeda-Morishita, Visualization and quantitative assessment of the brain distribution of insulin through nose-to-brain delivery based on the cell-penetrating peptide noncovalent strategy, *Mol. Pharm.* 13 (2016) 1004–1011. <https://doi.org/10.1021/acs.molpharmaceut.5b00854>.
- [153] Z.Z. Yang, Y.Q. Zhang, Z.Z. Wang, K. Wu, J.N. Lou, X.R. Qi, Enhanced brain distribution and pharmacodynamics of rivastigmine by liposomes following intranasal administration, *Int. J. Pharm.* 452 (2013) 344–354. <https://doi.org/10.1016/j.ijpharm.2013.05.009>.
- [154] S.N. El-helaly, A.A. Elbary, M.A. Kassem, S.N. El-helaly, A.A. Elbary, M.A. Kassem, M.A. El-nabarawi, Electrosteric stealth Rivastigmine loaded liposomes for brain targeting: preparation, characterization, ex vivo, bio-distribution and in vivo pharmacokinetic studies Electrosteric stealth Rivastigmine loaded liposomes for brain targeting: preparation, *Drug Deliv.* 7544 (2017) 692–700. <https://doi.org/10.1080/10717544.2017.1309476>.
- [155] M. Yasir, A. Zafar, K.M. Noorulla, A.J. Tura, U.V.S. Sara, D. Panjwani, M. Khalid, M.J. Haji, W.G. Gobena, T. Gebissa, D.D. Dalecha, Nose to brain delivery of donepezil through surface modified NLCs: Formulation development, optimization, and brain targeting study, *J. Drug Deliv. Sci. Technol.* 75 (2022). <https://doi.org/10.1016/J.JDDST.2022.103631>.
- [156] Y.-H. Yang, R. Liscic, J. Dominguez, Framework of treating Alzheimer's dementia.pdf, *Brain Sci. Adv.* 5 (2020) 82–93. <https://doi.org/10.1177/2096595820902580>.

- [157] M. Bhandari, J. Shah, B. Gorain, A.B. Nair, S. Jacob, S.M.B. Asdaq, S. Fattepur, A.S. Alamri, W.F. Alsanie, M. Alhomrani, S. Nagaraja, M.K. Anwer, Optimized rivastigmine nanoparticles coated with Eudragit for intranasal application to brain delivery: Evaluation and nasal ciliotoxicity studies, *Materials (Basel)*. 14 (2021) 6291. <https://doi.org/10.3390/ma14216291>.
- [158] P. Wavikar, R. Pai, P. Vavia, Nose to brain delivery of rivastigmine by in situ gelling cationic nanostructured lipid carriers: enhanced brain distribution and pharmacodynamics, *J. Pharm. Sci.* 106 (2017) 3613–3622. <https://doi.org/10.1016/j.xphs.2017.08.024>.
- [159] F.M. Elsenosy, G.A. Abdelbary, A.H. Elshafeey, I. Elsayed, A.R. Fares, Brain targeting of Duloxetine HCl via intranasal delivery of loaded cubosomal gel: In vitro characterization, ex vivo permeation, and in vivo biodistribution studies, *Int. J. Nanomedicine*. 15 (2020) 9517. <https://doi.org/10.2147/IJN.S277352>.
- [160] P.R. Wavikar, P.R. Vavia, Rivastigmine-loaded in situ gelling nanostructured lipid carriers for nose to brain delivery, *J. Liposome Res.* 25 (2015) 141–149. <https://doi.org/10.3109/08982104.2014.954129>.
- [161] N.S. Hinge, M.M. Pandey, Sensitive RP-HPLC method of rivastigmine for applicative quantification of nanostructured lipid carriers, *Microchem. J.* 188 (2023) 108341. <https://doi.org/10.1016/J.MICROC.2022.108341>.
- [162] L. Ramezanzade, S.F. Hosseini, B. Akbari-Adergani, A. Yaghmur, Cross-linked chitosan-coated liposomes for encapsulation of fish-derived peptide, *LWT*. 150 (2021) 112057. <https://doi.org/10.1016/J.LWT.2021.112057>.
- [163] T. Date, V. Nimbalkar, J. Kamat, A. Mittal, R.I. Mahato, D. Chitkara, Lipid-polymer

- hybrid nanocarriers for delivering cancer therapeutics, *J. Control. Release.* 271 (2018) 60–73. <https://doi.org/10.1016/J.JCONREL.2017.12.016>.
- [164] S.S. Pukale, S. Sharma, M. Dalela, A. kumar Singh, S. Mohanty, A. Mittal, D. Chitkara, Multi-component clobetasol-loaded monolithic lipid-polymer hybrid nanoparticles ameliorate imiquimod-induced psoriasis-like skin inflammation in Swiss albino mice, *Acta Biomater.* 115 (2020) 393–409. <https://doi.org/10.1016/J.ACTBIO.2020.08.020>.
- [165] I. Shahzadi, M.H. Asim, A. Dizdarević, J.D. Wolf, M. Kurpiers, B. Matuszczak, A. Bernkop-Schnürch, Arginine-based cationic surfactants: Biodegradable auxiliary agents for the formation of hydrophobic ion pairs with hydrophilic macromolecular drugs, *J. Colloid Interface Sci.* 552 (2019) 287–294. <https://doi.org/10.1016/j.jcis.2019.05.057>.
- [166] B.M. Shah, M. Misra, C.J. Shishoo, H. Padh, Nose to brain microemulsion-based drug delivery system of rivastigmine: Formulation and ex-vivo characterization, *Drug Deliv.* 22 (2015) 918–930. <https://doi.org/10.3109/10717544.2013.878857>.
- [167] B. Shah, D. Khunt, H. Bhatt, M. Misra, H. Padh, Application of quality by design approach for intranasal delivery of rivastigmine loaded solid lipid nanoparticles: Effect on formulation and characterization parameters, *Eur. J. Pharm. Sci.* 78 (2015) 54–66. <https://doi.org/10.1016/J.EJPS.2015.07.002>.
- [168] M. Bhanderi, J. Shah, B. Gorain, A.B. Nair, S. Jacob, S.M.B. Asdaq, S. Fattepur, A.S. Alamri, W.F. Alsanie, M. Alhomrani, S. Nagaraja, M.K. Anwer, Optimized rivastigmine nanoparticles coated with Eudragit for intranasal application to brain delivery: Evaluation and nasal ciliotoxicity studies, *Materials (Basel)*. 14 (2021) 6291.

<https://doi.org/10.3390/MA14216291>.

- [169] Y. Cai, Q. Tian, C. Liu, L. Fang, Development of long-acting rivastigmine drug-in-adhesive patch utilizing ion-pair strategy and characterization of controlled release mechanism, *Eur. J. Pharm. Sci.* 161 (2021) 105774. <https://doi.org/10.1016/J.EJPS.2021.105774>.

CHAPTER 2

DRUG PROFILE

2.1 Physicochemical properties of rivastigmine hydrogen tartrate

2.1.1 Description

Rivastigmine hydrogen tartrate (RIV-HT) is a white to off-white, fine crystalline powder. Chemically it is known as (S)-N-Ethyl-N-methyl-3-[1(dimethylamino)ethyl]-phenyl carbamate hydrogen-(2R,3R)-tartrate (**Fig.2.1**). It has an empirical formula of $C_{14}H_{22}N_2O_2 \cdot C_4H_6O_6$ with molecular weight of 400.43. In pharmacological literature, RIV-HT is referred as SDZ ENA 713 or ENA 713 [1].

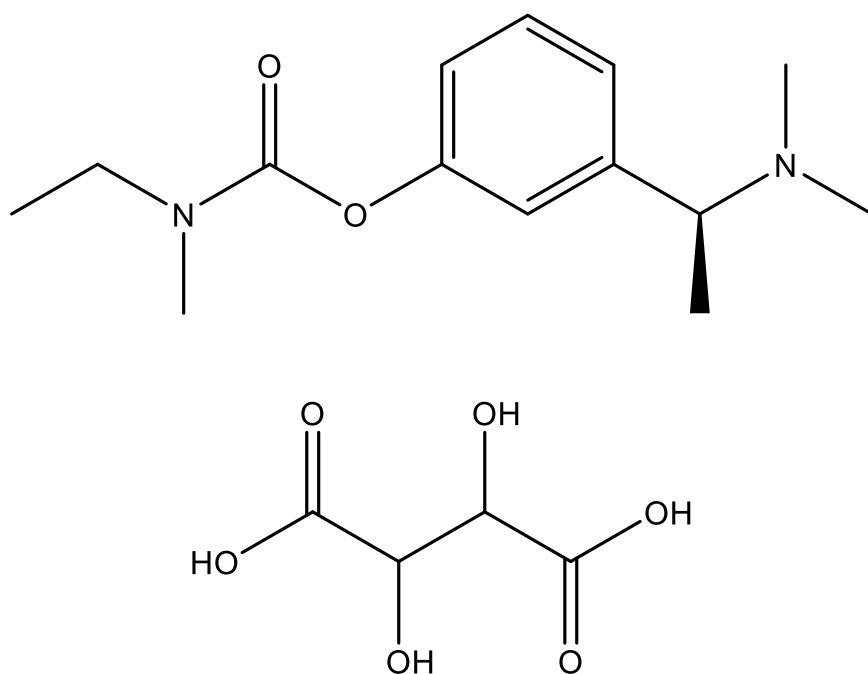


Fig. 2.1. Chemical structure of rivastigmine hydrogen tartrate

2.1.2 Solubility

RIV-HT is very soluble in water, soluble in ethanol, and acetonitrile. It is slightly soluble in n-octanol and very slightly soluble in ethyl acetate. Its distribution coefficient is observed to be 3 in n-octanol/phosphate buffer pH 7.0, at 37° C [1].

2.1.3 Polymorphism

Polymorphic forms of a crystalline drug exhibit different physicochemical properties. RIV-HT exists in two polymorphic forms: Form I and Form II. RIV-HT, Form I is recrystallized using isopropanol, and Form II is obtained by recrystallization in ethanol [2]. The crystal morphology of Form I exhibits a plate-like structure (**Fig.2.2A**), whereas Form II exists as a needle-shaped structure [2].

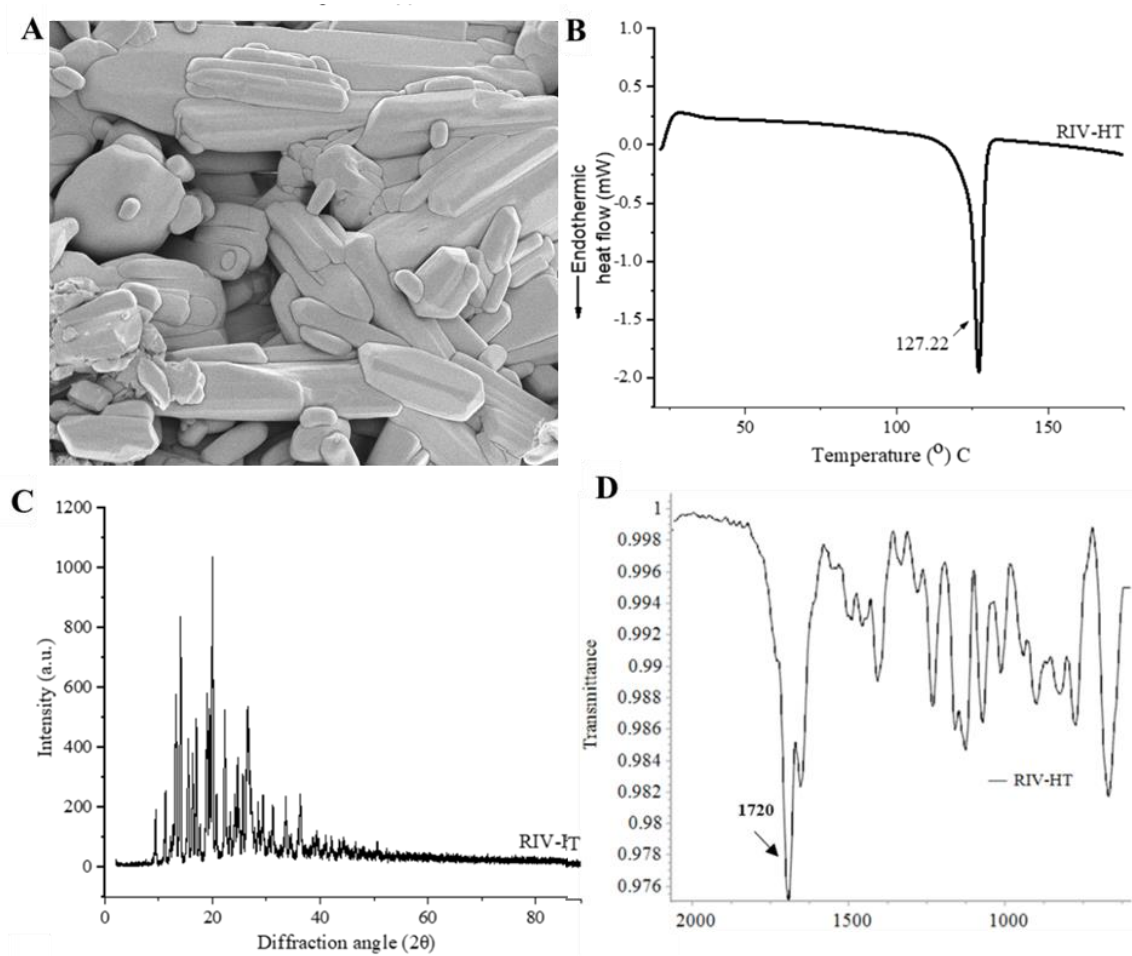


Fig. 2.2. (A) SEM of RIV-HT shows the presence of plate-like structure, (B) DSC, (C) X-ray diffraction graph exhibit polymorphic Form I and (D) represents FTIR spectra of RIV-HT, Form I shows carbamate absorption at 1720 cm^{-1}

Form I show melting point at 127.22° C ($\Delta H = -1.94$) (**Fig.2.2B**) and it is the stable polymorphic form of RIV-HT utilized in marketed formulation. Form II is a metastable form

that shows the presence of two melting endotherms. The presence of X-ray diffractogram (XRD) peaks at 5.1° , 14.7° , 16.5° , 17.6° , 18.6° , 20.4° , 21.1° (**Fig.2.2C**) is characteristics of Form I. While XRD peaks at: 9.5° , 11.3° , 14.2° , 15.5° , 19.1° and 20.0° 2θ are characteristic peaks for Form II. Fourier transform infra-red (FTIR) analysis of RIV-HT, Form I, represents the characteristic peak of carbamate at 1720 cm^{-1} (**Fig.2.2D**), while Form II shows carbamate peak at 1693 cm^{-1} [2].

Based on the scanning electron microscopy, differential scanning calorimetry, XRD and FTIR analysis results, it can be concluded that polymorphic Form I (stable form) was employed for research work. The marketed formulation of RIV-HT is available as polymorphic Form I

Table 2.1. Physicochemical properties of RIV-HT

Parameters	Description
Drug	Rivastigmine hydrogen tartrate
BCS class	Class 3
Chemical name	(S)-N-Ethyl-N-methyl-3-[1(dimethylamino)ethyl]-phenyl carbamate hydrogen-(2R,3R)-tartrate
Chemical formula	$\text{C}_{14}\text{H}_{22}\text{N}_2\text{O}_2 \cdot \text{C}_4\text{H}_6\text{O}_6$
Molecular weight	400.43
Physical state	Solid, crystalline
Melting point	127° C
Ionization constant (pKa)	8.8

Data taken from available literature

2.1.4 Stability and storage

RIV-HT is very hygroscopic and deliquescent. At relative storage humidity above 55%, it should be stored in packaging impermeable to moisture. RIV-HT is not sensitive to light [3].

2.2 Clinical pharmacology

2.2.1 Mechanism of action

The neuropathological changes in Alzheimer's and related dementia involve a cholinergic pathway that extends from basal forebrain to cerebral cortex and hippocampus [4]. These pathways are responsible for cognition, learning, memory, and attention. RIV-HT exerts therapeutic effect by its action on cholinergic neurons [5]. It increases the concentration of acetylcholine by reversible inhibition of acetylcholinesterase's. RIV-HT may slow down disease progression and may improve the functionality of cholinergic neurons. [6].

2.2.2 Absorption

RIV-HT absolute bioavailability is 36 % after administration of 3mg dose. The plasma maximum concentration (C_{max}) is achieved approximately at 1h. The presence of food delays T_{max} and reduces C_{max} by 30%, but increases the area under curve (AUC) by approximately 30 % [6].

2.2.3 Distribution

RIV-HT volume of distribution is in the range of 1.8-2.7 L/Kg. The mean AUC ratio of CSF/plasma is $40 \pm 0.5\%$. At a 1-400 ng/mL therapeutic concentration, 40 % drug is bound to plasma protein. RIV-HT penetrates the blood-brain barrier, with C_{max} achieved at 1.4-2.6 h [6].

2.2.4 Metabolism

RIV-HT is converted to decarbamylated metabolite, primarily metabolized by cholinesterase-mediated hydrolysis [7]. It is majorly metabolized by cytochrome CYP 450 isozyme. RIV-HT reports no drug interaction with cytochrome CYP 450 [6].

2.2.5 Excretion

90 % of the drug is eliminated through kidneys and 0.4% through feces. 40% of RIV-HT is excreted as decarbamylated metabolite in urine. No parent drug is detected in urine. Mean oral clearance of RIV-HT is 1.8 ± 0.6 L/min after twice-a-day administration of 6 mg dose [6].

2.2.6 Adverse effects

Oral therapy of RIV-HT is associated with gastrointestinal cholinergic-mediated side effects such as nausea and vomiting [8]. In some cases, it leads to drug-associated hepatotoxicity leading to cessation of therapy in severe cases [9].

2.3 Marketed formulation

2.3.1 Exelon[®]

RIV-HT is marketed as an oral capsule and solution by Novartis under the brand name Exelon[®]. RIV-HT equivalent 1.5, 3, 4.5 and 6 mg dose of rivastigmine base available as oral capsule. Oral solution of RIV-HT equivalent to 2mg/mL dose of RIV base is available as a marketed formulation [6].

2.4 Drawbacks of currently available therapy

The available therapy of RIV-HT exhibits lesser oral bioavailability (36 %) [1]. Furthermore, the hydrophilic RIV-HT represents a lesser drug concentration in CNS due to limited permeability across BBB [10]. Upon intravenous administration of RIV-HT, only 40 % drug reaches the brain [1]. RIV-HT exhibits shorter half-life (90 min) due to extensive first-pass metabolism [10]. Thereby oral therapy requires frequent dose administration, leading to gastrointestinal cholinergic mediated side-effects [8]. In some cases, greater systemic drug exposure causes hepatotoxicity, leading to cessation of therapy [9].

2.5 Conclusion

The physicochemical properties of RIV-HT were studied. SEM analysis, FTIR, DSC and powder XRD evaluation describe the presence of polymorphic Form I of RIV-HT. This chapter also enabled a detailed understanding of physicochemical properties, pharmacokinetic behavior, and marketed formulation of RIV-HT. This chapter also describes the adverse effects of RIV-HT and drawbacks of currently available oral therapy.

References

- [1] F. Luis, G. Moncayo, Exelon (rivastigmine tartrate) Capsules, 2020. https://www.accessdata.fda.gov/drugsatfda_docs/label/2000/20823lbl.pdf.
- [2] M.I. Amaro, A. Simon, L.M. Cabral, V.P. De Sousa, A.M. Healy, Rivastigmine hydrogen tartrate polymorphs: Solid-state characterisation of transition and polymorphic conversion via milling, *Solid State Sci.* 49 (2015) 29–36. <https://doi.org/10.1016/j.solidstatesciences.2015.09.004>.
- [3] Patel, Scientific discussion, 2019. https://www.ema.europa.eu/en/documents/scientific-discussion-variation/exelon-h-c-169-x-0038-epar-scientific-discussion-extension_en.pdf.
- [4] T. H. Ferreira-Vieira, I. M. Guimaraes, F. R. Silva, F. M. Ribeiro, Alzheimer's disease: Targeting the Cholinergic System, *Curr. Neuropharmacol.* 14 (2016) 101–115. <https://doi.org/10.2174/1570159x13666150716165726>.
- [5] M.E. Hasselmo, M. Sarter, Modes and models of forebrain cholinergic neuromodulation of cognition, *Neuropsychopharmacology.* 36 (2011) 52–73. <https://doi.org/10.1038/npp.2010.104>.
- [6] Exelon (Rivastigmine tartrate) Capsule and oral solution,. https://www.accessdata.fda.gov/drugsatfda_docs/label/2006/020823s016,021025s0081bl.pdf.
- [7] N.S. Hinge, M.M. Pandey, Sensitive RP-HPLC method of rivastigmine for applicative quantification of nanostructured lipid carriers, *Microchem. J.* 188 (2023) 108341. <https://doi.org/10.1016/J.MICROC.2022.108341>.
- [8] P. Wavikar, R. Pai, P. Vavia, Nose to brain delivery of rivastigmine by in situ gelling

- cationic nanostructured lipid carriers: Enhanced brain distribution and pharmacodynamics, *J. Pharm. Sci.* 106 (2017) 3613–3622. <https://doi.org/10.1016/J.XPHS.2017.08.024>.
- [9] H. Hirono, K. Watanabe, K. Hasegawa, K. Hiroyasu, K. Shibasaki, S. Ohkoshi, Anti-Dementia drugs and hepatotoxicity—report of two cases, *Int. J. Gerontol.* 12 (2018) 261–263. <https://doi.org/10.1016/j.ijge.2018.02.008>.
- [10] P.R. Wavikar, P.R. Vavia, Rivastigmine-loaded in situ gelling nanostructured lipid carriers for nose to brain delivery, *J. Liposome Res.* 25 (2015) 141–149. <https://doi.org/10.3109/08982104.2014.954129>.

CHAPTER 3

ANALYTICAL AND BIOANALYTICAL METHOD

DEVELOPMENT AND VALIDATION FOR

ESTIMATION OF RIV-HT

3.1 Analytical and bioanalytical method development and validation

Analytical method development and validation is essential in drug discovery and development [1]. Method development can be described as procedures followed for identifying, separating and quantifying an analyte in a pharmaceutical compound [2]. Analytical techniques are developed to test specific characteristics of the analyte with predetermined acceptance criteria. Analytical method development involves optimization and selection of a precise analytical procedure for determination of the analyte. Method validation is concerned with testing the suitability of analytical procedures for the quantification of an analyte [3]. Generally, analytical techniques are developed for identification, impurity testing, quantification of impurity, and drug assay testing. Analytical method development and validation should be performed as per protocol described by international guidelines such as the International Council for Harmonisation, United States Food and Drug Administration, European Medical Agency etc. [4]. Method validation parameters include evaluation of specificity, linearity, range, LOD, LOQ, accuracy, precision and robustness. [3].

RIV-HT, (S)-N-Ethyl-N-methyl-3-[1-(dimethylamino)ethyl]-phenyl carbamate hydrogen-(2R,3R)-tartrate, is an approved drug to alleviate symptoms of mild to moderate Alzheimer's disease [5]. It includes activity towards acetylcholine and butyrylcholine receptors with more selectivity towards brain acetylcholinesterase. It can potentially delay the degradation of acetylcholine and ameliorate cholinergic transmission at synapses [6]. RIV-HT exhibits a shorter half-life (90 min) due to extensive metabolism, *via.* cholinesterase-mediated hydrolysis and first-pass metabolism [5,7]. It is also associated with drawbacks such as cholinergic adverse effects (gastrointestinal mediated), frequent dose administration, and intra-individual variability [8]. For our research work, an analytical method was developed and validated to determine and quantify RIV-HT in bulk and formulations. Estimation of drug solubility at

different pH range and solvents was evaluated. Preliminary formulation development stages, include a large number of samples. So, there is a requirement for a rapid, simple, sensitive, accurate, and cost-effective analytical method for quick estimation of drugs. For this purpose, a spectrofluorimetric method was developed and validated for the estimation of RIV-HT. The validated method was utilized in initial formulation development to determine drug solubility in various surfactant, oils and lipids. Furthermore, the percent encapsulation efficiency of the developed nanoparticles was determined using the validated spectrofluorimetric method. Furthermore, a sensitive method was required to determine *in-vitro* drug release, *ex-vivo* permeation studies of developed nanoparticle formulation. An HPLC method was required for evaluation of stability studies, drug-excipient compatibility and forced degradation study. Therefore, a simple, sensitive, accurate, analytical method of RIV-HT was developed and validated using HPLC. Furthermore, the nanoparticle formulation was evaluated *in-vivo* for estimation of RIV-HT in brain and plasma. A precise, accurate, robust and sensitive bioanalytical method in rat brain and plasma matrices was developed and validated for the estimation of RIV-HT in pharmacokinetic (PK) samples.

This chapter is divided into 3 parts

Part 1: Method I: Fluorescence-based analytical method for estimation of RIV

Part 2: Method II: HPLC-based analytical method for quantification of RIV

Part 3: Method III: HPLC-based bioanalytical method for quantification of RIV in brain and plasma samples

Method I: Fluorescence-based method for estimation of RIV

3.1.1 Introduction

Spectrophotometric methods are rapid, simple and provide quick estimation of drugs in bulk and formulations. The literature review suggests ultraviolet-visible (UV) spectrophotometric-based analytical method for the estimation of RIV-HT. Srujana *et al.*, developed a UV-Visible spectrophotometric method at absorption maxima of 725 nm with a calibration range within 25 to 150 $\mu\text{g/mL}$ [9]. Arora *et al.*, developed a comparatively sensitive method within calibration range of 5-60 $\mu\text{g/mL}$ [10]. The method was reported at absorption maxima 263 nm in simulated nasal fluid for estimation of the drug in intranasal formulations. As compared to UV method, spectrofluorimetric methods are sensitive and selective for analyte determination. A spectrofluorimetric method reported by Kapil and Singh was observed to be more sensitive than the UV-Visible spectrophotometric method with a calibration range within 100-4000 ng/mL . The method was developed in triple distilled water as a solvent system. This is the only method reported for the spectrofluorimetric determination of RIV-HT [11]. As fluorescence intensity is highly sensitive to pH, it is always preferred to develop a method using buffers as solvent systems [12]. Fluorescence-based determination is rapid, simple, sensitive, accurate, cost-effective, and involves relatively simple instrumentation. Our method was developed in pH 6.4 phosphate buffer solution, similar to nasal pH for estimation of the drug in intranasal formulations. This research aims to develop and validate of fluorescence-based analytical method for the estimation of RIV-HT in bulk and nanocarrier-based delivery systems. The developed method can be successfully applied for preliminary formulation development and estimation of % encapsulation efficiency. So, there is a requirement for a rapid, simple, specific and accurate spectrofluorimetric method for the estimation of drug in bulk and formulations.

3.1.2 Material and method

3.1.2.1 Material

RIV-HT was received as a generous gift sample from Torrent Pharmaceuticals Ltd. (Ahmedabad, India). Potassium dihydrogen phosphate was purchased from SD Fine Chemicals (Mumbai, India). Sodium hydroxide, ortho-phosphoric acid, triethylamine, and HPLC-grade acetonitrile were purchased from Merck Pvt. Ltd. (Mumbai, India). All the reagents were of analytical grade, and Milli-Q water was obtained from our institute's Millipore Direct-Q ultra-pure water system (Millipore, Bedford, USA).

3.1.2.2 Instrumentation

The estimation was performed using FluorologTM, Horiba (Kyoto, Japan) instrument. The system is equipped with xenon arc lamp, the operation and data processing was performed using FluroEssence software program version 3.8. The estimation was performed using a 4 nm slit width with 0.6 cm cuvette size.

3.1.2.3 Preparation of standard solutions

The primary stock solution of 100 µg/mL concentration was prepared in acetonitrile. 10 mg RIV-HT was accurately weighed, and further volume was made upto 100 mL using acetonitrile. For the preparation of calibration curve standards, standard solutions of 0.1, 1, 5, 10, 15, and 20 µg/mL were prepared in pH 6.4 phosphate buffer as a solvent system. Four quality control (QC) samples i.e., 0.15 µg/mL as low (LQC), 1 µg/mL as medium (MQC-1), 12 µg/mL as MQC-2 and 20 µg/mL as high (HQC) quality control standard solutions were prepared. Fluorescence intensity was measured at excitation and emission wavelengths of 264 and 290 nm, respectively. The blank sample was measured using the same excitation and emission wavelength.

3.1.2.4 Method validation

The proposed RIV-HT fluorescence method was validated concerning the specificity, linearity, accuracy, precision, and robustness according to guidelines stated by the International Council for Harmonisation (Q2R2) [13].

3.1.2.4.1 Specificity

The specificity of the method was evaluated in the presence of blank nanoparticle formulation (Composition: Glyceryl monostearate, Miglyol 812, tween 80, span 80). Independent concentrations of pure drug and drug spiked in nanoparticle excipient of 0.1 µg/mL were prepared, and fluorescence intensity was measured at 264 nm wavelength (n = 5).

3.1.2.4.2 Calibration curve, linearity, and range

The calibration curve was obtained within the range of 0.1 to 20 µg/mL, generating 3 calibration curves in triplicates (n = 9). The graph was plotted against fluorescence intensity vs concentration, and the values of slope, intercept and R^2 were determined. The % RSD was calculated for each response to establish an appropriate calibration range.

3.1.2.4.3 Accuracy

The accuracy was determined by calculating the percentage recovery from injected QC samples. The QC samples represent 4 levels of concentrations, viz. LQC, MQC-1, MQC-2 and HQC covered a majority of the linearity range. The accuracy was determined by assessing the respective QC sample, and percentage recovery was calculated.

3.1.2.4.4 Precision

To determine precision of the developed method, QC samples were prepared from an independent pure drug stock solution. To assess reproducibility, LQC, MQC-1, MQC-2 and HQC concentrations were prepared in triplicate. Samples were analyzed three times a day to determine intra-day precision. Inter-day precision was performed by analyzing samples for

three consecutive days. Inter-day and intra-day precision were assessed by calculating % RSD at all QC levels. Inter-instrument variability was assessed by performing analysis of similar QC samples (n = 3) on another Fluorolog instrument.

3.1.2.4.5 Robustness

Robustness was performed to determine the ability of the proposed method to resist slight changes in the experimental condition, such as pH (± 0.2) of the solvent system. Further, the % recovery was calculated for each standard QC sample.

3.1.2.4.6 Limit of detection and limit of quantification

LOD and LOQ were derived from calibration curves using the following formula:

$$LOD = 3.3 \sigma/S \quad \dots (1)$$

$$LOQ = 10\sigma/S \quad \dots (2)$$

Where “S” is the average slope of three calibration curves and “ σ ” is the standard deviation (SD) of the y-intercept calculated from three calibration curves.

3.1.2.4.7 Stability study

It was performed to evaluate the solution state stability of the samples at various storage conditions. For this, the QC samples were analyzed in triplicates to assess the benchtop stability (24 h, room temperature), and short-term stability (7 days at 4°C).

3.1.3 Result and discussion

3.1.3.1 Method development

The fluorescence intensity of RIV-HT exhibited maximum fluorescence intensity at acidic pH of 3. It showed a pattern of decreased fluorescence intensity with an increase in the pH of the phosphate buffer solution. This is due to the ionization of RIV-HT at lower pH. Although the

RIV-HT showed maximum fluorescence intensity at pH 3, the method was developed in phosphate buffer pH 6.4 as the pH of the nasal cavity lies within 5.5 to 6.4.

3.1.3.2 Method validation

The RIV-HT standard solution exhibited excitation and emission wavelength at 264 and 290 nm (**Table 3.1**) respectively. The method was validated as per the specifications of ICH Q2R2 guidelines [13].

Table 3.1. Analytical parameters of RIV-HT-based fluorescence method

Parameters	Result
Excitation wavelength	264 nm
Emission wavelength	290 nm
Slit width	4 nm
Linearity, range	0.1-20 $\mu\text{g/mL}$
Correlation coefficient	0.9979
Slope	2241
Limit of detection	0.28 $\mu\text{g/mL}$
Limit of quantification	0.84 $\mu\text{g/mL}$

3.1.3.2.1 Calibration curve, linearity, and range

The calibration curve was plotted in the concentration range of 0.1–20 $\mu\text{g/mL}$ (**Fig.3.1 and Fig.3.2**). Values of regression equation and regression coefficient were obtained from the calibration curve. The lower values of standard error, slope, and intercept represent higher precision of the proposed method (**Table 3.1**). Slope and intercept values were calculated with 95% confidence interval.

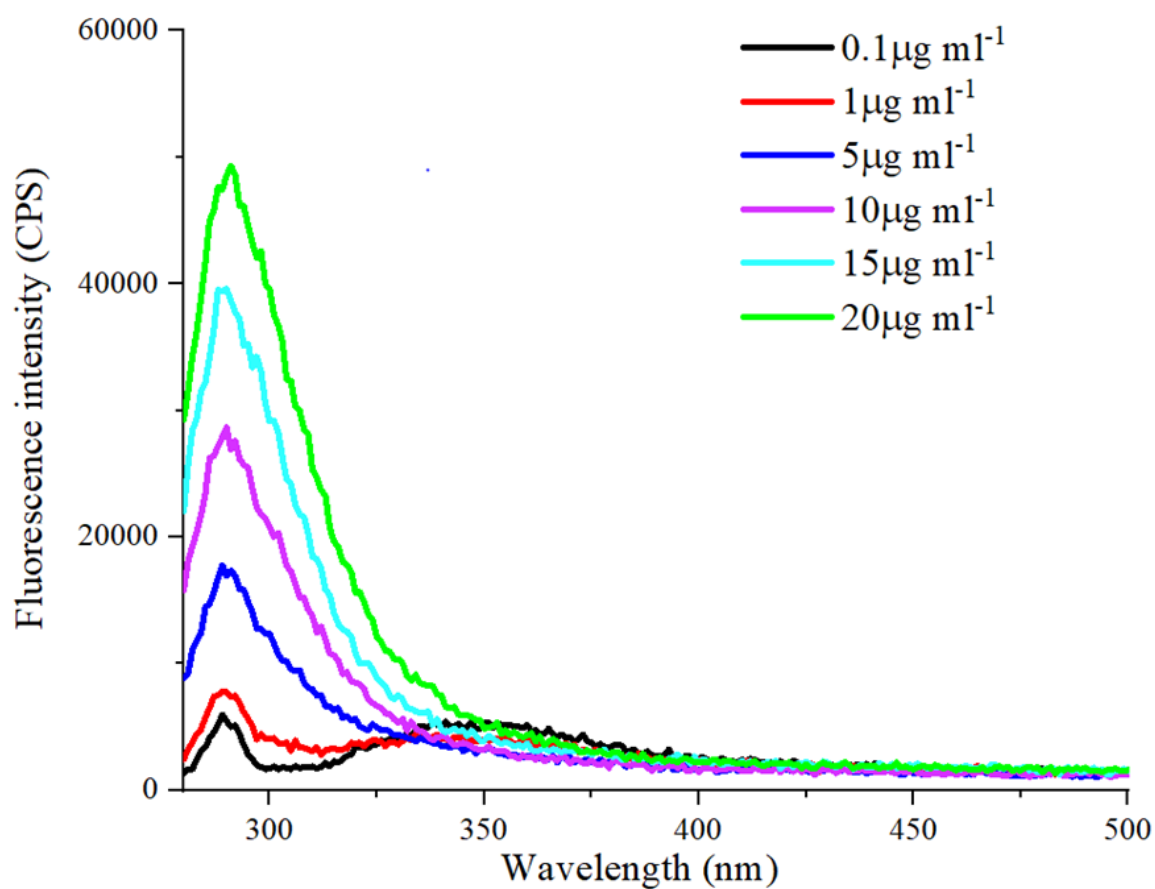


Fig. 3.1. Overlay spectra of calibration curve concentrations

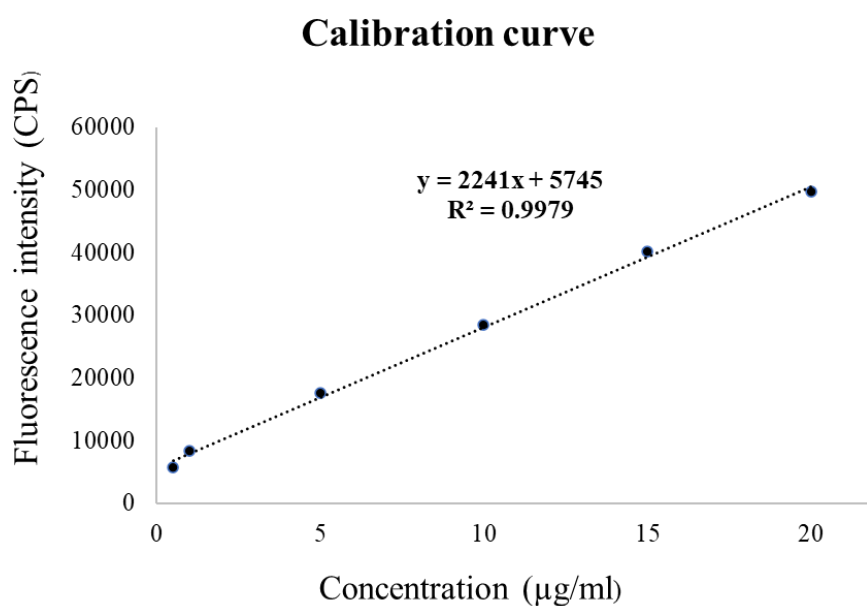


Fig. 3.2. Graph represents calibration curve of concentration vs fluorescence intensity graph.

3.1.3.2.2 Specificity

The specificity of the method was evaluated in the presence of blank and RIV-HT-loaded nanoparticles (**Table 3.2**). The results showed observation of no interference due to the presence of formulation excipients. Thus, confirming the specificity of the proposed method for RIV-HT.

Table 3.2. Specificity data for pure drug and drug-loaded formulation components. Standard concentration of 0.1 $\mu\text{g/mL}$ was utilized for analysis (n = 5)

Parameter	Mean	SD	% RSD
Pure drug	5717.5	86.71	1.51
Formulation	5704.87	94.23	1.65

3.1.3.2.3 Accuracy

Results of the accuracy study of the proposed method are presented in **Table 3.3**. All the samples showed nearly 100% mean percent recovery with SD values less than 2. Mean percent recovery and SD for LQC, MQC1, MQC 2,[13] and HQC was observed to be $96.23 \pm 0.51\%$, 98.36 ± 1.02 , $99.92 \pm 1.47\%$, and $98.73 \pm 1.11\%$ (**Table 3.3**). Thus, the above results justify that small changes in the drug concentration can be accurately estimated using proposed method.

Table 3.3. Accuracy data at different quality control levels (n = 3)

Concentration Level ($\mu\text{g/mL}$) ^a	Measured concentration ^b ($\mu\text{g/mL}$) \pm SD	% Recovery \pm SD	% RSD	Percent bias ^c
LQC	0.14 ± 0.002	96.23 ± 0.51	0.53	-3.76
MQC-1	0.96 ± 0.01	98.36 ± 1.02	1.41	-1.7
MQC-2	11.99 ± 0.17	99.92 ± 1.47	1.47	-0.07

Concentration Level ($\mu\text{g/mL}$) ^a	Measured concentration ^b ($\mu\text{g/mL}$) \pm SD	% Recovery \pm SD	% RSD	Percent bias ^c
HQC	16.78 \pm 0.18	98.73 \pm 1.11	1.12	-1.26

Standard deviation (SD) and % relative standard deviation (% RSD)

^a LQC, MQC-1, MQC-2 and HQC are 0.15, 1, 12 and 17 $\mu\text{g/mL}$

^b Measured concentration of rivastigmine was calculated by linear regression equation.

^c Accuracy is given in % bias = $100 \times [(\text{predicted concentration} - \text{nominal concentration})/\text{nominal concentration}]$.

3.1.3.2.4 Precision

The precision was analyzed measuring repeatability and intermediate precision. For inter-day repeatability studies, the obtained % RSD ranged from 0.28-1.52 % for all four levels of concentrations. To evaluate precision of the given method, samples were analyzed at fixed time intervals and also assessed inter-instrument variability. For intermediate precision study, % RSD values were observed to be less than 2 % for all the levels of concentrations representing the precision and repeatability of the proposed method (**Table 3.4**).

Table 3.4. Precision data at different quality control levels

Concentration Levels ^a ($\mu\text{g/mL}$)	Intra-day %RSD (n = 9)	Inter-day %RSD (n = 3)			Inter-instrument variability (n = 3)
		Day 1	Day 2	Day 3	
LQC	1.58	1.32	0.28	1.31	1.34
MQC-1	0.56	0.93	1.20	1.47	1.67
MQC-2	1.98	1.27	1.03	1.52	1.76
HQC	0.41	0.73	0.87	0.939	1.28

% Relative standard deviation (% RSD)

^a LQC, MQC-1, MQC-2 and HQC are 0.15, 1, 12 and 17 $\mu\text{g/mL}$

3.1.3.2.5 Limit of detection and limit of quantification

LOD and LOQ for the proposed method were found to be 0.28 and 0.84 $\mu\text{g/mL}$ (**Table 3.1**).

These results indicate that the developed analytical method is sensitive.

3.1.3.2.6 Robustness

Variation in pH of solvent system by ± 0.2 did not demonstrate any significant effect on absorbance values. The mean % recovery (SD) was found within 93.55-99.64 % (**Table 3.5**).

Table 3.5. Robustness data at different pH conditions

Nominal Concentration ^a ($\mu\text{g/mL}$)	Measured concentration ($\mu\text{g/mL}$) \pm SD	Percent recovery ^b \pm SD	% RSD
At 6.2 pH			
LQC	0.14 \pm 0.002	97.33 \pm 1.88	1.93
MQC-1	0.96 \pm 0.01	96.12 \pm 1.41	1.47
MQC-2	11.86 \pm 0.12	98.83 \pm 1.41	1.43
HQC	16.94 \pm 0.18	99.64 \pm 1.49	1.50
At 6.6 pH			
LQC	0.14 \pm 0.001	97.33 \pm 0.94	0.96
MQC-1	0.98 \pm 0.05	98.23 \pm 0.70	0.72
MQC-2	11.72 \pm 0.12	98.81 \pm 0.20	0.20
HQC	16.84 \pm 0.15	93.55 \pm 1.20	1.28

Standard deviation (SD) and % relative standard deviation (% RSD)

^a LQC, MQC-1, MQC-2 and HQC are 0.15, 1, 12 and 17 $\mu\text{g/mL}$

^b % recovery = [(Nominal concentration/Mean measured concentration) \times 100]

3.1.3.2.7 Stability

Stability studies of RIV-HT were performed evaluating bench-top and short-term stability. The percentage recovery for all stability samples was observed within 97.33-99.58 % with % RSD values less than 2% at all levels of QC concentrations. The results demonstrate the stability of RIV-HT under different storage conditions as represented in **Table 3.6**.

Table 3.6. Stability data at different storage conditions

Concentration Levels ^a (µg/mL)	Mean measured Concentration (µg/mL) ± SD	Percent recovery ^b ± SD	% RSD
Short term stability (4°C, 7 days)			
LQC	0.14 ± 0.02	98.23 ± 1.41	1.44
MQC-1	0.95 ± 0.009	95.67 ± 1.27	1.33
MQC-2	11.72 ± 0.14	97.66 ± 1.68	1.72
HQC	16.59 ± 0.13	97.58 ± 1.08	1.12
Bench stock stability (at RT)			
LQC	0.49 ± 0.004	97.33 ± 1.27	1.28
MQC-1	0.95 ± 0.006	96.23 ± 0.82	0.83
MQC-2	11.93 ± 0.12	99.41 ± 1.44	1.45
HQC	16.93 ± 0.18	99.58 ± 1.52	1.52

Standard deviation (SD), % relative standard deviation (% RSD), Room temperature (RT)

^a LQC, sMQC-1, MQC-2 and HQC are 0.15, 1, 12 and 17 µg/mL

^b % recovery = [(Nominal concentration/Mean measured concentration) × 100]

3.1.4 Conclusion

The fluorescence-based analytical method for the estimation of RIV-HT was developed and validated as per ICH Q2R2 guidelines. The results supported the proposed method to be specific, sensitive, accurate, precise and robust. The developed method can be successfully applied for the evaluation of preliminary formulation development and % encapsulation efficiency of developed nanoparticles.

3.2 Method II: HPLC-based analytical method for quantification of RIV

3.2.1 Introduction

The present section compiles the HPLC method for quantitative estimation of RIV-HT in bulk and nanocarrier-based formulation. The presently available literature reports for RIV-HT lack sensitivity. The hydrophilic RIV shows a lesser permeation profile across nasal barrier [14]. The *ex-vivo* permeation studies of pure drug and its formulations therefore necessitate the development of a sensitive method. It is also required for determining the *in-vitro* drug release of a sustained-release formulation. In fewer applications, the sensitive method enables determining samples with trace amounts of RIV-HT [15]. Literature reports are available on the development and validation of RP-HPLC methods for determining stability [14,16], impurities [17] and assay of RIV-HT in bulk and pharmaceutical formulations [18]. Literature also states the development of liquid chromatography-tandem mass spectrometry (LC-MS-MS) method for estimating RIV-HT impurities and quantifying drug in biological samples such as plasma [19,20] and urine [21]. Li *et al.* developed and validated the RP-HPLC method using 90:10 (v/v) methanol: water with a calibration range of 10.9-163.5 $\mu\text{g/mL}$ [22]. Rao *et al.* developed another RP-HPLC method for the estimation of RIV-HT within a calibration range of 25-150 $\mu\text{g/mL}$ [14,23]. Choudhury *et al.* developed and validated a method for quantifying RIV-HT within a linearity range of 50-300 $\mu\text{g/mL}$ with a run time of 15 min [18]. All the reported methods are associated with some serious limitations. These methods require a higher proportion of organic phase [22], longer run time [18] and lack of sensitivity having calibration range in microgram level [10,15]. Also, the reported LC-MS-MS method is expensive and unsuitable for routine estimation of the drug in bulk and formulations. There is no RP-HPLC method available in the literature for analysis of RIV-HT in nanogram range. Furthermore, only one article is available stating quantification of RIV-HT in nanocarriers-based delivery

system. The scarcity of literature concerns demonstrating application of method using nanocarriers-based delivery system. In order to optimize various process parameters affecting %encapsulation efficiency and *in-vitro* drug release of nanoformulations, a sensitive, accurate and simple RP-HPLC method is essential. So, there is a pressing need for the development of a rapid, sensitive, cost-effective and eco-friendly analytical method for estimation of RIV-HT in pharmaceutical nanoformulations.

The research aims to develop and validate the RP-HPLC method for estimating RIV-HT at nanogram levels to meet the scarcity of the same in the present literature. The method was developed and validated as per the specifications of the International Council for Harmonisation and USFDA guidelines. A forced degradation study was performed to evaluate the specificity of the proposed method. Lastly, the validated method was successfully applied to determine the percent encapsulation efficiency, *in-vitro* drug release, and *ex-vivo* permeation efficiency of the prepared nanoformulation.

3.2.2 Material and method

3.2.2.1 Material

RIV-HT was received as a generous gift sample from Torrent Pharmaceuticals Ltd. (Ahmedabad, India). Potassium dihydrogen phosphate was purchased from SD Fine Chemicals (Mumbai, India). Sodium hydroxide, ortho-phosphoric acid, triethylamine, and HPLC-grade acetonitrile were purchased from Merck Pvt. Ltd. (Mumbai, India). All the reagents were of analytical grade, and Milli-Q water was obtained from our institute's Millipore Direct-Q ultra-pure water system (Millipore, Bedford, USA).

3.2.2.2 Instrumentation

RP-HPLC method was developed using Shimadzu HPLC system (Kyoto, Japan) equipped with a pulse-free solvent system consisting of binary pumps (LC-20 AD), 5 degassers (DGU-

20A5R), a sample cooler and an automated autosampler (SIL-20AC HT). The column temperature was maintained using system system-equipped heat block-type column oven (CTO-10AS VP). Detection was performed using system inbuilt, dual-wavelength, UV-visible detector (SPD-20A). The system was operated using LC Solutions software, version 6.110.

3.2.2.3 Chromatographic conditions

The separation of RIV-HT was performed using Hypersil[®] BDS C₁₈ column (250 x 4.6 mm) with 50 µL injection volume. The column was allowed to equilibrate for 40 min before assessing the samples. The proposed method consisted of isocratic elution mode with column temperature maintained at 30 °C. The mobile phase consisted of A: acetonitrile constituting 0.05% (v/v) triethylamine, B: pH 5.5 phosphate buffer (10 mM) and C: iso-propyl alcohol with a composition of 33:65:2 (%A: %B: %C). The flow rate was maintained at 0.9 mL/min. The analysis was performed at a detection wavelength of 215 nm and peak area was utilized for the quantification of RIV-HT [24].

3.2.2.4 Preparation of standard solutions

The primary stock solution of 100 µg/mL concentration was prepared in acetonitrile. For this, 10 mg RIV-HT was accurately weighed, and further volume was made upto 100 mL using acetonitrile. For preparation of calibration curve standards, 1 µg/mL working standard solution was stepwise diluted with mobile phase to make 25, 50, 100, 200, 400 and 600 ng/mL solution. QC samples were also prepared from 1 µg/mL working standard solution. QC samples representing LQC, MQC and HQC samples of 30, 300 and 500 ng/mL concentrations were utilized in the analysis.

3.2.2.5 Method validation

System suitability was performed to evaluate the suitability of the liquid chromatographic system for the developed analytical method. For this, six replicates of RIV-HT standard

solution (500 ng/mL) were injected and deviation in retention time (min), tailing factor (10%), retention factor (k), number of theoretical plates (N) and height equivalent to theoretical plate were represented with respect to % RSD.

The proposed RIV-HT method was validated with respect to the specificity, linearity, accuracy, precision, and robustness according to guidelines stated by International Council for Harmonisation (Q2R2) [13] along with United States pharmacopeial guidelines [25] specified for RIV-HT.

3.2.2.5.1 Specificity

Forced degradation studies

The study was performed using RIV-HT standard solution to evaluate the stability indicating property in various stress conditions such as acid, alkali, oxidation, hydrolysis etc. Forced degradation studies were conducted to confirm specificity of the developed analytical method. For this, 2 mL RIV-HT (1 mg/mL) solution was exposed to different stress conditions. To assess acid and base degradation patterns, samples were treated with 0.5N HCl and 0.5N NaOH separately, at 60 °C for 48 h. For hydrolysis and oxidative degradation studies, samples were treated with water (H₂O) and 3% hydrogen peroxide (H₂O₂) separately at 60 °C for 48 h. Further, samples were suitably diluted to obtain the concentration of 500 ng/mL and assessed using the proposed RP-HPLC method. For the solid-state degradation study, 5 mg drug sample was kept in presence of heat (60 °C) and UV light separately for 10 days. 1 mg samples were withdrawn and suitably diluted with mobile phase to obtain a concentration of 500 ng/mL. The samples were further analyzed using the developed method to assess drug degradation.

The specificity of the developed method was assessed by spiking a standard solution of RIV-HT (500 ng/mL) with excipients (of nanoformulation) to check interference with the elution of RIV-HT peak. For this, the supernatant solution consisting of blank and RIV-HT

nanoformulation were suitably diluted and analyzed. Also, matrix interferences were determined in the components of *in-vitro* release and *ex-vivo* permeation medium.

3.2.2.5.2 Calibration curve, linearity, and range

The calibration curve was obtained within the range of 25-600 ng/mL, generating 3 calibration curves in triplicates (n = 9). The graph was plotted against peak area vs concentration, and the values of slope, intercept and R^2 were determined. The % RSD was calculated for each response to establish an appropriate calibration range. One-way analysis of variance was utilized for calculating F-value that determines homoscedasticity within linearity variables (n = 9).

3.2.2.5.3 Accuracy

The accuracy was determined by calculating the percentage recovery from injected QC samples. The QC samples represent 3 levels of concentrations, *viz.* LQC, MQC and HQC covered majority of the linearity range. The accuracy was performed by assessing respective QC samples and percentage recovery was calculated.

3.2.2.5.4 Precision

In order to determine precision of the developed method, QC samples were prepared from an independent pure drug stock solution. To assess reproducibility, LQC, MQC, and HQC concentrations were prepared in triplicate, and the samples were analysed three times in a day to determine intra-day precision. Inter-day precision was performed by analyzing samples for three consecutive days. Inter-day and intra-day precision were assessed by calculating %RSD at all QC levels. Inter-instrument variability was assessed by performing analysis of similar QC samples on another HPLC instrument (n = 3). Inter-instrument variability was performed using another HPLC system (LC-20 AD, Shimadzu, Kyoto, Japan) constituting binary pumps

and a UV-Visible detector (SPD-20 A) with system-generated software, LC solution version 5.97.

3.2.2.5.5 *Robustness*

Robustness was performed to determine the ability of the proposed method to resist slight changes in the chromatographic condition. It was assessed by deliberately introducing slight modifications in the proposed chromatographic conditions such as flow rate (± 0.1 mL/min), pH of the mobile phase (± 0.1), column temperature ($\pm 1^\circ$ C) and mobile phase ratio ($\pm 2\%$). Further, the % recovery was calculated from chromatographic response with respect to standard QC sample.

3.2.2.5.6 *Limit of detection and limit of quantification*

Limit of detection (LOD) and limit of quantification (LOQ) were derived from calibration curves using the following formula:

$$LOD = 3.3 \sigma/S \quad \dots (1)$$

$$LOQ = 10\sigma/S \quad \dots (2)$$

Where “S” is the average slope of three calibration curves and “ σ ” is the standard deviation (SD) of the y-intercept calculated from three calibration curves.

3.2.2.5.7 *Stability studies*

Stability studies were performed to evaluate the solution state stability of RIV-HT at various storage conditions. For this, the QC samples were analyzed in triplicates to assess the bench top stability (24 h, room temperature), auto-sampler stability (24 h at 25° C), short-term stability (7 days at 4° C), and long-term stability (1 month at -20° C). Stability samples used in the analysis were compared with respective QC standard solutions.

3.2.3 Result and discussion

3.2.3.1 Method development

The preliminary studies for method development were initiated with 10 mM phosphate buffer, pH 3.0 that resulted in faster elution of RIV-HT at 5.2 min. A sequential increase in pH of phosphate buffer from 4.5 to 5.0 and 5.5 showed a significant increase in peak area from 4370 ± 33.45 to 5830 ± 14.03 and 10381 ± 241.07 mV ($p < 0.05$), respectively (**Table 3.7**). Further increment in pH to 6.0 showed a declined peak shape and peak area (6036 ± 237.4 mV). Thereby pH 5.5 phosphate buffer was selected as the desired pH for the aqueous phase. The reason may be due to weakly basic characteristics of RIV-HT that will ionise completely at acidic pH of 2.6. This in turn leads to faster elution of drug at acidic pH, whereas increment in pH results in increased retention time [16]. Thereafter, mobile phase consisting of varying ratios of ACN: phosphate buffer such as 25:75, 30:70 and 35:65 were evaluated with respect to peak area, retention time, tailing factor and theoretical plates as demonstrated in **Table 3.7**. The increased ACN proportion of the mobile phase from 25 % to 30% and 35 % resulted in decreased retention time from 10.25 to 9.08 and 8.4 min respectively. In addition, it resulted in significantly increased peak area (10179 to 15990 and 20040), number of theoretical plates (from 1755 to 2653 and 5211), and improved tailing factor (from 1.72 to 1.56 and 1.47). The peak tailing was observed when the column temperature was maintained at 25 °C, which was overcome by increasing the column temperature to 30° C. Further, an increase in column temperature to 35° C resulted in no change in the tailing factor. Therefore, we opted for 30° C column temperature. The flow rate maintained at 0.8 and 1.0 ml/min showed a declined peak area owing to increased longitudinal diffusion and higher mass transfer at lower and higher flow rates, resulting in decreased peak area.

Table 3.7. Optimization of mobile phase using 100 ng/mL RIV-HT solution (n = 3)

Parameters	Limit	Result							
		Effect of pH				Effect of mobile phase ratio (% v/v)			
		4.5	5	5.5	6	25:75:0	30:70:0	35:65:0	33:65:2
Area (mV)	-	4370 ± 33.45	5830 ± 14.03	10381 ± 241.24	6036 ± 237.4	10179 ± 50.36	15990 ± 236.4	20040 ± 147.28	28648 ± 240.12
Retention time (min)	-	6.98 ± 0.07	8.28 ± 0.02	10.26 ± 0.03	11.5 ± 0.03	10.25 ± 0.01	9.08 ± 0.001	8.4 ± 0.002	8.19 ± 0.03
Tailing factor (10%)	0.8-1.5	1.71 ± 0.09	1.66 ± 0.02	1.69 ± 0.02	1.69 ± 0.07	1.72 ± 0.03	1.56 ± 0.04	1.47 ± 0.02	1.45 ± 0.02
Theoretical plate (N)	>2000	1362.52 ± 133.52	1424.47 ± 47.64	1729.18 ± 94.93	1752 ± 51.62	1755 ± 181.72	2653.01 ± 94.77	5211.0 ± 83.28	7982.12 ± 77.68

Thereby, the method was optimized with 0.9 mL/min flow rate. However, the mobile phase ratio constituting 35: 65 ACN: phosphate buffer pH 5.5, 0.9 mL/min flow rate at 30° C column temperature resulted in peak tailing at higher concentration. To avoid this problem, iso-propyl alcohol was incorporated in the mobile phase. The introduction of iso-propyl alcohol improved peak characteristics such as peak area, tailing factor and theoretical plates as shown in **Table 3.7**. In addition, it considerably improved peak tailing at higher concentrations. Therefore, ACN: phosphate buffer: IPA in ratio of 33: 65: 2 (pH 5.5, 10 mM), with 0.9 mL/min flow rate at 30° C was selected as the optimized conditions for the analytical method.

3.2.3.2 Method validation

The system suitability data is represented in **Table 3.8**. The peak area, retention time and tailing factor for 500 ng/mL concentration was observed to be 133339 ± 420.02 mV, 8.19 ± 0.03 min and 1.45 ± 0.02 respectively.

Table 3.8. Chromatographic condition representing system suitability parameters

Parameters	Acceptable limit	Mean \pm SD	% RSD
Area (mV)	-	133339 ± 420.02	0.31
Retention time (min)	-	8.19 ± 0.03	0.42
Tailing factor	0.8-1.5	1.45 ± 0.02	1.55
HETP	-	14.15 ± 0.23	1.68
Theoretical plate (N)	>5000	7995 ± 112.03	1.40
Retention factor (k)	$2 < k < 10$	2.64 ± 0.01	0.53

Standard deviation (SD), % relative standard deviation (% RSD), n = 6 samples in all cases

The results of chromatographic parameters fall within the acceptance criteria with % RSD values < 2%. The values of tailing factor (10%) (<1.5) and theoretical plates (>5000) lie as per United States Pharmacopoeia guidelines thus passing system suitability parameters.

3.2.3.2.1 Specificity

The specificity of the proposed method was evaluated using forced degradation study and in the presence of formulation matrix, *in-vitro* release and *ex-vivo* permeation medium. The results were compared with working standard solution of RIV-HT (500 ng/mL) (**Fig.3.3A**). The Forced degradation study in presence of NaOH showed the appearance of well separated degradant peak (at 7.45 min) with a slight shift in retention time of RIV-HT at 8.55 ± 0.04 min (resolution: 4.3 ± 1.36) (**Fig.3.3C**). The percentage recovery was observed to be $40.16 \pm 1.25\%$ (**Table 3.9**) representing degradation of the drug with alkali treatment. Forced degradation in the presence of acid (**Fig.3.3B**), water (**Fig.3.3D**), H₂O₂ (**Fig.3.3E**), heat (**Fig.3.3F**) and UV light (**Fig.3.3G**) did not result in occurrence of the additional peaks. Retention time and percentage recovery of RIV-HT under different stress conditions have been mentioned in (**Table 3.9**). Similar observations are reported by Rao *et al.* at all the degradation conditions. Thus, forced degradation study ensures specificity of the proposed method for quantification of RIV-HT [14].

The specificity results in presence of formulation matrix (**Fig.3.3H**) showed well separation of RIV-HT peak (**Fig.3.3I**) with resolution greater than 2.5 (**Table 3.9**). The samples in presence of *in-vitro* release medium (**Fig.3.3J**) and *ex-vivo* permeation medium (**Fig.3.3K**) showed observation of no interfering peak with that of the drug. Thus, results demonstrate that the proposed method is specific for determination of RIV-HT.

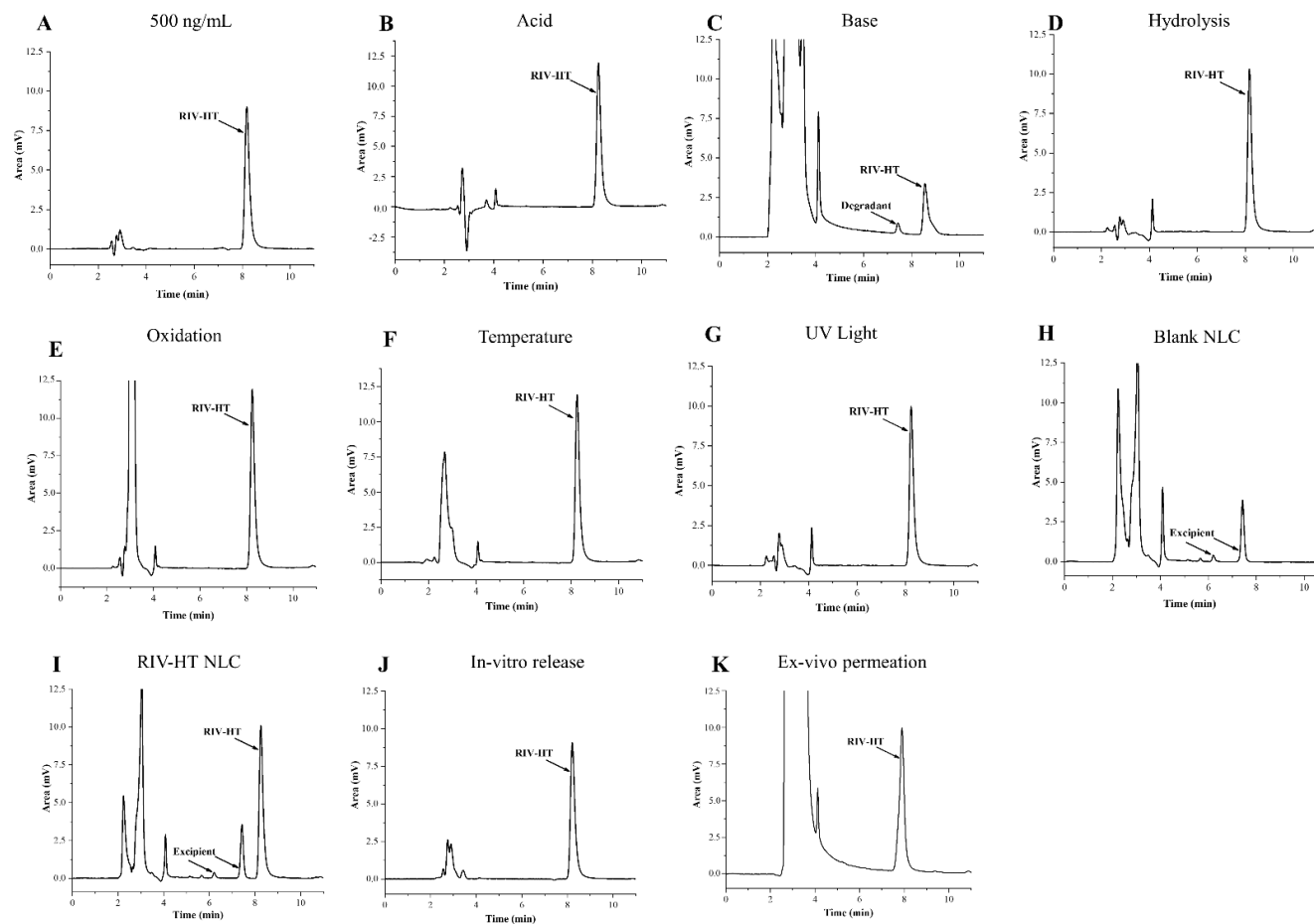


Fig. 3.3. Chromatogram of (A) RIV-HT standard solution (500 ng/mL) and forced degradation study demonstrating the specificity of the drug in presence of (B) acid, (C) base, (D) water, (E) H_2O_2 , (F) temperature and (G) UV light (H) Represents chromatogram of blank formulation matrix, (I) RIV-HT loaded formulation matrix, and specificity of the drug in presence of (J) *in-vitro* release medium and (K) *ex-vivo* permeation medium

Table 3.9. Assay of RIV-HT solution in presence of varying stress conditions using 500 ng/mL RIV-HT solution (n = 3)

Condition	Sample condition	Retention time (min)	Additional peaks (min)	% Recovery ^a	Resolution
Acid	0.5 N HCl, 60° C 48 h	8.25 ± 0.01	No	99.29 ± 1.06	-
Base	0.5 M NaOH, 60° C, 48 h,	8.55 ± 0.04	Yes, 7.45 ± 0.02	40.16 ± 1.25	4.3 ± 1.36
Oxidation	3% H ₂ O ₂ at 60 °C for 48 h	8.24 ± 0.02	No	96.23 ± 1.72	-
Hydrolysis	Water, 60° C for 48 h	8.16 ± 0.03	No	99.73 ± 0.63	-
Heat	60 °C, 10 days	8.25 ± 0.01	No	98.26 ± 1.03	-
Light	UV light, 10 days	8.23 ± 0.03	No	97.84 ± 2.03	-

^a % recovery = [(Measured concentration / Actual concentration) × 100]

3.2.3.2.2 Calibration curve, linearity, and range

The calibration curve was plotted in the concentration range of 25-600 ng/mL (**Fig. 3.4**). The lower values of slope, intercept and standard error represent higher precision of the proposed method. The slope and intercept values were calculated with 95% confidence interval. Best-fit regression equation showed regression coefficient (R^2) value of 0.9996. The calculated F-value (2.02) was observed to be lesser ($p < 0.998$) than the critical F-value (3.68), representing homoscedasticity within the linearity range. The linear equation for the calibration curve was as follows-

$$y = 261.19x + 711.13$$

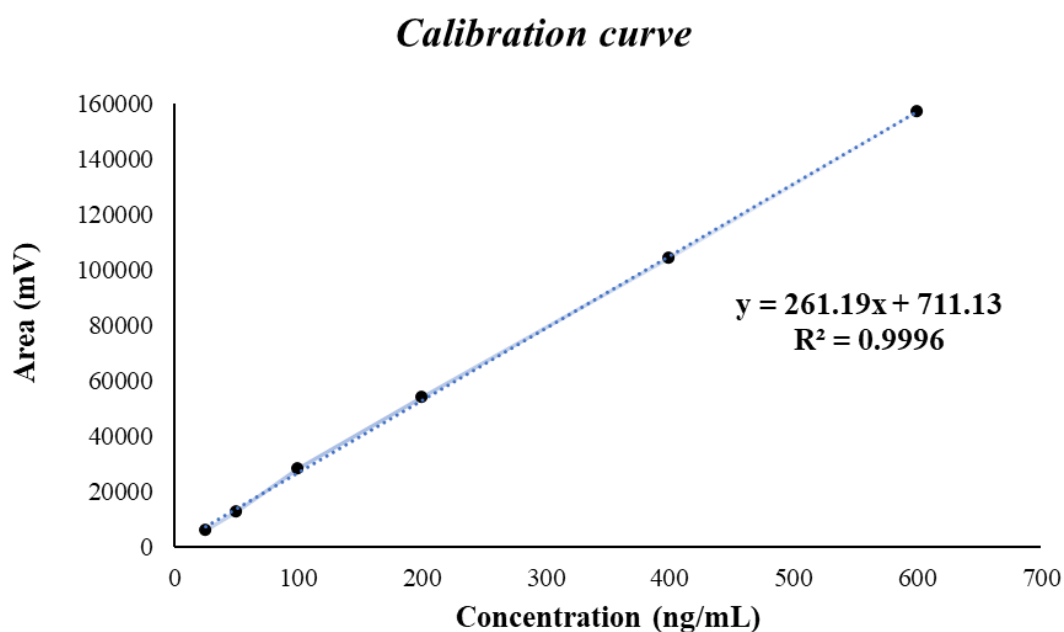


Fig. 3.4. Calibration curve of RIV-HT representing linearity range within 25-600 ng/mL

3.2.3.2.3 Accuracy

The accuracy results of the proposed method are represented in **Table 3.10**. The overlay of LQC, MQC and HQC peaks has been represented in **Fig.3.5**. The mean percentage recovery \pm

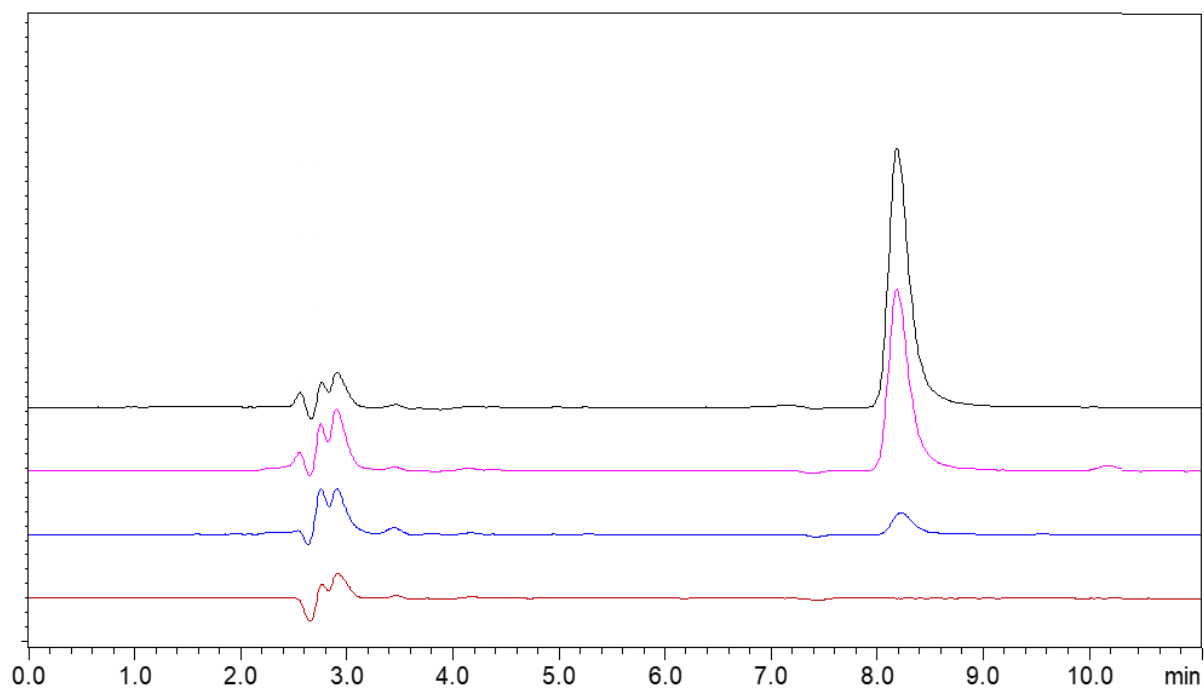


Fig. 3.5. Representative overlay of blank and RIV-HT at LQC (30 ng/mL), MQC (300 ng/mL) and HQC (500 ng/mL) concentrations

SD for LQC, MQC and HQC were observed to be $97.92 \pm 0.64\%$, $99.44 \pm 0.68\%$ and $99.38 \pm 0.22\%$. Thus, the above results justify that a small change in the concentration of drug solution can be determined using the proposed HPLC method.

Table 3.10. Accuracy data at different quality control levels (n = 3)

Standard deviation (SD) and % relative standard deviation (% RSD)

Concentration levels ^a	Measured concentration ^b		Mean % recovery (\pm SD)	% bias ^c
	Mean (\pm SD)	% RSD		
LQC	29.37 ± 0.19	0.65	97.92 ± 0.64	-2.07
MQC	298.32 ± 2.05	0.68	99.44 ± 0.68	-0.55
HQC	496.91 ± 1.14	0.23	99.38 ± 0.22	-0.61

^a LQC, MQC and HQC are 30, 300 and 500 ng/mL

^b Measured concentration of rivastigmine was calculated by linear regression equation.

^c Accuracy is given in % bias = $100 \times [(\text{predicted concentration} - \text{nominal concentration}) / \text{nominal concentration}]$.

3.2.3.2.4 Precision

The precision was studied, measuring repeatability and intermediate precision. For repeatability studies, %RSD values ranged from 0.58%–0.73% for all three levels of concentrations (**Table 3.11**). To evaluate precision of the given method, samples were analyzed at fixed time intervals and also inter-instrument variability was assessed. In intermediate precision, % RSD values were not more than 1.5 for all the levels of concentrations representing the precision and repeatability of the proposed analytical method (**Table 3.11**).

Table 3.11. Precision data at different quality control levels

Concentration levels ^a	Inter-day repeatability % RSD			Intra-day repeatability % RSD	Inter-instrument variability % RSD
	Day 1	Day 2	Day 3		
LQC	0.80	0.64	1.10	0.73	0.82
MQC	0.75	0.81	0.57	0.61	0.82
HQC	0.30	0.57	0.43	0.58	0.24

% Relative standard deviation (% RSD)

^a LQC, MQC and HQC are 30, 300 and 500 ng/mL RIV-HT solution (n = 3)

3.2.3.2.5 Limit of detection and limit of quantification

LOD and LOQ values calculated from equations 1 and 2 were observed to be 7.32 and 24.15 ng/mL. The results indicate adequate sensitivity of the proposed method and is even better than previously published RIV-HT reports.

3.2.3.2.6 Robustness

Deliberate variation in instrument and chromatographic conditions (mobile phase ratio, pH of mobile phase, column temperature and flow rate) did not affect recovery of the quality control samples. Wherein the percentage recovery for all quality control samples were observed within 97.02 ± 1.02 to $100.79 \pm 0.68\%$ (**Table 3.12**), demonstrating the robustness of the proposed HPLC method.

Table 3.12. Robustness data at different chromatographic conditions

Parameters	Level	% Recovery (\pm SD) ^b		
		LQC ^a	MQC ^a	HQC ^a
Flow rate (0.9 \pm 0.1 mL)	0.8 mL	97.02 \pm 1.02	99.43 \pm 0.22	98.20 \pm 0.45
	1.0 mL	97.81 \pm 0.34	100.49 \pm 0.07	97.70 \pm 0.28
ACN: Buffer: IPA (33:65:2)	35:63:2	98.99 \pm 0.53	99.76 \pm 0.13	99.58 \pm 1.50
	31:67:2	98.66 \pm 1.31	98.66 \pm 1.02	97.78 \pm 0.12
Mobile phase pH (5.5 \pm 0.1)	5.4	98.99 \pm 0.53	99.76 \pm 0.13	99.58 \pm 1.5
	5.6	99.01 \pm 0.78	100.79 \pm 0.68	98.54 \pm 0.49
Temperature (\pm 1 °C)	29	98.32 \pm 0.56	100.06 \pm 0.18	97.70 \pm 0.28
	31	98.80 \pm 0.75	98.33 \pm 0.78	99.29 \pm 1.23

Standard deviation (SD)

^a LQC, MQC and HQC are 30, 300 and 500 ng/mL RIV-HT solution (n = 3)^b % recovery = [(Nominal concentration/Mean measured concentration) \times 100]

3.2.3.2.7 Stability

Stability studies of RIV-HT were performed evaluating bench-top, auto-sampler, short-term, long term and stock solution stability. The percentage recovery for all stability samples was observed within 97.08-100.39 % with % RSD values less than 2% at all levels of QC concentrations. The results demonstrate the stability of RIV-HT under different storage conditions as represented in **Table 3.13**.

Table 3.13. Stability data at different storage conditions

Parameters	% Recovery (\pm SD) ^b		
	LQC ^a	MQC ^a	HQC ^a
Bench-top stability (Room temperature, 24 h)	97.57 \pm 0.81	100.01 \pm 1.45	98.10 \pm 0.28
Autosampler stability (25 °C, 24 h)	97.08 \pm 0.53	99.78 \pm 0.48	100.02 \pm 0.59
Short term stability (4 °C, 7 days)	98.47 \pm 0.62	98.77 \pm 0.78	98.83 \pm 0.93

Parameters	% Recovery (\pm SD) ^b		
	LQC ^a	MQC ^a	HQC ^a
Long term stability (-20 °C, 1 month)	98.56 \pm 0.91	97.84 \pm 1.25	99.72 \pm 0.19
Stock solution stability (-20 °C, 1 month)	97.65 \pm 0.58	100.39 \pm 1.40	99.09 \pm 1.19

Standard deviation (SD)

^a LQC, MQC and HQC are 30, 300 and 500 ng/mL RIV-HT solution (n = 3)

^b % recovery = [(Nominal concentration/Mean measured concentration)×100]

3.2.4 Conclusion

A newer, simple, rapid RP-HPLC method was developed and validated as per the International Council for harmonization guidelines for estimating rivastigmine in bulk and nanoformulations. Various chromatographic parameters were optimized during the development stage of the method. The proposed method was found to be accurate, precise, specific and robust for analysis of the drug. Also, the sensitivity of the method enabled the quantification of rivastigmine at nanogram level as a requirement for release and permeation studies of nanoformulations. The forced degradation study also ensured the specificity of the proposed method.

3.3 Method III: Bioanalytical method for quantification of RIV in plasma and brain samples

3.3.1 Introduction

The preclinical and clinical studies have shown reliability and therapeutic effectiveness upon treatment with RIV-HT. The therapeutic efficacy of RIV-HT has urged researchers to develop newer formulation strategies such as intranasal [26], transdermal [27], buccal [28] and microparticle [29] based systems to improve brain delivery. Commonly, pre-clinical pharmacokinetic evaluation is usually performed in rats. So, there is a need for the development of a bioanalytical method for pharmacokinetic evaluation of RIV-HT-based formulation in brain and plasma matrices.

There are several literature reports available for the quantification of RIV-HT in plasma and brain samples. Literature states the development of LC-MS-MS method for estimation of RIV-HT and its major metabolite in human plasma [19,20]. In another study, bioanalytical HPLC method employing fluorescence detection was developed and validated for the estimation of drugs in brain and rat plasma. The mobile phase consisted of 76:24 (v/v) ratio of ammonium acetate buffer:acetonitrile (pH 4.5, 20mM). The method was observed to be sensitive with a calibration range within 10-1000 ng/mL [30]. Gopalan *et al.*, developed quality-by-design based HPLC method for estimation of RIV-HT in rat brain and plasma. Mobile phase comprised of pH 4.5 phosphate buffer:acetonitrile in ratio 72.5:27.5 (v/v). The lowest detection concentration was reported as 75 ng/mL for brain and plasma matrices [31]. Our developed method was comparatively sensitive with limit of quantification as 45.56 ng/mL and 46.90 ng/mL in plasma and brain matrices. The present work describes the development and validation of a simple, rapid, sensitive and economical RP-HPLC method for quantification of

RIV-HT in rat plasma and brain matrices. The method can be applied for pre-clinical pharmacokinetic evaluation of RIV-HT formulations.

3.3.2 Material and method

3.3.2.1 Material

RIV-HT and venlafaxine hydrochloride (VEL) was received as a generous gift sample from Torrent Pharmaceuticals Ltd. (Ahmedabad, India) and Dr. Reddy's Laboratories (Hyderabad, India) respectively. Potassium dihydrogen phosphate was purchased from SD Fine Chemicals (Mumbai, India). Sodium hydroxide, ortho-phosphoric acid, triethylamine, and HPLC-grade acetonitrile were purchased from Merck Pvt. Ltd. (Mumbai, India). Plasma and brain were collected from Wistar rats (females; 8–12 weeks, 220-250 g), procured from the Central Animal Facility, BITS-Pilani (Pilani, Rajasthan, India) and stored at -80°C. The Institutional Animal Ethics Committee (IAEC) approved the animal protocols, BITS-Pilani (Protocol no: IAEC/RES/32/05), and experiments were conducted as per CPCSEA guidelines. All the reagents were of analytical grade, and Milli-Q water was obtained from our institute's Millipore Direct-Q ultra-pure water system (Millipore, Bedford, USA).

3.3.2.2 Instrumentation

HPLC method was developed using Shimadzu HPLC system (Kyoto, Japan) equipped with binary pumps (LC-20 AD), pulse-free solvent system consisting of 5 degassers (DGU-20A5R), sample cooler and an automated autosampler (SIL-20AC HT). HPLC system consisted of heat block type column oven (CTO-10AS VP). A dual wavelength, system-equipped UV-Visible detector (SPD-20A) was used for peak detection. The system hardware and data processing were performed using computer-operated software LC solutions version 6.110.

3.3.2.3 Collection of blood and brain from rats

Institutional Animal Ethics Committee (Protocol number: IAEC/RES/32/05) protocol was approved for the procurement of rats. Wistar rats weighing 230-260 g. Animals were caged in a facility compliant with authority guidelines. Blood was withdrawn using retro-orbital puncture technique. 10% (w/v) disodium EDTA solution (20 μ L) was used for 200 μ L blood volume (an anti-coagulant). For separation of plasma, blood samples were centrifuged at 5000 rpm, for 10 min at 4 $^{\circ}$ C. The supernatant was separated and plasma was withdrawn using a micropipette in a centrifuge tube and stored at -80° C till further use.

For the collection of brain tissue, animals were anesthetized and exsanguinated using spinal-cord dislocation technique. The whole brain was separated and collected carefully, blotted to remove excess fluids and debris sticking to it. The brain samples were stored at -80° C till further use.

3.3.2.4 Sample extraction technique

RIV-HT and VEL as internal standard (IS) were extracted from brain and plasma samples using protein precipitation followed by solvent evaporation. To 80 μ L plasma, 10 μ L RIV-HT and 10 μ L IS working standards were added and vortexed for 2 min. 10 μ L, 0.1 M sodium sulphate solution was added followed by the addition of 1mL acetonitrile and vortexed for 5 min. Samples were centrifuged at 17,000 rpm for 10 min and transferred to a centrifuge tube (1.5 mL) for overnight drying at 37 $^{\circ}$ C. The dried samples were reconstituted with 100 μ L mobile phase, vortexed for 2 min and further centrifuged at 17,000 rpm at 4 $^{\circ}$ C for 10 min. The supernatant was separated and analyzed using the developed chromatographic method.

In case of brain homogenate preparation, the brain was weighed and further processed. 3 mL/gm water was added to the tissue sample and further homogenized at 8,000 rpm for 5 min. The homogenate was centrifuged at 17,000 rpm, 4 $^{\circ}$ C for 10 min and the supernatant was

separated. The brain sample extraction followed the same procedure as that of plasma samples. 80 μ L brain homogenate, 10 μ L RIV-HT and 10 μ L IS working standards were added and vortexed for 2 min. 10 μ L, 0.1 M sodium sulphate solution was added followed by the addition of 1 mL acetonitrile and vortexed for 5 min. Samples were centrifuged at 17,000 rpm for 10 min and transferred to a centrifuge tube (1.5 mL) for overnight drying at 37 °C. The dried samples were reconstituted with 100 μ L mobile phase, vortexed for 2 min and further centrifuged at 17,000 rpm at 4 °C for 10 min. The supernatant was separated and analyzed using the developed chromatographic method.

3.3.2.5 Chromatographic conditions

The chromatographic separation was performed using Hypersil[®] BDS C₁₈ column (250x4.6 mm). The column was equilibrated for 40 min before the sample analysis. The proposed method consisted of an isocratic elution mode with 50 μ L injection volume. The mobile phase consisted of A: acetonitrile constituting 0.05% (v/v) triethylamine, B: pH 6.0 phosphate buffer (10 mM) and C: iso-propyl alcohol with a composition of 36:60:4 (%A:%B:%C) and flow rate of 0.8 mL/min. The column temperature was maintained at 30 °C with a detection wavelength at 215nm. The retention time of RIV and VEL in plasma samples was observed at 8.8 and 13.9 min. While for brain matrices it was observed at 9.1 and 14.0 min respectively.

3.3.2.6 Preparation of standard solutions

The primary stock solution of RIV and IS were prepared separately using acetonitrile (10 mg in 100 mL). For brain and plasma samples, seven RIV standard solutions within the range of 50-1000 ng/mL (50, 100, 200, 400, 600, 800, 1000) and 1000 ng/mL IS standard solution were employed for brain and plasma calibration curves. Quality control samples representing the low limit of quantification (LLOQ), LQC, MQC and HQC samples of 50, 75, 500 and 900 ng/mL concentrations of brain and plasma samples were prepared.

3.3.2.7 Method validation

The method developed for both matrices was performed as per the procedure described by the International Council for Harmonisation and USFDA guidelines. The samples were assessed for selectivity, linearity, accuracy, precision and stability.

3.3.2.7.1 *Selectivity*

Selectivity of the method was assessed by comparing chromatograms of blank brain and blank plasma samples with RIV, IS spiked brain and plasma samples (n = 6).

3.3.2.7.2 *Linearity, range, and calibration curve*

Linearity was assessed by plotting the graph of peak area of RIV-HT/IS against nominal concentration of RIV-HT. Six calibration curves were analyzed within the range of 50-1000 ng/mL for brain samples and % RSD was determined. The standard deviation, slope and regression coefficient values were determined from calibration curve.

3.3.2.7.3 *Limit of detection and limit of quantification*

LOD and LOQ values for brain and plasma samples were determined using the equation described in section 3.2.2.5.8.

3.3.2.7.4 *Accuracy*

Accuracy was assessed by determining percentage recovery from the analyte sample. The observed concentration was calculated from area ratio of RIV/IS using regression equation and respective nominal concentration was employed to determine percentage bias (n = 3).

3.3.2.7.5 *Precision*

Precision study employed determination of reproducibility and intermediate precision. To determine reproducibility of the proposed method, respective brain and plasma samples of LLQC, LQC, MQC and HQC (n = 3) were analyzed three times in a day (intra-day precision)

and % RSD was determined. To assess inter-day precision, samples (brain and plasma) were analyzed for three consecutive days and % RSD was determined.

3.3.2.7.6 Stability studies

It was performed to evaluate the stability of brain and plasma matrices at different storage conditions. The quality control samples were assessed in triplicate to determine autosampler stability (24 h, RT), bench-top stability (24 h, RT), freeze-thaw stability (3 cycles), short-term stability (7 days at -20 °C), long-term (1 month at -20 °C) and stock solution stability (1 month at -20 °C).

3.3.2.7.7 Dilution integrity

It was performed for analyzing samples that lie above the linearity range. For this brain and plasma matrices of 3 times the highest concentration (of linearity range) were prepared. Dilution standards of similar concentration were then compared with respective blank matrices.

3.3.3 Result and discussion

3.3.3.1 Method validation

3.3.3.1.1 Selectivity

The protein precipitation with acetonitrile followed by evaporation and reconstitution with mobile phase showed effective and reliable determination of brain and plasma samples. **Fig.3.6A** and **Fig.3.6B** show overlay chromatograms of QC standards in brain and plasma matrices along with their respective blank samples. No interference peak was observed at the retention time of RIV and IS in respective biological matrices.

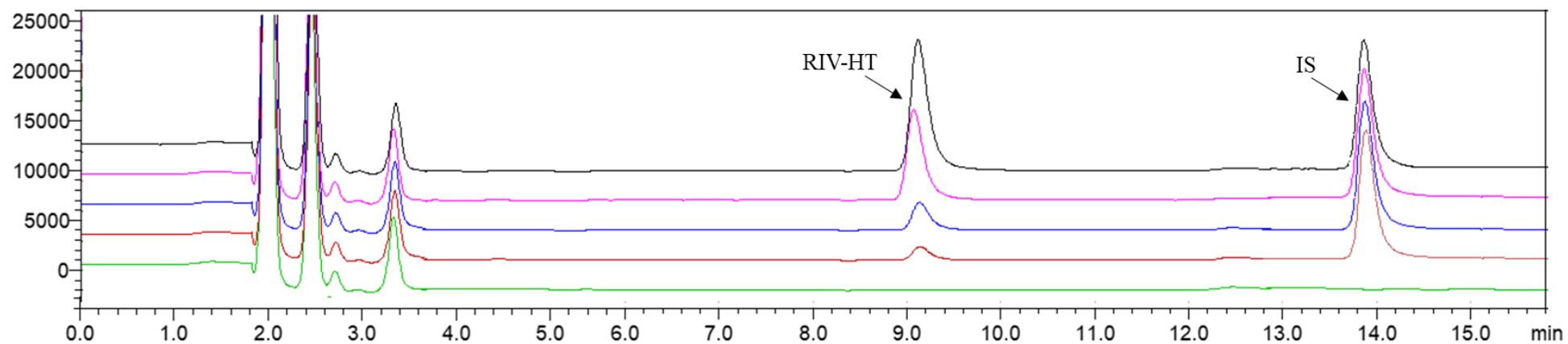
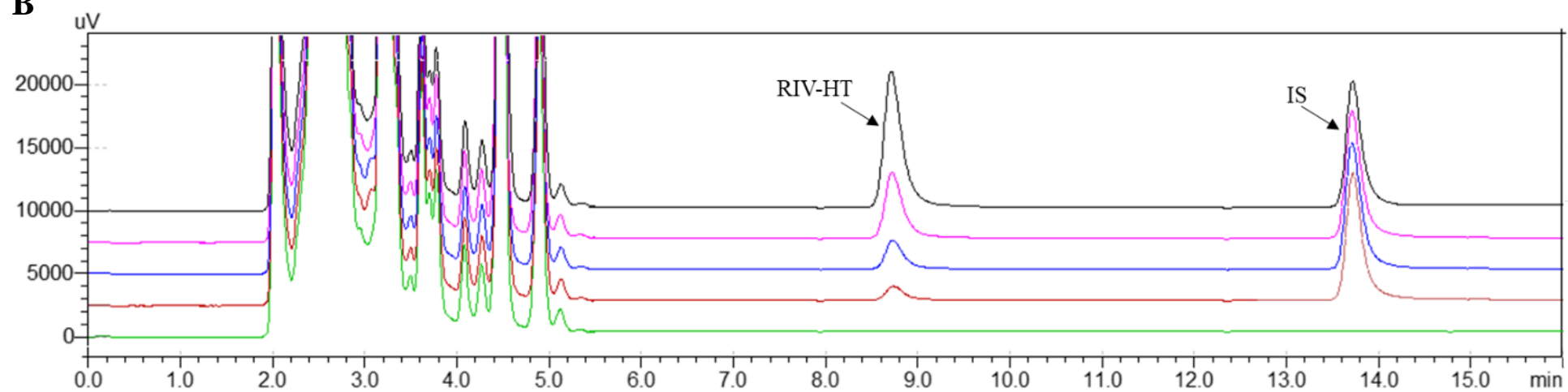
A**B**

Fig. 3.6. Overlay of Blank, LLQOC, LQC, MQC and HQC sample of (A) brain and (B) plasma matrices representing selectivity of the method with presence of no interfering peak at the retention time of RIV-HT and internal standard

3.3.3.1.2 Calibration curve, linearity, and range

The calibration curve was observed to be linear within the concentration range of 50-1000 ng/mL for brain and plasma samples (**Fig. 3.7A and 3.7B**). The calibration curve was plotted against the peak area ratio of RIV-HT/IS vs concentration of RIV-HT. The lower values of standard error, slope and intercept represent higher precision of the proposed method. In both brain and plasma, the F_{cal} was observed to be significantly greater than F_{crit} , indicating regression is good.

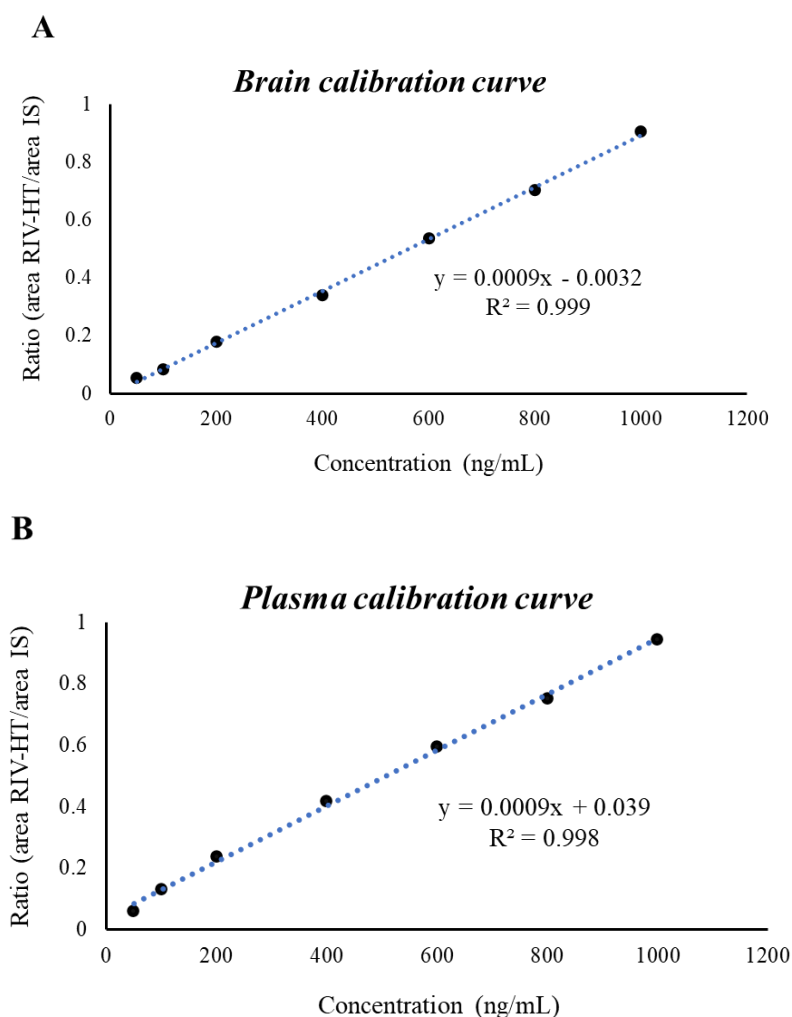


Fig. 3.7. Graph represents calibration curve of (A) brain and (B) plasma matrices.

3.3.3.1.3 Limit of detection and limit of quantification

The LOD and LOQ values calculated from the equation were observed to be 15.47 and 46.90 ng/mL in the brain. whereas LOD and LOQ values in plasma samples were observed to be 15.03 and 45.56 ng/mL respectively. The lower value of LOQ indicates the method to be highly sensitive.

3.3.3.1.4 Accuracy

The accuracy results of the proposed method are mentioned in **Table 3.14**. The mean percentage recovery for all levels of QC samples was observed within 97.65-99.75% and 96.23-98.43% for brain and plasma samples respectively. The percent bias ranged between -0.68 to -2.34 and -1.56 to -3.76 % for brain and plasma samples indicating the accuracy of the proposed method for the estimation of RIV.

Table 3.14. Accuracy data at different quality control levels (n = 3)

Matrices	Concentration levels ^a	Measured concentration ^b		% RSD	% bias ^c
		Mean (\pm SD)	% Recovery (\pm SD)		
Brain	LLQC	49.65 \pm 0.71	99.31 \pm 1.42	1.43	-0.68
	LQC	74.46 \pm 1.36	99.75 \pm 1.41	1.83	-0.71
	MQC	494.39 \pm 13.31	98.87 \pm 2.66	2.69	-1.12
	HQC	878.88 \pm 8.61	97.65 \pm 0.95	0.98	-2.34
Plasma	LLQC	49.2 \pm 6.81	98.43 \pm 13.62	13.83	-1.56
	LQC	72.71 \pm 6.45	96.23 \pm 8.60	8.94	-3.76
	MQC	487.13 \pm 17.71	97.42 \pm 3.43	3.52	-2.57
	HQC	878.22 \pm 20.49	97.58 \pm 2.22	2.33	-2.41

Standard deviation (SD) and % relative standard deviation (% RSD)

^a LLQC, LQC, MQC and HQC are 50, 75, 500 and 900 ng/mL

^b Measured concentration of rivastigmine was calculated by linear regression equation.

^c Accuracy is given in % bias= $100 \times [(\text{predicted concentration} - \text{nominal concentration})/\text{nominal concentration}]$.

3.3.3.1.5 Precision

The intra-day precision of all QC samples for both matrices showed % RSD values less than 5. Whereas inter-day precision studies showed % RSD values within 1.18-13.13 % and 1.90-11.81 % for brain and plasma matrices (**Table 3.15**). The % RSD values are within acceptable limits indicating intermediate precision of the proposed method for brain and plasma samples.

Table 3.15. Precision data at different quality control levels

Matrices	Concentration levels ^a	Inter-day repeatability % RSD			Intra-day repeatability % RSD
		Day 1	Day 2	Day 3	
Brain	LLQC	4.28	7.63	1.90	1.63
	LQC	8.73	8.20	11.81	3.19
	MQC	3.26	3.16	4.90	4.17
	HQC	5.14	2.58	4.75	0.82
Plasma	LLQC	1.80	13.13	2.9	2.23
	LQC	2.93	7.52	5.03	2.81
	MQC	5.39	3.48	3.12	1.67
	HQC	4.84	1.18	4.19	1.04

% Relative standard deviation (% RSD)

^a LLQC, LQC, MQC and HQC are 50, 75, 500 and 900 ng/mL

3.3.3.1.6 Recovery

The recovery of RIV was determined in all standard solution samples. The RIV peak area was determined for both drug-spiked matrices and compared with equivalent concentrations of aqueous samples. The % recovery for brain matrices at all concentrations were observed within 91.59-97.82%. Whereas it was observed to be 91.46-99.05 % for plasma samples. The % RSD values for both matrices were less than 10 % indicating higher extraction efficiency of the proposed method. The extraction performed using acetonitrile using protein precipitation method thus resulted higher % recovery in brain and plasma samples.

3.3.3.1.7 Stability

The stability studies of RIV were performed evaluating bench-top (24h, RT), autosampler (24 h), freeze-thaw (3 cycles), short-term (7 days at -20 °C), long-term (1 month at -20 °C) and stock solution stability (1 month at -20 °C) for both brain and plasma matrices. The percent recovery for all QC samples of plasma samples was observed between 93.46-100.08 % with % an RSD value less than 10%. Whereas the percent recovery for the brain samples was observed to be between 93.04-101.87% with % RSD values less than 14% for all QC levels of concentration (**Table 3.16**).

Table 3.16. Stability data at different storage conditions

Matrices	Parameters	% Recovery (\pm SD) ^b			
		LLQC ^a	LQC ^a	MQC ^a	HQC ^a
Brain	Bench-top stability (24h, RT)	96.58 \pm 6.67	94.48 \pm 3.18	100.57 \pm 5.33	97.71 \pm 1.19
	Autosampler stability (24 h)	97.94 \pm 4.34	98.22 \pm 9.66	97.33 \pm 7.06	98.17 \pm 2.59
	Freeze thaw stability (3 cycles)	94.91 \pm 13.22	101.37 \pm 11.68	93.19 \pm 1.21	99.32 \pm 5.39
	Short term stability(7 days at -20 °C)	101.87 \pm 9.84	97.30 \pm 8.06	93.04 \pm 9.31	100.08 \pm 4.74
	Long term stability (1 month at -20 °C)	95.78 \pm 9.71	97.42 \pm 3.23	100.06 \pm 5.43	99.54 \pm 5.05
	Stock solution stability (1 month at -20 °C)	96.46 \pm 2.56	96.69 \pm 5.24	96.77 \pm 6.03	99.16 \pm 1.79
Plasma	Bench-top stability (24h, RT)	96.47 \pm 5.61	93.46 \pm 3.51	96.93 \pm 5.53	99.46 \pm 4.95
	Autosampler stability (24 h)	98.24 \pm 1.78	94.71 \pm 3.68	96.25 \pm 9.5	99.68 \pm 5.11
	Freeze thaw stability (3 cycles)	94.08 \pm 8.27	96.76 \pm 4.45	98.14 \pm 0.45	99.07 \pm 2.88
	Short term stability(7 days at -20 °C)	99.68 \pm 5.71	97.19 \pm 9.20	98.96 \pm 1.07	100.08 \pm 4.74
	Long term stability (1 month at -20 °C)	95.72 \pm 9.28	97.22 \pm 8.31	96.91 \pm 6.41	99.55 \pm 2.36
	Stock solution stability (1 month at -20 °C)	96.20 \pm 9.08	96.49 \pm 5.78	96.95 \pm 4.46	97.82 \pm 1.85

Standard deviation (SD)

^aLLQC, LQC, MQC and HQC are 50, 75, 500 and 900 ng/mL^b % recovery = [(Nominal concentration/Mean measured concentration) \times 100]

3.3.4 Conclusion

The HPLC bioanalytical method for RIV was developed and validated as per ICH Q2R2 guidelines. The results supported the selectivity, precision, and accuracy of the proposed method with better correlation within the linearity range of 50-1000 ng/mL for plasma and brain matrices. The validated method enables the estimation of RIV in brain and plasma samples.

References

- [1] R. Kapil, S. Dhawan, B. Singh, Development and validation of a spectrofluorimetric method for the estimation of rivastigmine in formulations, *Indian J. Pharm. Sci.* 71 (2009) 585–589. <https://doi.org/10.4103/0250-474X.58179>.
- [2] An Introduction to Analytical Method Development and Validation in Early Phase Clinical Trials - Sofpromed. <https://www.sofpromed.com/an-introduction-to-analytical-method-development-and-validation-in-early-phase-clinical-trials> (accessed April 15, 2023).
- [3] Method Development and Validation of Analytical Procedures Kapil Kalra Dev Bhoomi Institute of Pharmacy and Research, Dehradun, Uttarakhand (accessed April 15, 2023).
- [4] A. Kumar, L. Kishore, N. Kaur, A. Nair, Method development and validation: Skills and tricks, *Chronicles Young Sci.* 3 (2012) 3. <https://doi.org/10.4103/2229-5186.94303>.
- [5] F. Luis, G. Moncayo, Exelon (rivastigmine tartrate) Capsules, 2020. https://www.accessdata.fda.gov/drugsatfda_docs/label/2000/208231bl.pdf.
- [6] N.S. Hinge, H. Kathuria, M.M. Pandey, Engineering of structural and functional properties of nanotherapeutics and nanodiagnostics for intranasal brain targeting in Alzheimer's, *Appl. Mater. Today.* 26 (2022) 101303. <https://doi.org/10.1016/J.APMT.2021.101303>.
- [7] P. Wavikar, R. Pai, P. Vavia, Nose to brain delivery of rivastigmine by in situ gelling cationic nanostructured lipid carriers: Enhanced brain distribution and pharmacodynamics, *J. Pharm. Sci.* 106 (2017) 3613–3622. <https://doi.org/10.1016/j.xphs.2017.08.024>.
- [8] S.K.L. Rompicherla, K. Arumugam, S.L. Bojja, N. Kumar, C.M. Rao, Pharmacokinetic

- and pharmacodynamic evaluation of nasal liposome and nanoparticle based rivastigmine formulations in acute and chronic models of Alzheimer's disease, *Naunyn-Schmiedeberg's Arch. Pharmacol.* 394 (2021) 1737–1755. <https://doi.org/10.1007/S00210-021-02096-0/FIGURES/13>.
- [9] P. Srujana, P.R. Sougandhi, T. Shobha Rani, R. Gangadhara, A Rapid, simple and sensitive method of rivastigmine tartrate by visible spectrophotometric method, (2019) 331. www.jetir.org (accessed May 3, 2023).
- [10] D. Arora, M. Kumar, S. Bhatt, Y. Taneja, A. Tiwari, V. Tiwari, UV Spectrophotometric Method for Quantification of Rivastigmine Tartrate in Simulated Nasal Fluid: Development and Validation, *Biomed. Pharmacol. J.* 14 (2021) 2165–2172. <https://doi.org/10.13005/BPJ/2314>.
- [11] V.R. Salvi, P. Pawar, Nanostructured lipid carriers (NLC) system: A novel drug targeting carrier, *J. Drug Deliv. Sci. Technol.* 51 (2019) 255–267. <https://doi.org/10.1016/J.JDDST.2019.02.017>.
- [12] P. Saha, M.M. Pandey, A new fluorescence-based method for rapid and specific quantification of rotigotine in chitosan nanoparticles, *Spectrochim. Acta Part A Mol. Biomol. Spectrosc.* 267 (2022) 120555. <https://doi.org/10.1016/J.SAA.2021.120555>.
- [13] D. To, U. For, G. Clinical, International council for harmonisation of technical requirements for pharmaceuticals for human use, 2016. https://database.ich.org/sites/default/files/ICH_Q2-R2_Document_Step2_Guideline_2022_0324.pdf.
- [14] B.M. Rao, M.K. Srinivasu, K.P. Kumar, N. Bhradwaj, R. Ravi, P.K. Mohakhud, G.O. Reddy, P.R. Kumar, A stability indicating LC method for rivastigmine hydrogen tartrate,

- J. Pharm. Biomed. Anal. 37 (2005) 57–63. <https://doi.org/10.1016/J.JPBA.2004.09.041>.
- [15] D. Sonawane, A.K. Sahu, T. Jadav, R.K. Tekade, P. Sengupta, Innovation in Strategies for Sensitivity Improvement of Chromatography and Mass Spectrometry Based Analytical Techniques, Crit. Rev. Anal. Chem. 0 (2021) 1–17. <https://doi.org/10.1080/10408347.2021.1969887>.
- [16] N.H. Huda, B. Gauri, H.A.E. Benson, Y. Chen, A stability indicating HPLC assay method for analysis of rivastigmine hydrogen tartrate in dual-ligand nanoparticle formulation matrices and cell transport medium, J. Anal. Methods Chem. 2018 (2018) 1841937. <https://doi.org/10.1155/2018/1841937>.
- [17] M.Y. Salem, A.M. El-Kosasy, M.G. El-Bardicy, M.K. Abd El-Rahman, Spectrophotometric and spectrodensitometric methods for the determination of rivastigmine hydrogen tartrate in presence of its degradation product, Drug Test. Anal. 2 (2010) 225–233. <https://doi.org/10.1002/DTA.121>.
- [18] M.A. Choudhury, RP-HPLC method for the estimation of rivastigmine in bulk and in dosage forms, J. Pharm. Res. 4 (2011) 1007–1009. <https://www.researchgate.net/publication/289536457> (accessed May 14, 2022).
- [19] J. Bhatt, G. Subbaiah, S. Kambli, B. Shah, S. Nigam, M. Patel, A. Saxena, A. Baliga, H. Parekh, G. Yadav, A rapid and sensitive liquid chromatography-tandem mass spectrometry (LC-MS/MS) method for the estimation of rivastigmine in human plasma, J. Chromatogr. B. Analyt. Technol. Biomed. Life Sci. 852 (2007) 115–121. <https://doi.org/10.1016/J.JCHROMB.2007.01.003>.
- [20] F. Pommier, R. Frigola, Quantitative determination of rivastigmine and its major metabolite in human plasma by liquid chromatography with atmospheric pressure

- chemical ionization tandem mass spectrometry, *J. Chromatogr. B Anal. Technol. Biomed. Life Sci.* 784 (2003) 301–313. [https://doi.org/10.1016/S1570-0232\(02\)00816-4](https://doi.org/10.1016/S1570-0232(02)00816-4).
- [21] K. Arumugam, M.R. Chamallamudi, R.R. Gilibili, R. Mullangi, S. Ganesan, S.S. Kar, R. Averineni, G. Shavi, N. Udupa, Development and validation of a HPLC method for quantification of rivastigmine in rat urine and identification of a novel metabolite in urine by LC-MS/MS, *Biomed. Chromatogr.* 25 (2011) 353–361. <https://doi.org/10.1002/bmc.1455>.
- [22] W. LI, Cheng-ping; Zheng, Lan-jun; Mao, Mao; Rao, Gui-wei; Shan, HPLC determination of rivastigmine hydrogen tartrate capsules: Ingenta Connect, *J. Pharm. Anal.* 31 (2011) 1123–1125. <https://www.ingentaconnect.com/content/jpa/cjpa/2011/00000031/00000006/art00027> (accessed July 7, 2022).
- [23] S. Alex, R. Diwedi, T. Ashok, M. Ch, rasekhar, A validated RP-HPLC method for estimation of rivastigmine in pharmaceutical formulations, *Der Pharm. Lett.* 3 (2011) 421–426. https://www.researchgate.net/publication/287118084_A_validated_RP-HPLC_method_for_estimation_of_Rivastigmine_in_pharmaceutical_formulations.
- [24] N.S. Hinge, M.M. Pandey, Sensitive RP-HPLC method of rivastigmine for applicative quantification of nanostructured lipid carriers, *Microchem. J.* 188 (2023) 108341. <https://doi.org/10.1016/J.MICROC.2022.108341>.
- [25] Rivastigmine Tartrate Capsules, (2018). https://www.uspnf.com/sites/default/files/usp_pdf/EN/USPNF/revisions/rivastigmine-tartrate-caps-rb.pdf (accessed July 10, 2022).

- [26] S. Salatin, J. Barar, M. Barzegar-Jalali, K. Adibkia, M. Jelvehgari, Thermosensitive in situ nanocomposite of rivastigmine hydrogen tartrate as an intranasal delivery system: Development, characterization, ex vivo permeation and cellular studies, *Colloids Surf. B. Biointerfaces*. 159 (2017) 629–638. <https://doi.org/10.1016/j.colsurfb.2017.08.031>.
- [27] Y. Cai, Q. Tian, C. Liu, L. Fang, Development of long-acting rivastigmine drug-in-adhesive patch utilizing ion-pair strategy and characterization of controlled release mechanism, *Eur. J. Pharm. Sci.* 161 (2021) 105774. <https://doi.org/10.1016/J.EJPS.2021.105774>.
- [28] R. Kapil, S. Dhawan, S. Beg, B. Singh, Buccoadhesive films for once-a-day administration of rivastigmine: systematic formulation development and pharmacokinetic evaluation, *Drug Dev. Ind. Pharm.* 39 (2013) 466–480. <https://doi.org/10.3109/03639045.2012.665926>.
- [29] Y. Gao, W.H. Almalki, O. Afzal, S.K. Panda, I. Kazmi, M. Alrobaian, H.A. Katouah, A.S.A. Altamimi, F.A. Al-Abbasi, S. Alshehri, K. Soni, I.A.A. Ibrahim, M. Rahman, S. Beg, Systematic development of lectin conjugated microspheres for nose-to-brain delivery of rivastigmine for the treatment of Alzheimer's disease, *Biomed. Pharmacother.* 141 (2021). <https://doi.org/10.1016/J.BIOPHA.2021.111829>.
- [30] K. Arumugam, M.R. Chamallamudi, S.R. Mallayasamy, R. Mullangi, S. Ganesan, L. Jamadar, A. Ranjithkumar, N. Udupa, High Performance Liquid Chromatographic Fluorescence Detection Method for the Quantification of Rivastigmine in Rat Plasma and Brain: Application to Preclinical Pharmacokinetic Studies in Rats, *J. Young Pharm.* 3 (2011) 315–321. <https://doi.org/10.4103/0975-1483.90244>.
- [31] D. Gopalan, P.H. Patil, P. Channabasavaiah Jagadish, S.G. Kini, A.T. Alex, N. Udupa,

S. Mutalik, QbD-driven HPLC method for the quantification of rivastigmine in rat plasma and brain for pharmacokinetics study ARTICLE INFO, J. Appl. Pharm. Sci. 12 (2022) 56–067. <https://doi.org/10.7324/JAPS.2022.120606>.

CHAPTER 4

RIVASTIGMINE-DHA ION-PAIR COMPLEX IMPROVED LOADING IN HYBRID NANOPARTICLES FOR BETTER AMYLOID INHIBITION AND NOSE-TO- BRAIN TARGETING IN ALZHEIMER'S

4.1 Introduction

Alzheimer's disease (AD) is a progressive neurodegenerative disorder. The growing number of AD cases among the elderly and adults around the globe is a major concern [1]. The clinical condition is characterized by reduced cholinergic activity, leading to impaired cognition, memory and psychiatric symptoms [1]. The therapeutic approach involves targeting cholinergic synapses and increasing acetylcholine levels in the brain. Rivastigmine hydrogen tartrate (RIV-HT) is a widely used drug in Alzheimer's therapy. It is a dual inhibitor of acetyl and butyrylcholinesterase. RIV-HT exhibits low oral bioavailability (36 %) and low drug concentration in the brain [2,3]. The disadvantages of available drug therapy are extensive first-pass metabolism, short half-life (90 min), intra-individual variability, frequent dose administration and risk of peripheral cholinergic side effects [4,5]. Intranasal delivery can directly transport drugs to the brain, negating the blood-brain barrier [6,7]. It can also overcome drugs' first-pass metabolism and reduce systemic exposure, reducing cholinergic-mediated side effects [8].

Several reports show nanoparticles can enhance the nose-to-brain (N2B) absorption of hydrophilic and hydrophobic drugs [9–11]. Several formulations have been developed to enhance RIV-HT N2B delivery, such as microemulsion [12], lipidic (solid lipid nanoparticle (SLN), nanostructured lipid carriers (NLC), liposomes) [3,13,14], and polymeric [2] nanocarriers. In recent years, hybrid nanoparticles have gained tremendous interest as they can overcome the drawbacks of individual nanocarriers. For example, Lipid Polymer Hybrid (LPH) nanoparticles can overcome issues of lipidic and polymeric nanocarriers. The polymer-based nanocarriers have disadvantages, such as limited drug loading capacity and complex preparation steps, while lipidic nanoparticles show a high polydispersity index (PDI) and poor drug loading for hydrophilic drugs [15]. In contrast, LPH offers improved colloidal stability,

biocompatibility, controlled, sustained drug release, and improved cellular uptake efficiency. However, the drug loading and surface properties should be optimized for drug formulation.

Nanoparticle characteristics can affect N2B targeting and amyloid inhibition [16,17]. The impact of nanoparticle attributes such as particle size [18,19], shape [20] and surface hydrophobicity [21] has been studied in *in-vitro* amyloid aggregation inhibition and N2B drug transport. The effect of nanoparticle surface charge has a considerable role in intranasal drug transport but has been minimally studied. One such study reported the role of nanoparticle surface charge in brain sub-localization of rhodamine B nanoparticles using fluorescence bioimaging [22]. The surface charge also plays a crucial role in amyloid inhibition, promoting interaction with negatively charged amyloid β_{1-42} [23]. The degree of interaction of amyloid β_{1-42} with nanoparticles shows the extent of amyloid aggregation inhibition. The extent of amyloid β_{1-42} inhibition increases with an increase in its interaction with the nanoparticle [24].

Delivering RIV-HT through the intranasal route remains challenging, which is minimally absorbed through the nasal cavity because of its hydrophilic properties [4,25]. Further, its hydrophilic character also makes the encapsulation into nanoparticles challenging. Therefore, there is a need for a better delivery system for improving brain concentration, targeting, and extending therapeutic effects. Developing such actives into hydrophobic ion pair complexes (IPC) has been a promising approach [26]. Samaridou *et al.* developed RNA nanocomplexes for the ailment of neurodegenerative disorders using hydrophobic octa-arginine derivative (conjugated with lauric acid), intended to enhance RNA stability and mucodiffusion across olfactory nasal mucosa [27]. The complexes improve lipophilicity without altering the chemical structure, with reversible aqueous solubility of a hydrophilic drug. Further, the improvement in lipophilic character mainly relies upon the physicochemical characteristics of the counterion molecule [28]. The IPC of RIV-HT has not been explored for N2B delivery.

The study hypothesized that the IPC of RIV can improve the loading of LPH nanoparticles for intranasal delivery, thereby improving drug brain delivery.

Further, the essential omega fatty acid-based IPC can provide neuroprotective, anti-inflammatory and anti-oxidative activity [29,30]. The interaction of amyloid precursor proteins (APP) with β -secretases and γ -secretases leads to $A\beta_{1-42}$ oligomerization, which eventually leads to $A\beta$ -fibrillation and amyloid plaques formation [30]. It also modulates apolipoprotein-E isoforms, a clearance mechanism of $A\beta$ -peptide [31]. Regular docosahexaenoic acid (DHA) supplementation improves cognitive function and spatial memory in the early and later stages of Alzheimer's [31,32]. The essential fatty acids can improve drugs translocation efficiency, C_{max} and area under the curve (AUC) after intranasal administration [33–35]. Amongst essential fatty acids, DHA has been widely reported in preventing or improving Alzheimer's symptoms. It promotes APP interaction with α -secretase and shields γ -secretases responsible for AD initiation [30,31]. So far, DHA has been used to improve drug CNS concentrations [35] but has not been explored as IPC intended for CNS disorders. Further, DHA can target the brain with the fatty acids transporter proteins or intracellular fatty acids binding proteins and passive transport [35,36].

In this study, RIV-loaded LPH nanoparticles are prepared. The RIV:DHA was formulated and loaded into LPH for better encapsulation efficiency. This RIV:DHA was characterized for complexation efficiency. The complexation was confirmed using Fourier transform infra-red analysis (FTIR), and proton nuclear magnetic resonance spectroscopy (1H NMR). The two LPH nanoparticle types were developed, i.e., RIV:DHA LPH(+ve) and RIV:DHA LPH(-ve). The amyloid aggregation inhibition for varied LPH concentrations of both LPH types was evaluated. Thioflavin T assay, dynamic light scattering, ATR-FTIR analysis and microscopic evaluation were performed to determine *in-vitro* amyloid inhibition. For *in-vivo* study, the optimum LPH nanoparticles were embedded into thermoresponsive hydrogel. The mucociliary

clearance time, improved brain concentrations, DTE (%), DTP (%) indices for RIV:DHA LPH(-ve) gel and RIV:DHA LPH(+ve) gel were evaluated in rats. Lastly, histopathological examination was done for brain and nasal tissue to assess the safety of intranasally administered LPH gel.

4.2 Material and method

4.2.1 Material

A gift sample of Rivastigmine hydrogen tartrate (RIV-HT) was received from Torrent Pharmaceuticals Ltd. (Ahmedabad, India) and docosahexaenoic acid from Bioplus Life Sciences Pvt. Ltd. (Bangalore, India). Poly (lactic-co-glycolic acid), Resomer™ RG 504 and Miglyol®812 were obtained as gift samples from Orbicular Pharmaceutical Technology Pvt. Ltd. (Hyderabad, India). Glyceryl monostearate (GMS), Precirol® ATO 5, stearic acid, Compritol® 888 ATO, Gelucire® 44/14, and Gelucire® 50/13 (PEG-32-stearate) were received as gift samples from Gattefosse (Mumbai, India). Stearylamine was purchased from Tokyo Chemical Industries (Chennai, India). Capmul® MCM C8 and Captex® 355, castor oil, and soyabean oil were provided as gift samples by Abitec corporation (Columbus, USA). Soluplus®, Kolliphor® P 407, and Kolliphor® P 188, were received as gift samples from BASF (Mumbai, India). Span 80, tween 80, Polyvinyl alcohol, glacial acetic acid, and potassium dihydrogen phosphate were purchased from SD Fine Chemicals Ltd. (Mumbai, India). Sodium hydroxide, orthophosphoric acid, triethyl amine, glacial acetic acid, and sodium dihydrogen phosphate was procured from Merck (Mumbai, India). Hydrochloric acid, calcium chloride, sodium chloride, potassium chloride, and disodium ethylene diamine tetra-acetic acid was purchased from Central Drug House Pvt. Ltd. (New Delhi, India). Thioflavin-T was purchased from Dev Nitin & Co. (Mumbai, India). Sodium azide and Tris(hydroxymethyl)aminomethane were obtained from Tokyo Chemical Industries (Chennai, India). Amyloid- β_{1-42} protein

fragment was purchased from Merck (Mumbai, India). Acetone was purchased from Rankem (Haryana, India) and dichloromethane (DCM) from Spectrochem Pvt. Ltd. (Mumbai, India). HPLC-grade acetonitrile was purchased from Merck (Mumbai, India). Isoflurane USP was purchased from Abbott Laboratories (Mumbai, India). Deionized water was obtained from our institute's Millipore Direct-Q ultra-pure water system (Millipore, Bedford, USA) unit facility.

4.2.2 RIV:DHA preparation for loading in LPH nanoparticles

RIV:DHA was prepared to improve the lipophilicity of RIV-HT to facilitate its loading in LPH nanoparticles [37]. Briefly, the drug (100 mg in 0.3 mL) was neutralized using NaOH (12 mg) to convert it into free RIV. Different molar concentrations of DHA solutions in acetone were prepared based on RIV:DHA ratios i.e., 1:0.5, 1:1, 1:3 and 1:5. The organic phase was added dropwise to the aqueous phase, followed by rapid vortexing using a cyclomixer resulting in spontaneous precipitation of RIV:DHA (**Fig.4.1**).

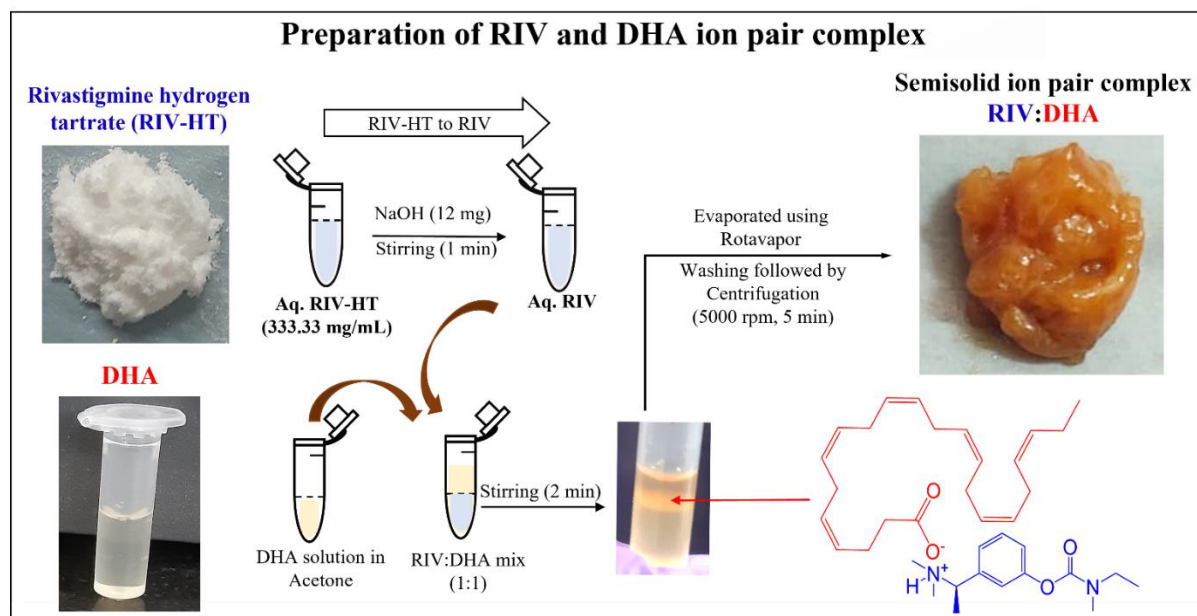


Fig. 4.1. Schematic showing the preparation of RIV:DHA ion pair complex. The alkalinized RIV-HT mixed with equal parts of DHA gave ion pair complex (RIV:DHA), which was purified and concentrated to get a semisolid mass. Aq.: Aqueous; DHA: docosahexaenoic acid RIV-HT: Rivastigmine hydrogen tartrate; RIV: Rivastigmine

The acetone was evaporated using a rotary vacuum evaporator (Buchi R-210, St. Gallen, Switzerland) for 1.5 h. Further, the precipitate was water-washed (thrice). The complex was separated after centrifugation (Remi CPR 24, Mumbai, India) at 5,000 rpm for 5 min (**Fig.4.1**).

The precipitate was dried overnight in a vacuum oven at 37° C to obtain dried RIV:DHA.

4.2.3 RIV:DHA characterization

4.2.3.1 Percent complexation efficiency

The percentage complexation efficiency at different RIV and DHA molar ratios was evaluated by indirect method [28]. The pellet constituting RIV:DHA was separated, and the concentration of residual free RIV in the supernatant was determined using the validated HPLC method [38].

The percentage complexation efficiency was calculated using the following formula:

$$\% CE = \frac{(Total\ RIV - Free\ RIV)}{Total\ RIV} \times 100$$

4.2.3.2 Water/octanol Partition coefficient

The log P of pure drug and 1:1 RIV:DHA was determined using water/octanol partitioning. 10 mg drug equivalent ion-pair complex (20 mg) was dissolved in 20 mL of water:n-octanol (1:1) mixture and shaken well on orbital shaker for 24 h at 25°C. The samples (n = 3) from each layer were withdrawn. The amount of drug in each layer was quantified using the validated RP-HPLC method. The log P was determined to study the influence of complexation on the partitioning behavior of RIV in the presence of DHA in ion-pair complex [37].

4.2.3.3 Particle size, zeta potential and viscosity measurements

The mean particle size, PDI and zeta potential measurements were performed using Malvern Nano ZS (Malvern, England) instrument with temperature maintained at 25 °C for all samples. The particle size and PDI analysis was conducted at 173° scattering angle with suitable

dilutions with Milli-Q water. The measurements were performed in triplicates, representing mean \pm SD. The samples were diluted (1:10) with Milli-Q water for measurements.

Rheological measurements were performed using Anton Paar rheometer. For viscosity determination (n=3), 1:1 molar ratio of RIV:DHA was used. The sample was equilibrated for 60 s at 25° C. The shear rate (1/s) of 10 s^{-1} for 3 min was applied and an average of last value was recorded and denoted as viscosity (mPa.s).

4.2.3.4 Proton nuclear magnetic resonance spectroscopy (^1H NMR)

The complexation between RIV, DHA (for all molar ratios) was also confirmed using proton NMR. It elucidated the formation of IPC at varying molar ratios of RIV and DHA. ^1H NMR was performed for RIV-HT, DHA, and all ratios of RIV:DHA using Bruker Advance II 400 NMR spectrometer (Billerica, USA). The instrument was loaded with Topspin 1.3 software (Bruker, Billerica, USA). All the samples were prepared in DMSO.

4.2.3.5 Fourier transform infrared spectroscopy (FTIR)

The optimum RIV: DHA molar ratio was further analysed using FTIR. The spectrum was recorded using Alpha (Bruker, Billerica, USA) system in which samples were analyzed in %transmission mode between the spectral range of $400\text{-}4000 \text{ cm}^{-1}$. FTIR analysis was performed to elucidate possible interaction between RIV and DHA followed by the formation of IPC. Spectrum measurements were conducted for RIV-HT, DHA, 1:1 ratio of physical mixture and optimized ratio of RIV:DHA (1:1 molar ratio).

4.2.3.6 Molecular modeling

It was performed to evaluate interactive forces between developed RIV:DHA (1:1 molar ratio) compared to RIV and DHA alone [37]. The Avogadro molecular mechanics program (Version CS ChemDraw 2015, USA) was utilized in this study. The mm2 force field was used for

geometry-optimization and energy calculations. The interactive energies between RIV and DHA were elucidated by calculating energies after combining and as separate components using the formula [37] provided below.

$$E_{\text{int}} = E_{\text{RIV+DHA}} - E_{\text{RIV}} - E_{\text{DHA}}$$

Where, E_{int} , $E_{\text{RIV+DHA}}$, E_{RIV} , E_{DHA} are the interaction energies, and energies of RIV with DHA, RIV and DHA respectively. Each component was geometrically optimized before energy calculation, with lower energy (more negative charge) representing comparatively stronger attractive forces.

4.2.3.7 Differential scanning calorimetry (DSC) and powdered X-ray diffraction (PXRD)

DSC and PXRD study determined the crystalline or amorphous state of the IPC. DSC analysis was performed for RIV-HT, 1:1 (w/w) ratio of physical mixture and RIV:DHA using an instrument (DSC-60 plus, Shimadzu, Tokyo, Japan) equipped with system-generated software (TA-60 WS thermal analyser), where sample (4 mg) was placed in aluminium pan and sealed with aluminium lid. The empty sealed pans were used as reference, and samples were heated at temperatures between 25-200 °C with an increment of 10 °C/min and supply of nitrogen air at a 50 mL/min flow rate.

PXRD analysis was performed under Cu K α radiation ($\lambda=1.5418 \text{ \AA}$) at 2θ range over 5-90° angle at a scanning rate of 0.5°/min. The analysis was performed using X-ray diffractometer (Rigaku Miniflex II, Tokyo, Japan) for RIV-HT, 1:1 ratio of physical mixture and RIV:DHA.

4.2.4 Preliminary screening of ingredients for LPH nanoparticles

The preliminary screening of ingredients is crucial in terms of entrapment efficiency. Therefore, lipids, oils and surfactants exhibiting maximum solubility of RIV:DHA were selected to develop LPH nanoparticles. Solubility studies were performed by adding an excess

amount of RIV:DHA in 0.3 mL surfactant (0.5% w/v), which were tween 80, tween 60, polyvinyl alcohol, Gelucire 44/14, poloxamer 188, PEG-32-stearate, soluplus (**Fig.4.2**). The mixture was saturated for 24 h. The samples were then centrifuged to remove the undissolved drug. The supernatant was collected and analyzed using the validated HPLC method [38].

Enough RIV:DHA was added to lipids (100 mg) to measure saturation solubility. The lipid and drug mixtures were maintained at 5°C above the melting point of respective lipids, and allowed to saturate for 24 h. Glyceryl monostearate (GMS), Compitrol® 888 ATO, Precirol® ATO 5, stearyl amine and stearic acid were screened (**Fig.4.2**). The saturated lipids in a molten state were centrifuged at 17000 rpm for 1 min to settle the undissolved drug. The supernatant was mixed in acetonitrile and analyzed for drug content.

Similarly, solubility in different oils was performed for 0.3 mL Capmul® MCM C8, Miglyol® 812, Captex® 355, soyabean oil, and castor oil, with water bath maintained at 25°C for 24 h (**Fig.4.2**). The saturated oils were then centrifuged to settle the undissolved drug. The supernatant was collected, mixed with acetonitrile, and analyzed for drug content.

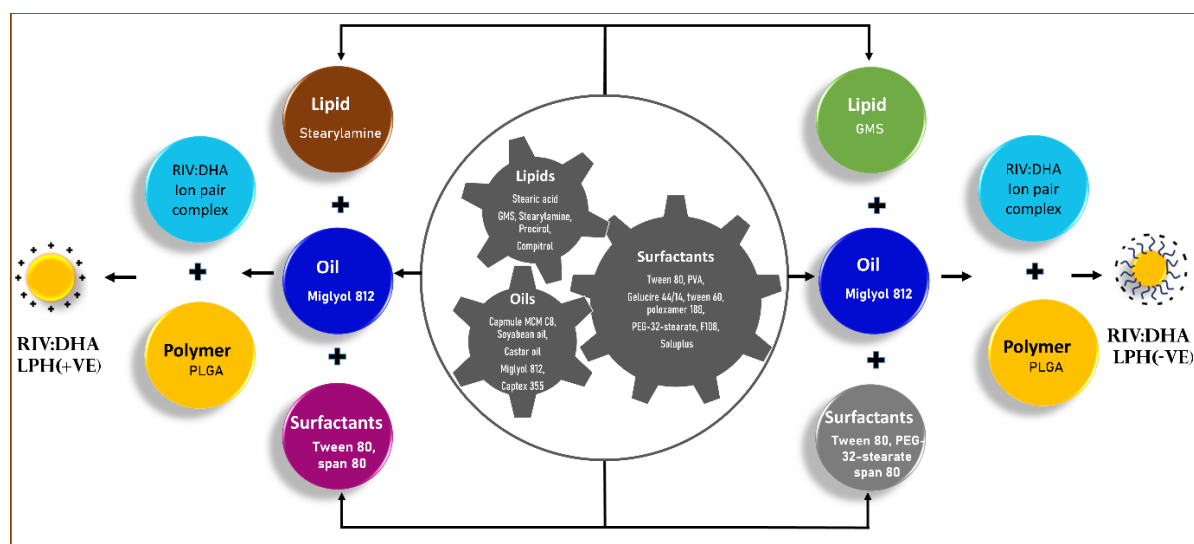


Fig. 4.2. Image represents screening of lipids, oils, surfactant, and composition of RIV:DHA LPH(+ve) and RIV:DHA LPH(-ve) based formulation

4.2.5 LPH nanoparticles preparation loaded with RIV:DHA

LPH nanocarriers with positive and negative charges were prepared (**Fig.4.3**). Both LPH nanoparticles were prepared using hydrophobic poly(lactic-co-glycolic acid) polymer, Resomer™ RG 504 (molecular weight 38000- 54000), with the combination of solid lipid (GMS, Compitrol® 888 ATO, Precirol® ATO 5, stearyl amine and stearic acid), liquid lipid (Miglyol 812), and surfactants (tween 80 and span 80) to study their effect on particle size, PDI and encapsulation efficiency. For RIV:DHA LPH(+ve) nanoparticles, 20 mg drug equivalent RIV:DHA (40 mg), stearyl amine (120 mg), PLGA (60 mg), and Miglyol 812 (40 mg), 0.5 % (w/v) span 80 (15 mg) dissolved in 0.7 mL dichloromethane (DCM). It was heated at 60° C in a water bath for 2 h to remove DCM (**Fig.4.3A**). Further, 3 mL aqueous solution containing 0.5 % (w/v) (15 mg) tween 80 was added to lipid-polymer matrix. Size reduction was performed using probe sonication (25% amplitude, 4 min), followed by centrifugation at 5,000 rpm for 5 min (**Fig.4.3A**). The supernatant containing RIV:DHA LPH(+ve) was collected and analyzed for particle size, PDI and zeta potential.

The RIV:DHA LPH(-ve) was prepared using emulsification solvent evaporation and ultrasonication. The batch was prepared using 20 mg drug equivalent RIV:DHA (40 mg), GMS (80 mg), PEG-32-stearate (40 mg), PLGA (60 mg), Miglyol 812 (40 mg) and span 80 (15 mg) were dissolved in 0.5 mL DCM (**Fig.4.3B**). The organic phase was added dropwise (rate of addition 1 mL/min) into 3 mL aqueous phase containing 0.5 % (w/v) tween 80 followed by probe sonication. It was subjected 2 h to a rotary vacuum evaporator (temperature 40° C) to remove DCM. Further, the resultant LPH was centrifuged (5,000 rpm, 5 min) to settle any unencapsulated RIV:DHA. The supernatant containing RIV:DHA LPH(-ve) was collected and analyzed for particle size, PDI, zeta potential and encapsulation efficiency. particle size analysis was performed with respective 1:2 dilution with Milli-Q water.

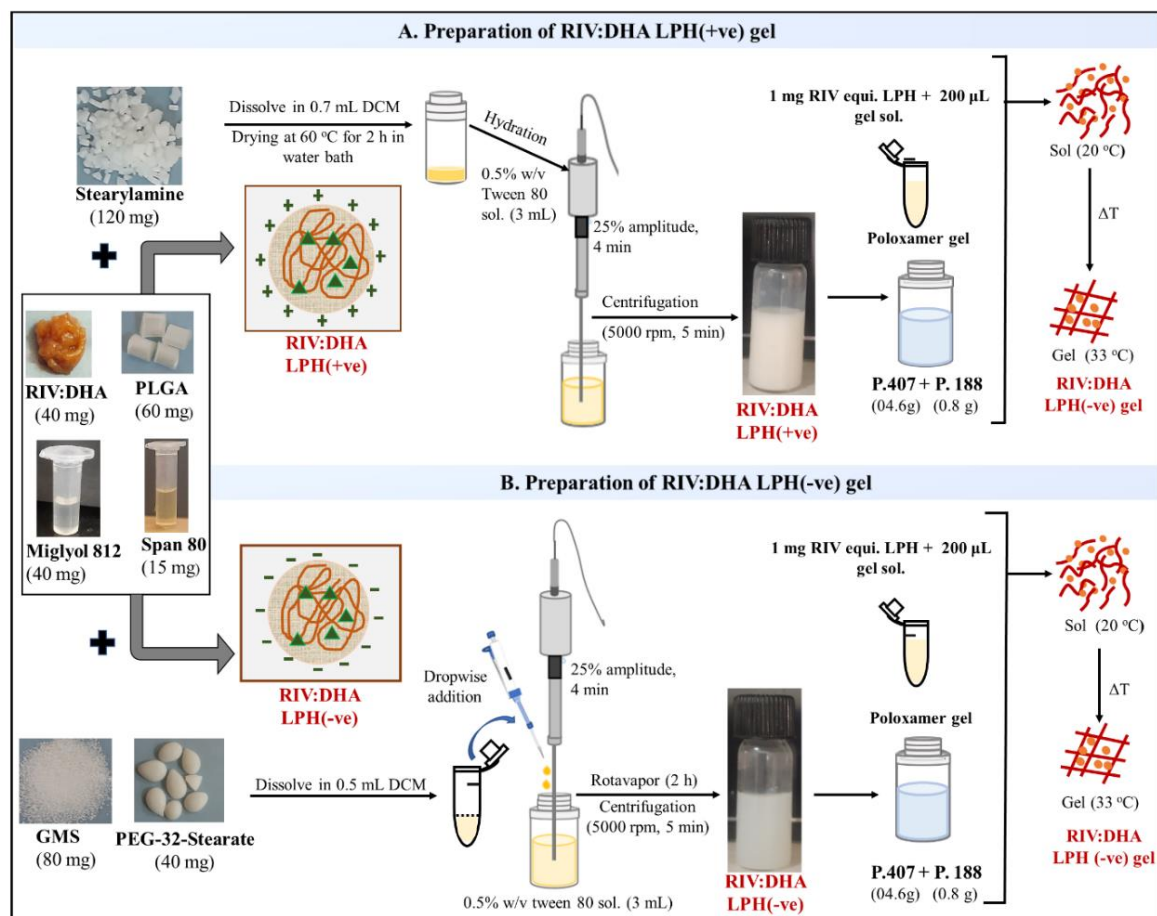


Fig. 4.3. Schematic showing (A) loading of RIV using RIV-DHA to prepare RIV:DHA LPH(+ve) and RIV:DHA LPH(+ve) gel (B) loading of RIV using RIV-DHA to prepare RIV:DHA LPH(-ve) and RIV:DHA LPH(-ve) gel. DHA: docosahexaenoic acid; DCM: dichloromethane; GMS: glyceryl monostearate; PEG: polyethylene glycol; LPH: Lipid polymer hybrid nanoparticles; PLGA: Poly (lactic-co-glycolic acid); RIV: Rivastigmine, RIV:DHA: RIV and DHA ion pair complex.

For determination of encapsulation efficiency, 0.1 mL formulation was diluted upto 1 mL with acetonitrile, giving the clear solution, followed by heating at 70° C. Subsequently, the sample was centrifuged at 10,000 rpm for 10 min. The dissolved encapsulated drug in the supernatant was analyzed using HPLC. FTIR analysis was also performed to explain the encapsulation of RIV:DHA into LPH nanoparticles. The analysis also was performed for pure RIV-HT, RIV:DHA LPH(-ve) and RIV:DHA LPH(+ve), and their blank and respective gel.

4.2.6 *In-vitro* amyloid aggregation inhibition using LPH nanoparticles

In-vitro amyloid aggregation inhibition was evaluated for RIV:DHA LPH(-ve) and RIV:DHA LPH(+ve). Amyloid beta₁₋₄₂ (A β ₁₋₄₂) fibril sample was prepared using a previously reported method by dissolving amyloid beta (0.5 mg) in 0.5ml 50:50 (v/v) ratio of 0.1 % (v/v) NH₄OH and 100 mM tris buffer, 0.02 % (w/v) NaN₃, pH 7.4 [39]. The solution was centrifuged at 48,000 rpm for 1 h at 4° C to remove pre-existing amyloid fibrils. The supernatant was collected, and the resultant amyloid concentration was determined spectrophotometrically at 275 nm. Further, the supernatant was diluted to 0.1 μ M with 13 mM sodium phosphate buffer, 0.02% NaN₃, pH 7.4. The solution was instantly used in the following experiments. For evaluating amyloid inhibition, RIV:DHA LPH(-ve) and RIV:DHA LPH(+ve) were tested at varying drug concentrations of 50, 100, 200 and 400 ng/mL.

4.2.6.1 ThT fluorescence Assay

The amyloid beta inhibition was evaluated using ThT fluorescence intensity, which is proportional to the amyloid content in the sample. 90 μ L of 0.1 μ M A β ₁₋₄₂ was treated with 200 μ M ThT (from a 2 mM stock solution in water) per well was incubated in the absence (control group) or presence of LPH nanoparticle. 10 μ L LPH nanoparticles (cationic and anionic LPH taken separately) were mixed into each well and incubated at 37° C. ThT

fluorescence intensity was evaluated at excitation and emission wavelength of 440 and 480 nm [40]. Amyloid inhibition at a predetermined time (0 to 48 h) was evaluated using 96-well plates.

4.2.6.2 Particle size and zeta potential measurements

Zeta potential of amyloid β_{1-42} in the absence and presence of LPH nanoparticles at different concentrations was performed. Time dependant amyloid inhibition was performed using dynamic light scattering (DLS) to evaluate the sizes of amyloid beta affected by LPH nanoparticles [41]. The particle size analysis was performed directly without further dilution.

4.2.6.3 ATR-FTIR spectroscopy and microscopy

RIV:DHA LPH(-ve) and RIV:DHA LPH(+ve) exhibiting maximum inhibition were chosen for further analysis. ATR FTIR study was performed to elucidate time dependant change in the secondary structure of amyloid β_{1-42} , where the spectra were read in wavenumber ranging from 1700 to 1500 cm^{-1} [42]. The microscopic images were captured in fluorescence and bright field mode using electron microscope (Axio Vert. A1 FL, Carl Zeiss, Jena, Germany) at 6, 12, 24 and 48 h [23]. It was done to evaluate the amyloid aggregate inhibition effect of nanoparticles.

4.2.7 Preparation of hydrogel embedded with LPH nanoparticles

The *in-situ* thermoresponsive gel was prepared using cold process [43]. Poloxamer 407 shows effective gelling at nasal cavity temperature [44]. Poloxamer-based gel containing 0.5 % (w/v) drug equivalent were prepared. Briefly, poloxamer 407 (4.6 g) and poloxamer 188 (0.8 g) were mixed by stirring in 15 mL Milli-Q water and stored overnight at 2-8° C for complete hydration. Further, 2 g propylene glycol was added to the poloxamer solution, and the final volume was made upto 20 mL with Milli-Q water. Finally, the gel was stored at 2-8° C, and RIV-HT was added just before the initiation of rheological experiments. Similarly, 1 mg drug equivalent of

RIV:DHA LPH(-ve) and RIV:DHA LPH(+ve), were incorporated in 200 μL hydrogel for further experiments (**Fig.4.3**).

4.2.8 Hydrogel rheological characterization

Rheological studies were performed using MCR 92 rheometer (Anton Paar, Austria). The 25 mm parallel plate geometry with standard gap of 0.5 mm between 2 plates was maintained for all experiments [44,45]. First, the amplitude sweep test was performed to determine the linear viscoelastic range. The elastic properties of the gel were evaluated using frequency sweep test at constant temperature (33° C), with increasing frequency within 0.1 to 10 Hz. For viscosity determination ($n = 3$), 1:1 molar ratio of RIV:DHA was used. The sample was equilibrated for 60 s at 25° C. The shear rate (1/s) of 10 s^{-1} for 3 min was applied and an average of last value was recorded and denoted as viscosity (mPa.s). Rheological studies for all hydrogel-loaded formulations, (RIV:DHA LPH(+ve) and RIV:DHA LPH(-ve)), were measured; where the temperature dependant viscosity was performed within the temperature range of 20-35 °C and viscosity of gel at nasal cavity temperature, viz. 33° C was noted. Elastic modulus indicates gel strength and is widely accepted measure for rheological studies. First, the amplitude sweep test was performed to determine linear viscoelastic range (LVER). Sample was allowed to equilibrate for 120 s onto rheometer platform. Storage modulus (G'), loss modulus (G''), loss tangent ($\tan \delta$) and dynamic viscosity were determined from rheological measurements. The elastic properties of gel were evaluated using frequency sweep test, with increasing frequency value within the range of 0.1 to 10 Hz with temperature maintained constant at 33 °C.

4.2.8.1 Scanning electron microscopy

RIV:DHA LPH(-ve) and RIV:DHA LPH(+ve) and their corresponding hydrogel nanoparticles were placed onto the coverslip, and the smear was dried overnight at room temperature. The sample coverslips were placed on metal stubs and fixed using double-sided carbon tape. It was

gold coated for 60 s using Q150TES sputter coater (Quorum Technologies, East Sussex, UK). The samples were analyzed using Field emission-scanning electron microscopy, FE-SEM (FEI, Hillsboro, USA), with 20 kV high vacuum within suitable magnification range.

4.2.9 Stability study

The study was performed for RIV:DHA LPH(-ve) gel and RIV:DHA LPH(+ve) gel at refrigerated conditions (2-8°C). The samples were collected at 0, 30, 60, 90, and 180 days and compared with freshly prepared samples. The particle size, PDI and zeta-potential was determined, and statistical analysis was performed to assess the stability of the samples at each time point.

4.2.10 *In-vitro* drug release of RIV from LPH hydrogel

In-vitro drug release from LPH nanoparticle gel was done using dialysis [46]. Briefly, the nano gel (1 mg drug equivalent /200 µL gel) was filled in dialysis bag (Himedia dialysis membrane-110, molecular weight cut off 12000-14000) containing 1 mL nasal simulated fluid (NSF, composition: 8.77 g L⁻¹ NaCl, 2.98 g L⁻¹ KCl, 0.59 g L⁻¹ CaCl₂·2H₂O in deionized water, pH 6.4), which was further placed in tubes containing 25 mL phosphate buffer saline (PBS), pH 7.4. The tubes were kept on stirring at 100 rpm using a magnetic stirrer at 33 ± 1°C. Sampling was performed at predetermined time (0.08 h to 72 h) and replenished with the same volume of fresh medium. Samples were centrifuged at 15,000 rpm for 10 min; the supernatant was collected and analysed using the validated HPLC method [38]. A mathematical comparison was performed by applying the dissimilarity factor (f1) and similarity factor (f2) to investigate the differences between the dissolution profiles. The drug release data were fitted into various kinetic models such as zero order, first order, Higuchi, Hixson-Crowell, Korsmeyer-Peppas to explore the mechanism of drug release using DD solver software program.

4.2.11 *Ex-vivo* permeation of RIV from hydrogel

Ex-vivo permeation study was performed using the Franz diffusion cell apparatus [47]. Freshly excised goat nasal mucosa was procured from a local abattoir and rinsed with freshly prepared PBS (pH 7.4). The nasal mucosa was separated from the septum by removing extraneous tissue. Further, the tissue was rinsed with PBS (pH 7.4), and its thickness was measured using a Vernier calliper. The nasal mucosa was placed in the Franz cell and equilibrated with PBS (pH 6.4) for 15-20 min. The samples containing 1 mg RIV-HT gel and 1 mg drug equivalent RIV:DHA gel, RIV:DHA LPH(-ve) gel, and RIV:DHA LPH(+ve) gel were placed onto the tissue surface. The receptor compartment was filled with PBS (pH 6.4) solution. The sample (1 mL) was withdrawn at specific intervals (0.08 h to 6 h) and replenished with an equal volume of PBS pH 6.4. Further, the samples were centrifuged at 15,000 rpm for 15 min and analysed using the validated HPLC method [38]. The permeation coefficient (cm^2/h) and flux ($\mu\text{g}/\text{cm}^2/\text{h}$) were calculated from each permeation profile.

4.2.12 *In-vivo* study in rats

In-vivo study was performed using Wistar rats weighing 230-260 g. Animals were caged in a facility compliant with authority guidelines. The experiment followed a protocol issued by the institutional animal ethics committee (Protocol number: IAEC/RES/32/05). Animals were divided into four groups (15 animals in each group).

Group I: Intranasal administration of RIV-HT gel

Group II: Intravenous administration of RIV-HT sol

Group III: Intranasal administration of RIV:DHA LPH(-ve) gel

Group IV: Intranasal administration of RIV:DHA LPH(+ve) gel

Group I, III and IV received intranasal dosing equivalent to 2 mg/kg RIV-HT. The dose was administered using micropipette attached to 1.3 cm long soft polypropylene tube (Instech Laboratories, PA, USA). After giving anesthesia using isoflurane, animals were held upright in the supine position, and 50 μ L dose volume (total dose 500 μ g in 100 μ L) was instilled in each nostril. The animal was held in the same position for at least 30 sec or until recovery of anesthesia to ensure effective dosing or prevent drug loss from the nasal cavity. In group II, rats were anesthetized, and 2 mg/kg RIV-HT sol (total dose 500 μ g in 400 μ L) was administered intravenously through the tail vein.

4.2.12.1 Mucociliary clearance time

Mucociliary clearance time is the time a drug takes to reach the pharynx from the nasal cavity. The swab was taken from the oropharyngeal cavity at every 5 min interval upto 1 h. The samples were suitably diluted with the mobile phase (ACN: phosphate buffer: IPA, 33:65:2) and analysed using the validated HPLC method [38]. The first-time point at which drug was detected in the oropharyngeal swab was noted as mucociliary clearance time.

4.2.12.2 Pharmacokinetic study in rats

Blood samples were withdrawn from 0 (pre-dose) to 24 h through the retro-orbital puncture. Animals were sacrificed using cervical dislocation, and the whole brain was collected at different times. Brain and plasma samples were processed and analysed using the bioanalytical method described in Chapter 3, section 3.4.2.4 and section 3.4.2.5. The non-compartmental analysis was applied using Phoenix WinNonlin software (version 8.3, Pharsight Corporation, NC, USA) to determine brain and plasma PK parameters.

Drug targeting efficiency (DTE %) (equation 1) and drug transport percentage (DTP %) (equations 2 and 3) were calculated [11]. It evaluated the brain-targeting efficiency of

formulations. DTP (%) indicates the percentage of drug directly reaching the brain after intranasal delivery. Whereas DTE (%) indicates the total percentage of drug reaching the brain *via*. direct intranasal and indirect intranasal through systemic circulation to the brain.

$$DTE (\%) = \frac{\frac{(AUC_{brain})_{IN}}{(AUC_{plasma})_{IN}}}{\frac{(AUC_{brain})_{IV}}{(AUC_{plasma})_{IV}}} \times 100 \quad \dots (1)$$

$$DTP (\%) = \frac{(AUC_{brain})_{IN} - F}{(AUC_{brain})_{IN}} \times 100 \quad \dots (2)$$

$$F = \frac{(AUC_{brain})_{IV}}{(AUC_{plasma})_{IV}} \times (AUC_{plasma})_{IN} \quad \dots (3)$$

Where $(AUC_{brain})_{IN} = AUC_{0-t}$ in brain after intranasal administration and $(AUC_{plasma})_{IN} = AUC_{0-t}$ in plasma after intranasal administration.

$(AUC_{brain})_{IV} = AUC_{0-t}$ in the brain after intravenous administration and $(AUC_{plasma})_{IV} = AUC_{0-t}$ in plasma.

DTE (%) greater than 100 indicates enhanced brain targeting. Whereas DTP (%) greater than 0 indicates direct N2B drug transport. AUC_{0-t} was employed to calculate percent indices for respective formulations.

4.2.13 Histopathological study

The histopathological observation of nasal epithelium and brain were done after intranasal administration of formulations (2 mg/kg dose). Untreated rats were used as control. After 24 h, animals were sacrificed, and the brain and nasal epithelium carefully removed. The tissues were collected and washed with PBS pH 7.4 to remove the blood and connective tissue.

Further, it was fixed in 10 % (v/v) formalin. Samples were dehydrated with a series of methyl alcohol, ethyl alcohol, followed by absolute ethyl alcohol. The samples were treated with xylene, and tissue was embedded in molten paraffin (56° C) and stored for 24 h. The paraffin tissue blocks were sectioned (3-4 μ m) using a sledge microtome. Further, tissue was deparaffinized, stained with eosin and hematoxylin [48], and observed under the light microscope (Axio Vert. A1 FL, Carl Zeiss, Jena, Germany).

4.2.14 Statistical analysis

GraphPad Prism was used for statistical testing (GraphPad version 8 Software, La Jolla, CA, USA). All quantifiable data were described as mean \pm standard deviation (SD), and differences within treatment groups were investigated using ANOVA or student's t-test, followed by Tukey's multiple comparison test. The p-value less than 0.05 was considered statistically significant.

4.3 Result and discussion

4.3.1 RIV:DHA complex preparation for loading in LPH nanoparticles

The IPC of the hydrophilic drug with DHA, like RIV-HT increases the lipophilicity without altering chemical structure and renders reversible aqueous solubility [49]. The RIV:DHA IPC appeared brownish-yellow and lustrous semisolid (**Fig.4.1**). RIV-HT (**Fig.4.4A**) was converted to RIV (**Fig.4.4C**) after adding sodium hydroxide. Then the ion pairing of RIV with DHA (**Fig.4.4B**) led to the precipitation of hydrophobic RIV:DHA complex (**Fig.4.4D**). The 1:0.5, 1:1, 1:3, and 1:5 molar ratios of RIV to DHA were prepared to get RIV:DHA IPC.

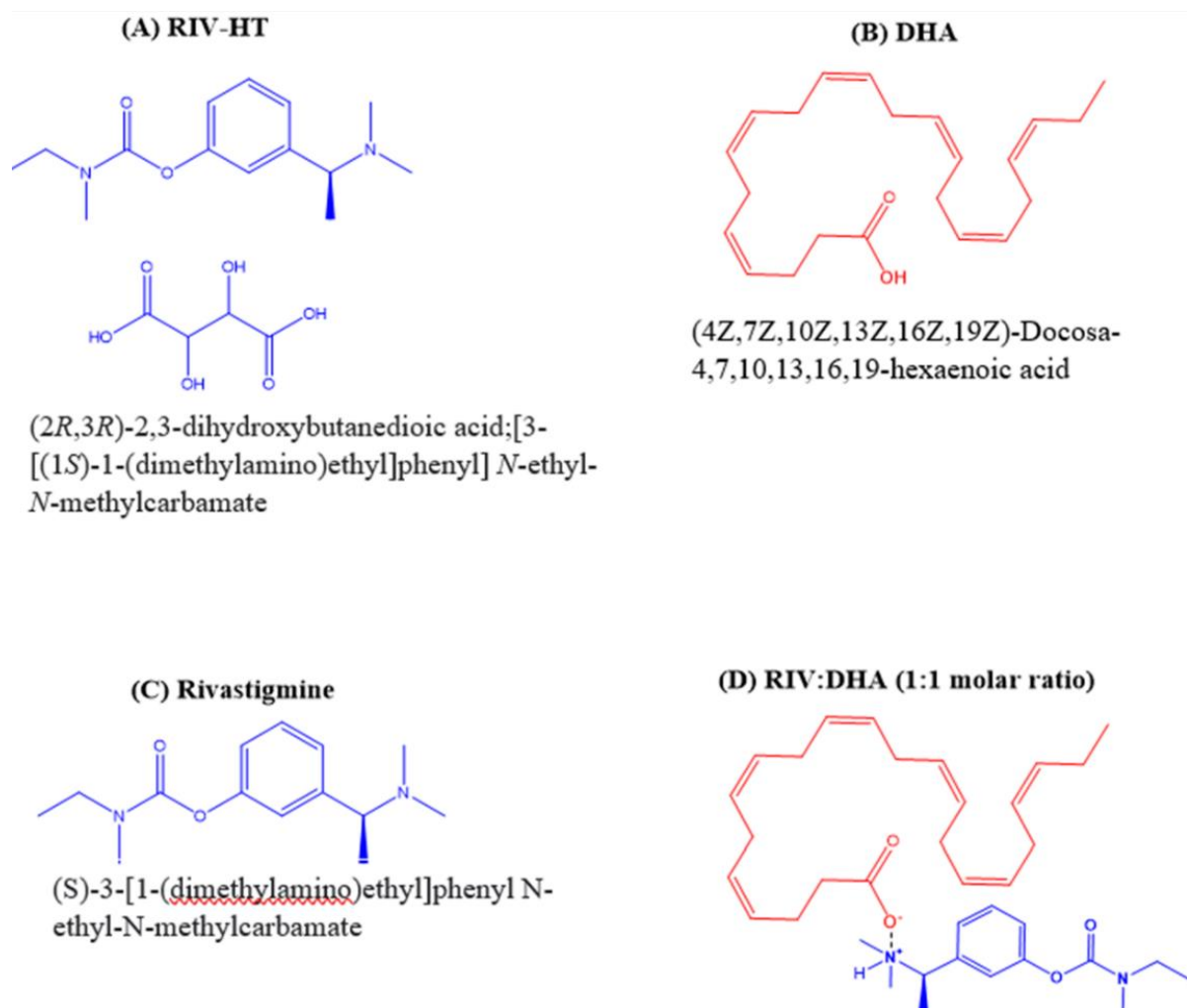


Fig. 4.4. Chemical structure of (A) RIV-HT, (B) DHA, (C) RIV and (D) RIV:DHA (1:1 molar ratio)

4.3.2 RIV:DHA characterisation

4.3.2.1 Complexation efficiency

The maximum complexation (99.91 ± 1.33 %) was achieved at 1:1 molar ratio. The RIV:DHA at 1:0.5 molar ratio of IPC had 65.56 ± 1.26 % complexation efficiency. The negative charge provided by the carboxylic group of DHA interacts with the positive charge on RIV, provided by nitrogen molecule, to form IPC (**Fig.4.4D**). A molar ratio 1:1 sufficed to saturate RIV positive charge, showing that 1:1 was the most efficient. Other studies also showed that an equivalent or slightly higher ratio is the most efficient for IPC formation [50]. Torky *et al.* reported similar findings, where 1:1 molar ratio of berberine: sodium oleate IPC had maximum

complexation efficiency [28]. IPC has also been explored in topical, ocular, and oral delivery, offering advantages such as improved saturation solubility in n-octanol, permeation capability, and enhanced loading efficiency with slow and controlled drug release patterns [37,49,51]. Cai *et al.* developed IPC of RIV with salicylic acid for a controlled and long-acting rivastigmine-adhesive patch. It showed 2.8 fold increase in permeation and enhanced *in-vivo* plasma concentration for up to 3 days [52]. Other fatty acids, such as oleic acid, pamoic acid, and linoleic acid [37,53–55] have also been explored for IPC. However, for intranasal delivery, DHA-based IPC has not been explored. A study reported *in-situ* doxorubicin-DHA IPC for increasing the entrapment efficiency in SLN. However, the major drawback associated with *in-situ* ion pairing involves non-specific complexation with any formulation component of the opposite charge. Therefore, in our study, the IPC was formulated first before loading into nanoparticles to avoid any competitive interaction with other formulation components.

4.3.2.2 Proton nuclear magnetic resonance spectroscopy

In the ^1H NMR (400 MHz, DMSO), the chemical shifts of RIV-HT protons were observed at δ 7.44 (t, $J = 7.9$ Hz, 1H), 7.31 (d, $J = 7.8$ Hz, 1H), 7.22 (s, 1H), 7.14 (d, $J = 8.0$ Hz, 1H), 4.16 (q, $J = 6.8$ Hz, 1H), 4.10 (s, 2H), 3.40 (q, $J = 6.9$ Hz, 1H), 3.29 (q, $J = 7.0$ Hz, 1H), 2.94 (d, $J = 50.6$ Hz, 3H), 2.49 (s, 6H), 1.51 (d, $J = 6.9$ Hz, 3H), 1.20 – 1.03 (m, 3H) (**Fig.4.5A**). Whereas chemical shifts of pure DHA protons were observed at δ 5.48 – 5.15 (m, 12H), 2.90– 2.62 (m, 8H), 2.24 (s, 5H), 2.01 (dt, $J = 14.6, 7.3$ Hz, 3H), 0.89 (t, $J = 7.5$ Hz, 3H) (**Fig.4.5A**). The chemical shifts for RIV:DHA (1:1 molar ratio) protons were observed at δ 7.31 (t, $J = 7.8$ Hz, 1H), 7.12 (d, $J = 7.7$ Hz, 1H), 6.98 (s, 1H), 6.95 (d, $J = 8.0$ Hz, 1H), 5.33 (dd, $J = 9.4, 5.2$ Hz, 12H), 4.02 (q, $J = 7.1$ Hz, 1H), 3.29 – 3.24 (m, 2H), 2.93 (d, $J = 49.8$ Hz, 3H), 2.05 (s, 6H), 2.00 (dd, $J = 14.1, 7.4$ Hz, 5H), 1.95 – 1.90 (m, 3H), 1.24 (d, $J = 6.7$ Hz, 3H), 1.07 (d, $J = 6.9$ Hz, 1.5H), 0.89 (d, $J = 7.5$ Hz, 3H), 0.82 (d, $J = 6.7$ Hz, 1.5H) (**Fig.4.5A**). Formation of IPC

led to conversion of RIV-HT into RIV base, resulting in loss of two -OH protons (present with -OH group of tartrate salt, 2,3-dihydroxybutanedioic acid) at δ 4.10 (s, 2H) in case of RIV:DHA (Fig.4.4D). Dimethyl amino protons (6H) in RIV-HT showed a chemical shift from δ 2.49 (s, 6H) to δ 2.05(s, 6H) (Fig.4.5A).

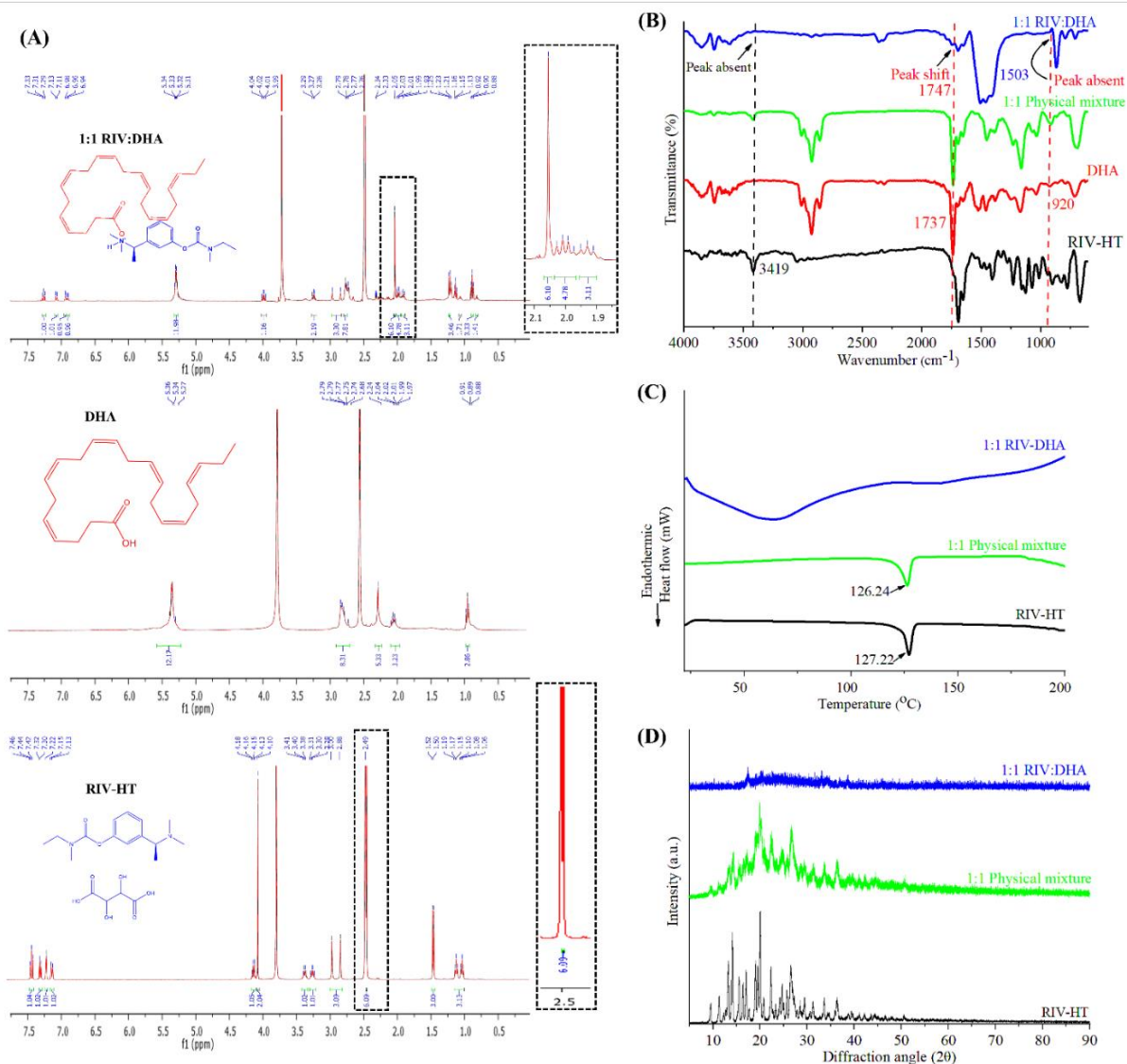


Fig. 4.5. (A) Proton NMR of RIV-HT, DHA and RIV:DHA demonstrate the formation of complex at 1:1 molar ratio. (B) FTIR spectra representing the formation of RIV:DHA. (C) DSC thermogram of RIV-HT, physical mixture and RIV:DHA showed conversion into amorphous form after formation of IPC, (D) X-ray diffraction studies of RIV-HT, physical mixture and RIV:DHA (1:1 ratio) demonstrate amorphous form of IPC. DHA: docosahexaenoic acid; RIV:

Rivastigmine; RIV-HT: Rivastigmine hydrogen tartrate, RIV:DHA: RIV and DHA ion pair complex.

This usually occurs due to the involvement of dimethyl amino nitrogen in forming IPC. The resultant upfield shift occurred due to intermolecular electrostatic interaction between RIV and DHA, exhibiting shielding of nitrogen with long chain hydrocarbon of DHA. It showed the involvement of one nitrogen in the formation of IPC with DHA, representing the presence of all DHA protons at 1:1 molar ratio of RIV:DHA.

4.3.2.3 Fourier transform infrared spectroscopy

The study was performed to elucidate the interaction between RIV and DHA in forming RIV:DHA. **Fig.4.5B** compares stretching vibrations of RIV-HT, DHA, physical mixture, and RIV:DHA. The FTIR spectra of RIV-HT showed characteristic peaks of OH (stretching) and CN (stretching) functional groups. The presence of hydroxyl group (-OH) corresponding to 2,3-dihydroxybutanedioic acid (tartrate salt) showed stretching vibration at 3419 cm^{-1} , whereas CN group showed stretching vibration at 1158.2 cm^{-1} (**Fig.4.5B**) [56]. The FTIR spectrum of pure DHA showed various peaks (**Fig.4.5B**). Wherein, characteristic peaks were observed at 1737.3 cm^{-1} (C=O stretching of COOH) [57] and 920.4 cm^{-1} (out-of plane O-H bending vibration of COOH) [52]. All major peaks of RIV-HT were retained in the physical mixture. For RIV:DHA, the characteristic hydroxyl peak (corresponding to 2,3-dihydroxybutanedioic acid or tartrate salt) showed an absence of stretching vibration at 3419 cm^{-1} due to the absence of tartrate salt in RIV:DHA. In case of DHA, it also led to the disappearance of characteristic OH bending vibration (carboxylic acid) at 920 cm^{-1} , due to the loss of OH proton (**Fig.4.5B**), resulting into COO^- on DHA. The interaction of nitrogen of RIV with COO^- of DHA led to peak broadening and shifting of peak at higher wavelength from 1737.3 cm^{-1} to 1747.7 cm^{-1} (C=O) (**Fig.4.5B**). Moreover, RIV:DHA showed a new peak $\sim 1503.2\text{ cm}^{-1}$ attributed due to

interaction between COO^- of fatty acid and nitrogen of RIV (**Fig.4.5B**) [59,60]. The carboxyl group of DHA interacting with nitrogen of RIV shows the formation of RIV:DHA [28].

4.3.2.4 Particle size, zeta potential, and viscosity measurement

RIV:DHA (1:1 molar) showed the development of coarse dispersion upon the addition of water. The formation of coarse dispersion is due to the unsaturated long-chain fatty acid of DHA, attributing hydrophobic characteristics to RIV:DHA. The particle size of 1:1 RIV:DHA was 1549.7 ± 195.3 nm (PDI 0.903 ± 0.029) and the zeta potential was $+5.5 \pm 1.1$ mV. The viscosity of RIV:DHA was 199.14 ± 17.43 mPa.s. The RIV:DHA had semisolid texture, while the RIV base exists as liquid form, which shows higher viscosity of RIV:DHA than RIV. Abouelmagd *et al.* developed gentamycin-tannic acid and colistin-tannic acid IPC demonstrating micron-sized particles at various molar ratios [61]. The positive zeta was due to carbamate nitrogen that remained surplus in RIV:DHA [62,63].

4.3.2.5 Differential scanning calorimetry and Powder X-ray powder diffraction

DSC thermogram of pure RIV-HT representing melting endotherm at 127.22°C ($\Delta H = -1.94$) (**Fig.4.5C**) [64]. The physical mixture showed melting peak of pure RIV-HT, showing the presence of crystalline form. However, it showed a slight shift in melting endotherm towards lower temperature 126.24°C ($\Delta H = -1.32$) owing to increased enthalpy, lowered melting point of RIV-HT in case of physical mixture (**Fig.4.5C**) [65]. Whereas RIV:DHA showed disappearance of the endothermic peak, representing the conversion of RIV-HT into amorphous form (**Fig.4.5C**).

Powder X-ray diffractograms of RIV-HT, physical mixture and RIV:DHA have been depicted in **Fig.4.5D**. RIV-HT shows intense peaks at 2θ diffraction angles of 9.5° , 11.3° , 14.1° , 15.5° , 17.0° , 19.0° , 20.0° and 29.4° , confirming its crystalline structure as represented by DSC

thermogram [64]. The physical mixture showed similar diffraction patterns as pure RIV-HT, representing retained crystalline structure. Whereas, RIV:DHA showed the disappearance of all the intense peaks depicted in pure RIV-HT, confirming conversion into an amorphous state due to the formation of RIV:DHA (**Fig.4.5D**).

4.3.3 Preliminary screening of ingredients for LPH nanoparticle

Surfactant screening showed maximum solubility of RIV:DHA in tween 80 (73.89 ± 0.73 mg) followed by PEG-32-stearate (73.78 ± 1.46 mg) and tween 60 (72.34 ± 0.73 mg) (**Fig.4.6A**). Among lipids, GMS, stearylamine and Compitrol 888 ATO exhibited solubility of 107.35 ± 6.8 , 92.59 ± 2.73 and 81.91 ± 1.95 mg (**Fig.4.6B**). Among oils, the highest solubility of RIV:DHA was shown by Miglyol 812 (50.30 ± 1.09 mg) followed by Capmul MCM C8 (43.37 ± 2.77) and castor oil (42.13 ± 2.19 mg) (**Fig.4.6C**).

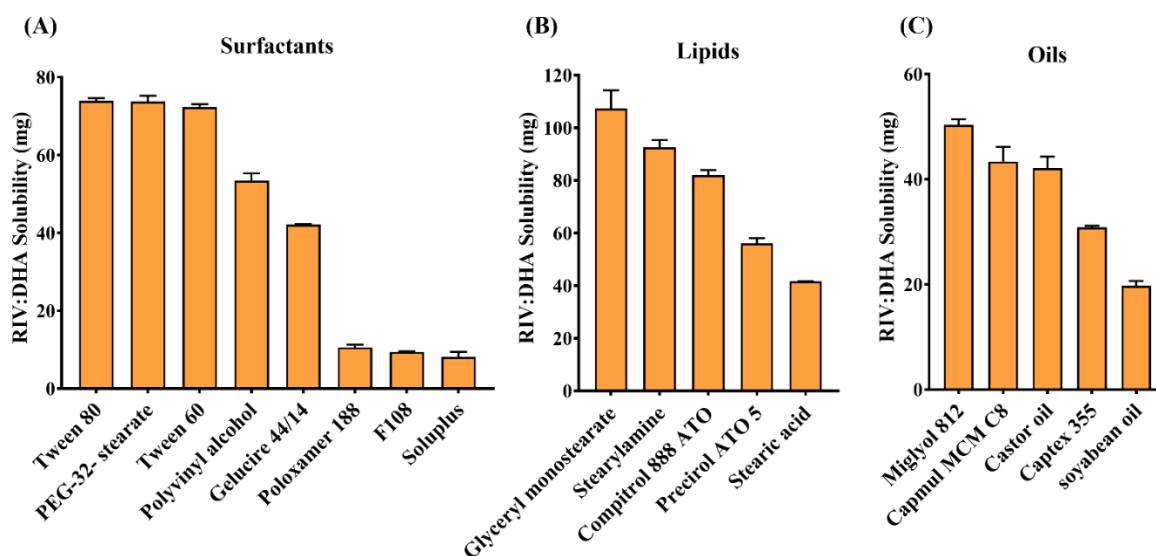


Fig. 4.6. Solubility studies of RIV:DHA in (A) 0.5% w/v surfactants, (B) solid lipids and (C) liquid lipids/oils. DHA: docosahexaenoic acid; RIV: Rivastigmine; RIV:DHA: RIV and DHA ion pair complex

The preliminary screening of lipids, oils, and surfactants is crucial in terms of entrapment efficiency. Therefore, lipids, oils, and surfactants representing maximum solubility were

selected for developing RIV:DHA based LPH nanoparticles [4]. Solid lipids (GMS and stearylamine), surfactant (Tween 80, span 80, and PEG-32-stearate), and oil (Miglyol 812) exhibiting maximum solubility in RIV:DHA were selected for the development of LPH nanoparticles.

4.3.4 LPH nanoparticles preparation loaded with RIV:DHA

The optimum RIV:DHA LPH(+ve) and RIV:DHA LPH(-ve) were prepared after studying the combination of solid lipids (GMS, Precirol ATO 5, stearic acid, Compritol 888 ATO), liquid lipid (Miglyol 812), and surfactants (tween 80, span 80, PEG-32-stearate). The various combination of these ingredients was studied for particle size and encapsulation efficiency (**Table 4.1 and Table 4.2**). The optimised formulations were prepared as shown in **Fig.4.3**. This method offered high drug-polymer-lipid miscibility, high loading efficiency, reduced particle size and enhanced storage stability. SLN prepared using mixture of tween 60 and span 60 has developed a stable formulation with low particle size [66]. Other reports have shown improved encapsulation in BSA-loaded microspheres using tween 80 and span 80 in 3:2 ratio [67].

The RIV:DHA LPH(+ve) consists of stearylamine (solid lipid), hydrophobic components such as PLGA polymer, and Miglyol 812 (liquid lipid) forming matrix-based system. Cationic stearylamine imparts positive surface charge, limiting aggregation of nanoparticles and exhibiting enhanced colloidal stability. The RIV:DHA LPH(-ve) consisted GMS as solid lipid, PLGA polymer, Miglyol 812 (liquid lipid) and emulsifier PEG-32-stearate, and PEG provided stealth layer. The negative surface charge is due to GMS and PEG moieties. The PEG moieties also impart colloidal steric stability.

The solid lipid, liquid lipid, PLGA polymer and surfactants were essential for developing RIV:DHA LPH(+ve). Batches of (RIV:DHA LPH(+ve)) when prepared without Miglyol 812

showed increased particle size (271.3 ± 2.2 nm) (**Table 4.1**) with compromised colloidal stability. Whereas, in case of RIV:DHA LPH(-ve), the batches failed when prepared without Miglyol 812.

Each batch of RIV:DHA LPH(+ve) prepared separately without span 80 and tween 80 showed significantly increased particle size (PDI) of 1119 ± 165.3 nm (0.88 ± 0.11) and 581.7 ± 24.5 nm (0.16 ± 0.05) (**Table 4.1**). Whereas RIV:DHA LPH(-ve) batches failed when prepared separately without span 80 and tween 80. Therefore, Miglyol 812, tween 80 and span 80 are used in developing RIV:DHA LPH(-ve) and RIV:DHA LPH(+ve). Tween 80 (HLB 15) and span 80 (HLB 4.3) are non-ionic surfactants with higher and lower HLB [3]. Addition of these surfactants in aqueous and organic phase led to the development of comparatively more stable surfactant film at the interface with reduced surface free energy. Addition of span 80 led to the development of nanoparticles with reduced particle size and improved colloidal stability. For the development and optimization of RIV:DHA LPH(+ve) and RIV:DHA LPH(-ve) based nanohybrid system, the effect of surfactant concentration (0.25 to 0.75 % (w/v)) on particle size, polydispersity index and percentage encapsulation efficiency were evaluated using equivalent ratios of tween 80 and span 80. Increasing surfactant concentration from 0.25 to 0.5% (w/v), resulted in decreased particle size of RIV:DHA LPH(+ve) from 152.2 ± 2.6 nm

Table 4.1 Effect of formulation parameters on characteristics of RIV:DHA LPH(+ve)

Parameter	Particle size (nm)	PDI*	Zeta potential (mV)	% Encapsulation efficiency
Effect of surfactants and Miglyol 812 on LPH* characteristics				
Without Miglyol 812	271.3 ± 2.2	0.252 ± 0.009	24.7 ± 0.3	-
Without span	1119.1 ± 165.3	0.883 ± 0.192	37.0 ± 1.2	-
Without tween	581.7 ± 24.5	0.164 ± 0.052	26.3 ± 1.1	-
Effect of surfactant concentration				
Low (0.25%)	152.2 ± 2.6	0.382 ± 0.024	32.4 ± 0.2	75.28 ± 0.82
Medium (0.5%)	132.4 ± 3.8	0.283 ± 0.015	36.4 ± 0.6	83.62 ± 1.62
High (0.75%)	137.1 ± 0.7	0.281 ± 0.012	28.7 ± 0.4	72.98 ± 1.46
Effect of Miglyol 812 concentration				
Low (15 mg)	146.6 ± 1.7	0.232 ± 0.015	31.2 ± 1.6	71.53 ± 2.93
Medium (20 mg)	132.4 ± 3.8	0.286 ± 0.014	36.4 ± 0.6	83.62 ± 1.62
High (25 mg)	153.5 ± 2.1	0.244 ± 0.004	34.3 ± 0.2	68.41 ± 9.58

*PDI: Polydispersity index

(0.38 ± 0.02) to 132.4 ± 3.8 nm (0.28 ± 0.01) with increased encapsulation efficiency from 75.28 ± 0.82 to 83.62 ± 1.62 %. While the further increase in surfactant ratio decreased encapsulation efficiency to 72.98 ± 1.46% with no further change in particle size and PDI of the developed formulations (**Table 4.1**). While RIV:DHA LPH(-ve) also exhibited a similar

pattern with an increase in surfactant concentration from 0.25 to 0.5 % (w/v), resulted in enhanced encapsulation efficiency from 62.31 ± 4.6 to $88.20 \pm 3.05\%$ with decreased particle size (PDI) from 384.6 ± 10.6 nm (0.408 ± 0.03) to 160.8 ± 0.5 nm (0.25 ± 0.03). The further increase in surfactant concentration decreased encapsulation to 76.59 ± 2.01 % and increased particle size to 231.7 ± 2.0 nm (**Table 4.2**). The increase in particle size and surfactant concentration has also been reported in the literature [4]. The amount of surfactant plays an important role, because it prevents coalescence of oil globules. The surfactant molecules tend to associate themselves at the droplet, thus reducing surface free energy at the interface and the resultant resist coalescence of nanodroplets. Small droplets have greater surface area and thus require more surfactant to stabilize the nanoemulsion [5]. Wherein, less surfactant may lead to the development of an unstable emulsion, indicating that 0.25% may be insufficient to stabilize the nanoemulsion /nanoparticles, leading to phase separation after a few hours. Further, increasing surfactant concentration above 0.5% resulted (at 0.75% w/v) in decreased encapsulation efficiency in both cases; similar results are reported in the literature [5]. RIV:DHA being lipophilic, tends to stay inside the hydrophobic core. Increasing the surfactant concentration in the aqueous phase lead to agglomeration of nanodroplets resulting in increased particle size of RIV:DHA LPH(-ve). Sharma et al. developed a paclitaxel-loaded polymeric PLGA nanoparticle using polyvinyl alcohol as a surfactant [5]. In RIV:DHA LPH(-ve), batches were prepared using selected solid lipids such as Compitrol, Precirol, stearic acid and GMS, keeping all other excipients constant. Batch prepared using GMS demonstrated higher encapsulation efficiency, with a reduced particle size range and narrow polydispersity index compared to other batches (**Table 4.2**). RIV:DHA loaded both LPH formulations from polymer embedded matrix along with solid lipid and liquid lipid, forming a hydrophobic matrix core, forming a less ordered structure with more imperfection, resulting in enhanced stability. The

presence of hydrophobic matrix core, help attain sustained drug release profiles even in the presence of liquid lipid.

Table 4.2. Effect of formulation parameters on characteristics of RIV:DHA LPH(-ve)

Parameters	Particle size (nm)	PDI*	Zeta potential (mV)	% Encapsulation efficiency
LPH(-ve) Compitrol	340.6 ± 2.4	0.23 ± 0.061	-31.6 ± 1.2	80.54 ± 0.42
LPH(-ve) Stearic acid	268.4 ± 3.8	0.28 ± 0.014	-24.0 ± 1.2	72.39 ± 0.44
LPH(-ve) GMS*	160.8 ± 0.5	0.25 ± 0.032	-39.3 ± 1.2	88.20 ± 3.05
LPH(-ve) Precirol	163.7 ± 1.2	0.367 ± 0.121	-1.9 ± 0.2	32.29 ± 0.49
Effect of surfactant concentration (% w/v)				
Low (0.25%)	384.6 ± 10.6	0.408 ± 0.036	-23.4 ± 0.9	62.31 ± 4.60
Medium (0.5%)	160.8 ± 0.5	0.25 ± 0.032	-39.3 ± 1.2	88.20 ± 3.05
High (0.75%)	231.7 ± 2.0	0.259 ± 0.021	-44.8 ± 0.5	76.59 ± 2.01

*PDI: Polydispersity index

LPH formulations showed presence of yellowish milky appearance (**Fig.4.7A and Fig.4.7B**) .

The optimized formulation of RIV:DHA LPH(+ve) showed particle size (PDI), zeta potential of 132.4 ± 3.8 nm (0.284 ± 0.010) and $+36.4 \pm 0.6$ mV (**Fig.4.7C and Fig.4.7D**), with encapsulation efficiency of 83.62 ± 1.62 % (**Table 4.3**). The optimised batch of RIV:DHA LPH(-ve) showed particle size (PDI) 160.8 ± 0.5 nm (0.254 ± 0.031), zeta potential of -39.3 ± 1.2 mV and encapsulation efficiency of 88.20 ± 3.05 % (**Table 4.3, Fig.4.7C and Fig.4.7D**).

Particle size has a crucial role in nasal drug delivery. Size range <1 μ m pass through nasal

cavity whereas, particles $>10 \mu\text{m}$ remain deposited in the front of the nose and exhibit less absorption [68].

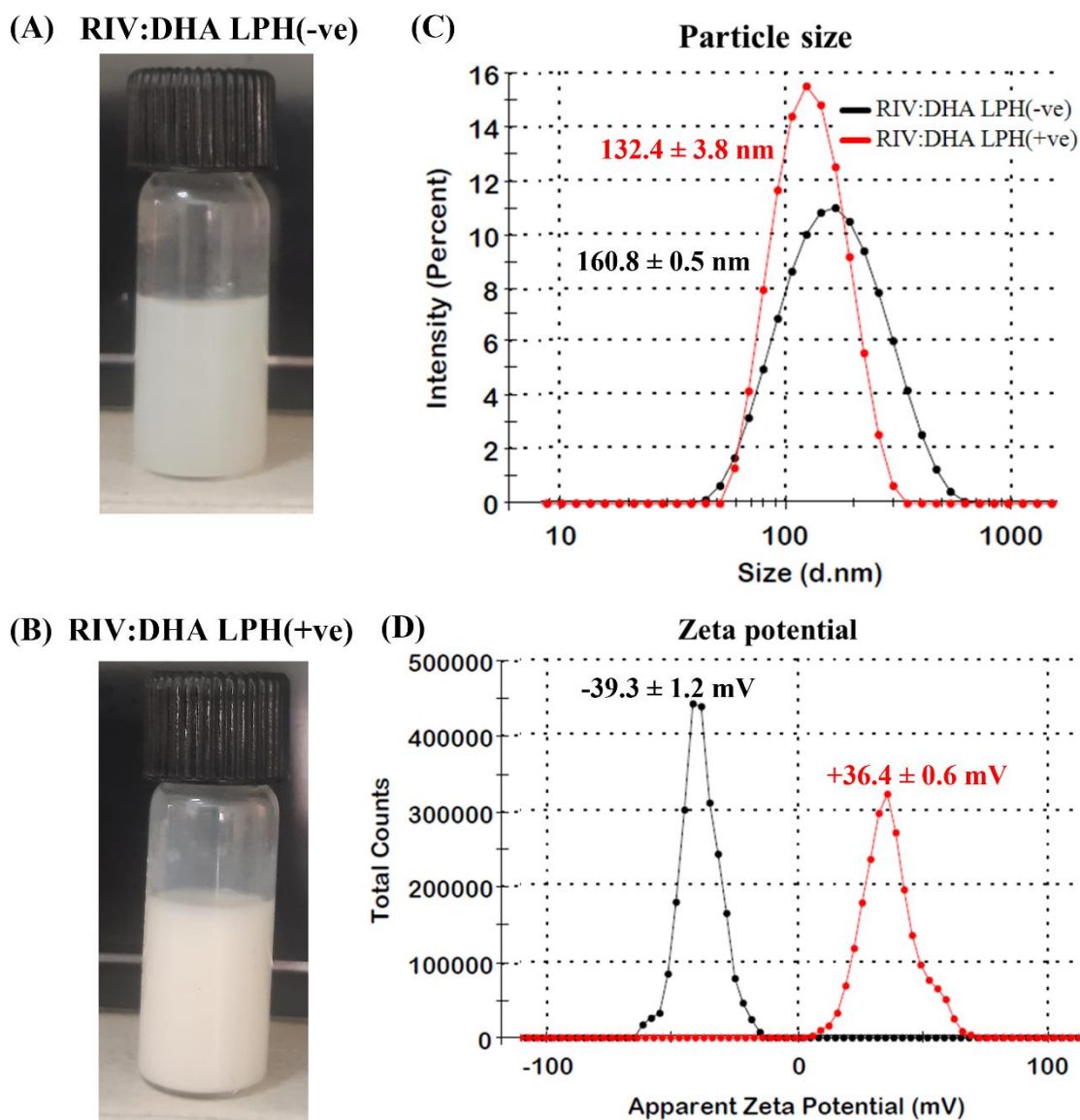


Fig. 4.7. Photographic image represents physical appearance of (A) RIV:DHA LPH(-ve), (B) RIV:DHA LPH(+ve). (C) and (D) represent particle size distribution and zeta potential of RIV:DHA LPH(-ve) and RIV:DHA LPH(+ve) formulation. DHA: docosahexaenoic acid; RIV: Rivastigmine; RIV:DHA: RIV and DHA ion pair complex, LPH: Lipid polymer hybrid nanoparticles

For N2B delivery, particle size less than 200 nm undergo brain targeting through olfactory and trigeminal nerve pathway [69]. Several studies have shown that particle size and surface characteristics of nanoparticles affect amyloid aggregation inhibition.

Loading of pure RIV-HT into RIV:DHA LPH(+ve) and RIV:DHA LPH(-ve) showed a poor encapsulation efficiency of 30.34 ± 1.03 % and 24.34 ± 0.15 %. The RIV:DHA LPH(+ve) showed 2.76-fold increase and RIV:DHA LPH(-ve) showed 3.62-fold increase in encapsulation efficiency after loading with RIV:DHA as compared to loading RIV-HT loaded LPH nanoparticles. The increase was statistically significant ($p < 0.05$) for both RIV:DHA LPH(-ve) and RIV:DHA LPH(+ve) compared to RIV-HT loaded LPH nanoparticles. The earlier study of RIV-HT loaded SLN and NLC showed lower encapsulation efficiency and faster *in-vitro* drug release within 6 h [38]. Further, the LPH nanoparticles loaded with RIV-HT also displayed low drug encapsulation (up to 30%) with complete drug release within 12 h. It can be attributed to the drugs hydrophilic nature, which limits encapsulation into nanoparticles. Therefore, a strategy that can modify the RIV-HT hydrophilic nature to hydrophobic can help in better encapsulation and drug delivery. However, the change must be reversible so that drug therapeutic properties and safety is unchanged. The RIV:DHA provided hydrophobic characteristics that enhanced encapsulation efficiency in LPH nanoparticles.

The LPH overcomes the individual drawbacks of lipidic and polymeric systems. They are highly efficient systems and offer advantages such as high drug-loading capacities, sustained drug release, improved permeation patterns, and colloidal stability. Kalhapure *et al.* developed IPC (berberine/linoleic acid ion pair complex) loaded SLN that showed 23.67% burst release within 2 h, and approximately 75% cumulative drug release upto 24 h [37]. Pandey *et al.* developed ciprofloxacin-based IPC-loaded NLC that showed 40 % burst release at similar intervals with complete drug release upto 10 h. In another study, RIV-HT loaded PLGA nanoparticles showed 50% drug release within 2 h followed by 75% drug release within 6 h

[70]. Chitosan nanoparticles showed more than 60% drug release within 5 h [71]. Whereas, lipidic (SLN, NLC and liposomes) nanoparticles showed complete drug release within 6 h [72,73]. However, for RIV-HT neither polymeric nor lipidic nanoparticles could achieve considerable sustained drug release.

Table 4.3. Characteristics of RIV:DHA LPH nanoparticles. Data is presented as mean \pm SD (n = 3)

Formulation	Particle size (nm)	Polydispersity index	Zeta potential (mV)	Encapsulation efficiency (%)
RIV:DHA LPH(-ve)	160.8 \pm 0.5	0.25 \pm 0.031	-39.3 \pm 1.2	88.20 \pm 3.05
RIV:DHA LPH(+ve)	132.4 \pm 3.8	0.284 \pm 0.010	36.46 \pm 0.6	83.62 \pm 1.62

4.3.5 *In-vitro* amyloid aggregation inhibition using LPH nanoparticles

It was performed to evaluate the pattern of amyloid aggregation inhibition with varying surface charge and LPH concentration (LPH carrying drug concentration 50, 100, 200 and 400 ng/mL) (**Fig.4.8A**). The inhibition was monitored with ThT fluorescence intensity which is proportional to amyloid content in the sample (**Fig.4.8B**). The particle size outcomes were correlated with ThT fluorescence intensity to evaluate the overall inhibition of amyloid beta in presence and absence of LPH nanoparticles (**Fig.4.8B**). The concentration of LPH nanoparticles exhibiting maximum inhibition was further evaluated for microscopy and FTIR-ATR studies (**Fig.4.8C**). Amyloid β_{1-42} in absence of LPH nanoparticles (control) showed a slight increase in ThT fluorescence after 24 h of incubation. Amyloid β_{1-42} showed zeta potential of -20.1 ± 1.0 mV and presence of micron-sized amyloid β_{1-42} (**Fig.4.8D**). It showed presence of long $A\beta_{1-42}$ fibrils and $A\beta_{1-42}$ aggregates with phosphate buffer (**Fig.4.9A**).

Amyloid β_{1-42} treated with RIV:DHA LPH(+ve) showed concentration-dependant inhibition with decreased fluorescence intensity at higher concentrations.

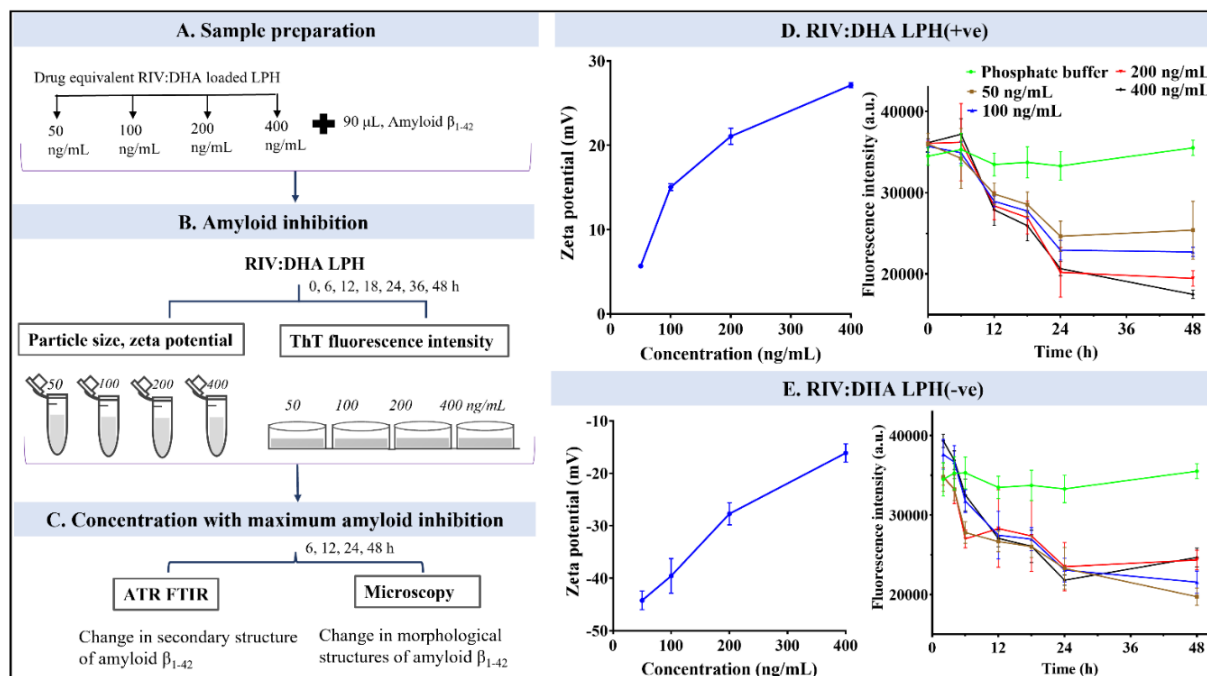


Fig. 4.8. Schematic representation, A) sample preparation of amyloid β_{1-42} treated with drug equivalent varying concentrations (50, 100, 200, 400 ng/mL) of RIV:DHA LPH(+ve) and RIV:DHA LPH(-ve). (B) Represents *in-vitro* amyloid inhibition, evaluating particle size and ThT fluorescence intensity of cationic and anionic LPH nanoparticles at different concentrations (50, 100, 200, 400 ng/mL). (C) Demonstrate the concentration of RIV:DHA LPH(+ve) and RIV:DHA LPH(-ve) with maximum amyloid inhibition was characterized for ATR-FTIR analysis and microscopic observation at 6, 12, 24 and 48 h. The zeta-potential and ThT fluorescence intensity of (D) RIV:DHA LPH(+ve) and (E) RIV:DHA LPH(-ve) at 50, 100, 200 and 400 ng/mL concentration. DHA: docosahexaenoic acid; RIV: Rivastigmine; RIV:DHA: RIV and DHA ion pair complex, LPH: Lipid polymer hybrid nanoparticles

After 6 h of incubation, all concentrations showed no difference in the fluorescence intensity. After 12 h of treatment, the ThT fluorescence intensity demonstrated concentration-dependant inhibition, indicating decreased ThT fluorescence intensity at maximum concentrations (**Fig.4.8A**). 400 ng/mL cationic LPH decreased fluorescence intensity around 20% at 12 h and 40% at 24 h. However, it was lesser at 50 ng/mL concentration, around 15% and 30%. Further

treatment with RIV:DHA LPH(+ve) up to 48 h resulted in no change in fluorescence intensity. This indicates that no further inhibition occurred at 50 ng/mL concentration. The DLS measurement of 50, 100, 200, and 400 ng/mL concentrations at 6 and 12 h exhibited the presence of micron sized, indicating the presence of amyloid fibrils and aggregates (data not shown). Likewise, the treatment of SPIONS with $A\beta_{1-42}$, have shown particles in micron size, indicating the presence of long amyloid fibrils and fibrillary aggregates [40]. At 18, 24, and 48 h, 50 ng/mL and 100 ng/mL concentration (RIV:DHA LPH(+ve)) showed particle size within micron range. This is due to the conversion of large $A\beta_{1-42}$ aggregates into smaller $A\beta_{1-42}$ aggregates and fibrillar structures [74]. Interestingly, 200 and 400 ng/mL RIV:DHA LPH(+ve), exhibited dramatically decreased particle size within 320-580 nm and 150-230 nm (data not shown). This confirms the fact that amyloid inhibition at higher concentrations leads to the conversion of larger fibrils into smaller fibrils and oligomeric structures of nanometric size range [42]. The zeta potential determined for all concentrations of RIV:DHA LPH(+ve), exhibited surface charge of +5.7, +15.0, +21.0 and +27.1 mV, with pattern of increment in surface charge with concentration (**Fig.4.8D**). The inhibitory effect of amyloid inhibition depends on surface charge. The greater surface charge resultant leads to stronger interaction with $A\beta_{1-42}$. The highest concentration of 400 ng/ mL, therefore, exhibited maximum inhibition. The electrostatic interaction occurs between cationic LPH and $A\beta_{1-42}$ carrying -20 mV charge, resulting in LPH-induced aggregation, and conformational transition of $A\beta_{1-42}$ leading to fibrillization inhibition [41]. Further, ATR FTIR and microscopic evaluation (fluorescent and bright field) performed for 400 ng/mL concentration evaluated the change in secondary $A\beta_{1-42}$ structure and $A\beta_{1-42}$ oligomers. The secondary $A\beta_{1-42}$ structures corresponding to $A\beta_{1-42}$ sheets and $A\beta_{1-42}$ oligomers showed FTIR absorption at 1632 cm^{-1} and $1510\text{-}1550\text{ cm}^{-1}$ [42]. The amyloid beta in the absence of LPH (control), exhibited higher absorbance at

1632 cm^{-1} and 1527 cm^{-1} , indicating a higher number of $\text{A}\beta_{1-42}$ fibrils and $\text{A}\beta_{1-42}$ oligomers (Fig.4.9B).

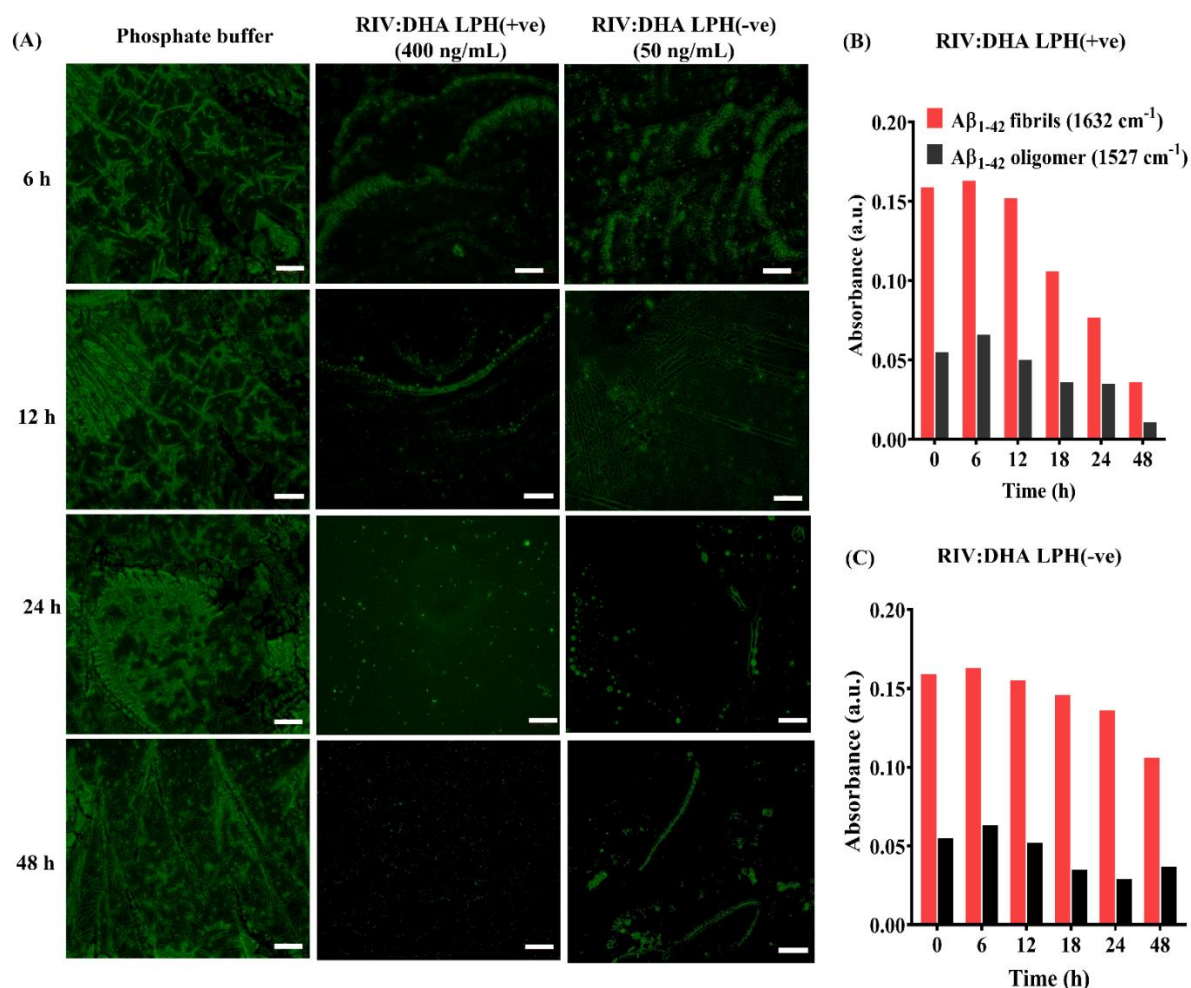


Fig. 4.9. (A) Fluorescent microscopic images of *in-vitro* $\text{A}\beta_{1-42}$ aggregation inhibition in presence and absence of RIV:DHA LPH(+ve) and RIV:DHA LPH(-ve), at various intervals. RIV:DHA LPH(+ve) (400 ng/mL) showed enhanced inhibition in comparison to RIV:DHA LPH(-ve) (50 ng/mL), demonstrating the presence of insoluble amyloid fibrils at 6 h, while that was reduced at 12 h. At 24 and 48 h, it showed the presence of soluble fibrils and soluble amyloid oligomers. Whereas RIV:DHA LPH(-ve) had insoluble amyloid fibrils and oligomer at all intervals of 6, 12, 24, and 48 h, exhibiting lesser and slower inhibition than RIV:DHA LPH(+ve) (magnification: 40x, scale bar: 50 μm). B) and C) represents ATR FTIR spectra of RIV:DHA LPH(+ve) and RIV:DHA LPH(-ve) treated $\text{A}\beta_{1-42}$ exhibiting decreased absorbance at different intervals. RIV:DHA LPH(+ve) showed comparatively reduced $\text{A}\beta_{1-42}$ fibrils and $\text{A}\beta_{1-42}$ oligomers in comparison to RIV:DHA LPH(-ve) at respective interval. DHA:

docosahexaenoic acid; RIV: Rivastigmine; RIV:DHA: RIV and DHA ion pair complex, LPH: Lipid polymer hybrid nanoparticles

Upon treatment with 400ng/mL RIV:DHA LPH(+ve), it showed 33%, 62% and 78% decreased absorbance at 1632 cm^{-1} , indicating decreased $A\beta_{1-42}$ sheets. Also, it resulted in 32%, 35%, and 80% decreased absorbance of $A\beta_{1-42}$ oligomers at 18, 24 and 48 h. (**Fig.4.9B**). Microscopic images of $A\beta_{1-42}$ control group (without LPH) showed presence of insoluble, long fibrillar structure and $A\beta_{1-42}$ aggregates (**Fig.4.9A** and **Fig.4.10**). At 12 h, RIV:DHA LPH(+ve) treated group showed decreased fluorescence intensity and lesser number of insoluble fibrillar structures than control (**Fig.4.9A**, **Fig4.9B** and **Fig.4.10**). Upto 24 h, it exhibited dramatically decreased $A\beta_{1-42}$ size, representing presence of only insoluble spherical structures (**Fig.4.9A** and **Fig.4.10**). At 48 h, RIV:DHA LPH(+ve) showed presence of even smaller, soluble spherical oligomeric structure with diminished fluorescence intensity (**Fig.4.9A**). The RIV:DHA LPH(-ve) showed comparatively reduced and delayed inhibition compared to RIV:DHA LPH(+ve). In RIV:DHA LPH(-ve), maximum inhibition was achieved in presence of lower concentration, whereas inhibition decreased with an increment in LPH concentration. ThT fluorescence of 50ng/mL concentration (RIV:DHA LPH(-ve)) exhibited 33% and 43% amyloid inhibition upto 24 h and 48 h (52 % at 48 h in 400 ng/mL, RIV:DHA LPH(+ve)). An increment in LPH concentration resulted in decreased fluorescent intensity representing 38 %, 30 % and 28 % inhibition at 48 h of treatment with 100, 200 and 400 ng/mL concentrations (**Fig4.8E**). The zeta potential measurements for different concentrations of RIV:DHA LPH(-ve) exhibited surface charge of -44.2, -39.6, -27.5 and -16.1 mV at 50, 100, 200 and 400 ng/mL concentration (**Fig.4.8E**). The amyloid inhibition in RIV:DHA LPH(-ve) is dependent on surface charge. The maximum inhibition was achieved at 50 ng/mL concentration of RIV:DHA LPH(-ve). This is due to lower zeta potential (-44.2 mV), owing to which LPH nanoparticles undergo adhesion onto $A\beta_{1-42}$ oligomer, *via* hydrophobic interaction resulting in $A\beta_{1-42}$

oligomer inhibition. At lower LPH concentration, hydrophobic interaction dominates steric repulsion, while at higher concentration zeta-potential increases, dominating steric repulsion over hydrophobic interaction. The ATR FTIR of 50 ng/mL RIV:DHA LPH(-ve) exhibited 10 %, 15 % and 34 % reduction in $A\beta_{1-42}$ fibrils and 36 %, 48 % and 33 % reduction in $A\beta_{1-42}$ oligomers at 18, 24 and 48 h (**Fig.4.9C**). Microscopic images showed insoluble amyloid fibrils and amyloid oligomer at all intervals (6, 12, 24 and 48 h), revealing lesser inhibition than RIV:DHA LPH(+ve) (**Fig.4.9A and Fig.4.10**).

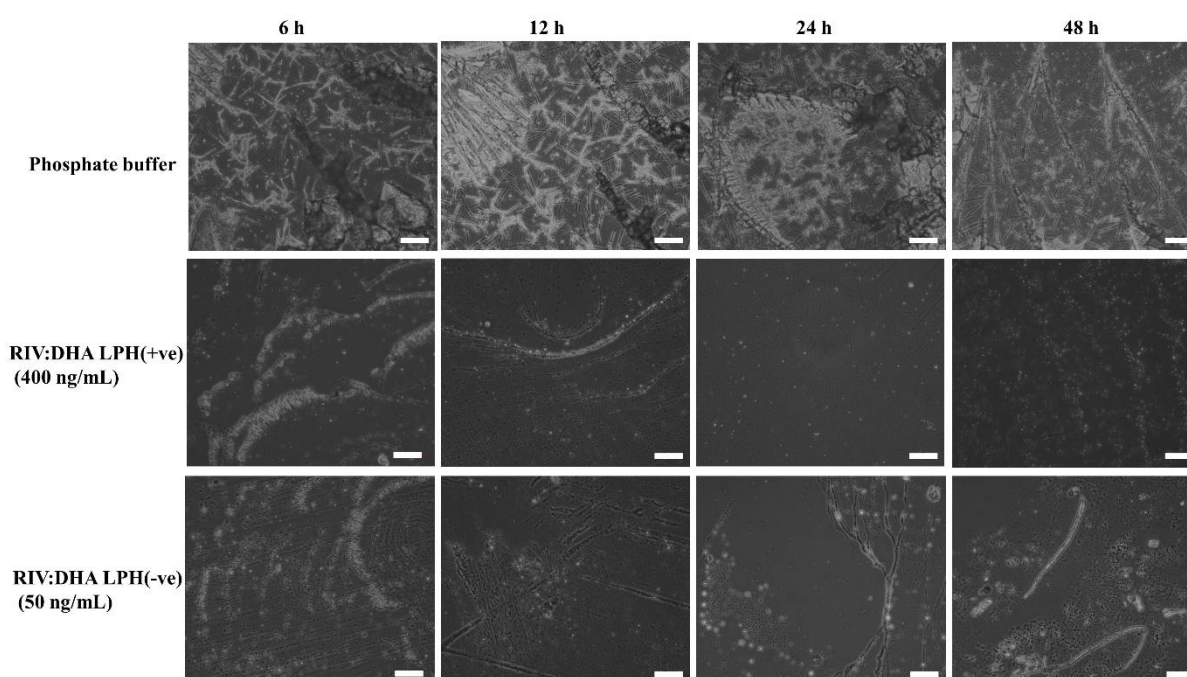


Fig. 4.10. Bright field microscopic images of *in-vitro* amyloid beta inhibition in presence and absence LPH, representing phosphate buffer as control (without LPH) at various time intervals. RIV:DHA LPH(+ve) (400 ng/mL) showed enhanced inhibition in comparison to RIV:DHA LPH(-ve) (50 ng/mL) demonstrating presence of insoluble amyloid fibrils at 6 h, while that has been observed to be significantly reduced at 12 h. At 24 and 48 h, it showed presence of soluble fibrils and soluble amyloid oligomers. Whereas RIV:DHA LPH(-ve) represents presence of insoluble amyloid fibrils and oligomer at all time intervals of 6, 12, 24 and 48 h exhibiting comparatively lesser and slower inhibition in comparison to RIV:DHA LPH(+ve) (magnification: 40x, scale bar: 50 μ m).

4.3.6 Preparation of hydrogel loaded with LPH nanoparticles

Intranasal gels can improve drug absorption residence time in the nasal cavity, thereby increasing brain bioavailability [10,75,76]. As these hydrogels improve drug mucoadhesion and retention in the nasal cavity [7]. Mucosal irritation, ciliotoxicity, epithelial lining damage and allergic response are some of the problems associated with intranasal formulations [9]. These issues can lead to nasal inflammation, affecting normal nasal airway and lung ventilation. Poloxamer 407 and poloxamer 188 based hydrogel are suitable candidates due to their established safety in intranasal delivery. It does not exhibit allergic reactions with no local tissue damage or ciliotoxicity [9]. The poloxamer based hydrogel prepared in this study was transparent with absolute uniformity at the desired temperature (33°C) (Fig.4.11A).

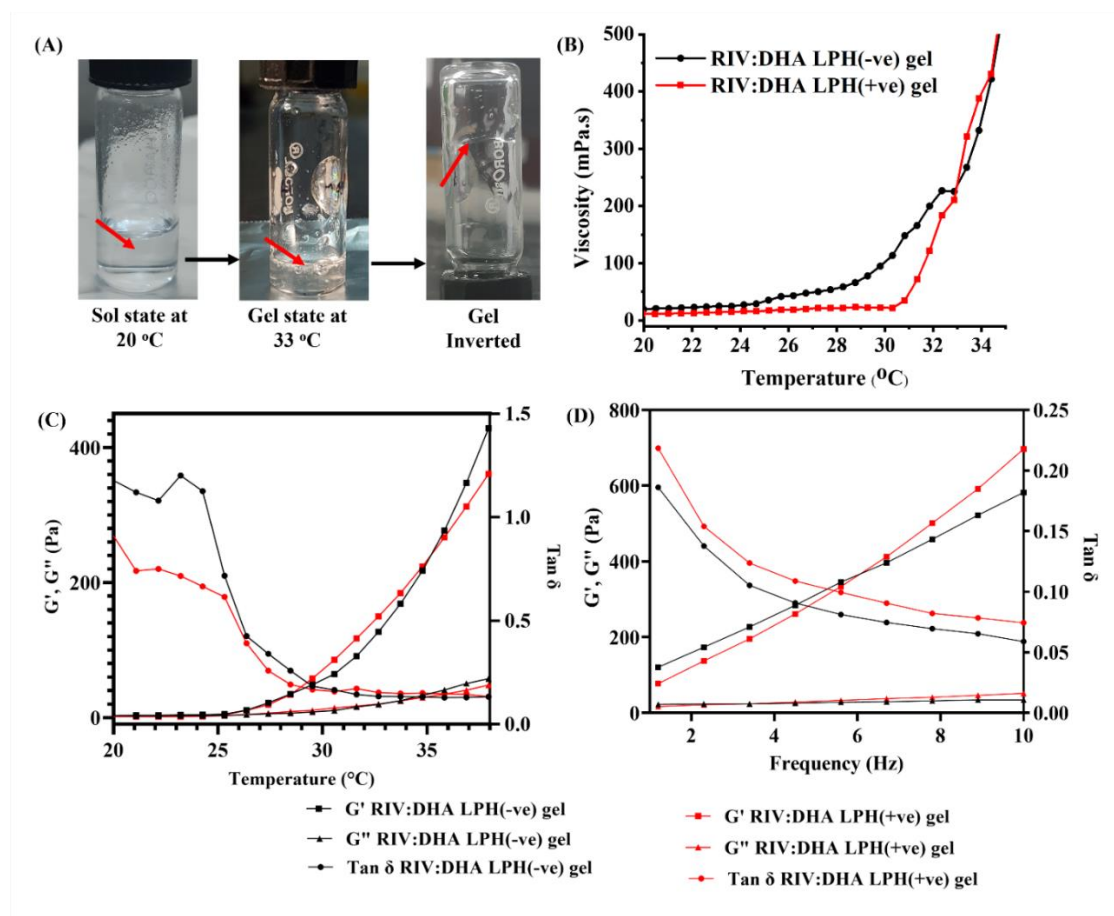


Fig. 4.11. Image (A) represents preliminary testing of sol-to-gel conversion with inversion tube test, (B) Temperature vs viscosity of, RIV:DHA LPH(-ve) gel and RIV:DHA LPH(+ve) gel

representing viscosity at 33° C. Storage modulus and loss modulus of RIV:DHA LPH(-ve) gel and RIV:DHA LPH(+ve) gel representing hydrogel behaviour at different (C) temperature and (D) angular frequency

In this, the concentration of poloxamer 407 played an important role in transitioning hydrogel from sol-to-gel at the desired temperature range. Initially, the blank gel was preliminarily tested using the inversion tube test to confirm the conversion of sol-to-gel state at 33° C (**Fig.4.11A**). Further, the formulation-embedded hydrogel, i.e., RIV-HT, RIV:DHA LPH(-ve) and, RIV:DHA LPH(+ve) containing 1 mg drug in 200 µL hydrogel were prepared for further experiments.

4.3.7 Hydrogel rheological characterization

Rheological studies were performed to evaluate the temperature dependant viscosity and various other viscosity parameters, along with elucidation of gel behavior at different angular frequencies. The LPH-embedded hydrogel was subjected to amplitude and frequency of 0.5% shear strain at 10 rads/s within linear viscoelastic range. The viscosity of RIV:DHA LPH(-ve) gel and RIV:DHA LPH(+ve) gel at 33° C was 267.63 ± 20.13 and 321.12 ± 34.62 mPa.s (**Fig.11B**). The storage modulus (G') and loss modulus (G'') vs temperature (**Fig.4.11C**) showed the presence of gel-like structure at nasal cavity temperature (33° C). The storage modulus and loss modulus at different angular frequencies is shown in **Fig.4.11D**. Samples maintained at 33° C showed $\tan \delta$ less than 1 (**Table 4.4**), demonstrating maintained integrity of gel at all angular frequencies [44].

All the developed nanoformulations were loaded into an *in-situ* hydrogel-based system, in which poloxamer 407, was crucial in forming gel at nasal cavity temperature. Rheological studies of all formulation loaded hydrogel evaluated viscosity and gel strength at predetermined temperature. At 20° C temperature, hydrogel remains in sol state, where the ability of polymer chains to disentangle and flow is greater, this leads to $G'' > G'$. In gelled state at 33° C

temperature, the entanglement in polymer chains leads to an increased G' (gel strength) above G'' , exhibiting typical gel-like characteristics (**Fig.4.11C**) [44]. The phase angle ($\tan \delta = G'' / G'$), is a measure of viscous components of a hydrogel. Hydrogel maintained at temperature 20°C exhibited phase angle >1 , reflecting a liquid-like response. As $\tan \delta$ decreases, the gel like characteristics improves, where the $\tan \delta$ less than 1 demonstrates, gel like response. In case of, RIV:DHA LPH(-ve) and RIV:DHA LPH(+ve) loaded hydrogels $\tan \delta$ was <1 , when temperature maintained at 33°C [45]. Both formulations were independent of frequency threshold, exhibiting gel-like characteristics, with $\tan \delta$ less than 1 within all frequency range (1-10 Hz) (**Table 4.4**). Such formulations could be referred as cross-linked gels that are not influenced by the oscillatory frequency and withstand greater elasticity that could be required for the retention of hydrogels in the nasal cavity [44].

Table 4.4. RIV:DHA LPH loaded gels representing viscosity, storage modulus and $\tan \delta$ at different oscillatory frequencies Viscosity of RIV:DHA LPH loaded gels (at 20°C and 33°C) and storage modulus at 33°C

Formulation	Viscosity (mPa·s) \pm SD		Storage modulus, G' (Pa) \pm SD at 33°C
	At	At	
	20°C	33°C	
RIV:DHA LPH(-ve) gel	17.98 ± 2.51	267.63 ± 20.13	158.07 ± 10.55
RIV:DHA LPH(+ve) gel	15.33 ± 4.15	321.12 ± 34.62	177.95 ± 5.92

4.3.7.1 Scanning electron microscopy

FE-SEM images of RIV-HT (**Fig.4.12A**) indicated the difference in physical appearance after formation of RIV:DHA (**Fig.4.12B**), RIV:DHA LPH(-ve) (**Fig.4.12C**) and RIV:DHA

LPH(+ve) (**Fig.4.12E**) indicated the formation of spherical shaped nanoparticles. Nanoformulation, when incorporated into a hydrogel may form aggregates that could impact the overall therapeutic efficacy. The FE-SEM analysis of RIV:DHA LPH(-ve) gel (**Fig.4.12D**) and RIV:DHA LPH(+ve) gel (**Fig.4.12F**) showed presence of intact spherical nanoparticles with no signs of aggregation after loading it into a hydrogel.

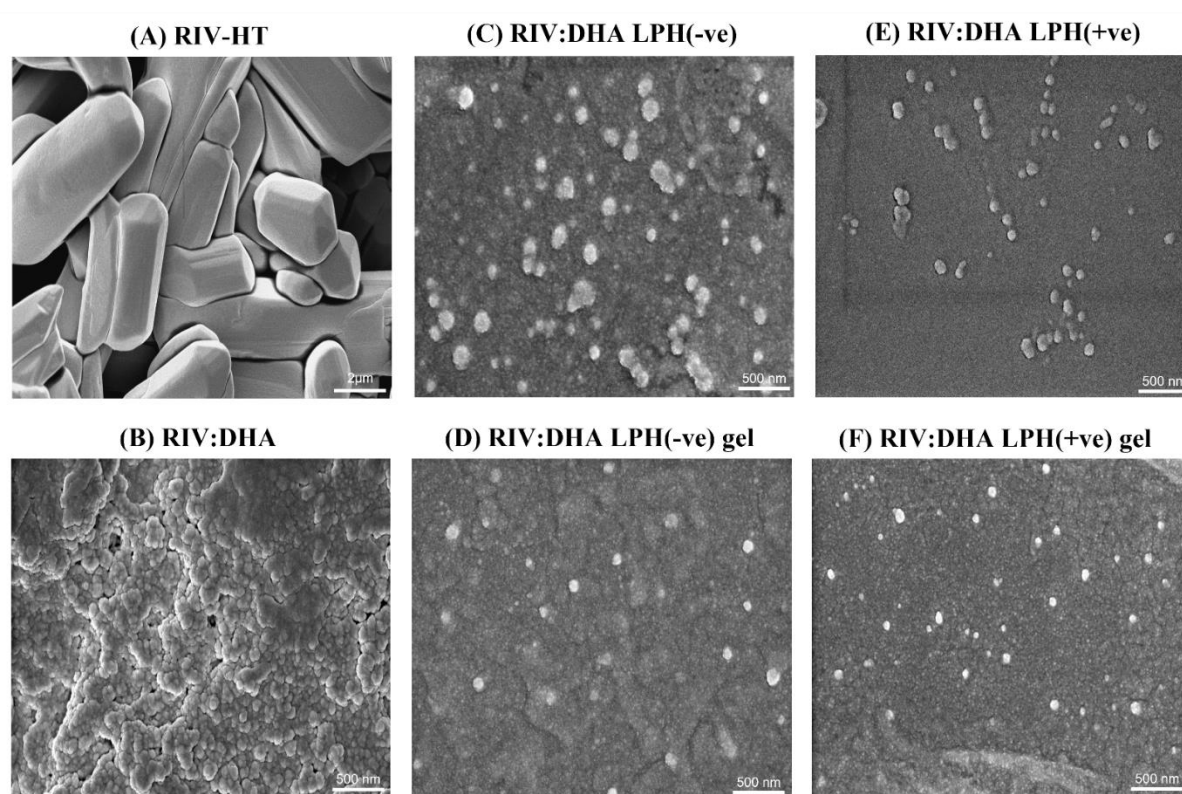


Fig. 4.12. FE-SEM micrograph of (A) RIV-HT (Magnification: 30000X, scale bar: 2µm), (B) RIV:DHA (1:1 molar ratio) (C) RIV:DHA LPH(-ve) (D) RIV:DHA LPH(-ve) gel, (E) RIV:DHA LPH(+ve) and (F) RIV:DHA LPH(+ve) gel (Magnification: 100000X, scale bar: 500nm)

4.3.7.2 Fourier transform infra-red analysis

FTIR studies were performed to evaluate the encapsulation of RIV:DHA into LPH nanoparticles. For this, RIV:DHA LPH were compared with their respective blank and hydrogel-loaded formulations. In case of RIV:DHA LPH(-ve) and RIV:DHA LPH(-ve) gel, the characteristic spectra of RIV:DHA (particularly peaks at 1503 cm^{-1}) disappeared, this might be due to the encapsulation of RIV:DHA into LPH (Fig.4.13). The intensity of respective peaks in RIV:DHA LPH(-ve) was shorter and slightly broadened than blank LPH(-ve).

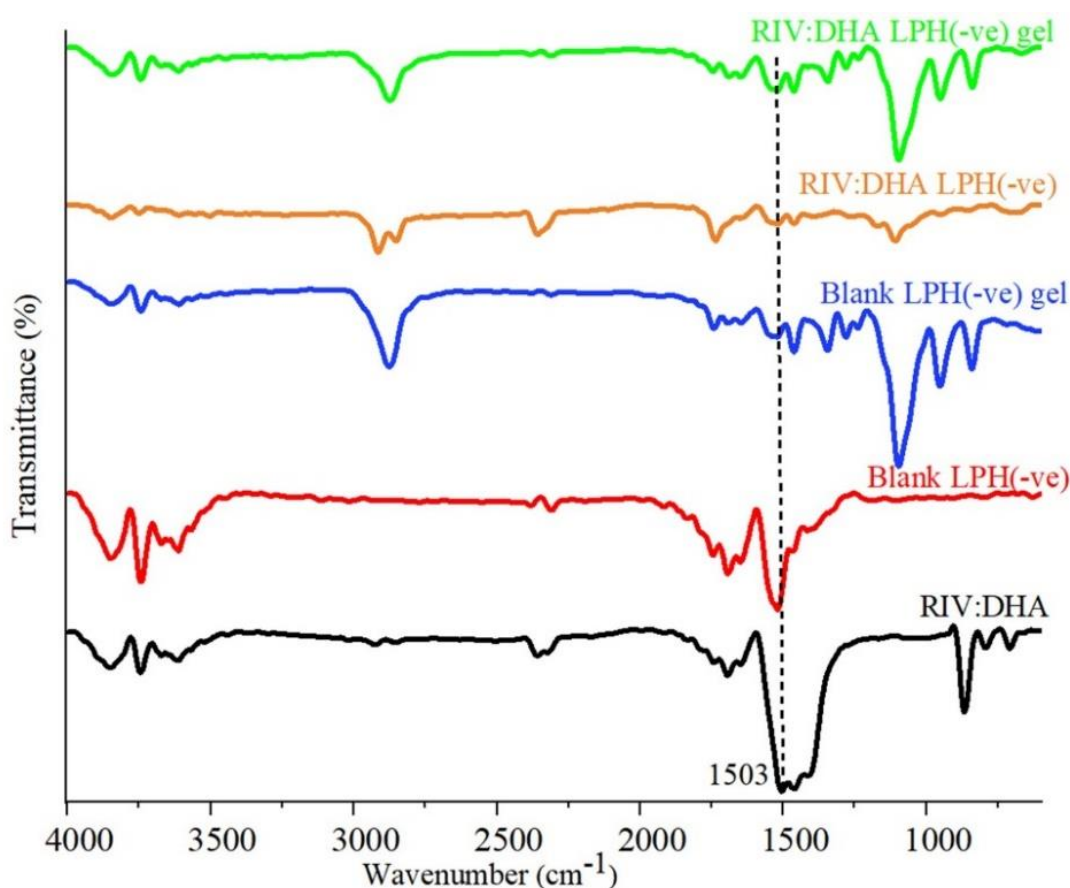


Fig. 4.13. FTIR spectra of RIV:DHA (1:1 molar ratio), blank LPH(-ve), blank LPH(-ve) gel, RIV:DHA LPH(-ve) and RIV:DHA LPH(-ve) gel to evaluate encapsulation of RIV:DHA into LPH based nanoformulation

It also led to slight peak shifting of RIV:DHA LPH(-ve), which might be attributed to the interaction of RIV:DHA with nanoparticle components in the encapsulated form. The

comparison of blank LPH(-ve) gel and RIV:DHA LPH(-ve) gel spectra showed slight shifting of peaks with decreased intensities in comparison to blank LPH(-ve) and RIV:DHA LPH(-ve), respectively. It is due to the interaction of hydrogel components with LPH nanoparticles. Similar observations were recorded in blank LPH(+ve) and RIV:DHA LPH(+ve) compared to respective gel-loaded formulations.

In RIV:DHA LPH(+ve) and RIV:DHA LPH(+ve) gel, the characteristic peak of RIV:DHA also disappeared, which can be attributed to the encapsulation in LPH nanoparticles (**Fig.4.14**). The intensity of RIV:DHA LPH(+ve) and blank LPH(+ve) was higher than RIV:DHA LPH(+ve) gel and blank LPH(+ve) gel, may be due to higher feed ratio in nanoparticles or may be due to interaction of hydrogel components with nanoparticles.

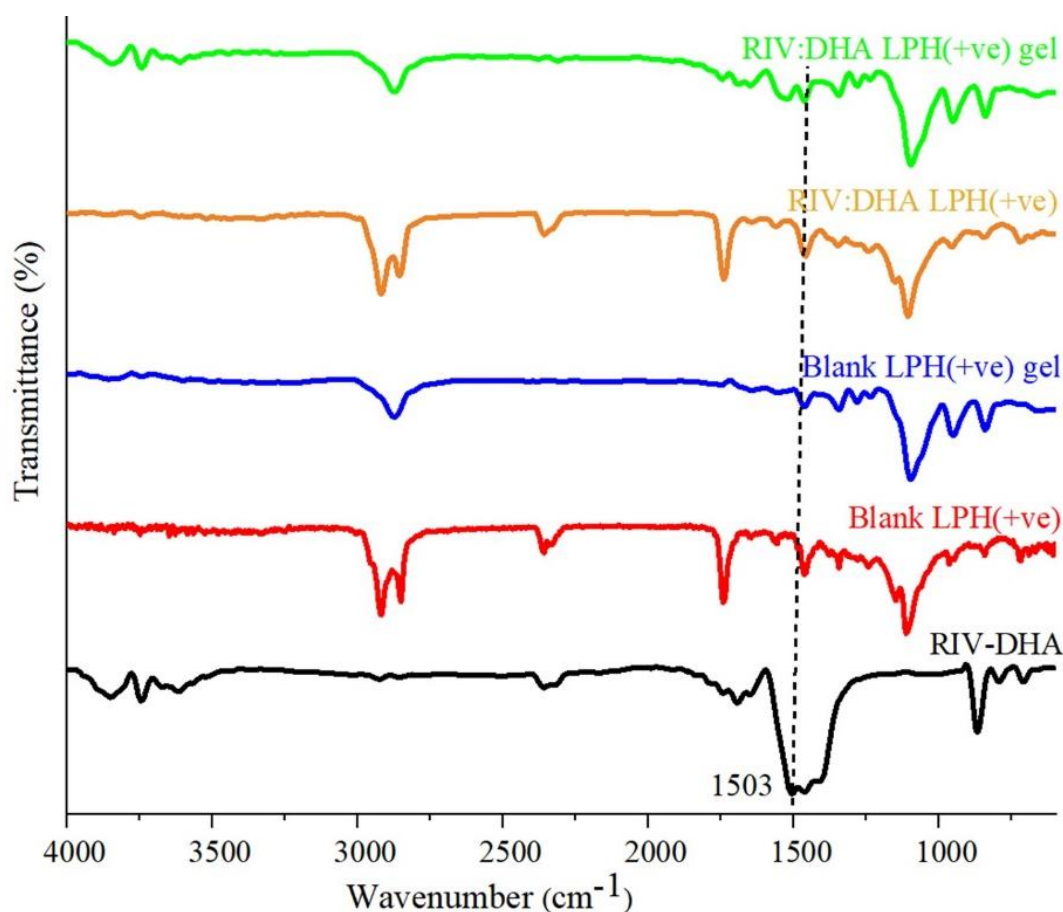


Fig. 4.14. FTIR spectra of RIV:DHA (1:1 molar ratio), blank LPH(+ve), blank LPH(+ve) gel, RIV:DHA LPH(+ve) and RIV:DHA LPH(+ve) gel to evaluate encapsulation of RIV:DHA into LPH based nanoformulation

4.3.8 Stability study

The stability of RIV:DHA LPH(-ve) gel and RIV:DHA LPH(+ve) gel was evaluated at storage conditions. The increased particle size, PDI and change in zeta-potential indicate nanoparticle aggregation and instability. RIV:DHA LPH(-ve) gel (**Fig.4.15A**) and RIV:DHA LPH(+ve) gel (**Fig.4.15B**) exhibited no significant increase in particle size, PDI and zeta potential upto 180 days. Thus, formulations were stable for at least 6 months at the storage conditions. The stable formulation can be collectively attributed to the small nanoparticle size, low PDI, enough zeta potential, and optimum gel rheology.

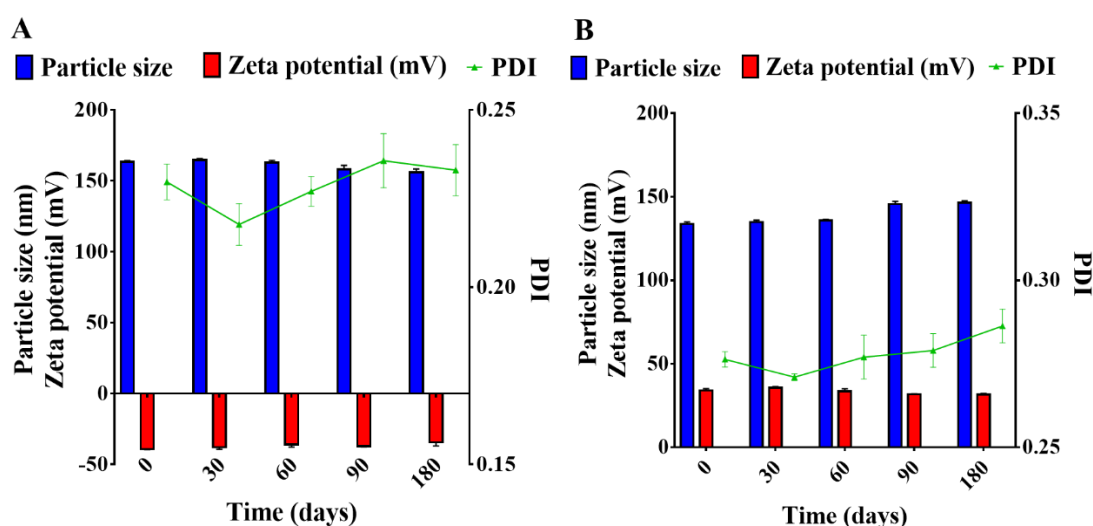


Fig. 4.15. Image represents stability indicating graph of (A) RIV:DHA LPH(-ve) gel and (B) RIV:DHA LPH(+ve) gel evaluated on particle size (nm), PDI, zeta potential (mV) vs time (days). The graph represented no significant increase in particle size, PDI, of nanoparticles upto 180 days, representing stability of formulation upto 6 months.

4.3.9 *In-vitro* drug release of RIV from hydrogel

The development of RIV:DHA gel provides sustained release of drug upto 24 h in comparison to pure RIV-HT gel demonstrating complete drug release within 4 h (**Fig.4.16A**). The development of RIV:DHA loaded LPH gel systems further sustained the drug release upto 72 h. There was no burst effect observed in both LPH formulations. The RIV:DHA LPH(-ve) gel

and RIV:DHA LPH(+ve) gel showed 44.98 ± 1.78 and 17.74 ± 0.59 % drug release upto 24 h. T25, T50 and T75 for RIV:DHA LPH(-ve) gel and RIV:DHA LPH(+ve) gel were found to be 12.71, 28.06, 44.60 h and 29.15, 46.91, 61.98 h respectively. The drug release rate constant (k) for RIV:DHA LPH(-ve) and RIV:DHA LPH(+ve) was found to be 2.70 and 0.18 h^{-1} (Table 4.5). *In-vitro* release profiles of RIV:DHA LPH(-ve) gel and RIV:DHA LPH(+ve) gel, when compared with RIV-HT gel, demonstrated f1 and f2 as 15.56, 14.85, and 97.00, 99.43 respectively (Table 4.5). Thus, the drug release profiles of pure RIV-HT gel, RIV:DHA LPH(-ve) gel and RIV:DHA LPH(+ve) gel have substantial dissimilarity (Fig.4.16A).

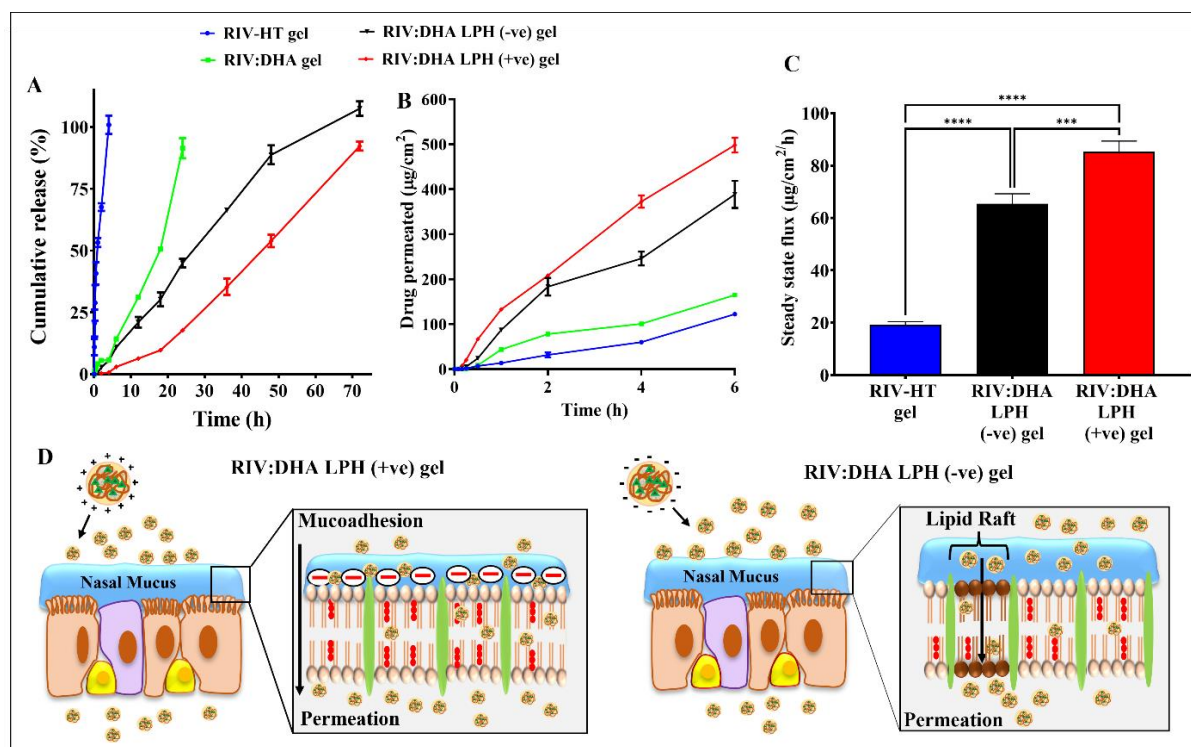


Fig. 4.16. (A) *In-vitro* cumulative drug release representing sustained RIV release from RIV:DHA LPH gel upto 72 h. (B) *Ex-vivo* permeation study representing improved drug permeation efficiency of RIV:DHA LPH across nasal epithelium. (C) Steady-state flux of RIV:DHA LPH gels and RIV-HT gel. (D) Schematic showing mechanism for improved drug permeation of LPH nanoparticle across the nasal epithelium.

Drug release data were fitted into kinetic release models, including zero order, first order, Higuchi, Korsmeyer-Peppas and Hixson-Crowell. The LPH nanoparticles loaded gel followed

Korsmeyer-Peppas model. The ‘n’ value obtained from Korsmeyer-Peppas model indicated that RIV:DHA LPH(-ve) showed ($R^2=0.9893$) ($n=0.87$) anomalous transport and RIV:DHA LPH(+ve) ($R^2=0.9983$) ($n=1.45$) showed super case II transport [77].

The *in-vitro* release studies of both LPH formulations exhibited slow and sustained drug release due to RIV:DHA and LPH-based systems. The encapsulation hydrophobic RIV:DHA in nanoparticles did not show burst effect in *in-vitro* release studies for both formulations. The *in-vitro* release studies of RIV:DHA LPH(+ve) showed comparatively slower release than RIV:DHA LPH(-ve). This is attributed to PEGylation with PEG-32-stearate that forms hydrophilic surfaces, allowing comparatively faster drug release. The *in-vitro* release studies of free drug-loaded hydrogel exhibit complete drug release within 4 h wherein, both LPH-loaded hydrogels showed slow and sustained release profiles upto 72 h.

Table 4.5. Kinetic parameters of RIV release from RIV:DHA based nanoformulations

Formulation	Release model		Release rate	In-vitro release comparison	
	Model type	n	constant, k (h ⁻¹)	Difference factor (f1)	Similarity factor (f2)
RIV:DHA LPH(-ve) gel	Korsmeyer- Peppas	0.875	2.7	97.0	15.05
RIV:DHA LPH(+ve) gel	Korsmeyer- Peppas	1.475	0.184	99.43	14.85

4.3.10 *Ex-vivo* nasal permeation of RIV from hydrogel

It was performed to evaluate the nasal permeation behaviour of formulations. The amount of drug permeated for RIV:DHA gel was higher than RIV-HT gel. The RIV:DHA gel showed enhanced drug diffusion upto $164.85 \pm 1.97 \mu\text{g}/\text{cm}^2$ than pure drug-loaded gel ($122.32 \pm 2.55 \mu\text{g}/\text{cm}^2$) (**Fig.4.16B**). RIV-HT leads to limited permeation across lipophilic nasal barriers due

to its hydrophilic nature. Whereas RIV:DHA LPH(-ve) gel and RIV:DHA LPH(+ve) gel showed $388.63 \pm 30.45 \mu\text{g}/\text{cm}^2$ and $498.12 \pm 16.32 \mu\text{g}/\text{cm}^2$ drug permeation, resulting in 3.18-fold and 4.07-fold enhanced permeation across the nasal membrane. Flux ($\mu\text{g}/\text{cm}^2/\text{h}$) and permeability coefficient (cm/h) were calculated from permeation profiles (**Fig.4.16C** and **Table 4.6**).

The higher permeation for RIV:DHA LPH(+ve) gel was due to the cationic charge that promotes interaction with anionic moieties of the nasal mucosa (**Fig.4.16D**) [78,79]. The improved permeation of RIV from RIV:DHA LPH(-ve) gel is due to negatively charged LPH that interacts with sterols and sphingolipids, resulting in enhanced permeation through lipid raft mediated transport (**Fig.4.16D**) [16].

Table 4.6. Permeation kinetics of RIV:DHA LPH loaded hydrogel.

Formulation	Kinetic model	Steady state flux ($\mu\text{g}/\text{cm}^2 \text{h}^{-1}$)	Amount permeated ($\mu\text{g}/\text{cm}^2$)	Permeability Coefficient (cm/h)
RIV:DHA LPH(-ve) gel	Hixon Crowell	65.38 ± 3.87	388.63 ± 30.45	0.39 ± 0.03
RIV:DHA LPH(+ve) gel	Hixon Crowell	85.30 ± 4.04	498.12 ± 16.32	0.51 ± 0.03

Data is expressed as mean \pm SD (n = 3)

4.3.11 *In-vivo* study in rats

4.3.11.1 Mucociliary clearance time

Intranasal administration as an *in-situ* gelling system delays innate mucociliary drug clearance, improving drug retention and absorption from the nasal cavity. The mucociliary time was 16.75 ± 3.41 min for RIV-HT gel, 24.22 ± 2.5 for RIV:DHA LPH(-ve) gel, and 33.23 ± 3.07 min for

RIV:DHA LPH(+ve) gel (**Fig.4.17A**). The drug mucociliary clearance for LPH nanoparticle gel was significantly delayed compared to RIV-HT gel ($p < 0.05$). This could be attributed to gel viscosity providing mucoadhesion, LPH nanoparticles delaying drug release, and RIV:DHA IPC that also control drug release. Collectively these factors restrict rapid drug mucociliary clearance, unlike in free drug or free drug gel where drug clearance is high. Amongst LPH nanoparticles, RIV:DHA LPH(+ve) gel exhibited substantially delayed ($p < 0.05$) drug mucociliary clearance time in comparison to RIV:DHA LPH(-ve) gel. The cationic surface charge of LPH nanoparticles could facilitate mucoadhesion due to electrostatic interaction, thereby delaying mucociliary drug clearance [10].

4.3.11.2 Pharmacokinetic study in rats

PK study evaluated brain targeting efficiency of intranasally administered RIV:DHA LPH(-ve) gel, RIV:DHA LPH(+ve) gel comparing RIV-HT gel. The brain drug profile, plasma drug profiles, and PK parameters elucidated N2B transport efficiency of LPH nanoparticles (**Fig.4.17B and Fig.4.17C**). In brain, the LPH nanoparticles significantly improved C_{max} by 1.99-fold with RIV:DHA LPH(-ve) gel and 2.37-fold with RIV:DHA LPH(+ve) gel. Further, both LPH gels showed higher brain concentrations at all time points than RIV-HT gel. In comparison to RIV-HT gel, brain PK showed 5.63-fold higher MRT for RIV:DHA LPH(-ve) gel and 9.26-fold higher MRT for RIV:DHA LPH(+ve) gel. While brain AUC_{0-t} increased 5.18-fold for RIV:DHA LPH(-ve) gel and 7.67-fold for RIV:DHA LPH(+ve) gel. The DTE (%) was significantly different ($p < 0.05$) in order of RIV-HT gel (281.28 %) < RIV:DHA LPH(-ve) gel (672.26 %) < RIV:DHA LPH(+ve) gel (792.47 %). The DTP (%) were also significantly different ($p < 0.05$) in order of RIV-HT gel (64.44 %) < RIV:DHA LPH(-ve) gel (85.12 %) < RIV:DHA LPH(+ve) gel (87.38 %) (**Table 4.7**).

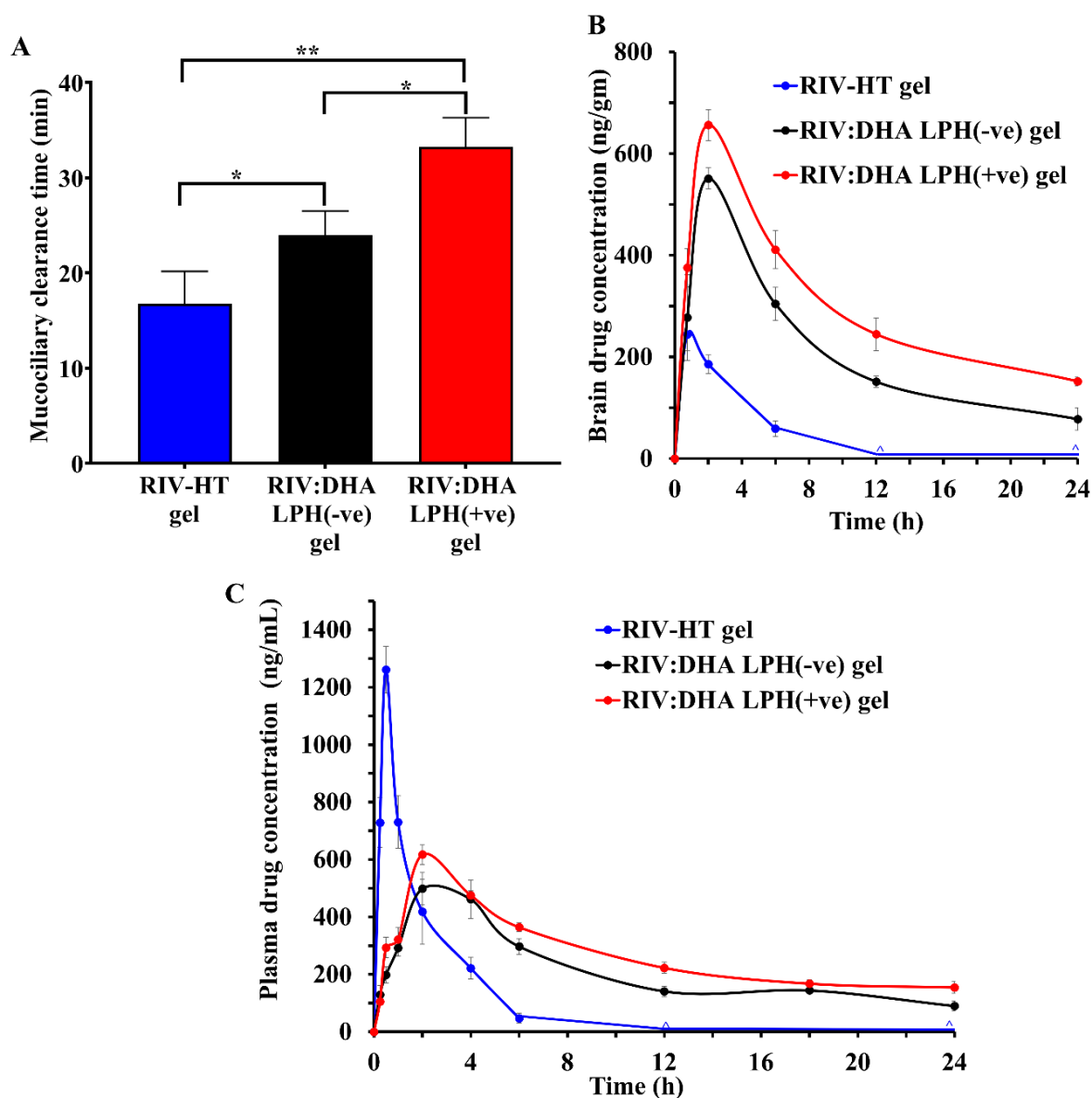


Fig. 4.17. *In-vivo* studies of RIV:DHA LPH(-ve) gel, RIV:DHA LPH(+ve) gel and RIV-HT gel (2 mg/kg) showed (A) significantly increased mucociliary clearance time of RIV:DHA LPH(+ve) gel (* signify $p < 0.05$, ** represents $p < 0.005$). (B) Brain profile of RIV formulations demonstrate significantly improved brain concentrations and mean residence time of RIV in RIV:DHA LPH(+ve) gel. (C) Represents plasma profile of RIV formulations in which RIV gel showed distinctly higher plasma concentrations, while RIV:DHA LPH(-ve) gel and RIV:DHA LPH(+ve) gel showed comparatively reduced plasma concentration of RIV. ‘^’ show data points which were analysed but could not be quantified as these were below quantifiable limit.

The improved DTE (%), DTP (%) confirms the efficient brain targeting of LPH nanoparticles compared to RIV-HT gel. This reveals that LPH nanoparticles undergo major drug transport through direct N2B delivery, *via*. olfactory and trigeminal nerve mediated pathways [80]. The improved drug concentrations in the brain and other pharmacokinetics parameters are due to collective factors. These factors include mucoadhesion, controlled drug release, low drug mucociliary clearance, LPH nano size and better N2B transport of LPH nanoparticles. The nanoparticles below 200 nm facilitate direct N2B drug transport through the olfactory pathway [38,81,82]. The hydrophobic characteristics of nanoparticles also increase drug permeation, brain concentrations and N2B targeting efficiency [83]. The brain PK profile of RIV:DHA LPH(-ve) gel, RIV:DHA LPH(+ve) gel and RIV-HT gel at respective time points (0.75, 2, 6, 12 and 24 h) is shown in **Fig.4.18** (with statistical comparison for each time point). For RIV-HT gel, the C_{max} was achieved within 0.75 h. In contrast, at 0.75 h though brain C_{max} was not achieved for RIV:DHA LPH(-ve) gel, it showed higher brain concentration than RIV-HT gel. The LPH nanoparticles achieved C_{max} at 2 h, and brain concentrations were much higher than RIV-HT gel ($p < 0.05$). The RIV:DHA LPH(+ve) gel showed distinctly higher C_{max} concentrations than RIV:DHA LPH(-ve) gel. At 6 h, RIV-HT gel showed lower brain concentration near to drug quantitation limit (58.86 ± 15.72 ng/g), while it was much higher for LPH nanoparticles (304.04 ± 32.59 ng/g for anionic LPH and 411 ± 37.17 ng/g for cationic LPH). At 12 h, RIV-HT gel drug brain concentration was completely diminished either due to drug elimination or below the quantifiable limit. Whereas LPH nanoparticles still had much higher brain concentrations at 12 h (151.39 ± 11.70 ng/g for anionic LPH and 244.80 ± 31.76 ng/g for cationic LPH) and 24 h (77.72 ± 22.04 ng/g for anionic LPH and 152.02 ± 8.43 ng/g for cationic LPH). RIV:DHA LPH(+ve) gel had distinctly higher brain concentration at all-time points than RIV:DHA LPH(-ve) gel ($p < 0.05$), except at 0.75 h. RIV:DHA LPH(+ve) gel showed significantly higher C_{max} , MRT and AUC_{0-t} than RIV:DHA LPH(-ve) gel.

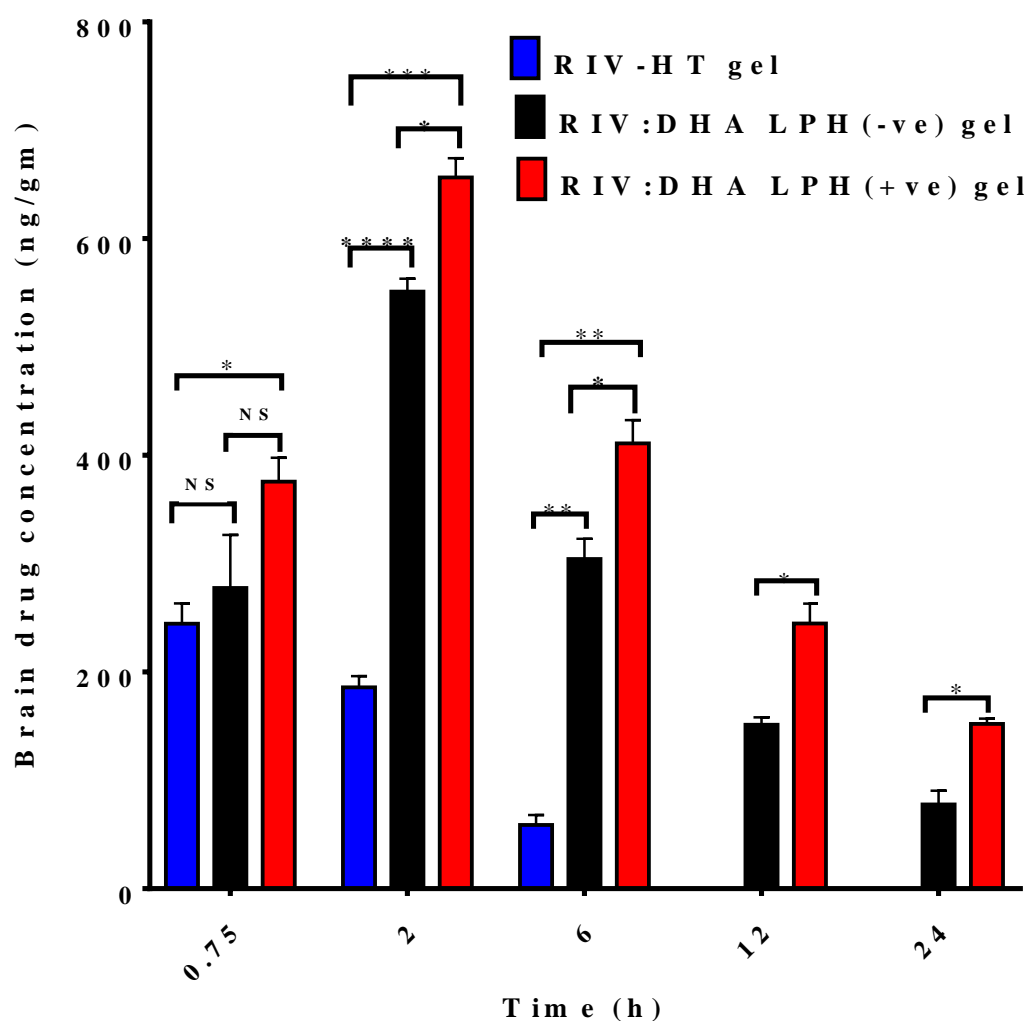


Fig. 4.18. *In-vivo* study demonstrate comparative evaluation of RIV formulations in brain at 0.75, 2, 6, 12 and 24 h. RIV:DHA LPH(+ve) gel demonstrated distinctly improved brain concentrations at all time points as compared to RIV:DHA LPH(-ve) gel and RIV-HT gel (* signify $p < 0.05$, ** represents $p < 0.005$, *** represents $p < 0.001$, **** represents $p < 0.0001$ and NS signify no significant difference).

The RIV:DHA LPH(+ve) gel resulted in 2.13-fold higher half-life and 1.64-fold higher MRT than RIV:DHA LPH(-ve) gel. The higher C_{max} , half-life, MRT and AUC_{0-t} of cationic LPH gel than anionic LPH gel showed better N2B targeting of cationic LPH, which is also confirmed with higher DTE (%) and DTP (%). The olfactory pathway takes 1.5-6 h for nanoparticles to reach the brain, while the trigeminal nerve pathway takes 17-56 h [16]. In a study, the negatively charged PLGA nanoparticles were transported through the olfactory pathway,

whereas chitosan-coated PLGA nanoparticles with positive charge were transported through the trigeminal nerve pathway [22]. The higher C_{max} , half-life, MRT and AUC_{0-t} showed better N2B targeting of cationic LPH gel than anionic LPH gel. The higher DTE (%) and DTP (%) of cationic LPH also confirmed better brain targeting than anionic LPH gel. The improved N2B drug uptake could reduce systemic exposure and associated side effects. Overall, the optimized LPH nanoparticles address the associated drawbacks of oral therapy and intranasal delivery of RIV-HT. Since the drug remains in the brain for up to 24 h when administered as intranasal RIV:DHA LPH(+ve) gel, it may reduce the frequency of dose administration.

Table 4.7 Brain and plasma PK parameters after intranasal administration of RIV-HT gel, RIV:DHA LPH(+ve) gel and RIV:DHA LPH(-ve) gel

Matrix	PK parameters	RIV-HT gel	RIV:DHA LPH(-ve) gel	RIV:DHA LPH(+ve) gel
Brain	C_{max} (ng/g)	277.38 ± 0.20	551.17 ± 159.60	656.50 ± 30.77
	T_{max} (h)	0.66 ± 0.08	2.00	2.00
	$T_{1/2}$ (h)	1.32 ± 0.26	7.34 ± 0.74	15.67 ± 1.65
	MRT (h)	2.02 ± 0.45	11.38 ± 0.46	18.71 ± 0.74
	AUC_{0-t} (ng/g*h)	934.91 ± 49.86	4840.54 ± 192.48	7175.35 ± 185.07
Plasma	C_{max} (ng/mL)	1261.21 ± 80.83	517.06 ± 58.83	628.04 ± 35.21
	T_{max} (h)	0.50	2.66 ± 0.66	2.00
	$T_{1/2}$ (h)	1.28 ± 0.09	14.60 ± 1.75	16.81 ± 1.10
	MRT (h)	1.94 ± 0.16	19.15 ± 1.23	22.79 ± 1.21
	AUC_{0-t} (ng/ml*h)	2363.14 ± 358.88	5119.45 ± 557.95	6437.65 ± 366.64
-	DTE (%)	281.28	672.26	792.47
-	DTP (%)	64.44	85.12	87.38

Data is expressed as mean ± standard error of mean (n = 3)

4.3.12 Histopathological study

The histological sections of the formulation-treated group showed intact morphological structures of nasal epithelium and brain, like in the control group. The brain specimens showed typical morphological structures with no histological alterations in neuronal cells, cerebral cortex, hippocampus and striatum (Fig.4.19).

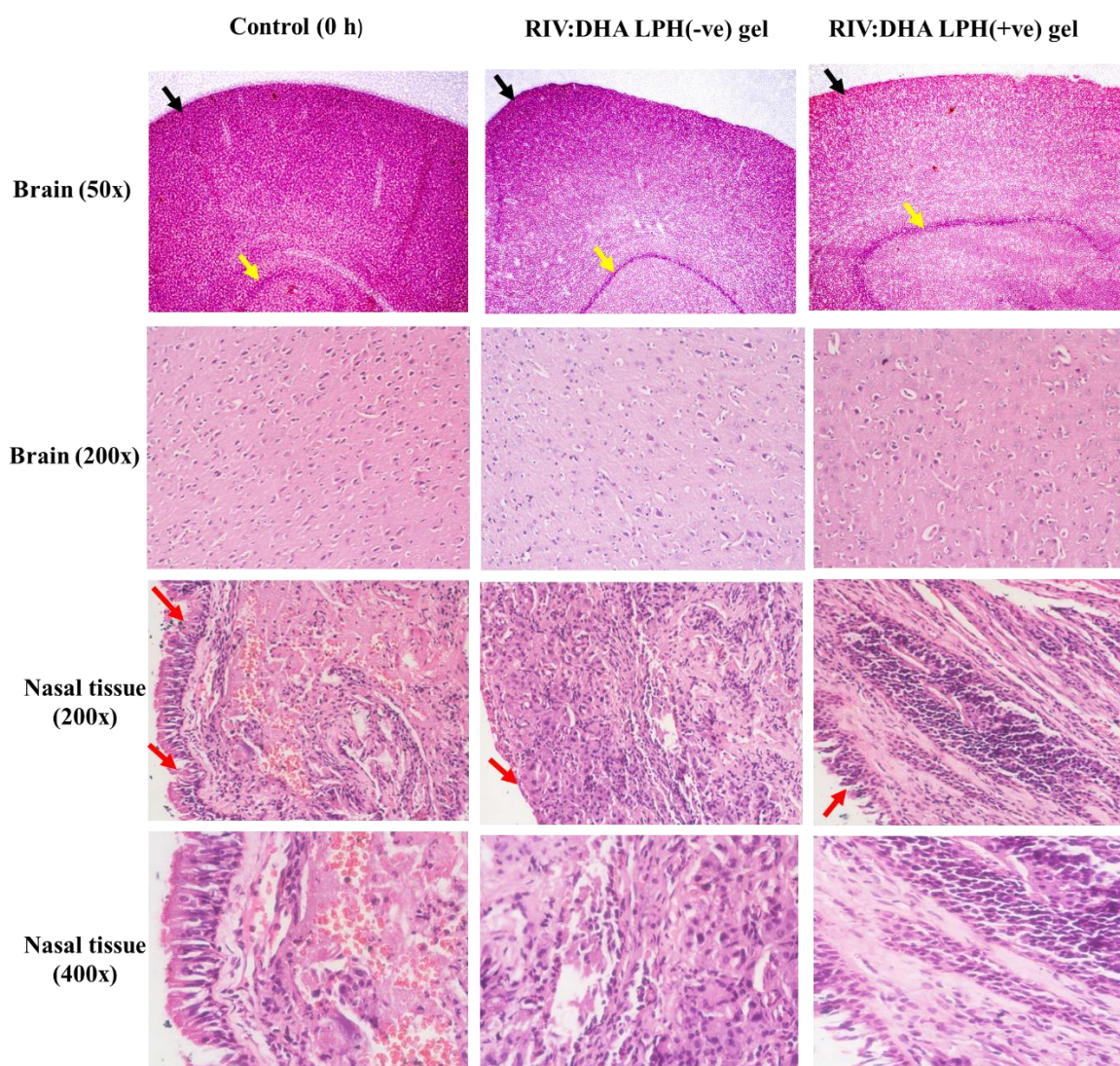


Fig. 4.19. Hematoxylin and eosin stained histopathological specimen of rat brain and nasal epithelium upon intranasal administration of RIV:DHA LPH(-ve) gel and RIV:DHA LPH(+ve) gel (2 mg/kg). Microscopic observation of brain tissue showed normal morphological structures with no alterations in brain. The nasal epithelium also showed an intact, normal structure of pseudostratified ciliated columnar cells compared to the control group. 5x, 20x and

40x shows magnification of objective lens, where eyepiece lens magnification was 10x. Black arrow: Cerebral cortex, Yellow arrow: Hippocampus, Red arrow: Ciliated columnar cells

While nasal epithelium also demonstrated intact, normal structures of pseudostratified ciliated columnar cells like in the control group (**Fig.4.19**). The treated groups showed no signs of toxicity or damage to the nasal epithelium and brain tissue, thus assuring the safety of LPH gels.

4.4 Conclusion

The study developed a DHA-based ion pair complex of RIV that enhanced the RIV loading into LPH nanoparticles. The nanoparticles-loaded gel showed sustained drug release for up to 3 days. The gel system increased nasal permeation 3.18 to 4.07-fold. However, the nanoparticle's charge affected the amyloid inhibition differently. The positively charged LPH showed concentration dependant amyloid inhibition, and the higher concentration exhibited improved $A\beta_{1-42}$ inhibition. In contrast, negatively charged LPH nanoparticles showed maximum amyloid inhibition at the lowest concentration, which decreased with increasing concentrations. The LPH nanoparticles improved C_{max} , half-life, MRT and AUC_{0-t} brain concentrations compared to RIV-HT gel. The RIV:DHA LPH(+ve) gel has significantly higher DTE, DTP than RIV:DHA LPH(-ve) gel. It also had better brain bioavailability than RIV:DHA LPH(-ve) gel. The intranasally administered LPH nanoparticles were safe and could efficiently improve nose-to-brain targeting in managing brain disorders.

References

- [1] G.V. Paraskevi Papakyriakopoulou , Evangelos Balafas , Gaia Colombo , Dimitrios M. Rekkas , Nikolaos Kostomitsopoulos, Nose-to-Brain delivery of donepezil hydrochloride following administration of an HPMC-Me- β -CD-PEG400 nasal film in mice, *J. Drug Deliv. Sci. Technol.* 84 (2023) 104463. <https://doi.org/https://doi.org/10.1016/j.jddst.2023.104463>.
- [2] M. Bhanderi, J. Shah, B. Gorain, A.B. Nair, S. Jacob, S.M.B. Asdaq, S. Fattepur, A.S. Alamri, W.F. Alsanie, M. Alhomrani, S. Nagaraja, M.K. Anwer, Optimized rivastigmine nanoparticles coated with Eudragit for intranasal application to brain delivery: Evaluation and nasal ciliotoxicity studies, *Materials (Basel)*. 14 (2021) 6291. <https://doi.org/10.3390/ma14216291>.
- [3] P. Wavikar, R. Pai, P. Vavia, Nose to brain delivery of rivastigmine by in situ gelling cationic nanostructured lipid carriers: Enhanced brain distribution and pharmacodynamics, *J. Pharm. Sci.* 106 (2017) 3613–3622. <https://doi.org/10.1016/J.XPHS.2017.08.024>.
- [4] P.R. Wavikar, P.R. Vavia, Rivastigmine-loaded in situ gelling nanostructured lipid carriers for nose to brain delivery, *J. Liposome Res.* 25 (2015) 141–149. <https://doi.org/10.3109/08982104.2014.954129>.
- [5] F.J.A. Dhara Jain, Nazeer Hasan, Sobiya Zafar, Jitesh Thakur, Kashif Haider, Suhel Parvez, Transferrin functionalized nanostructured lipid carriers for targeting rivastigmine and resveratrol to Alzheimer’s disease: Synthesis, in vitro characterization and brain uptake analysis, *J. Drug Deliv. Sci. Technol.* 104555 (2023). <https://doi.org/https://doi.org/10.1016/j.jddst.2023.104555>.
- [6] M. Agrawal, S. Saraf, S. Saraf, S.G. Antimisiaris, M.B. Chougule, S.A. Shoyele, A.

- Alexander, Nose-to-brain drug delivery: An update on clinical challenges and progress towards approval of anti-Alzheimer drugs, *J. Control. Release.* 281 (2018) 139–177. <https://doi.org/10.1016/j.jconrel.2018.05.011>.
- [7] M.C. Bruno Fonseca-Santos, Camila André Cazarin, Patrícia Bento da Silva, Kaio Pini dos Santos, Márcia Cristina Oliveira da Rocha, Sônia Nair Bão, Márcia Maria De-Souza, Intranasal in situ gelling liquid crystal for delivery of resveratrol ameliorates memory and neuroinflammation in Alzheimer's disease Author links open overlay panel, *Nanomedicine Nanotechnology, Biol. Med.* (2023) 102689. <https://doi.org/https://doi.org/10.1016/j.nano.2023.102689>.
- [8] M.J.N. Esraa Taha, Samia A. Nour, Wael Mamdouh, Adli A. Selim, Mohamed M. Swidan, Ahmed B. Ibrahim, Cod liver oil nano-structured lipid carriers (Cod-NLCs) as a promising platform for nose to brain delivery: Preparation, in vitro optimization, ex vivo cytotoxicity & in vivo biodistribution utilizing radioiodinated zopiclone, *Int. J. Pharm. X.* 5 (2023) 100160. <https://doi.org/https://doi.org/10.1016/j.ijpx.2023.100160>.
- [9] P. Saha, H. Kathuria, M.M. Pandey, Intranasal nanotherapeutics for brain targeting and clinical studies in Parkinson's disease, *J. Control. Release.* 358 (2023) 293–318. <https://doi.org/10.1016/J.JCONREL.2023.04.021>.
- [10] P. Saha, P. Singh, H. Kathuria, D. Chitkara, M.M. Pandey, Self-assembled lecithin-chitosan nanoparticles improved Rotigotine Nose-to-Brain delivery and brain targeting efficiency, *Pharmaceutics.* 15 (2023) 851. <https://doi.org/10.3390/PHARMACEUTICS15030851/S1>.
- [11] P. Saha, H. Kathuria, M.M. Pandey, Nose-to-brain delivery of rotigotine redispersible nanosuspension: In vitro and in vivo characterization, *J. Drug Deliv. Sci. Technol.* 79 (2023) 104049.

-
- [12] B.M. Shah, M. Misra, C.J. Shishoo, H. Padh, Nose to brain microemulsion-based drug delivery system of rivastigmine: Formulation and ex-vivo characterization, *Drug Deliv.* 22 (2015) 918–930. <https://doi.org/10.3109/10717544.2013.878857>.
- [13] S.N. El-helaly, A.A. Elbary, M.A. Kassem, S.N. El-helaly, A.A. Elbary, M.A. Kassem, M.A. El-nabarawi, Electrosteric stealth Rivastigmine loaded liposomes for brain targeting: preparation, characterization, ex vivo, bio-distribution and in vivo pharmacokinetic studies Electrosteric stealth Rivastigmine loaded liposomes for brain targeting: preparation, *Drug Deliv.* 7544 (2017) 692–700. <https://doi.org/10.1080/10717544.2017.1309476>.
- [14] B. Shah, D. Khunt, H. Bhatt, M. Misra, H. Padh, Application of quality by design approach for intranasal delivery of rivastigmine loaded solid lipid nanoparticles: Effect on formulation and characterization parameters, *Eur. J. Pharm. Sci.* 78 (2015) 54–66. <https://doi.org/10.1016/j.ejps.2015.07.002>.
- [15] T. Date, V. Nimbalkar, J. Kamat, A. Mittal, R.I. Mahato, D. Chitkara, Lipid-polymer hybrid nanocarriers for delivering cancer therapeutics, *J. Control. Release.* 271 (2018) 60–73. <https://doi.org/10.1016/J.JCONREL.2017.12.016>.
- [16] N.S. Hinge, H. Kathuria, M.M. Pandey, Engineering of structural and functional properties of nanotherapeutics and nanodiagnostics for intranasal brain targeting in Alzheimer's, *Appl. Mater. Today.* 26 (2022) 101303. <https://doi.org/10.1016/J.APMT.2021.101303>.
- [17] W. Wang, Y. Han, Y. Fan, Y. Wang, Effects of gold nanospheres and nanocubes on amyloid- β peptide fibrillation, *Langmuir.* 35 (2019) 2334–2342. <https://doi.org/10.1021/acs.langmuir.8b04006>.
- [18] N. Chen, Size and surface properties determining nanoparticle uptake and transport in

- the nasal mucosa, University of Iowa, 2013.
- [19] M. Abdulhussein, H. Albarki, In vitro assessment of the transport of Poly D, L Lactic-Co-Glycolic Acid (PLGA) nanoparticles across the nasal mucosa, (2016). <https://doi.org/10.17077/etd.cl2e1klm>.
- [20] R.N. Utami, Assessment of the toxicity of lipid nanocapsules and polymer nanoparticles on a neuronal cell model as a first step towards their development for nose-to-brain drug delivery, 2019. <https://etheses.bham.ac.uk/id/eprint/9022/1/Utami2019MSc.pdf> (accessed November 24, 2020).
- [21] A. Mistry, S. Stolnik, L. Illum, Nose-to-Brain delivery: investigation of the transport of nanoparticles with different surface characteristics and sizes in excised porcine olfactory epithelium, *Mol. Pharm.* 12 (2015) 2755–2766. <https://doi.org/10.1021/acs.molpharmaceut.5b00088>.
- [22] A. Bonaccorso, T. Musumeci, M.F. Serapide, R. Pellitteri, I.F. Uchegbu, G. Puglisi, Nose to brain delivery in rats: Effect of surface charge of rhodamine B labeled nanocarriers on brain subregion localization, *Colloids Surfaces B Biointerfaces*. 154 (2017) 297–306. <https://doi.org/10.1016/j.colsurfb.2017.03.035>.
- [23] Y. Kim, J.H. Park, H. Lee, J.M. Nam, How do the size, charge and shape of nanoparticles affect amyloid β aggregation on brain lipid bilayer?, *Sci. Rep.* 6 (2016) 1–13. <https://doi.org/10.1038/srep19548>.
- [24] N. Javdani, S.S. Rahpeyma, Y. Ghasemi, J. Raheb, <p>Effect of superparamagnetic nanoparticles coated with various electric charges on α -synuclein and β -amyloid proteins fibrillation process</p>, *Int. J. Nanomedicine*. 14 (2019) 799–808. <https://doi.org/10.2147/IJN.S190354>.

-
- [25] A. Froelich, T. Osmałek, B. Jadach, V. Puri, B. Michniak-Kohn, Microemulsion-based media in nose-to-brain drug delivery, *Pharmaceutics*. 13 (2021) 1–37. <https://doi.org/10.3390/pharmaceutics13020201>.
- [26] K.D. Ristroph, R.K. Prud'homme, Hydrophobic ion pairing: Encapsulating small molecules, peptides, and proteins into nanocarriers, *Nanoscale Adv.* 1 (2019) 4207–4237. <https://doi.org/10.1039/c9na00308h>.
- [27] E. Samaridou, H. Walgrave, E. Salta, D.M. Álvarez, V. Castro-López, M. Loza, M.J. Alonso, Nose-to-brain delivery of enveloped RNA - cell permeating peptide nanocomplexes for the treatment of neurodegenerative diseases, *Biomaterials*. 230 (2020) 119657. <https://doi.org/10.1016/J.BIOMATERIALS.2019.119657>.
- [28] A.S. Torkey, M.S. Freag, M.M.A. Nasra, O.Y. Abdallah, Novel skin penetrating berberine oleate complex capitalizing on hydrophobic ion pairing approach, *Int. J. Pharm.* 549 (2018) 76–86. <https://doi.org/10.1016/j.ijpharm.2018.07.051>.
- [29] L.P.B. Guerzoni, V. Nicolas, A. Angelova, In Vitro Modulation of TrkB Receptor Signaling upon Sequential Delivery of Curcumin-DHA Loaded Carriers Towards Promoting Neuronal Survival, *Pharm. Res.* 34 (2017) 492–505. <https://doi.org/10.1007/s11095-016-2080-4>.
- [30] C. Song, C.H. Shieh, Y.S. Wu, A. Kalueff, S. Gaikwad, K.P. Su, The role of omega-3 polyunsaturated fatty acids eicosapentaenoic and docosahexaenoic acids in the treatment of major depression and Alzheimer's disease: Acting separately or synergistically?, *Prog. Lipid Res.* 62 (2016) 41–54. <https://doi.org/10.1016/j.plipres.2015.12.003>.
- [31] G.A. Jicha, W.R. Markesbery, Omega-3 fatty acids: Potential role in the management of early Alzheimer's disease, *Clin. Interv. Aging.* 5 (2010) 45–61. <https://doi.org/10.2147/cia.s5231>.

- [32] H. Chew, V.A. Solomon, A.N. Fonteh, Involvement of lipids in Alzheimer's disease pathology and potential therapies, *Front. Physiol.* 11 (2020) 1–28. <https://doi.org/10.3389/fphys.2020.00598>.
- [33] R.L. Shinde, P. V. Devarajan, Docosahexaenoic acid-mediated, targeted and sustained brain delivery of curcumin microemulsion, *Int. J. Pharm.* 24 (2017) 152–161. <https://doi.org/10.1080/10717544.2016.1233593>.
- [34] 2020 Alzheimer's disease facts and figures, *Alzheimer's Dement.* 16 (2020) 391–460. <https://doi.org/10.1002/alz.12068>.
- [35] D. Khunt, M. Shrivastava, S. Polaka, P. Gondaliya, M. Misra, Role of omega-3 Fatty acids and butter oil in targeting delivery of donepezil hydrochloride microemulsion to brain via the intranasal route: a comparative study, *AAPS PharmSciTech.* 21 (2020). <https://doi.org/10.1208/s12249-019-1585-7>.
- [36] A.H.S. Mona Elhabak, Abeer A.A. Salama, Nose-to-brain delivery of galantamine loaded nanospray dried polyacrylic acid/taurodeoxycholate mixed matrix as a protective therapy in lipopolysaccharide-induced Alzheimer's in mice model, *Int. J. Pharm.* 632 (2023) 122588. <https://doi.org/10.1016/j.ijpharm.2023.122588>.
- [37] R.S. Kalhapure, C. Mocktar, D.R. Sikwal, S.J. Sonawane, M.K. Kathiravan, A. Skelton, T. Govender, Ion pairing with linoleic acid simultaneously enhances encapsulation efficiency and antibacterial activity of vancomycin in solid lipid nanoparticles, *Colloids Surfaces B Biointerfaces.* 117 (2014) 303–311. <https://doi.org/10.1016/j.colsurfb.2014.02.045>.
- [38] N.S. Hinge, M.M. Pandey, Sensitive RP-HPLC method of rivastigmine for applicative quantification of nanostructured lipid carriers, *Microchem. J.* 188 (2023) 108341.

- <https://doi.org/10.1016/J.MICROC.2022.108341>.
- [39] S. Mirsadeghi, R. Dinarvand, M.H. Ghahremani, M.R. Hormozi-Nezhad, Z. Mahmoudi, M.J. Hajipour, F. Atyabi, M. Ghavami, M. Mahmoudi, Protein corona composition of gold nanoparticles/nanorods affects amyloid beta fibrillation process, *Nanoscale*. 7 (2015) 5004–5013. <https://doi.org/10.1039/c4nr06009a>.
- [40] S. Mirsadeghi, S. Shanehsazzadeh, F. Atyabi, R. Dinarvand, Effect of PEGylated superparamagnetic iron oxide nanoparticles (SPIONs) under magnetic field on amyloid beta fi brillation process, *Mater. Sci. Eng. C*. 59 (2016) 390–397. <https://doi.org/10.1016/j.msec.2015.10.026>.
- [41] Z. Jiang, X. Dong, Y. Sun, Charge effects of self-assembled chitosan-hyaluronic acid nanoparticles on inhibiting amyloid β -protein aggregation, *Carbohydr. Res*. 461 (2018) 11–18. <https://doi.org/10.1016/j.carres.2018.03.001>.
- [42] S. Sudhakar, P. Kalipillai, P.B. Santhosh, E. Mani, Role of surface charge of inhibitors on amyloid beta fibrillation, *J. Phys. Chem. C*. 121 (2017) 6339–6348. <https://doi.org/10.1021/acs.jpcc.6b12307>.
- [43] J. Ma, C. Wang, Y. Sun, L. Pang, S. Zhu, Y. Liu, L. Zhu, S. Zhang, L. Wang, L. Du, Comparative study of oral and intranasal puerarin for prevention of brain injury induced by acute high-altitude hypoxia, *Int. J. Pharm.* 591 (2020) 120002. <https://doi.org/10.1016/j.ijpharm.2020.120002>.
- [44] P. Pandey, P.J. Cabot, B. Wallwork, B.J. Panizza, H.S. Parekh, Formulation, functional evaluation and ex vivo performance of thermoresponsive soluble gels - A platform for therapeutic delivery to mucosal sinus tissue, *Eur. J. Pharm. Sci.* 96 (2017) 499–507. <https://doi.org/10.1016/j.ejps.2016.10.017>.

- [45] C.T. Uppuluri, P.R. Ravi, A. V. Dalvi, S.S. Shaikh, S.R. Kale, Piribedil loaded thermo-responsive nasal in situ gelling system for enhanced delivery to the brain: formulation optimization, physical characterization, and in vitro and in vivo evaluation, *Drug Deliv. Transl. Res.* 11 (2021) 909–926. <https://doi.org/10.1007/s13346-020-00800-w>.
- [46] S. Salatin, J. Barar, M. Barzegar-Jalali, K. Adibkia, M. Jelvehgari, Thermosensitive in situ nanocomposite of rivastigmine hydrogen tartrate as an intranasal delivery system: Development, characterization, ex vivo permeation and cellular studies, *Colloids Surf. B. Biointerfaces.* 159 (2017) 629–638. <https://doi.org/10.1016/j.colsurfb.2017.08.031>.
- [47] K. Florence, L. Manisha, B.A. Kumar, K. Ankur, M.A. Kumar, M. Ambikanandan, Intranasal clobazam delivery in the treatment of status epilepticus, *J. Pharm. Sci.* 100 (2011) 692–703. <https://doi.org/10.1002/JPS.22307>.
- [48] H. Kathuria, H.K. Handral, S. Cha, D.T.P. Nguyen, J. Cai, T. Cao, C. Wu, L. Kang, Enhancement of Skin Delivery of Drugs Using Proposome Depends on Drug Lipophilicity, *Pharmaceutics.* 13 (2021) 1457. <https://doi.org/10.3390/pharmaceutics13091457>.
- [49] I. Shahzadi, M.H. Asim, A. Dizdarević, J.D. Wolf, M. Kurpiers, B. Matuszczak, A. Bernkop-Schnürch, Arginine-based cationic surfactants: Biodegradable auxiliary agents for the formation of hydrophobic ion pairs with hydrophilic macromolecular drugs, *J. Colloid Interface Sci.* 552 (2019) 287–294. <https://doi.org/10.1016/j.jcis.2019.05.057>.
- [50] S. Bonengel, M. Jelkmann, M. Abdulkarim, M. Gumbleton, V. Reinstadler, H. Oberacher, F. Prüfert, A. Bernkop-Schnürch, Impact of different hydrophobic ion pairs of octreotide on its oral bioavailability in pigs, *J. Control. Release.* 273 (2018) 21–29. <https://doi.org/10.1016/j.jconrel.2018.01.012>.
- [51] T. Ren, X. Lin, Q. Zhang, D. You, X. Liu, X. Tao, J. Gou, Y. Zhang, T. Yin, H. He, X.

- Tang, Encapsulation of azithromycin ion pair in liposome for enhancing ocular delivery and therapeutic efficacy on dry eye, *Mol. Pharm.* 15 (2018) 4862–4871. <https://doi.org/10.1021/ACS.MOLPHARMACEUT.8B00516>.
- [52] Y. Cai, Q. Tian, C. Liu, L. Fang, Development of long-acting rivastigmine drug-in-adhesive patch utilizing ion-pair strategy and characterization of controlled release mechanism, *Eur. J. Pharm. Sci.* 161 (2021) 105774. <https://doi.org/10.1016/J.EJPS.2021.105774>.
- [53] H. Zhao, H. Lu, T. Gong, Z. Zhang, Nanoemulsion loaded with lycobetaine-oleic acid ionic complex: Physicochemical characteristics, in vitro, in vivo evaluation, and antitumor activity, *Int. J. Nanomedicine.* 8 (2013) 1959–1973. <https://doi.org/10.2147/IJN.S43892>.
- [54] S. Zhao, L. Van Minh, N. Li, V.M. Garamus, U.A. Handge, J. Liu, R. Zhang, R. Willumeit-Römer, A. Zou, Doxorubicin hydrochloride-oleic acid conjugate loaded nanostructured lipid carriers for tumor specific drug release, 2016. <https://doi.org/10.1016/j.colsurfb.2016.04.027>.
- [55] Y.H. Song, E. Shin, H. Wang, J. Nolan, S. Low, D. Parsons, S. Zale, S. Ashton, M. Ashford, M. Ali, D. Thrasher, N. Boylan, G. Troiano, A novel in situ hydrophobic ion pairing (HIP) formulation strategy for clinical product selection of a nanoparticle drug delivery system, *J. Control. Release.* 229 (2016) 106–119. <https://doi.org/10.1016/J.JCONREL.2016.03.026>.
- [56] M.K. Chauhan, P.K. Sharma, Optimization and characterization of rivastigmine nanolipid carrier loaded transdermal patches for the treatment of dementia, *Chem. Phys. Lipids.* 224 (2019) 104794. <https://doi.org/10.1016/j.chemphyslip.2019.104794>.
- [57] A.S. Vaziri, I. Alemzadeh, M. Vossoughi, A.C. Khorasani, Co-microencapsulation of

- Lactobacillus plantarum and DHA fatty acid in alginate-pectin-gelatin biocomposites, *Carbohydr. Polym.* 199 (2018) 266–275. <https://doi.org/10.1016/j.carbpol.2018.07.002>.
- [58] D.L. Pavia, G.M. Lampman, G.S. Kriz, J.R. Vyvyan, *Introduction to spectroscopy*, 5th ed., Brok/Cole Cengage Learning, 2009. <http://dl.iranchembook.ir/ebook/organic-chemistry-2753.pdf> (accessed July 12, 2022).
- [59] L. He, D. Xiong, L. Ma, Y. Liang, T. Zhang, Z. Wu, H. Tang, X. Wu, Ion-pair compounds of strychnine for enhancing skin permeability: Influencing the transdermal processes in vitro based on molecular simulation, *Pharmaceuticals*. 15 (2022). <https://doi.org/10.3390/ph15010034>.
- [60] H. Zhao, C. Liu, P. Quan, X. Wan, M. Shen, L. Fang, Mechanism study on ion-pair complexes controlling skin permeability: Effect of ion-pair dissociation in the viable epidermis on transdermal permeation of bisoprolol, *Int. J. Pharm.* 532 (2017) 29–36. <https://doi.org/10.1016/j.ijpharm.2017.08.080>.
- [61] S.A. Abouelmagd, N.H. Abd Ellah, O. Amen, A. Abdelmoez, N.G. Mohamed, Self-assembled tannic acid complexes for pH-responsive delivery of antibiotics: Role of drug-carrier interactions, *Int. J. Pharm.* 562 (2019) 76–85. <https://doi.org/10.1016/j.ijpharm.2019.03.009>.
- [62] S. Sun, N. Liang, Y. Kawashima, D. Xia, F. Cui, Hydrophobic ion pairing of an insulin-sodium deoxycholate complex for oral delivery of insulin., *Int. J. Nanomedicine*. 6 (2011) 3049–3056. <https://doi.org/10.2147/ijn.s26450>.
- [63] J. Griesser, G. Hetényi, M. Moser, F. Demarne, V. Jannin, A. Bernkop-Schnürch, Hydrophobic ion pairing: Key to highly payloaded self-emulsifying peptide drug delivery systems, *Int. J. Pharm.* 520 (2017) 267–274. <https://doi.org/10.1016/J.IJPHARM.2017.02.019>.

- [64] M.I. Amaro, A. Simon, L.M. Cabral, V.P. De Sousa, A.M. Healy, Rivastigmine hydrogen tartrate polymorphs: Solid-state characterisation of transition and polymorphic conversion via milling, *Solid State Sci.* 49 (2015) 29–36. <https://doi.org/10.1016/j.solidstatesciences.2015.09.004>.
- [65] M.T. Ansari, A. Hussain, S. Nadeem, H. Majeed, S. Saeed-Ul-Hassan, I. Tariq, Q. Mahmood, A.K. Khan, G. Murtaza, Preparation and characterization of solid dispersions of artemether by freeze-dried method, *Biomed Res. Int.* 2015 (2015). <https://doi.org/10.1155/2015/109563>.
- [66] S.S. Rostamkalaei, J. Akbari, M. Saeedi, K. Morteza-Semnani, A. Nokhodchi, Topical gel of Metformin solid lipid nanoparticles: A hopeful promise as a dermal delivery system, *Colloids Surfaces B Biointerfaces.* 175 (2019) 150–157. <https://doi.org/10.1016/J.COLSURFB.2018.11.072>.
- [67] X. Chen, G. Lv, J. Zhang, S. Tang, Y. Yan, Z. Wu, J. Su, J. Wei, Preparation and properties of bsa-loaded microspheres based on multi-(amino acid) copolymer for protein delivery, *Int. J. Nanomedicine.* 9 (2014) 1957–1965. <https://doi.org/10.2147/IJN.S57048>.
- [68] Y. Su, B. Sun, X. Gao, X. Dong, L. Fu, Y. Zhang, Z. Li, Intranasal delivery of targeted nanoparticles loaded with miR-132 to brain for the treatment of neurodegenerative diseases, *Front. Pharmacol.* 11 (2020) 1–13. <https://doi.org/10.3389/fphar.2020.01165>.
- [69] A. Sarma, M.K. Das, Nose to brain delivery of antiretroviral drugs in the treatment of neuroAIDS, *Mol. Biomed.* 1 (2020) 1–23. <https://doi.org/10.1186/s43556-020-00019-8>.
- [70] S. Kumar, L.R. Karthik, A. Sree, L. Bojja, N. Kumar, C.M. Rao, Pharmacokinetic and pharmacodynamic evaluation of nasal liposome and nanoparticle based rivastigmine

- formulations in acute and chronic models of Alzheimer ' s disease, *Naunyn-Schmiedeberg's Arch. Pharmacol.* (2021). <https://doi.org/10.1007/s00210-021-02096-0>.
- [71] M. Fazil, S. Md, S. Haque, M. Kumar, S. Baboota, J.K. Sahni, J. Ali, Development and evaluation of rivastigmine loaded chitosan nanoparticles for brain targeting, *Eur. J. Pharm. Sci.* 47 (2012) 6–15. <https://doi.org/10.1016/j.ejps.2012.04.013>.
- [72] S. Cunha, C.P. Costa, J.A. Loureiro, J. Alves, A.F. Peixoto, B. Forbes, J.M.S. Lobo, A.C. Silva, Double optimization of rivastigmine-loaded nanostructured lipid carriers (NLC) for nose-to-brain delivery using the quality by design (QbD) approach: Formulation variables and instrumental parameters, *Pharmaceutics*. 12 (2020) 1–27. <https://doi.org/10.3390/pharmaceutics12070599>.
- [73] Z.Z. Yang, Y.Q. Zhang, Z.Z. Wang, K. Wu, J.N. Lou, X.R. Qi, Enhanced brain distribution and pharmacodynamics of rivastigmine by liposomes following intranasal administration, *Int. J. Pharm.* 452 (2013) 344–354. <https://doi.org/10.1016/j.ijpharm.2013.05.009>.
- [74] A. Sukhanova, S. Poly, S. Bozrova, É. Lambert, M. Ewald, A. Karaulov, M. Molinari, I. Nabiev, Nanoparticles with a specific size and surface charge promote disruption of the secondary structure and amyloid-like fibrillation of human insulin under physiological conditions, *Front. Chem.* 7 (2019) 1–13. <https://doi.org/10.3389/fchem.2019.00480>.
- [75] S. Cunha, M. Swedrowska, Y. Bellahnid, Z. Xu, J.M. Sousa Lobo, B. Forbes, A.C. Silva, Thermosensitive in situ hydrogels of rivastigmine-loaded lipid-based nanosystems for nose-to-brain delivery: characterisation, biocompatibility, and drug deposition studies, *Int. J. Pharm.* 620 (2022). <https://doi.org/10.1016/J.IJPHARM.2022.121720>.
- [76] P.S. Rawat, P.R. Ravi, S.I. Mir, M.S. Khan, H. Kathuria, P. Katnapally, U. Bhatnagar,

- Design, Characterization and Pharmacokinetic–Pharmacodynamic Evaluation of Poloxamer and Kappa-Carrageenan-Based Dual-Responsive In Situ Gel of Nebivolol for Treatment of Open-Angle Glaucoma, *Pharmaceutics*. 15 (2023) 405. <https://doi.org/10.3390/pharmaceutics15020405>.
- [77] P. Costa, J.M. Sousa Lobo, Modeling and comparison of dissolution profiles, *Eur. J. Pharm. Sci.* 13 (2001) 123–133. [https://doi.org/10.1016/S0928-0987\(01\)00095-1](https://doi.org/10.1016/S0928-0987(01)00095-1).
- [78] N. Dhas, T. Mehta, Cationic biopolymer functionalized nanoparticles encapsulating lutein to attenuate oxidative stress in effective treatment of Alzheimer’s disease: A non-invasive approach., *Int. J. Pharm.* 586 (2020) 119553. <https://doi.org/10.1016/j.ijpharm.2020.119553>.
- [79] A.T. Chatzitaki, S. Jesus, C. Karavasili, D. Andreadis, D.G. Fatouros, O. Borges, Chitosan-coated PLGA nanoparticles for the nasal delivery of ropinirole hydrochloride: In vitro and ex vivo evaluation of efficacy and safety, *Int. J. Pharm.* 589 (2020) 119776. <https://doi.org/10.1016/j.ijpharm.2020.119776>.
- [80] T.T.L. Nguyen, H.J. Maeng, Pharmacokinetics and pharmacodynamics of intranasal solid lipid nanoparticles and nanostructured lipid carriers for Nose-to-Brain delivery, *Pharmaceutics*. 14 (2022). <https://doi.org/10.3390/PHARMACEUTICS14030572>.
- [81] S. Bahadur, D.M. Pardhi, J. Rautio, J.M. Rosenholm, K. Pathak, Intranasal nanoemulsions for direct nose-to-brain delivery of actives for cns disorders, *Pharmaceutics*. 12 (2020) 1–27. <https://doi.org/10.3390/pharmaceutics12121230>.
- [82] R. Boyuklieva, B. Pilicheva, Micro- and nanosized carriers for nose-to-brain drug delivery in neurodegenerative disorders, *Biomedicines*. 10 (2022). <https://doi.org/10.3390/BIOMEDICINES10071706>.

- [83] C.P. Costa, J.N. Moreira, J.M. Sousa Lobo, A.C. Silva, Intranasal delivery of nanostructured lipid carriers, solid lipid nanoparticles and nanoemulsions: A current overview of in vivo studies, *Acta Pharm. Sin. B.* 11 (2021) 925–940. <https://doi.org/10.1016/j.apsb.2021.02.012>.

CHAPTER 5

RIVASTIGMINE-DHA ION-PAIR COMPLEX- BASED NANODISPERSION FOR IMPROVED NOSE- TO-BRAIN TARGETING IN ALZHEIMER'S DISEASE

5.1 Introduction

AD is a progressive neurodegenerative disorder growing in elders above age 65 years. The clinical condition is characterized by reduced cholinergic activity, leading to impaired cognition, memory and psychiatric symptoms [1]. The therapeutic approach involves targeting cholinergic synapses and increasing acetylcholine levels in the brain. RIV-HT has been a drug of choice due to its dual action toward acetylcholinesterase and butyrylcholinesterase [2]. The hydrophilic nature of RIV-HT unable them to pass across BBB, limiting its entry into brain [3]. It also undergoes extensive first-pass metabolism, resulting shorter half-life (90 min). Also, Frequent drug administration leads to greater accumulation in peripheral organs resulting in gastrointestinal cholinergic-mediated side effects [4].

In this regard, intranasal delivery is a promising approach for directly delivering actives to the CNS with its physiological ability to circumvent BBB [5]. Intranasal delivery lacks first-pass metabolism and reduces drug localization in peripheral tissues [6]. However RIV-HT may hinder drug diffusion across nasal pathways due to its limited lipophilicity [7]. To overcome this problem, the fabrication of actives into hydrophobic ion pair complexes (IPC) has been a promising approach for modulating lipid solubility of small molecules [8]. IPC involves electrostatic interaction between two oppositely charged ionizable groups to form an amphiphilic molecule with altered lipophilicity [9]. The improved lipophilicity is based on hydrophobicity of the counterion molecule [9].

Amongst essential fatty acids, DHA promotes the interaction of APP with α -secretase by shielding γ -secretase [10,11]. It also has a role in modulation of apolipoprotein-E isoforms, a clearance mechanism of A β -peptide [10,12]. Regular supplementation with DHA have ability to improve cognitive function and restoration of spatial memory in early and later stages of Alzheimer's [11,13]. It also has a role in improving translocation efficiency of actives across

nasal pathways [14]. DHA also improved C_{\max} and AUC concentrations of drugs after intranasal administration [15,16].

Fabrication of IPC (RIV:DHA) using DHA may improve drug permeation across nasal barriers. RIV:DHA was developed into a nanodispersion (RIV:DHA ND) based formulation. The RIV:DHA ND was further embedded into poloxamer-based thermoresponsive hydrogel (RIV:DHA ND gel) to provide sustained drug release, mucoadhesion and delayed mucociliary drug clearance. The *in-vitro* drug release and *ex-vivo* permeation studies were performed to evaluate drug release pattern and mucosal permeation efficiency of RIV:DHA ND gel. The pharmacokinetic (PK) study in rats will determine mucociliary drug clearance, direct transport percentage (DTP) (%), drug transport efficiency (DTE) (%) and pharmacokinetic drug profile in brain and plasma. Further, histopathological examination will assess the microscopic evaluation of RIV:DHA ND gel treated sections of rat brain and nasal tissue to ensure the safety of the developed formulation.

5.2 Material and method

5.2.1 Material

Rivastigmine hydrogen tartrate and docosahexaenoic acid were received as a gift sample from Torrent Pharmaceuticals Ltd. (Ahmedabad, India) and Bioplus Life Sciences Pvt. Ltd. (Bangalore, India). Capmul® MCM C8 and Captex® 355, castor oil, and soyabean oil were provided as gift samples from Abitec corporation (Columbus, USA). Miglyol®812 was obtained as a gift sample from Orbicular Pharmaceutical Technology Pvt. Ltd. (Hyderabad, India). Soluplus®, Kolliphor® P 407, and Kolliphor® P 188 were received as a gift sample from BASF (Mumbai, India). Span 80, tween 80, Polyvinyl alcohol, glacial acetic acid, and potassium dihydrogen phosphate were purchased from S.D. Fine Chemicals Ltd. (Mumbai, India). Sodium hydroxide, orthophosphoric acid, triethyl amine, glacial acetic acid, and sodium dihydrogen phosphate were purchased from Merck (Mumbai, India). Hydrochloric

acid, calcium chloride, sodium chloride, and potassium chloride, disodium ethylene diamine tetra-acetic acid were purchased from Central Drug House Pvt. Ltd. (New Delhi, India). HPLC-grade acetonitrile was purchased from Merck (Mumbai, India). Isoflurane USP was purchased from Abbott Laboratories (Mumbai, India) for inhalational anesthesia. HPLC grade Milli-Q water was obtained from our institute's Millipore Direct-Q ultra-pure water system (Millipore, Bedford, USA) unit facility.

5.2.2 Preparation and characterization of RIV:DHA

RIV:DHA was prepared as per the procedure described in Chapter 4, section 4.2.2. Further, the optimized 1:1 molar ratio of RIV:DHA was characterized as the procedure described in Chapter 4, section 4.2.3.

5.2.3 Preliminary screening of surfactant for preparation of RIV:DHA ND

The solubility study was performed for screening of surfactants. Enough RIV:DHA was added in 0.3 mL, 0.5% (w/v) surfactant solution, *viz.*, tween 80, tween 60, polyvinyl alcohol, Gelucire 44/14, poloxamer 188, PEG-32-stearate, and soluplus. The mixture was saturated for 24 h with continuous stirring, and samples were centrifuged to remove the undissolved drug. The supernatant was collected and analyzed using the validated HPLC method [17].

5.2.4 Preparation of RIV:DHA ND

RIV:DHA ND was prepared using emulsification solvent evaporation method [18]. 20 mg drug equivalent RIV:DHA (40 mg) was dissolved in 0.5 mL methylene chloride. Separately, 3 mL aqueous solution containing 0.5% w/v tween 80 was prepared. Further, the organic phase was dropwise (flow rate 1 mL/min) added into the aqueous phase, with simultaneous probe sonication for 3 min at 25 % amplitude. The organic solvent was removed using rotary evaporator at 40 °C for 2 h. Further, RIV:DHA ND was centrifuged at 5000 rpm for 5 min to remove coarse particles as shown in **Fig.5.1**. The developed RIV:DHA ND was characterized

for particle size, PDI and zeta potential using Malvern Nano ZS. The Particle size measurement was performed with 2x dilution with Milli-Q water.

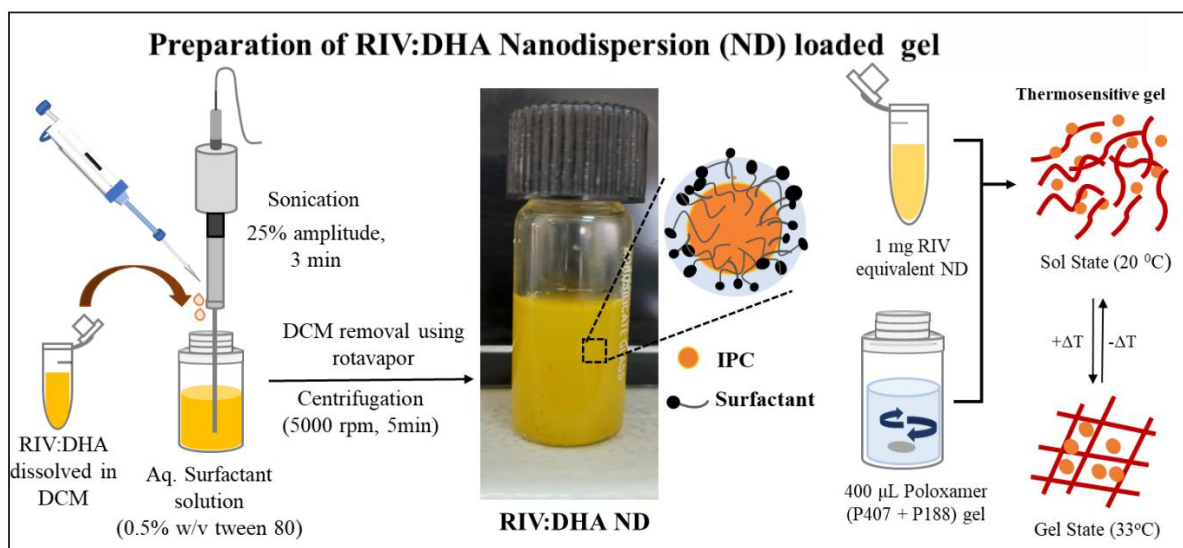


Fig. 5.1. Schematic representation for preparation of RIV:DHA ND and RIV:DHA ND gel. RIV:DHA was dissolved in DCM and organic phase was dropwise added to 0.5% w/v tween 80 solution, and reduced using probe sonication. DCM was evaporated and resultant RIV:DHA ND was loaded into poloxamer-based hydrogel. DCM: Dichloromethane, RIV:DHA: RIV, DHA ion pair complex, Aq: Aqueous, rpm: Rotation per minute, P407: Poloxamer 407, P188: Poloxamer 188.

5.2.5 Preparation of hydrogel loaded with RIV:DHA formulations

The *in-situ* thermoresponsive gel was prepared using a cold process [19]. Poloxamer 407 is reported for effective gelling at nasal cavity temperature and hydrogel containing 0.5 % (w/v) gel strength was prepared [20]. Poloxamer 407 (4.6 g) and 188 (0.8 g) were mixed thoroughly in 15 mL Milli-Q water. The mixture was stirred continuously and stored overnight for hydration at a temperature between 2-8° C. Further, 2 g propylene glycol was added into the poloxamer solution, and the final volume was made up to 20 mL with Milli-Q water. Finally, the gel mixture was stored overnight at 2-8° C, and RIV-HT was added just before the initiation of rheological experiments. Similarly, 1 mg drug equivalent formulation was incorporated in 200 µL hydrogel for further experiments.

5.2.6 Hydrogel rheological characterisation

The rheological study was performed using MCR 92 rheometer (Anton Par, Austria). The 25 mm parallel plate with a standard gap of 0.5 mm was maintained for all experiments [20,21]. The amplitude sweep test determined linear viscoelastic range (LVER). Further, temperature-dependant viscosity was performed within range of 20-35° C, and hydrogel viscosity at nasal cavity temperature (33° C) was noted. The sample was allowed to equilibrate for 120 s onto rheometer platform and storage modulus (G'), loss modulus (G''), loss tangent ($\tan \delta$) and dynamic viscosity was determined. The elastic properties of gel were evaluated using frequency sweep test with an oscillatory frequency range within 0.1 to 10 Hz at 33° C.

5.2.6.1 Scanning electron microscopy

RIV:DHA ND and their corresponding hydrogel nanoparticles were placed onto coverslip, and the smear was allowed to dry overnight at room temperature. The sample coverslips were placed on metal stubs and fixed using double-sided carbon tape. It was gold coated for 60 s using Quorum Technologies Q150TES sputter coater (East Sussex, England). The samples were analyzed using Field emission-scanning electron microscopy, FE-SEM (FEI Quanta FEG 250 SEM, Washington, USA) with 20 kV high vacuum within a suitable magnification range.

5.2.6.2 Stability study

The study was performed to elucidate the stability of RIV:DHA ND gel at refrigerated conditions (2-8° C). The samples were collected at 0, 30, 60, and 90 days and compared with freshly prepared samples (0 h). The particle size, PDI, and zeta-potential was determined. Statistical analysis was computed to determine the difference within samples at each time point.

5.2.7 *In-vitro* drug release

In-vitro drug release was evaluated by the widely used dialysis bag technique [22]. Briefly, RIV:DHA ND gel was filled in dialysis bag (Himedia dialysis membrane-110, molecular weight cut off 12000-14000) containing 1 mL nasal simulated fluid (NSF, composition: 8.77 g L⁻¹ of NaCl, 2.98 g L⁻¹ of KCl, 0.59 g L⁻¹ of CaCl₂·2H₂O in deionized water, pH 6.4), which was further placed in tubes containing 25 mL phosphate buffer saline (PBS), pH 7.4. The tubes were kept on stirring at 100 rpm at 33 ± 1° C using magnetic stirrer. Sampling was performed at predetermined time intervals (0.08-24 h), and replenished with the same volume of fresh release medium. Samples were centrifuged at 15,000 rpm for 10 min, the supernatant was collected and analyzed using the previously discussed HPLC method [17]. The drug release data were fitted into various kinetic models such as zero order, first order, Higuchi, Hixson Crowell, and Korsmeyer-Peppas to explore the mechanism of drug release from various formulations using D.D. solver software program.

5.2.8 *Ex-vivo* nasal permeation

Ex-vivo permeation study was performed following a previously reported protocol [23] using Franz diffusion cell apparatus. Freshly excised goat nasal mucosa was procured from a local slaughterhouse, and rinsed with freshly prepared PBS, pH 7.4. The nasal mucosa was separated from septum, and extraneous tissue was removed from the nasal mucosa. Further, the tissue was rinsed with PBS pH 7.4, and thickness was measured using a Vernier caliper. The tissue was sandwiched between the donor and receptor compartment and allowed to equilibrate with PBS pH 6.4 for 15-20 min. 1 mg drug equivalent formulation was placed onto tissue surface (n = 3). The receptor compartment was filled with PBS pH 6.4 solution. The sample (1 mL) was withdrawn at specific intervals (0.08 to 6 h) and replenished with an equal volume of PBS pH 6.4. Further, the samples were centrifuged at 15,000 rpm for 15 min and analyzed using the previously discussed HPLC method. From the obtained results, the

graph of percentage drug permeated *vs.* time (h) was plotted for each formulation [23]. Additionally, the amount of drug permeated across unit area of nasal mucosa ($\mu\text{g}/\text{cm}^2$) *vs.* time (h) was plotted for each formulation (RIV-HT gel, RIV:DHA gel, RIV:DHA ND gel). The values of permeation coefficient (cm/h) and flux ($\mu\text{g}/\text{cm}^2/\text{h}$) were calculated from the slopes of each respective graph. [24].

5.2.9 *In-vivo* study in rats

In-vivo study was performed using Wistar rats weighing 230-260 g. Animals were caged in facility compliant with authority guidelines. The experiment was performed as per protocol issued by the institutional animal ethics committee (Protocol number: IAEC/RES/32/05). Animals were divided into 3 groups (15 animals in each group).

Group I: Intranasal administration of RIV-HT gel

Group II: Intravenous administration of RIV-HT sol

Group III: Intranasal administration of RIV:DHA ND gel

Group I and III received intranasal dosing equivalent to 2 mg/kg RIV-HT. The dose was administered using a micropipette attached with 1.3 cm soft polypropylene tube (Instech Laboratories, PA,291 USA). After giving anesthesia using isoflurane, animals were held upright in the supine position and 100 μL dose volume was instilled in each nostril. The animal was held in the same position for atleast 30 sec or until recovery of anesthesia to ensure effective dosing or prevent drug loss from the nasal cavity. In group II, rats were anesthetized and 2mg/kg RIV-HT sol (400 μL) was administered intravenously through tail vein.

5.2.9.1 Mucociliary clearance time

Mucociliary clearance time can be described as the time the drug takes to reach pharynx from the nasal cavity. The swab was taken from oropharyngeal cavity after 5 min time interval

upto 1 h. The samples were suitably diluted with mobile phase (ACN: phosphate buffer: IPA, 33:65:2) and analyzed using a validated HPLC method [17]. The first time point at which RIV-HT was detected in the oropharyngeal swab was noted as mucociliary clearance time for respective formulation.

5.2.9.2 Pharmacokinetic study in rats

Blood samples were withdrawn through retro-orbital puncture at time 0 (pre-dose), 0.25, 0.5, 1, 2, 4, 6, 12, 18 and 24 h. Animals were sacrificed using cervical dislocation, and whole brain was collected at 0.75, 2, 6, 12 and 24 h time intervals. Brain and plasma samples were analyzed using the validated bioanalytical HPLC method described in Chapter 3, section 3.4.2.5. The samples were processed as per the procedure described in Chapter 3, section 3.4.2.4. Furthermore, to determine brain and plasma P.K. parameters, non-compartmental analysis was computed using Phoenix WinNonlin software (version 8.3, Pharsight Corporation, NC, USA).

DTE (%) (equation 1) and DTP (%) (equation 2 and 3) indices were calculated to evaluate the brain targeting efficiency of respective RIV-HT formulation. DTP (%) indicates the percentage of drug directly reaching brain, *via.* intranasal delivery. Whereas DTE (%) indicates total percentage of RIV-HT reaching brain, *via.* direct intranasal and indirect intranasal through systemic circulation to the brain.

$$DTE (\%) = \frac{\frac{(AUC_{brain})_{IN}}{(AUC_{plasma})_{IN}}}{\frac{(AUC_{brain})_{IV}}{(AUC_{plasma})_{IV}}} \times 100 \quad \dots (1)$$

$$DTP (\%) = \frac{(AUC_{brain})_{IN} - F}{(AUC_{brain})_{IN}} \times 100 \quad \dots (2)$$

$$F = \frac{(AUC_{brain})_{IV}}{(AUC_{plasma})_{IV}} \times (AUC_{plasma})_{IN} \quad \dots (3)$$

Where $(AUC_{\text{brain}})_{\text{IN}} = AUC_{0-t}$ in brain after intranasal administration and $(AUC_{\text{plasma}})_{\text{IN}} = AUC_{0-t}$ in plasma after intranasal administration $(AUC_{\text{brain}})_{\text{IV}} = AUC_{0-t}$ in brain after intravenous administration and $(AUC_{\text{plasma}})_{\text{IV}} = AUC_{0-t}$ in plasma after intravenous administration.

DTE (%) value greater than 100 indicates enhanced brain targeting through intranasal pathway than the intravenous route. Whereas DTP (%) value greater than 0 indicates direct nose-to-brain transport of the drug. AUC_{0-t} was employed to calculate percent indices for respective formulations.

5.2.10 Histopathological study

The study was performed for histopathological observation of nasal epithelium and brain, followed by intranasal administration of developed formulations. Untreated rats were used as control. After 24 h, animals were sacrificed, brain and nasal epithelium of the respective formulation-treated group (RIV-HT gel and RIV:DHA ND gel) was carefully removed. The tissues were collected and washed with PBS pH 7.4 to remove blood and connective tissue. Further, it was fixed in 10 % (v/v) formalin. Samples were dehydrated with a series of dilutions with methyl alcohol, ethyl alcohol, followed by absolute ethyl alcohol. The samples were treated with xylene, and tissue was embedded in molten paraffin (56° C) and stored for 24 h. The paraffin tissue blocks were sectioned (3-4 μm) using a sledge microtome. Further, tissue was deparaffinized, stained with eosin and hematoxylin [25], and observed under the light microscope (Axio Vert. A1 FL, Carl Zeiss, Jena, Germany).

5.2.11 Statistical analysis

Statistical testing was conducted using GraphPad Prism, version 8 (GraphPad Software, La Jolla, CA, USA). All quantifiable data was described as mean \pm standard deviation (S.D.), and differences within treatment groups were investigated using ANOVA or student's t-test

followed by Tukey's multiple comparison test. The value of 'p' <0.05 was considered as statistically significant.

5.3 Result

5.3.1 Preparation and characterization of RIV:DHA

The physical characteristics of dried RIV:DHA showed appearance of brownish-yellow, lustrous semisolid precipitate (**Fig.5.1**). The results of RIV:DHA characterization are described in Chapter 4, section 4.3.2.

5.3.2 Preliminary screening of surfactant for preparation of RIV:DHA ND

Surfactant screening demonstrated maximum solubility of RIV:DHA in tween 80 followed by PEG-32-stearate and tween 60 with 73.89 ± 0.73 , 73.78 ± 1.46 and 72.34 ± 0.73 mg, respectively. The surfactant exhibiting maximum solubility, *viz.*, tween 80 was selected for preparation of RIV:DHA ND.

5.3.3 Preparation of RIV:DHA ND

The optimized RIV:DHA ND showed particle size (PDI) and zeta potential of 152.2 ± 0.7 nm (0.243 ± 0.024) (**Fig.5.2A**) and -24.2 ± 0.8 mV (**Fig.5.2B**) respectively. Several reports suggest that nanoparticles with size below 200 nm have eligibility to pass through trigeminal nerve pathway mediated by axonal flow [26]. Additionally, negatively charged nanoparticles have a greater probability of transport through the olfactory pathway [27]. The zeta potential of nanoformulation could predict the stability of colloidal systems [28]. Generally, aqueous dispersion with zeta potential around ± 30 mV is considered to have good colloidal stability [29].

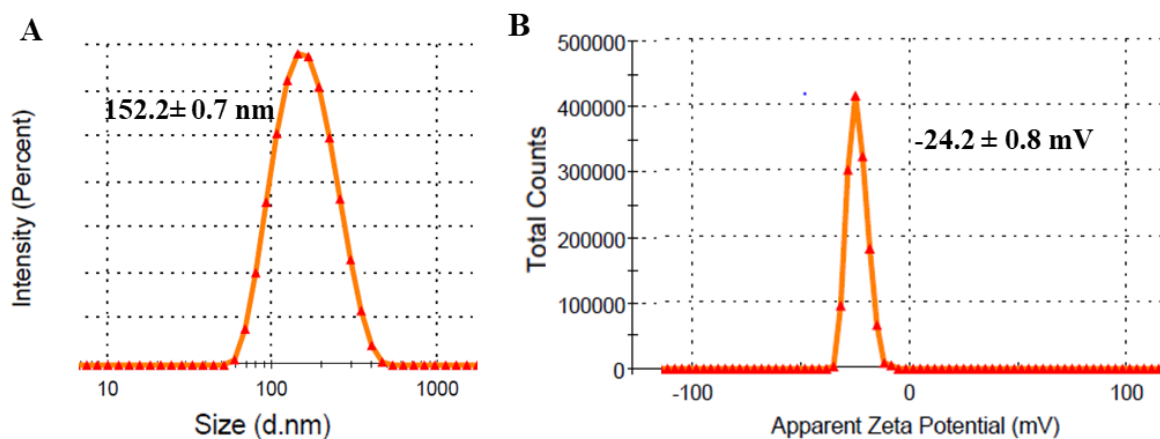


Fig. 5.2. Image represents (A) particle size and (B) zeta potential of RIV:DHA ND

5.3.4 Hydrogel rheological characterization

The rheological study evaluated temperature-dependent viscosity and various other viscosity parameters, along with gel behavior at different angular frequencies. RIV:DHA ND gel was subjected to amplitude and frequency of 0.5% shear strain at 10 rad/s within LVER. The viscosity of RIV:DHA ND gel at 33°C was 340.27 ± 26.04 mPa.s as shown in **Fig.5.3A**. The graph of storage modulus (G') and loss modulus (G'') vs temperature showed the presence of gel-like structure at nasal cavity temperature (33°C) (**Fig.5.3B**). The storage and loss modulus at different angular frequencies at constant temperature (at 33°C) was observed to be 208.17 ± 22.86 Pa and 30.09 ± 2.13 Pa, respectively (**Fig.5.3B**). Samples maintained at 33°C showed $\tan \delta$ value less than 1 (data not shown), demonstrating maintained integrity of gel at all angular frequencies (**Fig.5.3C**) [20].

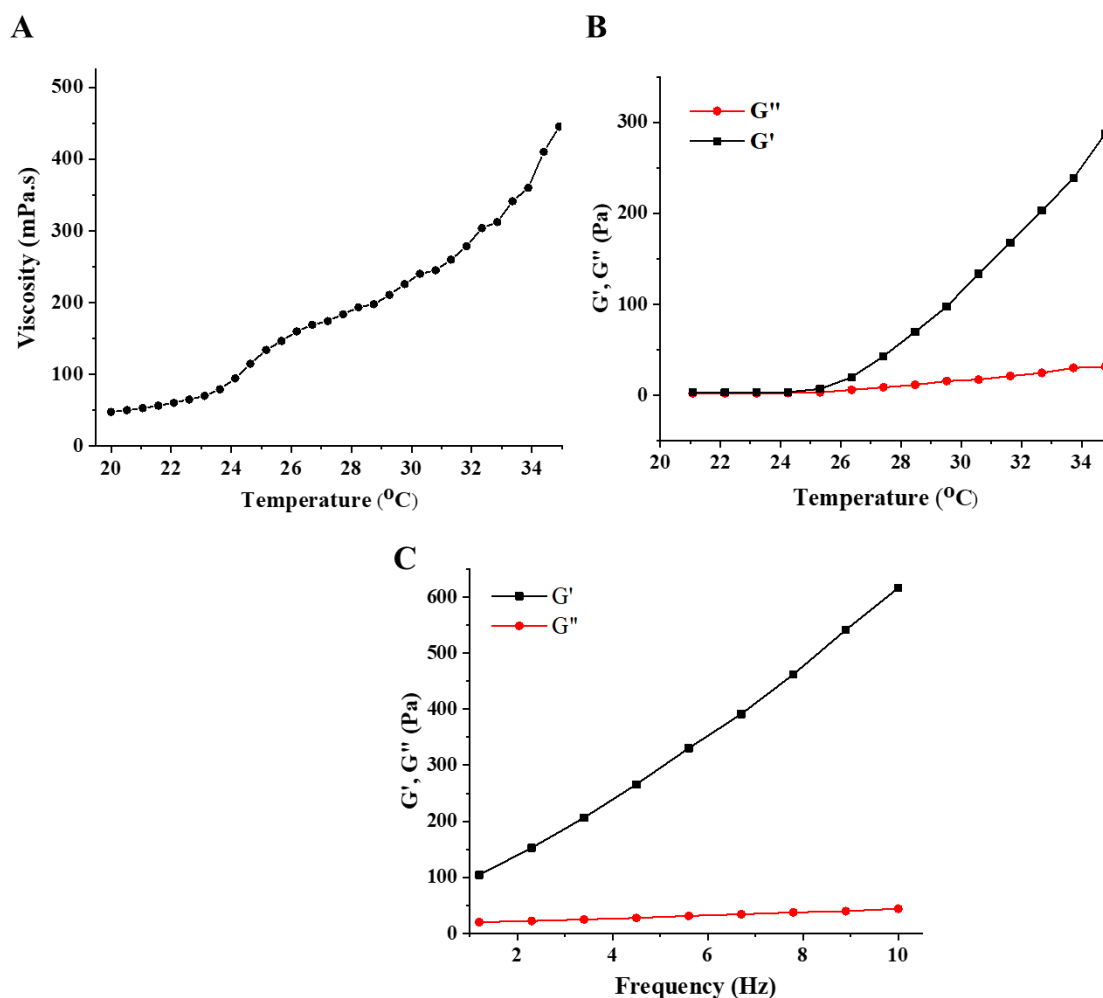


Fig. 5.3. (A) Graph of temperature vs viscosity of RIV:DHA ND gel representing viscosity at 33° C. Graph demonstrates storage modulus and loss modulus of RIV:DHA ND gel representing hydrogel behavior at different (B) temperature and (C) angular frequency.

5.3.4.1 Scanning electron microscopy

FE-SEM images of RIV-HT (**Fig.5.4A**) indicated a difference in physical appearance after formation of RIV:DHA (**Fig.5.4B**). RIV:DHA ND (**Fig.5.4C**) indicated the formation of spherical-shaped nanoparticles. Nanoformulation when incorporated into a hydrogel may form aggregates that could impact the overall therapeutic efficacy. The FE-SEM analysis of RIV:DHA ND gel (**Fig.5.4D**) showed an intact spherical shape with no signs of aggregation after loading into the hydrogel.

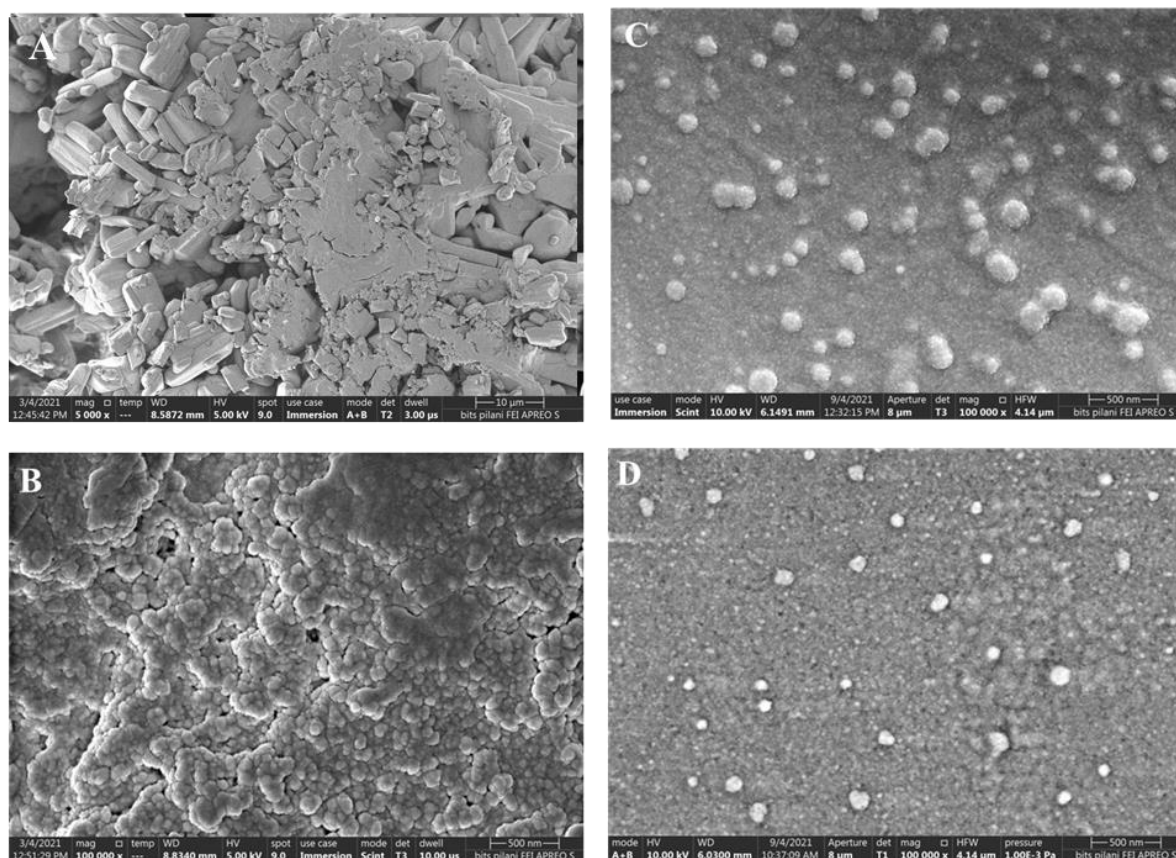


Fig. 5.4. SEM micrographs of (A) RIV-HT (Magnification: 5000X, scale bar: 2 μm), (B) RIV:DHA (1:1 molar ratio), (C) RIV:DHA ND and (D) RIV:DHA ND gel (Magnification: 100000X, scale bar: 500nm).

5.3.4.2 Stability study

The stability study of RIV:DHA ND gel was evaluated at refrigerated storage conditions. The particle size, PDI and zeta potential at each time point were compared with freshly prepared sample (0 h). Generally, nanoparticle aggregation and instability led to increased particle size, PDI and change in zeta-potential. RIV:DHA ND gel exhibited no significant change in particle size, PDI and zeta potential values upto 90 days (**Fig.5.5**). Thus, nanodispersion-embedded gel remained stable for at least 3 months at respective storage conditions.

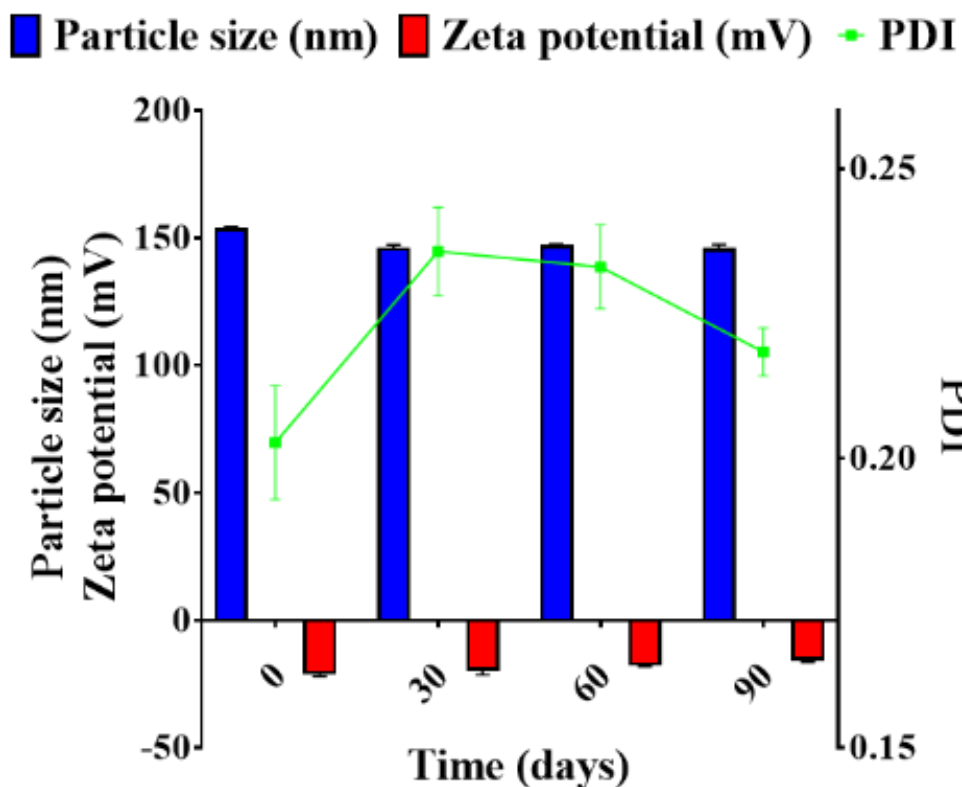


Fig. 5.5. Image represents stability study of RIV:DHA ND gel at refrigerated condition. The graph represented no significant increase in particle size, PDI of nanodispersion gel up to 90 days, representing stability of formulation upto 3 months.

5.3.5 *In vitro* drug release study

RIV:DHA ND gel exhibited slow, controlled drug release upto 24 hours, whereas RIV-HT gel showed 100 % release within 4 h. While, RIV:DHA ND gel showed only 18.55 ± 0.15 % drug release in 4 hours (**Fig.5.6A**). T_{25} , T_{50} and T_{75} values for RIV:DHA ND gel was observed to be 5.82, 11.88 and 18.07 h respectively. Drug release data fitted into kinetic release models demonstrated that RIV:DHA ND gel followed Korsmeyer's Peppas model. The 'n' value obtained from Korsmeyer's Peppas model ($n = 0.971$) indicated anomalous behavior or non-fickian diffusion exhibited by nanodispersion-loaded gel [27].

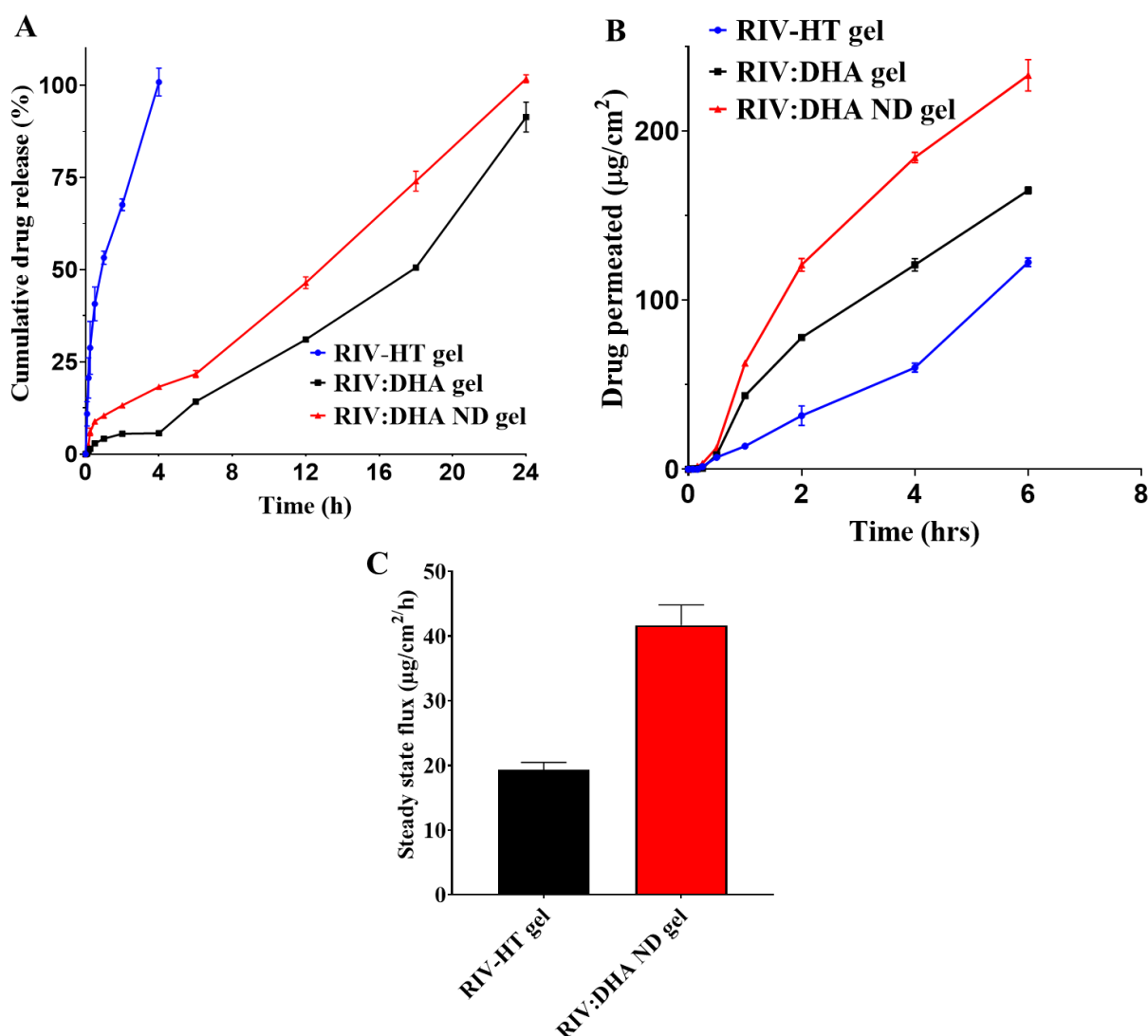


Fig. 5.6. *In-vitro* drug release profile from (A) RIV:DHA ND gel and (B) *ex-vivo* nasal permeation study showing the amount of drug permeated in case of RIV:DHA ND gel. (C) Represents improved steady-state flux of RIV:DHA ND gel as compared to RIV:HT gel.

5.3.6 *Ex-vivo* nasal permeation

The study evaluated the permeation behavior of developed RIV:DHA ND gel across nasal mucosa. Due to its hydrophilic nature, RIV:HT leads to limited permeation across lipophilic nasal barriers. The amount of drug permeated in case of RIV:DHA gel formulations was improved compared to RIV:HT gel. RIV:HT gel ($122.32 \pm 2.55 \mu\text{g}/\text{cm}^2$), RIV:DHA gel showed enhanced drug diffusion upto $164.85 \pm 1.97 \mu\text{g}/\text{cm}^2$ as shown in **Fig.5.6B**. Moreover, the reduced particle size in RIV:DHA ND gel showed further increase in permeation upto

$232.87 \pm 9.22 \mu\text{g}/\text{cm}^2$. The steady-state flux of RIV:DHA ND was significantly greater than RIV-HT gel (**Fig.5.6C**). The percentage cumulative diffusion data fitted into kinetic release models showed that RIV:DHA ND gel followed Korsmeyer's Peppas model. The n value obtained from Korsmeyer's Peppas model ($n= 1.097$) indicated super case II transport [30].

5.3.7 Pharmacokinetic study in rats

5.3.7.1 Mucociliary drug clearance

RIV-HT gel and RIV:DHA ND gel demonstrated mucociliary clearance time of 16.75 ± 3.41 , 23.33 ± 2.88 (**Fig.5.7A**). The mucociliary clearance time of RIV:DHA ND gel was observed to be slightly greater than RIV-HT gel. This may be due to the hydrophobic interaction of RIV:DHA ND with mucosa, which improved the drug residence time in the nasal cavity.

5.3.7.2 Pharmacokinetic study in rats

P.K. study evaluated RIV:DHA ND gel brain targeting efficiency compared to RIV-HT gel formulation. The brain (**Fig.5.7B**), plasma drug profiles (**Fig.5.7C**), and PK parameters elucidated enhanced nose-to-brain transport efficiency of RIV:DHA ND gel.

Interestingly, the brain profiles of RIV:DHA ND gel exhibited the substantially improved C_{max} in comparison to RIV-HT gel. The hydrophobic nanodispersion significantly improved brain C_{max} concentrations with 2.18 -fold improvement than RIV-HT gel ($p < 0.05$). It also demonstrated considerably higher brain concentrations at all time points than RIV-HT gel. The maximum brain concentrations achieved in RIV:DHA ND are due to greater drug permeation efficiency and reduced particle size (**Fig.5.7B**). Compared to RIV-HT gel formulation, brain PK parameters demonstrated 4.27-fold improved MRT of RIV:DHA ND gel (**Table 5.1**). The improved drug MRT is supported by significantly increased brain AUC_{0-t} concentrations (**Fig.5.7B**). The considerably improved brain transport efficiency portrayed significantly increased AUC_{0-t} of RIV:DHA ND gel. It exhibited 3.24-fold increased brain

AUC_{0-t} compared to RIV-HT gel. The DTE (%) values for RIV-HT gel, RIV:DHA ND gel was observed to be 281.28 % and 670.18 % ($p < 0.05$). Whereas DTP (%) values were observed to be 64.44 % and 85.07 % ($p < 0.05$), respectively (**Table 5.1**). The significantly improved DTE (%), DTP (%) values also confirm the efficient brain targeting of RIV:DHA ND gel compared to RIV-HT gel formulation.

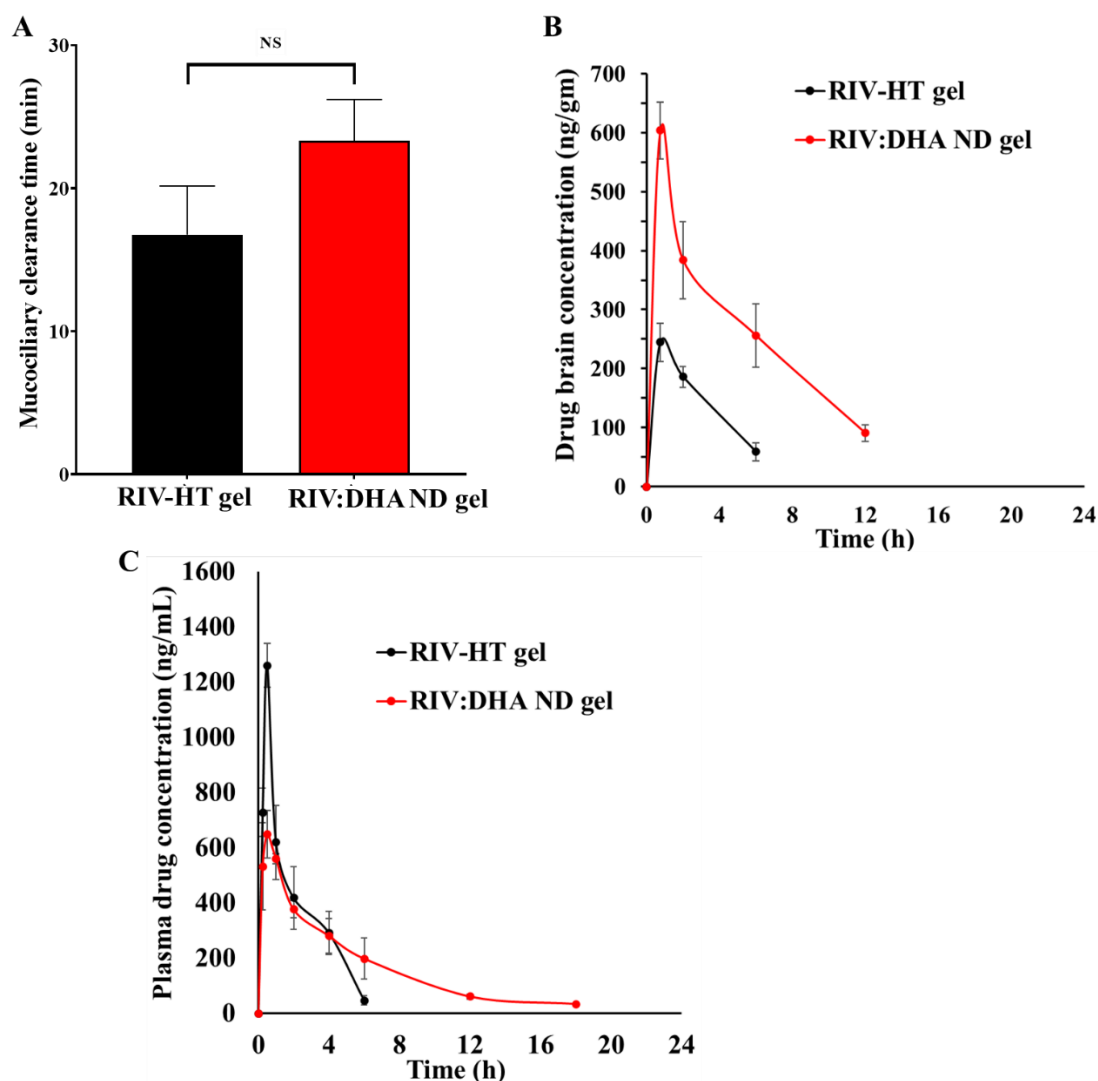


Fig. 5.7. (A) significantly increased mucociliary clearance time of RIV:DHA ND gel formulation (* signify $p < 0.05$ and N.S. signify no significant difference). (B) Brain profile of RIV-HT formulations demonstrate significantly improved brain concentrations and mean residence time of RIV in RIV:DHA ND gel formulation. (C) Represents plasma profile of RIV-HT formulations in which RIV-HT gel showed higher plasma concentrations and RIV:DHA ND gel showed comparatively reduced plasma concentration of RIV-HT.

Table 5.1. Brain and plasma P.K. parameters after intranasal administration of RIV-HT gel, RIV:DHA ND gel formulation

Matrix	PK parameters	RIV-HT gel	RIV:DHA ND gel
Brain	C_{\max} (ng/g)	277.38 ± 0.20	603.66 ± 104.51
	T_{\max} (h)	0.66 ± 0.08	0.75
	$T_{1/2}$ (h)	1.32 ± 0.26	6.27 ± 1.67
	MRT (h)	2.02 ± 0.45	8.62 ± 1.73
	AUC_{0-t} (ng/g*h)	934.91 ± 49.86	3029.61 ± 887.08
Plasma	C_{\max} (ng/mL)	1261.21 ± 80.83	677.02 ± 79.66
	T_{\max} (h)	0.50	0.58 ± 0.22
	$T_{1/2}$ (h)	1.28 ± 0.09	6.18 ± 2.05
	MRT (h)	1.94 ± 0.16	7.11 ± 0.80
	AUC_{0-t} (ng/ml*h)	2363.14 ± 358.88	3214.09 ± 625.06
-	DTE (%)	281.28	670.18
	DTP (%)	64.44	85.07

Data is expressed as mean ± standard error of mean (n = 3)

5.3.8 Histopathological study

The study evaluated the safety of developed RIV:DHA ND gel formulation upon intranasal administration in rats.

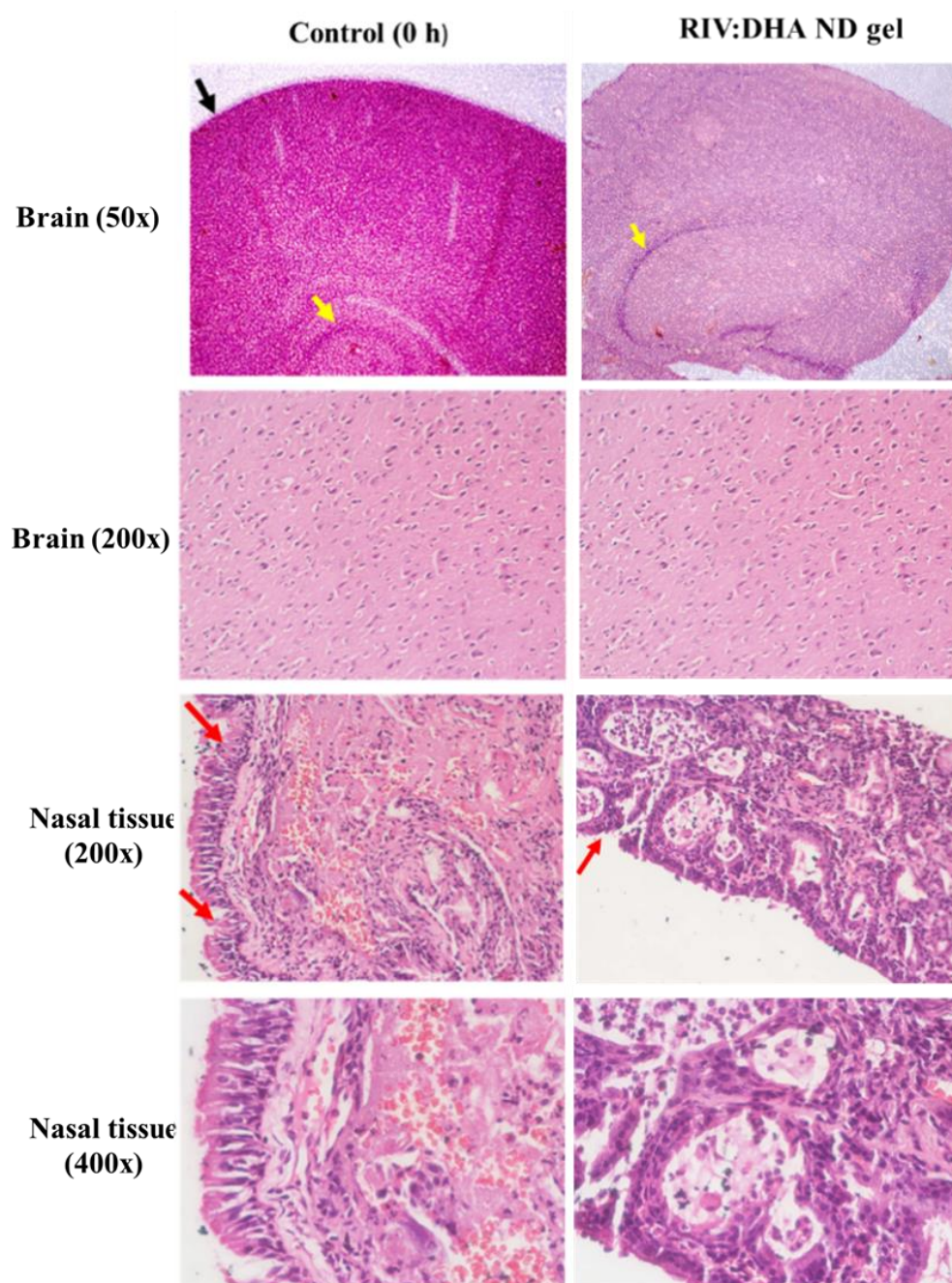


Fig. 5.8. Histopathological evaluation of nasal and brain tissue after intranasal administration of RIV:DHA ND gel were compared with control group. The microscopic images of brain showed no signs of damage/toxicity in cerebral cortex and hippocampus. Nasal tissue also

showed intact morphological structure of pseudostratified ciliated columnar cells of RIV:DHA ND gel formulation as that of control group

Arrow indications as follows- Black arrow: Cerebral cortex, Yellow arrow: Hippocampus, Red arrow: Ciliated columnar cells

The histological sections of the respective formulation-treated group showed intact morphological structures of nasal epithelium and brain as that of the control group (**Fig.5.8**).

The brain specimens showed typical morphological structures as that of the control with no histological alterations in the brain, ensuring safety of the developed RIV:DHA ND gel.

5.4 Conclusion

The present work demonstrated the exploration of DHA-based ion-pair complex for nose-to-brain delivery of Alzheimer's therapeutics. The developed RIV:DHA ND gel showed sustained *in-vitro* drug release upto 24 h. RIV:DHA ND gel resulted in 2.18, 4.27 and 3.24 fold improved brain C_{max} , MRT and AUC_{0-t} concentrations compared to RIV-HT gel. Histopathological examination of intranasally administered RIV:DHA ND gel assured the safety of the developed formulations. Thus, RIV:DHA ND gel system could be an efficient intranasal delivery system for improved nose-to-brain targeting in management of brain disorders.

References

- [1] G.V. Paraskevi Papakyriakopoulou, Evangelos Balafas , Gaia Colombo , Dimitrios M. Rekkas , Nikolaos Kostomitsopoulos, Nose-to-Brain delivery of donepezil hydrochloride following administration of an HPMC-Me- β -CD-PEG400 nasal film in mice, *J. Drug Deliv. Sci. Technol.* 84 (2023) 104463.
<https://doi.org/https://doi.org/10.1016/j.jddst.2023.104463>.
- [2] U. Kosak, B. Brus, D. Knez, R. Sink, S. Zakelj, J. Trontelj, A. Pisljar, J. Slenc, M. Gobec, M. Zivin, L. Tratnjek, M. Perse, K. Sałat, A. Podkova, B. Filipek, F. Nachon, X. Brazzolotto, A. Więckowska, B. Malawska, J. Stojan, I.M. Raščan, J. Kos, N. Coquelle, J.P. Colletier, S. Gobec, Development of an in-vivo active reversible butyrylcholinesterase inhibitor, *Sci. Rep.* 6 (2016) 1–16.
<https://doi.org/10.1038/srep39495>.
- [3] P. Wavikar, R. Pai, P. Vavia, Nose to brain delivery of rivastigmine by in situ gelling cationic nanostructured lipid carriers: Enhanced brain distribution and pharmacodynamics, *J. Pharm. Sci.* 106 (2017) 3613–3622.
<https://doi.org/10.1016/j.xphs.2017.08.024>.
- [4] P.R. Wavikar, P.R. Vavia, Rivastigmine-loaded in situ gelling nanostructured lipid carriers for nose to brain delivery, *J. Liposome Res.* 25 (2015) 141–149.
<https://doi.org/10.3109/08982104.2014.954129>.
- [5] F. Sonvico, A.R. Clementino, F. Buttini, G. Colombo, Surface-modified nanocarriers for nose-to-brain delivery : from bioadhesion to targeting, (2018).
<https://doi.org/10.3390/pharmaceutics10010034>.
- [6] M. Agrawal, S. Saraf, S. Saraf, S.G. Antimisiaris, M.B. Chougule, S.A. Shoyele, A. Alexander, Nose-to-brain drug delivery: An update on clinical challenges and progress

- towards approval of anti-Alzheimer drugs, *J. Control. Release.* 281 (2018) 139–177.
<https://doi.org/10.1016/j.jconrel.2018.05.011>.
- [7] A. Froelich, T. Osmałek, B. Jadach, V. Puri, B. Michniak-Kohn, Microemulsion-based media in nose-to-brain drug delivery, *Pharmaceutics.* 13 (2021) 1–37.
<https://doi.org/10.3390/pharmaceutics13020201>.
- [8] K.D. Ristroph, R.K. Prud'homme, Hydrophobic ion pairing: Encapsulating small molecules, peptides, and proteins into nanocarriers, *Nanoscale Adv.* 1 (2019) 4207–4237. <https://doi.org/10.1039/c9na00308h>.
- [9] A.S. Torky, M.S. Freag, M.M.A. Nasra, O.Y. Abdallah, Novel skin penetrating berberine oleate complex capitalizing on hydrophobic ion pairing approach, *Int. J. Pharm.* 549 (2018) 76–86. <https://doi.org/10.1016/j.ijpharm.2018.07.051>.
- [10] C. Song, C.H. Shieh, Y.S. Wu, A. Kalueff, S. Gaikwad, K.P. Su, The role of omega-3 polyunsaturated fatty acids eicosapentaenoic and docosahexaenoic acids in the treatment of major depression and Alzheimer's disease: Acting separately or synergistically?, *Prog. Lipid Res.* 62 (2016) 41–54.
<https://doi.org/10.1016/j.plipres.2015.12.003>.
- [11] G.A. Jicha, W.R. Markesbery, Omega-3 fatty acids: Potential role in the management of early Alzheimer's disease, *Clin. Interv. Aging.* 5 (2010) 45–61.
<https://doi.org/10.2147/cia.s5231>.
- [12] M. Tamaru, H. Akita, K. Kajimoto, Y. Sato, H. Hatakeyama, H. Harashima, An apolipoprotein E modified liposomal nanoparticle : Ligand dependent efficiency as a siRNA delivery carrier for mouse-derived brain endothelial cells, *Int. J. Pharm.* 465 (2014) 77–82. <https://doi.org/10.1016/j.ijpharm.2014.02.016>.

-
- [13] H. Chew, V.A. Solomon, A.N. Fonteh, Involvement of lipids in Alzheimer's disease pathology and potential therapies, *Front. Physiol.* 11 (2020) 1–28.
<https://doi.org/10.3389/fphys.2020.00598>.
- [14] R.L. Shinde, P. V. Devarajan, Docosahexaenoic acid-mediated, targeted and sustained brain delivery of curcumin microemulsion, *Drug Deliv.* 24 (2017) 152–161.
<https://doi.org/10.1080/10717544.2016.1233593>.
- [15] D. Khunt, S. Polaka, M. Shrivasa, M. Misra, Biodistribution and amyloid beta induced cell line toxicity study of intranasal Rivastigmine microemulsion enriched with Fish Oil and Butter oil, *J. Drug Deliv. Sci. Technol.* 57 (2020) 101661.
<https://doi.org/10.1016/j.jddst.2020.101661>.
- [16] M.M. Aakash Katdare, Dignesh Khunt, Shreya Thakkar, Surya Narayana Polaka, Comparative evaluation of fish oil and butter oil in modulating delivery of galantamine hydrobromide to brain via intranasal route: pharmacokinetic and oxidative stress studies., *Drug Deliv. Transl. Res.* 10 (2020) 1136–1146.
<https://doi.org/10.1007/S13346-020-00739-Y>.
- [17] N.S. Hinge, M.M. Pandey, Sensitive RP-HPLC method of rivastigmine for applicative quantification of nanostructured lipid carriers, *Microchem. J.* 188 (2023) 108341.
<https://doi.org/10.1016/J.MICROC.2022.108341>.
- [18] S. Uddin, M.R. Islam, M.R. Chowdhury, R. Wakabayashi, N. Kamiya, M. Moniruzzaman, M. Goto, Lipid-Based Ionic-Liquid-Mediated Nanodispersions as Biocompatible Carriers for the Enhanced Transdermal Delivery of a Peptide Drug, *ACS Appl. Bio Mater.* 4 (2021) 6256–6267. <https://doi.org/10.1021/acsabm.1c00563>.
- [19] J. Ma, C. Wang, Y. Sun, L. Pang, S. Zhu, Y. Liu, L. Zhu, S. Zhang, L. Wang, L. Du, Comparative study of oral and intranasal puerarin for prevention of brain injury

- induced by acute high-altitude hypoxia, *Int. J. Pharm.* 591 (2020) 120002.
<https://doi.org/10.1016/j.ijpharm.2020.120002>.
- [20] P. Pandey, P.J. Cabot, B. Wallwork, B.J. Panizza, H.S. Parekh, Formulation, functional evaluation and ex vivo performance of thermoresponsive soluble gels - A platform for therapeutic delivery to mucosal sinus tissue, *Eur. J. Pharm. Sci.* 96 (2017) 499–507. <https://doi.org/10.1016/j.ejps.2016.10.017>.
- [21] C.T. Uppuluri, P.R. Ravi, A. V. Dalvi, S.S. Shaikh, S.R. Kale, Piribedil loaded thermo-responsive nasal in situ gelling system for enhanced delivery to the brain: formulation optimization, physical characterization, and in vitro and in vivo evaluation, *Drug Deliv. Transl. Res.* 11 (2021) 909–926.
<https://doi.org/10.1007/s13346-020-00800-w>.
- [22] S. Salatin, J. Barar, M. Barzegar-Jalali, K. Adibkia, M. Jelvehgari, Thermosensitive in situ nanocomposite of rivastigmine hydrogen tartrate as an intranasal delivery system: Development, characterization, ex vivo permeation and cellular studies, *Colloids Surf. B. Biointerfaces.* 159 (2017) 629–638. <https://doi.org/10.1016/j.colsurfb.2017.08.031>.
- [23] K. Florence, L. Manisha, B.A. Kumar, K. Ankur, M.A. Kumar, M. Ambikanandan, Intranasal clobazam delivery in the treatment of status epilepticus, *J. Pharm. Sci.* 100 (2011) 692–703. <https://doi.org/10.1002/JPS.22307>.
- [24] B. Shah, D. Khunt, H. Bhatt, M. Misra, H. Padh, Application of quality by design approach for intranasal delivery of rivastigmine loaded solid lipid nanoparticles: Effect on formulation and characterization parameters, *Eur. J. Pharm. Sci.* 78 (2015) 54–66.
<https://doi.org/10.1016/J.EJPS.2015.07.002>.
- [25] S. Nageeb El-Helaly, A.A. Elbary, M.A. Kassem, M.A. El-Nabarawi, Electrosteric stealth Rivastigmine loaded liposomes for brain targeting: preparation,

- characterization, ex vivo, bio-distribution and in vivo pharmacokinetic studies, *Drug Deliv.* 24 (2017) 692–700. <https://doi.org/10.1080/10717544.2017.1309476>.
- [26] Y. Su, B. Sun, X. Gao, X. Dong, L. Fu, Y. Zhang, Z. Li, Intranasal delivery of targeted nanoparticles loaded with miR-132 to brain for the treatment of neurodegenerative diseases, *Front. Pharmacol.* 11 (2020) 1–13. <https://doi.org/10.3389/fphar.2020.01165>.
- [27] A. Bonaccorso, T. Musumeci, M.F. Serapide, R. Pellitteri, I.F. Uchegbu, G. Puglisi, Nose to brain delivery in rats: Effect of surface charge of rhodamine B labeled nanocarriers on brain subregion localization, *Colloids Surfaces B Biointerfaces.* 154 (2017) 297–306. <https://doi.org/10.1016/J.COLSURFB.2017.03.035>.
- [28] D. Sharma, D. Maheshwari, G. Philip, R. Rana, S. Bhatia, M. Singh, R. Gabrani, S.K. Sharma, J. Ali, R.K. Sharma, S. Dang, Formulation and optimization of polymeric nanoparticles for intranasal delivery of lorazepam using Box-Behnken design: In vitro and in vivo evaluation, *Biomed Res. Int.* 2014 (2014). <https://doi.org/10.1155/2014/156010>.
- [29] B. Cui, F. Gao, Z. Zeng, C. Wang, Y. Wang, C. Sun, X. Zhao, L. Guo, Y. Shen, G. Liu, H. Cui, Construction and characterization of avermectin B2 solid nanodispersion, *Sci. Rep.* 10 (2020) 1–9. <https://doi.org/10.1038/s41598-020-66098-3>.
- [30] P. Costa, J.M. Sousa Lobo, Modeling and comparison of dissolution profiles, *Eur. J. Pharm. Sci.* 13 (2001) 123–133. [https://doi.org/10.1016/S0928-0987\(01\)00095-1](https://doi.org/10.1016/S0928-0987(01)00095-1).

CHAPTER 6

**CHITOSAN-COATED LIPOSOMES EMBEDDED
INTO *IN-SITU* GEL SYSTEM IMPROVED NOSE-TO-
BRAIN TARGETING OF RIVASTIGMINE IN
ALZHEIMER'S DISEASE**

6.1 Introduction

AD is a progressive neurodegenerative disorder characterized by early signs of mild dementia, impaired cognition, and decision-making. The condition progressively culminates into chronic stage, which includes symptoms such as cognitive loss, impaired behavioral and memory function. It gradually turns into inability of the patient to perform daily routine activities and at the end-stage, the patient eventually becomes bedridden [1]. The increasing population of Alzheimer's is a serious concern in geriatrics and young adults (early Alzheimer's), increasing the social and economic burden globally [2]. Worldwide 50 million people have Alzheimer's and related dementias in 2018. Nearly every 3 second, someone in world develops AD-related dementia [3], making it the fifth leading cause of death globally amongst geriatrics beyond age 65 years [4].

RIV-HT is a reversible, para-symphomimetic drug, dual-acting cholinesterase used to treat mild to moderate Alzheimer's and related dementias [5]. Cholinergic synaptic deficit leads to AD-associated symptoms. Cholinesterase inhibitors increase acetylcholine concentration in the CNS, facilitating recovery of cholinergic synapses [2,5]. However, orally administered rivastigmine exhibits very low bioavailability (36%), extensive first-pass metabolism [5], shorter half-life (90 min), intra-individual variability, require repetitive dose administration and is associated with severe cholinergic gastro-intestinal mediated side-effects [6]. Furthermore, the hydrophilic RIV-HT represents a lesser concentration in CNS due to limited permeability across BBB. Therefore, the current oral therapy with RIV-HT necessitates the development of an alternative approach to improve brain targeting and therapeutic effectiveness in the treatment of AD.

Nose-to-brain delivery has emerged as a potential, non-invasive strategy for brain targeting. It facilitates the direct transport of drugs to the CNS, devoiding BBB, first-pass metabolism, minimal systemic exposure and associated peripheral drug side-effects [7]. The present study

attempted delivery of RIV-HT using intranasal route. However, intranasal delivery of RIV-HT as a free drug is associated with limitations such as limited permeability, rapid mucociliary clearance, enzymatic degradation, and inability to transport actives, *via.* olfactory and trigeminal nerve-mediated pathways [8,9]. These limitations of intranasal delivery could be overcome with nanoparticle-loaded *in-situ* hydrogel-based systems [9]. The hydrogel-based intranasal delivery has been extensively studied for brain targeting [10–12]. Thermoresponsive polymers such as poloxamer and poly(N-acrylamide) have been extensively reported in the development of intranasal hydrogels. These hydrogel undergoes sol-gel transitioning in the nasal cavity, delaying mucociliary clearance and improving drug absorption to the brain [11]. Nanoparticle-based intranasal delivery increases nasal permeation efficiency, and site-specific targeting, *via.* olfactory and trigeminal nerve-mediated pathways [13]. Amongst colloidal nanocarrier systems, liposomes are reported to be efficient for effective intranasal delivery of RIV-HT [14]. Furthermore, due to its structural and consequent functional versatile nature, it has been extensively utilized in loading of hydrophilic drugs [15–18]. However, liposomes are associated with some challenges such as compromised colloidal stability, prone to lipid oxidation [19], and drug leakage upon storage [20]. These drawbacks of RIV-HT Liposomes could be overcome with subsequent chitosan coating, which possesses the ability to lead to newer applications. Chitosan coating prevents undesired drug expulsion and provide sustained release profile [19,21]. Additionally, it offers several other advantages such as biocompatibility, mucoadhesion, and permeation enhancement [22,23]. It primarily interacts with anionic counterpart of mucous layers (sialic acid), and affects membrane permeability by transiently opening tight junctions in epithelial cells [2].

The present work hypothesized that chitosan coating onto RIV-HT Liposomes (CHT@RIV-HT Liposome) may improve stability, *in-vitro* drug release and permeation efficiency of hydrophilic RIV-HT. The optimized RIV-HT Liposome and CHT@RIV-HT Liposome were

loaded into an *in-situ* thermoresponsive gel (RIV-HT Liposome gel and CHT@RIV-HT Liposome gel) to enable longer drug retention in the nasal cavity. *In-vivo* PK study compared brain availability and N2B targeting efficiency of RIV-HT formulations. Further, the histopathological examination of brain and nasal tissue was conducted to ensure safety of the intranasally administered formulations.

6.2 Materials and method

6.2.1 Materials

Rivastigmine hydrogen tartrate and venlafaxine hydrochloride were obtained as a kind gift sample from Torrent Pharmaceuticals Ltd. (Ahmedabad, India) and Dr. Reddy's Laboratories Pvt. Ltd. (Hyderabad, India). Soya phosphatidylcholine (SPC) was obtained as a gift sample from Lipoid under brand name S100 (Ludwigshafen, Germany). Cholesterol was purchased from Merck (Mumbai, India). Low molecular weight chitosan (90% deacetylation) was purchased from SRL Laboratories Pvt. Ltd (Delhi, India). Glacial acetic acid and potassium dihydrogen phosphate were purchased from SD Fine Chemicals Ltd. (Mumbai, India). Hydrochloric acid, calcium chloride, sodium chloride, and potassium chloride were purchased from Central Drug House Pvt. Ltd. (New Delhi, India). Sodium hydroxide, orthophosphoric acid, triethyl amine and sodium dihydrogen phosphate were purchased from Merck (Mumbai, India). Chloroform was purchased from Spectrochem Pvt. Ltd. (Mumbai, India). HPLC-grade acetonitrile was purchased from Merck (Mumbai, India). Isoflurane USP was purchased from Abbott Laboratories (Mumbai, India) for inhalational anesthesia. Deionized (Milli-Q) water was obtained from our institute's central Millipore (Millipore®, Massachusetts, USA) unit facility.

6.2.2 Preparation of RIV-HT Liposome and CHT@RIV-HT Liposome

Liposomes were prepared using the thin film hydration method using different ratios of S100 and cholesterol to elucidate their effect on particle size and encapsulation efficiency. The schematic representation for preparation of RIV-HT Liposome gel and CHT@RIV-HT Liposome gel is provided in **Fig.6.1**. Briefly, S100 and cholesterol were dissolved in 1 ml chloroform. The solution was evaporated in a round bottom flask under vacuum rotary evaporator (Buchi R-210, St. Gallen, Switzerland) at 37 °C for 2 h to form a thin lipid film. Afterward, the film was stored overnight in a desiccator to ensure the complete removal of chloroform traces. The developed film was hydrated at 37 °C with an aqueous drug solution (10 mg/mL, 4mL) under continuous rotation on a rotary evaporator (200 rpm). The developed multilamellar liposomes were reduced using an ultrasonic probe sonicator at 25% amplitude for 3 min to obtain unilamellar liposomes. RIV-HT Liposome was prepared according to the procedure described in the previous report with minor modifications [24].

The formulation was adjusted to pH 7.4 using 0.1 M NaOH to develop a negative surface charge. The chitosan solution was prepared by dissolving low molecular chitosan in 1% (v/v) acetic acid solution. Equal volumes of RIV-HT Liposomes were gradually added to the chitosan solution with simultaneous rapid stirring for 1 h. Further, it was centrifugated (Remi CPR 24, Mumbai, India) at 5,000 rpm for 5 min to settle down coarse particles. The supernatant consisting of CHT@RIV-HT Liposome was separated and further characterized.

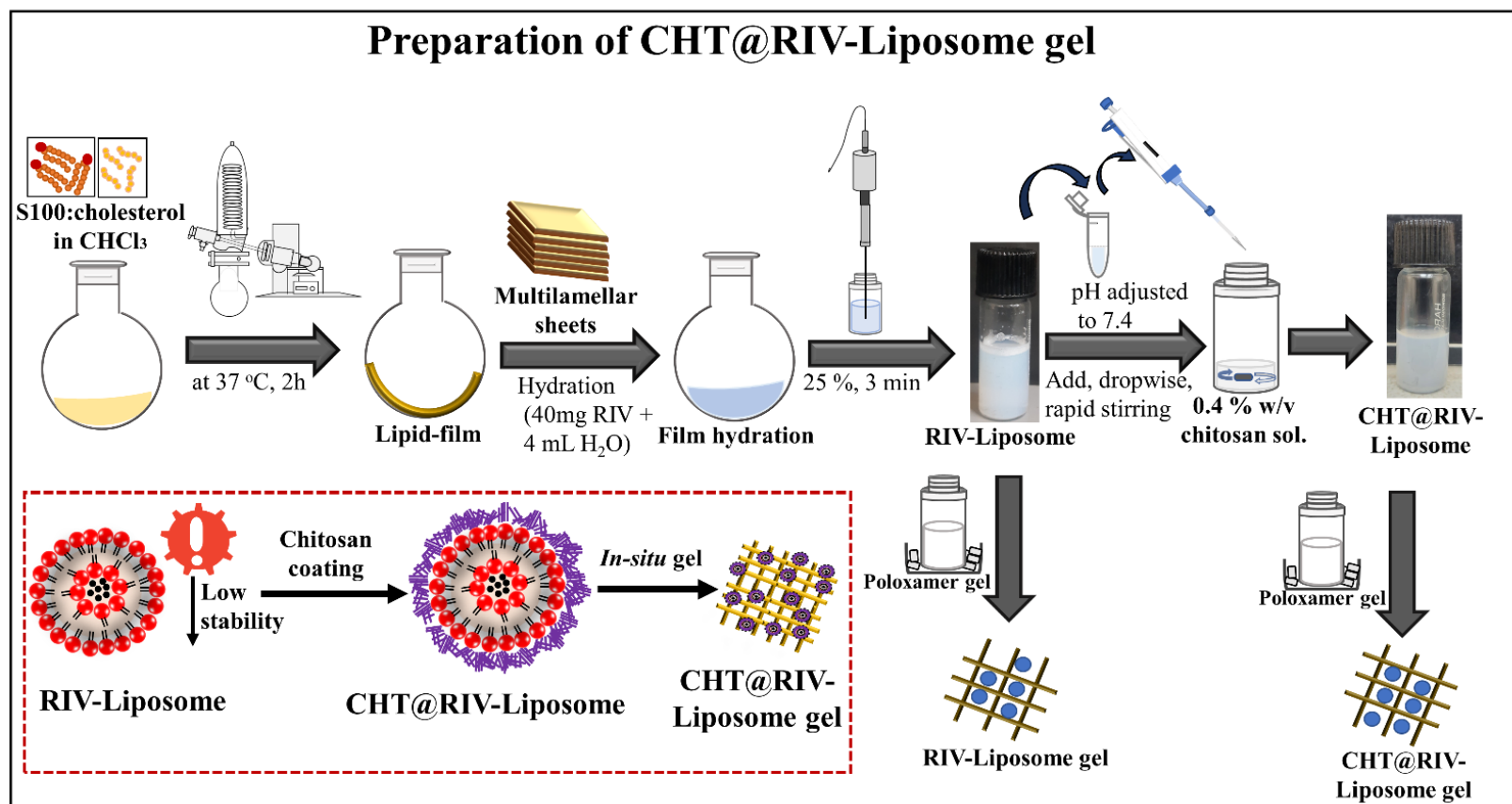


Fig. 6.1. Schematic representation for preparation of RIV-Liposome gel and CHT@RIV-Liposome gel formulation. The lipid thin film constituting S100:cholesterol was hydrated with drug solution, and reduced to form RIV-Liposome. Subsequent chitosan-coating of RIV-Liposome were loaded into thermoresponsive gel. RIV-Liposome: Rivastigmine liposome; CHT@RIV-Liposome: Chitosan coated rivastigmine liposome; Sol.: Solution

6.2.3 *In-vitro* characterisation

6.2.3.1 Particle size, polydispersity index, zeta potential and percent encapsulation efficiency

The mean particle size, polydispersity index (PDI) and zeta potential measurements of RIV-HT Liposome and CHT@RIV-HT Liposome was determined at 25° C using Malvern Nano ZS (Malvern, United Kingdom) instrument. The particle size (PDI) analysis was conducted at 173° scattering angle with double dilution with Milli-Q water.

The encapsulation efficiency (%) of the liposomal formulation was determined using the dialysis bag technique. For this, 1 mL formulation was taken in a dialysis bag (Himedia dialysis membrane-110, molecular weight cut off 12000-14000) and immersed in a tube containing 25 mL Milli-Q water. After 30 min, 0.1 mL formulation was withdrawn from the dialysis bag and diluted 10x with acetonitrile to extract encapsulated RIV-HT. The encapsulation efficiency samples were quantified using a validated HPLC method [25]. The analysis was performed using Shimadzu HPLC system (LC-2010HT, Shimadzu Corporation, Japan), employed with LC solution software, version 1.6. The system consisted of binary pumps (LC-20 AD), 5-line degasser (DGU-20A5R) and a UV-Visible detector (SPD-20A).

6.2.3.2 Transmission electron microscopy

The morphological characteristics of liposomal formulation was observed using transmission electron microscopy (TEM) (JEOL Ltd., Akishima, Tokyo, Japan) at a high voltage of 120 kV. The drop cast method was utilized for sample preparation. RIV-HT Liposome and CHT@RIV-HT Liposome was placed separately and casted onto carbon grid for few minutes. The excess sample was soaked and observed for microscopic evaluation.

6.2.4 Preparation of *in-situ* gel loaded with RIV-HT Liposome and CHT@RIV-HT

Liposome

The thermoresponsive *in-situ* gel was prepared using the cold technique. The percentage of poloxamer 407 is crucial for sufficient gel strength and for conversion into gel state at nasal cavity temperature [26]. Briefly, poloxamer 407 (4.6 g) and poloxamer 188 (0.8 g) were added to 15 mL Milli-Q water. The temperature was maintained between 2-8 °C throughout stirring. Further, 2 gm propylene glycol was added to the gel mixture, and volume was made up to 20 mL with Milli-Q water. The resultant gel mixture was stored overnight for hydration at refrigerated conditions. Further, pure drug and respective RIV-HT formulations (RIV-HT Liposome and CHT@RIV-HT Liposome) were mixed separately with gel mixture just before the initiation of rheological experiments. RIV-HT Liposome gel and CHT@RIV-HT Liposome gel with 0.5 % and 0.25 % (w/v) drug equivalent formulation in gel was prepared.

6.2.5 Rheological characterization of *in-situ* gel

Rheological characterization was performed for RIV-HT gel, RIV-HT Liposome gel and CHT@RIV-HT Liposome gel formulation using MCR 92 rheometer (Anton Par, Austria). A 0.5 mm standard gap was maintained throughout all experiments. 25 mm parallel plate was used for gel characterization. The gel was equilibrated for 120 s onto the rheometer platform. The temperature-dependent viscosity was determined within 20-35 °C, and gel viscosity at 33 °C was recorded. Firstly, the amplitude sweep test was performed to determine the linear viscoelastic range. Further, different rheological parameters such as storage modulus (G'), loss modulus (G'') and loss tangent ($\tan \delta$) were determined from rheological measurements. The graph of G' and G'' was plotted against temperature (20-35 °C) to elucidate gel behavior at different temperature. Elastic properties of gel were characterized by frequency-sweep test, within the frequency range of 0.1 to 10 Hz, at 33 °C.

6.2.6 Stability studies

It was performed to evaluate the storage conditions for RIV-HT Liposome gel and CHT@RIV-HT Liposome gel formulations. Samples were refrigerated (2-8 °C) and analyzed for particle size, PDI, zeta potential, and % encapsulation efficiency at 0, 10, 20, 30, 60 and 90 days. Statistical analysis (t-test , $p < 0.05$) was employed at each time point to determine the difference in stability samples.

6.2.7 *In-vitro* drug release

In-vitro drug release from RIV-HT Liposome gel and CHT@RIV-HT Liposome gel was determined using dialysis bag method. The dialysis bag containing gel-loaded nanoformulation and 1 mL simulated nasal fluid (Composition: 8.77 g L⁻¹ of NaCl, 2.98 g L⁻¹ of KCl, 0.59 g L⁻¹ of CaCl₂·2H₂O in deionized water, pH 6.4) were immersed in 25 mL phosphate buffer saline (PBS), pH 7.4 [27]. The samples were maintained at 34° C with continuous shaking at 100 rpm. 1 mL sample was withdrawn at 0.08, 0.16, 0.25, 0.5, 1, 2, 4, 6 and 12 h, and replenished with equal volumes of fresh release medium. The samples were centrifuged at 15,000 rpm and analyzed using a validated HPLC method [25]. Further, the graph of cumulative drug release (%) vs time (h) was plotted for respective formulations. The drug release data were fitted into various kinetic models such as zero order, first order, Higuchi, Hixson Crowell, Korsmeyer-Peppas to explore the mechanism of drug release from various formulations using DD solver software.

6.2.8 *Ex-vivo* nasal drug permeation

The study compared nasal permeation efficiency of RIV-HT Liposome gel and CHT@RIV-HT Liposome gel with that of RIV-HT gel formulation. For this, freshly procured goat nasal mucosa was separated from the septum and rinsed with PBS pH 7.4. The tissue was allowed to equilibrate for 15-20 min in phosphate buffer solution pH 6.4. Afterward, the nasal mucosa was sandwiched between donor and receptor compartment of the Franz diffusion cell apparatus

[28]. Gel-loaded liposomal formulations (RIV-HT gel, RIV-HT Liposome gel, CHT@RIV-HT Liposome gel) equivalent to 1 mg drug were placed onto nasal mucosa (n = 3). 6 mL phosphate buffer solution (pH 6.4) was placed in the donor compartment. Samples were withdrawn at particular time intervals (0.08 to 6 h) and replenished with the same volume of fresh medium. The samples withdrawn were centrifuged at 15,000 rpm for 10 min and analyzed using validated RP-HPLC method [25]. The amount of drug permeated across the unit area ($\mu\text{g}/\text{cm}^2$) vs time (h) was plotted for pure RIV-HT gel, RIV-HT Liposome gel, and CHT@RIV-HT Liposome gel formulation. Steady-state flux ($\mu\text{g}/\text{cm}^2/\text{h}$) was calculated from slopes of each respective plots. The data obtained from ex-vivo permeation was fitted into kinetic models such as zero order, first order, Higuchi, Hixson Crowell and Korsmeyer's Peppas model was evaluated using DD solver software.

6.2.9 Pharmacokinetic study in rats

A comparative *in-vivo* study was performed with Wistar rats weighing 230-260 g. Animals were housed in conditions compliant with authority guidelines. All experiments were performed as per protocol approved by Institutional animal ethics committee. For *in-vivo* study, animals were divided into four groups (15 animals in each group). 2 mg/kg dose was administered to rats in each group.

Group I: Intranasal administration of RIV-HT gel

Group II: Intranasal administration of RIV-HT Liposome gel

Group III: Intranasal administration of CHT@RIV-HT Liposome gel

Group IV: Intravenous administration of RIV-HT sol

6.2.9.1 Intranasal dosing

The dose was administered intranasally using 1.3 cm long soft polypropylene tube (Instech Laboratories, Pennsylvania, USA). It was attached with 100 μ L microtip to ensure effective dose delivery to the olfactory region of the nasal cavity. Prior to dosing, animals were anesthetized using isoflurane. A dose volume of 50-100 μ L (total dose 500 μ g) was instilled in each nostril and the animals were held upright in supine position for at least 30 sec until anesthesia recovery, to avoid seeping of dose from the nasal cavity.

6.2.9.2 Mucociliary clearance time

It can be described as the specific time point at which the drug appeared in the pharynx followed by intranasal administration. The swab was taken from the pharynx, *via*. oral cavity upto 60 min within an interval of 5 min. It was further processed by suitably diluting with mobile phase (ACN: phosphate buffer: IPA, 33:65:2) and analysed using reported RP-HPLC method [25]. The first-time point at which RIV-HT was detected in the oropharyngeal swab was noted as mucociliary clearance time for respective formulation.

6.2.9.3 Brain distribution and plasma pharmacokinetic study in rats

The preliminary PK study employed intranasal and intravenous administration of respective formulations to decide time points in brain and plasma. For group IV, 400 μ L (total dose 500 μ g) dose volume was administered intravenously through tail vein. 400 μ L plasma volume was collected in a centrifuge tube containing 40 μ L, 10 % (w/v), EDTA solution. Blood samples were collected at 0 (pre dose), 0.25, 0.5, 1, 2, 4, 6, 12, 18, 24 h through retro-orbital plexus. To evaluate brain distribution, animals (n = 3) were sacrificed at 0.75, 2, 6, 12 and 24 h using cervical dislocation and isolated whole brain tissue. The plasma and brain samples were analysed using bioanalytical method described in Chapter 3, section 3.4.2.4 and 3.4.2.5 . The

PK parameters were computed using Phoenix WinNonlin software (version 8.3, Pharsight Corporation, NC, USA) employing non-compartmental analysis.

Direct nose-to-brain delivery of formulations via intranasal route was determined using drug targeting efficiency (DTE (%)) and direct transport percentage (DTP (%)). The DTE(%) value (equation 1) indicates the total concentration of drug reaching brain, *via*. both systemic circulation and through direct nose-to-brain transport . While DTP (%) value (equation 2 and 3) estimates the concentration of drug reaching brain through direct nose-to-brain pathway only.

$$\% DTE = \frac{\frac{(AUC_{brain})_{IN}}{(AUC_{plasma})_{IN}}}{\frac{(AUC_{brain})_{IV}}{(AUC_{plasma})_{IV}}} \times 100 \quad \dots (1)$$

$$\% DTP = \frac{(AUC_{brain})_{IN} - F}{(AUC_{brain})_{IN}} \times 100 \quad \dots (2)$$

$$F = \frac{(AUC_{brain})_{IV}}{(AUC_{plasma})_{IV}} \times (AUC_{plasma})_{IN} \quad \dots (3)$$

Where $(AUC_{brain})_{IN} = AUC_{0-t}$ in brain after intranasal administration and $(AUC_{plasma})_{IN} = AUC_{0-t}$ in plasma after intranasal administration $(AUC_{brain})_{IV} = AUC_{0-t}$ in brain after intravenous administration and $(AUC_{plasma})_{IV} = AUC_{0-t}$ in plasma after intravenous administration.

DTE (%) value greater than 100 % represents efficient brain targeting through intranasal administration compared to the intravenous route. Whereas DTP (%) value greater than 0 indicates direct nose-to-brain transport of the drug.

6.2.10 Histopathological examination

The study evaluated the safety of intranasally administered RIV-HT Liposome gel and CHT@RIV-HT Liposome gel on rat nasal tissue and brain. The untreated rats were used as a control. Brain and nasal epithelium were removed from the respective formulation-treated

group at 24 h. The isolated tissues were cleaned with PBS pH 7.4 to remove blood and connective tissue and fixed in 10% (v/v) formalin solution. The specimens were dehydrated with methyl alcohol, ethyl alcohol, followed by treatment with absolute ethyl alcohol. The specimens were treated with xylene, and left embedded in paraffin wax for 24 h. The paraffin blocks were sectioned using sledge microtome, deparaffinized, followed by sequential treatment with hematoxylin and eosin [20] for observation under the light microscope (Axio Vert. A1 FL, Carl Zeiss, Jena, Germany).

6.2.11 Statistical analysis

Statistical tests were employed using GraphPad Prism, version 8 (GraphPad Software, La Jolla, CA, USA). All quantifiable data was reported as mean \pm standard deviation (SD) or mean \pm standard error of mean. The difference between tested groups were computed using student's t-test or ANOVA. The value of 'p' <0.05 was considered as statistically significant.

6.3 Results and discussion

6.3.1 Preparation of RIV-HT Liposome and CHT@RIV-HT Liposome

The preliminary screening of S100 and cholesterol ratio was optimized to obtain desired particle size, PDI and encapsulation efficiency (**Table 6.1**). Designing a liposome-based formulation for RIV-HT is a major challenge due to its hydrophilic characteristics resulting in lower encapsulation efficiency, greater particle size and lesser control on drug release etc. The chitosan coating of liposome provides improved stability, increased circulation time, sustained drug release, and greater accumulation in CNS.

Two critical parameters are involved in developing liposomal formulation: particle size and encapsulation efficiency. Moreover, the developed formulation should exhibit reliable *in-vitro* stability, avoiding unnecessary drug leakage over the time. This study investigated sequential optimization of the formulation parameters to achieve reduced particle size and maximum

encapsulation efficiency. Initially, the sequential optimization involved screening of S100:cholesterol ratio (1:1, 3:1, 5:1, 7:1 and 10:1 w/w) that significantly impacted particle size, PDI and encapsulation efficiency. Increasing S100:cholesterol ratio upto 5:1 is characterized by significantly decreased particle size, PDI, along with improved encapsulation efficiency and zeta-potential value. The equivalent ratios of S100:cholesterol resulted in particle size above 500 nm with PDI greater than 0.6. Such greater particle size and PDI is undesirable and occur due to the inability to stabilize the higher percentage of cholesterol, resulting in unstable formulation. Further, increasing the ratio to 3:1 and 5:1 resulted in decreased particle size and PDI with improved zeta-potential and encapsulation efficiency. The resultant zeta potential is the net charge obtained due to the presence of cholesterol and phospholipid. The cholesterol and phospholipids develop negative and positive zeta potential. The developed zeta potential also signifies the colloidal stability of the formulation. Interestingly, increasing the ratio to 7:1 and 10:1 resulted in increased particle size, PDI with drastically decreased encapsulation efficiency due to liposomal aggregation and instability (**Table 6.1**). Cholesterol up to a certain ratio usually increases liposomal stability since it reduces membrane permeability and bilayer fluidity. The increased stability probably leads to resultant increased encapsulation efficiency. Therefore increasing the phospholipid ratio above 5:1 leads to increased PDI due to consequent liposomal aggregation. Further increasing the ratio to 10:1 leads to decreased cholesterol proportion, resulting in increased particle size and PDI due to liposomal aggregation. The distinct observation of lowered encapsulation efficiency is supported by decreased liposomal stability due to enhanced membrane permeability and bilayer fluidity. The results agree with previous studies that demonstrated the desired particle and PDI of less than 200 nm and 0.3 was obtained at 4:1 ratio of phospholipid: cholesterol. Another approach for improving the encapsulation efficiency of hydrophilic drugs involves optimization of the drug containing aqueous phase volume. The particle size, PDI and encapsulation efficiency at 8 and 12 mL

aqueous drug volume was comparatively lesser due presence of lesser drug concentration in the latter case. The particle size, PDI, and encapsulation efficiency was higher at 4 > 8 > 12 mL due to higher drug loading inside liposome (**Table 6.1**).

The surface coating of liposomes with chitosan helps attain colloidal stability. The protective coating with chitosan depends on the ability of the polymer to remain adhered to the lipidic vesicles. Previous studies showed that interaction between chitosan and soya phosphatidylcholine liposome contributed to improved membrane rigidity and stability of lipid bilayer. Different concentrations of chitosan solution were investigated for coating. The results observed an increment in particle size and PDI with an increase in chitosan concentration. At 0.1% and 0.3% (w/v) chitosan solution, the particle size was observed to be less than 200 nm with significantly increased PDI to 0.275 and 0.383 (**Table 6.1**). This usually occurs due to chitosan coating. At 0.4 and 0.5% (w/v) chitosan coating, it significantly increased zeta potential to $+24.4 \pm 0.6$ and $+25.6 \pm 0.1$ mV with dramatically increased PDI values to 0.497 and 0.767. Moreover, 0.4% (w/v) chitosan coating resulted in particle size less than 200 nm, but coating with 0.5% (w/v) chitosan solution resulted in distinctly increased particle size above 500 nm. The particle size below 200 nm was desirable, therefore formulation with 0.4% chitosan solution was selected as the optimized formulation. The results agree with previous investigations that demonstrated coating with 0.5% (w/v) chitosan solution resulted in particle size within 300 nm with zeta potential values of approximately +23 mV [1].

Table 6.1. Effect of formulation parameters on characteristics properties of rivastigmine formulations (n = 3)

Parameter	Particle size (nm)	Polydispersity index	Zeta potential (mV)	Encapsulation efficiency (%)
Effect of S100:cholesterol ratio (w/w)				
1:1	545.7 ± 20.2	0.634 ± 0.031	3.9 ± 0.4	-
3:1	207.7 ± 0.4	0.296 ± 0.030	6.5 ± 0.4	27.25 ± 1.34
5:1	179.2 ± 1.8	0.297 ± 0.023	6.5 ± 0.3	35.06 ± 0.82
7:1	169.3 ± 1.0	0.354 ± 0.007	9.8 ± 0.6	30.32 ± 1.03
10:1	176.8 ± 0.5	0.398 ± 0.001	9.9 ± 0.2	12.42 ± 0.75
Effect of RBF size (mL)				
25	179.1 ± 1.8	0.297 ± 0.029	6.5 ± 0.4	35.03 ± 1.26
100	202.9 ± 3.1	0.327 ± 0.047	9.0 ± 0.1	39.10 ± 2.08
250	178.0 ± 2.3	0.271 ± 0.021	9.7 ± 0.5	44.52 ± 2.32
Effect of aqueous phase volume (mL)				
4	193.4 ± 1.4	0.277 ± 0.028	9.7 ± 0.6	71.12 ± 2.13
8	178.0 ± 2.3	0.227 ± 0.034	9.7 ± 0.5	33.02 ± 0.65
12	138.4 ± 1.1	0.215 ± 0.026	8.4 ± 0.1	16.92 ± 3.06
Effect of chitosan concentration (%w/v)				
0.1	137.1 ± 0.7	0.275 ± 0.005	13.7 ± 0.5	-
0.3	166.5 ± 5.1	0.383 ± 0.062	12.1 ± 1.6	-
0.4	189.9 ± 8.0	0.497 ± 0.002	24.4 ± 0.6	-
0.5	469.1 ± 42.9	0.767 ± 0.012	25.6 ± 0.1	-

6.3.2 *In-vitro* Characterization

6.3.2.1 Particle size, PDI, zeta potential, percent encapsulation efficiency

The particle size (PDI), zeta potential and percentage encapsulation efficiency of optimized RIV-HT Liposome was observed to be 137.1 ± 0.5 nm (0.275 ± 0.005), $+13.7 \pm 0.6$ mV and 72.23 ± 1.10 % respectively (**Table 6.2, Fig.6.2A and Fig.6.2B**). RIV-HT Liposome showed the presence of bluish-white appearance, as presented in **Fig.6.2C**. The increment in pH of

RIV-HT Liposome from 5.0 to 7.4, developed a negative surface zeta potential of -10.3 ± 0.3 mV promoting chitosan coating of liposome due to electrostatic interaction (**Table 6.2**).

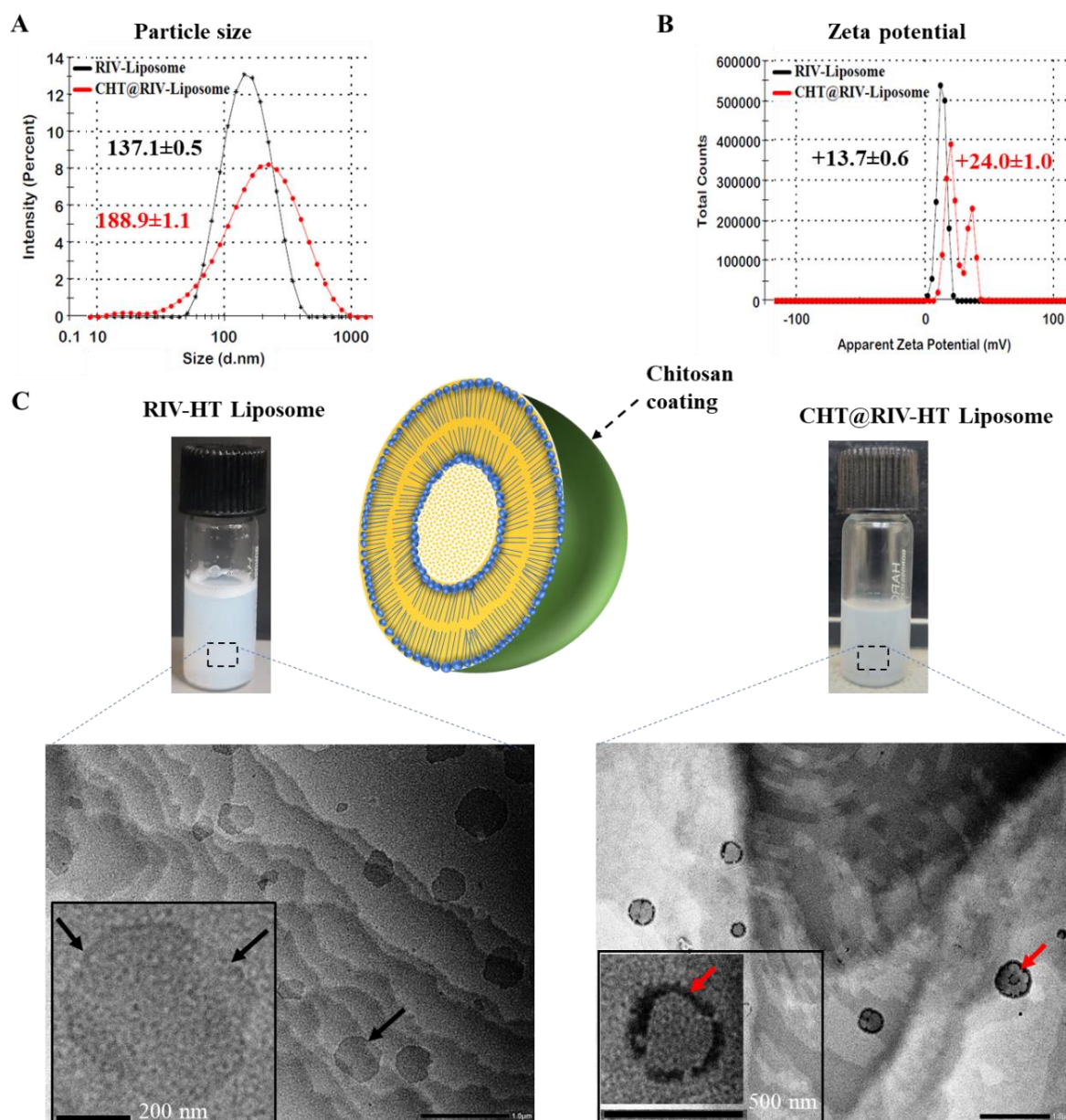


Fig. 6.2. (A) and (B) represents particle size and zeta potential of RIV-HT Liposome and CHT@RIV-HT Liposome formulation. (C) Represents physical appearance and TEM images of RIV-HT Liposome and CHT@RIV-HT Liposome demonstrating surface morphology, particle size and chitosan coating in case of CHT@RIV-HT Liposome.

The optimised CHT@RIV-HT Liposome comprised of 0.4 % (w/v) chitosan solution. The resultant formulation exhibited particle size (PDI), zeta potential and percent encapsulation

efficiency of 188.9 ± 1.1 nm (0.485 ± 0.028), $+24.0 \pm 1.0$ mV and 38.05 ± 1.72 %, respectively (**Table 6.2, Fig.6.2A and Fig.6.2B**). Since chitosan is positively charged, chitosan coating onto RIV-HT Liposome led to a drastic shift from negative to positive surface zeta potential [30]. The increase in particle size from 137.1 ± 0.5 to 188.9 ± 1.1 nm also agrees with chitosan-coating of RIV-HT Liposome [31]. Moreover, the positive zeta potential of CHT@RIV-HT Liposome is particularly responsible for physical stability due to steric repulsion.

6.3.2.2 Transmission electron microscopy

TEM analysis of RIV-HT Liposome and CHT@RIV-HT Liposome was performed to evaluate morphology and chitosan coating over RIV-HT Liposome. TEM images revealed almost spherically shaped CHT@RIV-HT Liposome and demonstrated the presence of core-shell structure due to chitosan coating (**Fig.6.2C**) [32]. The uncoated liposomes are somewhat irregular in shape (**Fig.6.2C**). This might be due to the drying of water during sample preparation [33]. TEM images of RIV-HT Liposome and CHT@RIV-HT Liposome showed no signs of aggregation, indicating colloidal stability of both formulations.

Table 6.2. Formulation characteristics of RIV-HT Liposome and CHT@RIV-HT Liposome formulation

Formulation	Particle size (nm)	Polydispersity index	Zeta potential (mV)	Encapsulation efficiency (%)
RIV-HT Liposome (before pH adjustment)	137.1 ± 0.5	0.275 ± 0.005	$+13.7 \pm 0.6$	72.23 ± 1.10
RIV-HT Liposome (after pH change to 7.4)	132.5 ± 0.7	0.267 ± 0.012	-10.3 ± 0.3	71.46 ± 1.84
CHT@RIV-HT Liposome	188.9 ± 1.1	0.485 ± 0.028	$+24.0 \pm 1.0$	38.05 ± 1.72

Data is expressed as mean \pm SD (n = 3)

6.3.3 Preparation of *in-situ* gel loaded with RIV-HT Liposome and CHT@RIV-HT Liposome

The blank gel was observed to be transparent with absolute uniformity at gelling temperature. The physical appearance of hydrogel mixture at sol and gel state is represented in **Fig.6.3A**. The preliminary testing of blank gel using inversion tube test demonstrated the conversion of sol to gel state at 33 °C as shown in **Fig.6.3A**.

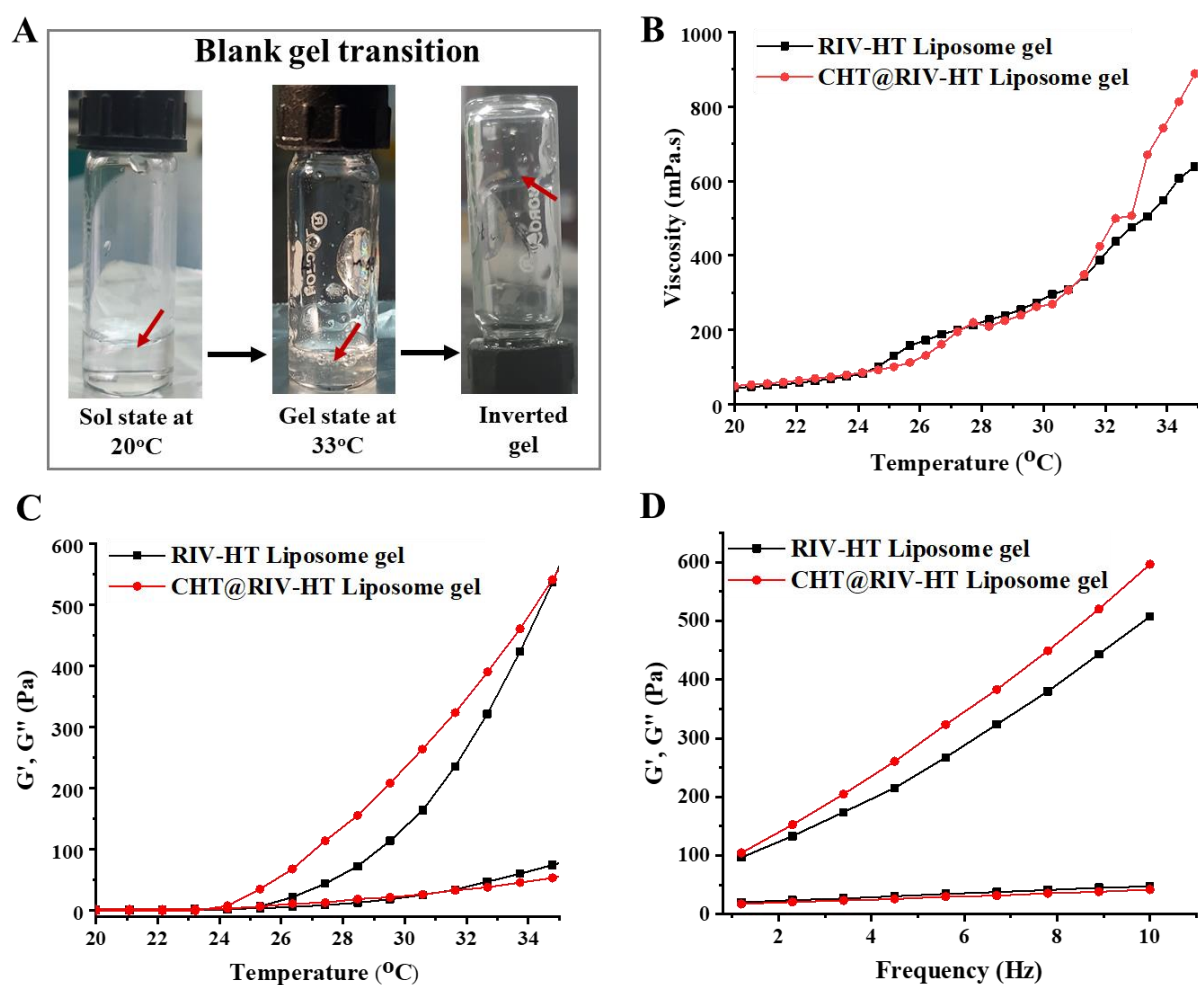


Fig. 6.3. (A) Represents physical appearance and transition of sol-to-gel state at 33° C. (B) Demonstrate temperature-dependent viscosity of RIV-HT Liposome and CHT@RIV-HT Liposome based gel formulations. (C) Represents temperature and (D) frequency dependent storage and loss modulus for liposome loaded gel formulations.

6.3.4 Rheological characterization of *in-situ* gel

Rheological studies were performed to elucidate temperature-dependent changes in viscosity and gel strength at different angular frequencies. The formulation-loaded gel was subjected to an amplitude and frequency of 0.5% shear strain at 10 rads/s within linear viscoelastic range. The viscosity of RIV-HT Liposome gel and CHT@RIV-HT Liposome gel was observed to be 475.70 ± 26.12 and 506.94 ± 14.56 mPa.s at 33° C, respectively, representing gel state (**Table 6.3 and Fig.6.3B**). Whereas, the viscosity was very less at 20 °C representing the presence of sol state (**Table 6.3**). At lower temperatures, the ability of polymer chains to disentangle and flow is greater, exhibiting $G'' > G'$. At 33° C, the entanglement of polymer chains lead to $G' > G''$, exhibiting a typical gel-like structure (**Fig.6.3C**). $\tan \delta$ ($\tan \delta = G'/G''$) value also represents the viscous hydrogel component. At the sol state, the phase angle value ($\tan \delta$) is usually <1 , and upon transitioning into the gel state leads to phase angle value >1 [34]. The phase angle value, $\tan \delta$ for respective gel formulation at different angular frequencies is represented in **Table 6.3 and Fig.6.3D**. Such formulation-loaded gels are not influenced by oscillatory frequencies and are generally referred as cross-linked gels. They withstand greater elasticity which is required to retain gel formulation in the nasal cavity [35]. The developed hydrogel also constitutes sufficient gel strength to improve drug residence time in the nasal cavity. This in turn is responsible for improved drug absorption from the nasal cavity.

Table 6.3. RIV-HT Liposome and CHT@RIV-HT Liposome loaded gels representing viscosity, storage modulus and $\tan \delta$ values at different oscillatory frequencies

Formulation	Viscosity (mPa·s) \pm SD		Storage modulus, G' (Pa) \pm SD at 33° C	$\tan \delta$ (Pa) \pm SD values at different angular frequency (Hz)		
	At 20° C	At 33° C		1.2	5.6	10
	RIV-HT Liposome gel	44.63 \pm 12.26		475.70 \pm 26.12	321.98 \pm 11.25	0.185 \pm 0.091
CHT@RIV-HT Liposome gel	49.66 \pm 9.25	506.94 \pm 14.56	390.56 \pm 13.78	0.191 \pm 0.032	0.094 \pm 0.01	0.079 \pm 0.004

SD: Standard deviation; Data is expressed as mean \pm SD (n = 3)

6.3.5 Stability study

The stability study of RIV-HT Liposome gel and CHT@RIV-HT Liposome gel was evaluated for particle size, PDI and zeta potential. The stability samples were compared with freshly prepared samples of respective formulations (day 0). Scanning electron microscopy of freshly prepared CHT@RIV-HT Liposome (**Fig.6.4A**) showed no signs of aggregation after loading into an *in-situ* gel-based system (**Fig.6.4B**). RIV-HT Liposome gel demonstrated significantly increased particle size, PDI ($p < 0.05$) on 30th day. The increased particle size and PDI usually occur due to colloidal instability resulting in fusion of liposomal vesicles, which leads to increased particle size and PDI. The resultant liposomal aggregation led to a significant change in zeta potential ($p < 0.05$) after 20 days (**Fig.6.4C**). Therefore, it can be stated that RIV-HT Liposome gel was stable upto 20 days at the storage condition. While CHT@RIV-HT Liposome gel showed no significant change in the particle size, PDI and zeta potential up to 90 days (**Fig.6.4D**). The results demonstrate the stability of CHT@RIV-HT Liposome gel for at least 3 months at particular storage conditions. The improved stability of liposomes due to chitosan-coating is attributed to steric repulsion from higher surface charge is responsible for colloidal stabilization [36]. Additionally, the structural rigidity imparted due to chitosan coating also prevented aggregation of CHT@RIV-HT Liposome.

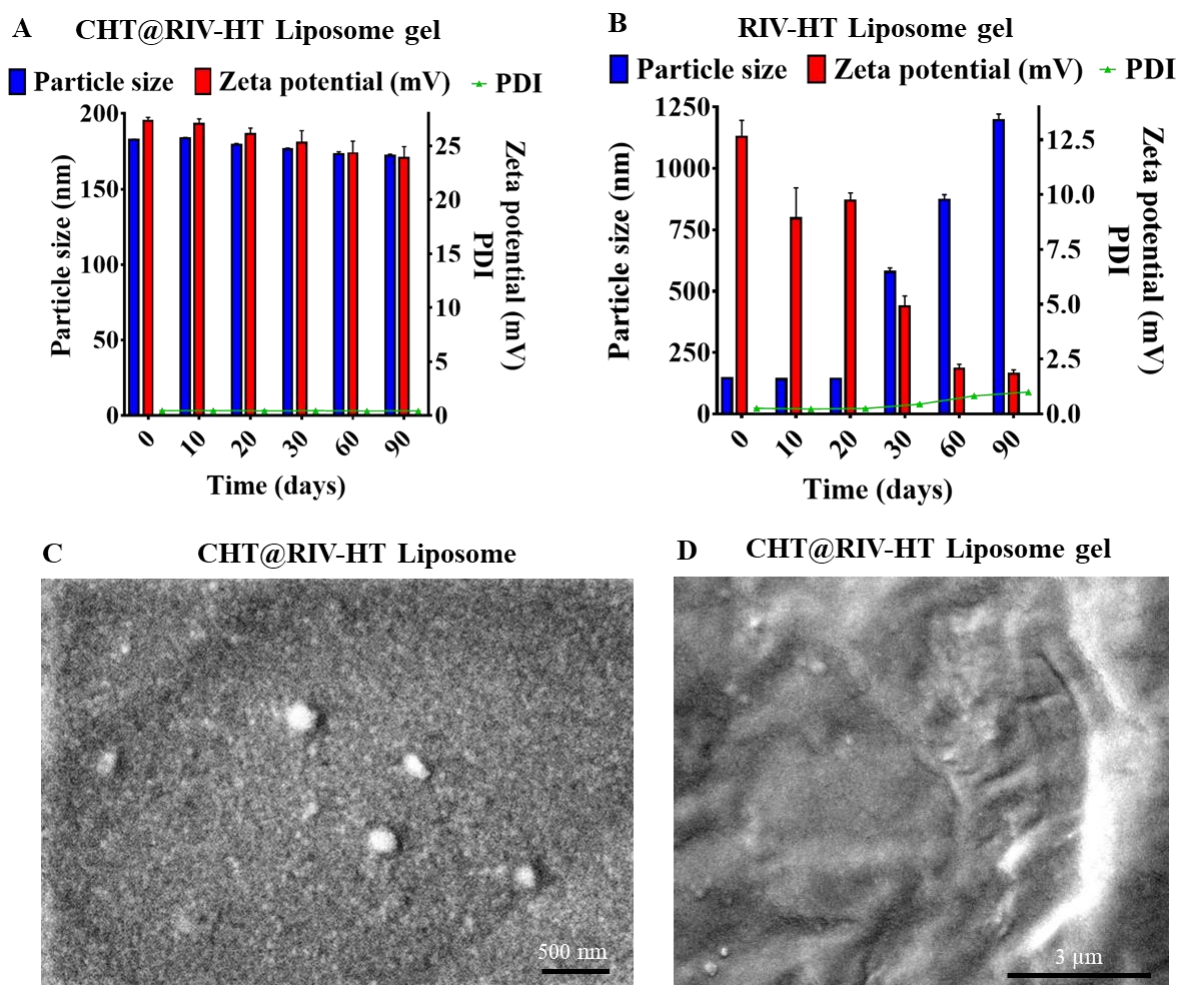


Fig. 6.4. Represents (A) stability of CHT@RIV-HT Liposome for 90 days. (B) Shows increased particle size, PDI and zeta potential of RIV-HT Liposome gel at 30 days, thus demonstrating the stability of formulation upto 20 days. (C) SEM images represent particle size and spherical shape of CHT@RIV-HT Liposome (D) exhibiting no aggregation after loading into *in-situ* gel based system.

6.3.6 *In-vitro* drug release

In-vitro release of RIV-HT Liposome gel and CHT@RIV-HT Liposome gel formulation was performed to evaluate the effect of chitosan coating on drug release pattern. The release profiles of formulation loaded gel is represented in **Fig.6.5A**. RIV-HT gel exhibited complete drug release within 4 h. RIV-HT Liposome gel is characterized with observation of rapid drug release upto 58.84 % within 2 h and complete drug release within 6 h. This is attributed to the lipid bilayer fluidity consisting of polar heads resulting in much faster release of hydrophilic

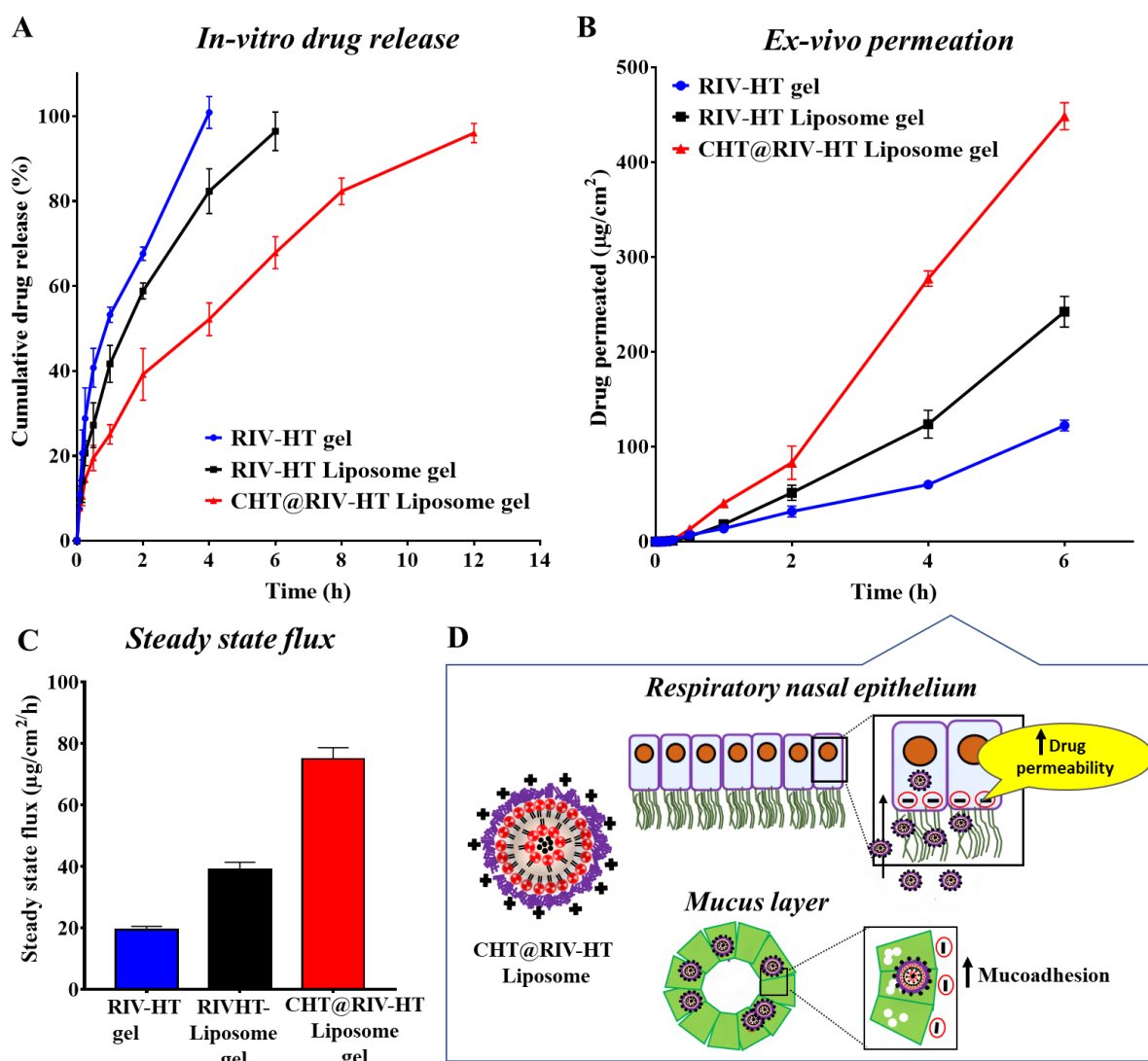


Fig. 6.5. Represents comparative evaluation of (A) *in-vitro* drug release, (B) amount of drug permeated across nasal mucosa and (C) steady-state flux of RIV-HT Liposome gel, CHT@RIV-HT Liposome gel and RIV-HT gel formulation. (D) represents a mechanistic approach for improved drug nasal permeation of CHT@RIV-HT Liposome gel formulation.

RIV-HT [37]. Moreover, CHT@RIV-HT Liposome demonstrated the drug release upto 39.22 ± 6.08 % within 2 h followed by sustained drug release upto 12 h (**Fig.6.5A**). The chitosan coating did not exhibit a significant difference in release pattern but, it is characterized by comparatively slower and sustained drug release compared to RIV-HT Liposome gel. This is attributed to the improved stability of nanoformulation in the form of CHT@RIV-HT Liposome. The sustained drug release is attributed to the distinct release mechanism involving

surface-adsorbed drug release (onto CHT@RIV-HT Liposome) followed by erosion of the chitosan coat and drug diffusion [32]. The sustained drug release is due to the protective effect of chitosan coating, contributing to reduced membrane permeability and improved stability of lipid vesicles [24,38].

Drug release data were fitted into various release kinetic models showing that RIV-HT formulations followed Korsmeyer's Peppas model (**Table 6.4**). The value of 'n' obtained from Korsmeyer's Peppas model suggested that RIV-HT Liposome gel followed Fickian diffusion ($n = 0.499$), whereas CHT@RIV-HT Liposome gel followed non-Fickian diffusion ($n = 0.518$). Drug release data were fitted into various release kinetic models showed that RIV-HT formulations

Table 6.4 . R^2 values for different *in-vitro* drug release models of rivastigmine formulations

Formulation	Zero order	First order	Korsmeyer - Peppas	Higuchi	Hixson- Crowell
RIV-HT Liposome gel	0.7717	0.9754	0.9975	0.9975	0.9552
CHT@RIV-HT Liposome gel	0.8274	0.9647	0.9973	0.9968	0.9526

Data is expressed as mean \pm SD ($n = 3$)

6.3.7 *Ex-vivo* nasal drug permeation

The study evaluated the permeation efficiency of RIV-HT Liposome gel, CHT@RIV-HT Liposome gel across nasal mucosa when compared to RIV-HT gel formulation. Both the liposomal gel formulations exhibited significantly improved permeation efficiency than pure drug-loaded gel ($p < 0.05$). The permeation rate constant for the liposomal formulations is presented in **Table 6.5**. The amount of drug permeated in case of CHT@RIV-HT Liposome gel, RIV-HT Liposome gel and RIV-HT gel, was observed to be 448.30 ± 14.29 , $242.27 \pm$

16.17 and $122.32 \pm 5.55 \mu\text{g}/\text{cm}^2$, respectively (**Fig.6.5B and Table 6.5**). The results demonstrated a significantly improved permeability coefficient with 4.00 ($0.44 \pm 0.01 \text{ cm/h}$) and 2.09-fold ($0.23 \pm 0.02 \text{ cm/h}$) improvement compared to RIV-HT gel ($0.11 \pm 0.01 \text{ cm/h}$). The steady-state flux is described as the amount of drug permeated per unit area of time. It was observed to be improved significantly for both the liposomal formulations ($p < 0.05$) as represented in **Fig.6.5C and Table 6.5**. The improved nasal absorption in RIV-HT Liposome gel is attributed to the reduced particle size and presence of drug in lipid nanocarrier system. The CHT@RIV-HT Liposome gel substantially improved ($p < 0.05$) permeation rate than RIV-HT Liposome gel formulation due to mucoadhesion and penetration-enhancing properties rendered by chitosan [39]. The positively charged chitosan interacts with nasal epithelium and helps open the tight junctions, thereby increasing drug permeability across nasal epithelium (**Fig.6.5D**) [39,40]. Thus, it can be concluded that chitosan-coated liposome distinctly increases nasal permeation efficiency across mucosal barriers, thus, it could also improve in-vivo drug concentration in brain.

Table 6.5. Permeation kinetics of RIV-HT Liposome gel and CHT@RIV-HT Liposome gel formulation

Formulation	Kinetic model	Steady state flux ($\mu\text{g}/\text{cm}^2 \text{ h}^{-1}$)	Amount permeated ($\mu\text{g}/\text{cm}^2$)	Permeability Coefficient (cm/h)
RIV-HT Liposome gel	Korsemeyer's Peppas	38.92 ± 2.36	242.27 ± 16.17	0.23 ± 0.02
CHT@RIV-HT Liposome gel	Korsemeyer's Peppas	74.90 ± 3.74	448.30 ± 14.29	0.44 ± 0.01

Data is expressed as mean \pm SD (n = 3)

6.3.8 *In-vivo* study in rats

6.3.8.1 Mucociliary clearance time

The RIV-HT nanoformulations were developed as *in-situ* hydrogel-based system to prevent rapid mucociliary drug clearance from the nasal cavity. The mucociliary clearance time for RIV-HT gel, RIV-HT Liposome gel and CHT@RIV-HT Liposome gel formulation was observed to be 16.75 ± 3.41 min, 18.23 ± 4.23 min and 27.48 ± 3.12 min, respectively (**Fig.6.6A**). RIV-HT Liposome showed comparatively similar mucociliary clearance time as that of RIV-HT gel. Whereas CHT@RIV-HT Liposome gel showed significantly improved retention time ($p < 0.05$) in comparison to RIV-HT Liposome gel and RIV-HT gel. This is attributed to the mucoadhesive property of chitosan that helped resist mucociliary clearance of the drug. Thus, the enhanced residence time of chitosan-coated liposomes in the nasal cavity renders improved drug transport to the CNS. Thus, it can be stated that the higher drug residence time in the nasal cavity evidences enhanced drug absorption and facilitates targeting to the brain [12].

6.3.8.2 Brain distribution and plasma pharmacokinetic study in rats

The study demonstrates a comparative evaluation of the brain and plasma PK profile of RIV-HT Liposome gel and CHT@RIV-HT Liposome gel. It also emphasizes the evaluation of brain targeting efficiency of both formulations, *via*. intranasal route. The brain (**Fig.6.6B**) and plasma PK profile (**Fig.6.6C**) of intranasally administered RIV-HT Liposome gel and CHT@RIV-HT Liposome gel was compared with pure drug gel formulation and represented in **Table 6.6**. The brain PK profiles of CHT@RIV-HT Liposome gel and RIV-HT Liposome gel showed 3.58 and 1.67-fold improvement in brain MRT values in comparison to pure drug gel formulation ($p < 0.005$ and $p < 0.05$) (**Fig.6.6B**). The MRT_{brain} values for all formulations were in order, CHT@RIV-HT Liposome gel > RIV-HT Liposome gel > RIV-HT gel ('>' indicating a

significant increase, $p < 0.05$) (**Table 6.6**). The result indicated that CHT@RIV-HT Liposome improved the residence time of RIV-HT in the brain than that of RIV-HT Liposome and RIV-HT gel formulation. The improved MRT of CHT@RIV-HT Liposome gel is also supported by improved AUC brain concentration.

Interestingly, CHT@RIV-HT Liposome gel exhibited much higher C_{\max} and AUC_{0-t} levels in the brain, displaying 2.25 and 3.20-fold improvement compared to pure drug gel formulation. Similarly, it also resulted in 1.64 and 2.38 -fold improvement in C_{\max} and AUC_{0-t} levels in brain when compared with RIV-HT Liposome gel formulation (**Fig.6.6B and Table 6.6**). The improved C_{\max} and AUC_{0-t} brain concentrations of CHT@RIV-HT Liposome is attributed to the increased drug residence time in the nasal cavity. Delayed mucociliary drug clearance of CHT@RIV-HT Liposome gel allowed enhanced drug absorption through olfactory and trigeminal nerve pathways. The PK profile of RIV-HT gel and RIV-HT Liposome gel represents higher AUC_{0-t} levels in plasma with comparatively lesser AUC_{0-t} concentration in the brain. Whereas the PK profile of CHT@RIV-HT Liposome gel is characterized by similar AUC_{0-t} levels in the brain as that of plasma. Thus, it can be stated that CHT@RIV-HT Liposome gel improved MRT, C_{\max} and AUC_{0-t} concentrations in the brain than that of RIV-HT Liposomes gel and RIV-HT-gel. The results also agree with previous reports that suggested chitosan coating improves drug concentration in the brain. It is well established that chitosan improves mucoadhesion, improves permeation efficiency in nose-to-brain delivery, and facilitates drug transport to the CNS [41,42] .

The brain PK profile of RIV-HT formulations (RIV-HT gel, RIV-HT Liposome and CHT@RIV-HT Liposome) at particular time points (0.75, 2 and 6 h) was statistically compared. RIV-HT Liposome gel and CHT@RIV-HT Liposome gel demonstrated comparatively lesser brain concentrations at initial time point. RIV-HT Liposome gel and CHT@RIV-HT Liposome achieved C_{\max} within 2 h. Furthermore, CHT@RIV-HT Liposome

gel showed significantly higher C_{\max} concentrations than RIV-HT Liposome and RIV-HT gel formulation. At 6 h of time interval, RIV-HT gel and RIV-HT Liposome gel evidenced elimination phase (58.86 ± 15.72 and 80.31 ± 10.15 ng/gm), whereas CHT@RIV-HT Liposome gel still exhibited significantly higher concentrations in brain till 6 h and 12 h (151.39 ± 11.70 and 77.72 ± 22.04 ng/gm) respectively. Enhanced and sustained brain concentrations in CHT@RIV-HT Liposome gel is due to improved absorption and targeting through olfactory and trigeminal nerve pathway. It can also be confirmed by improved AUC_{0-t} and MRT levels of brain in comparison to RIV-HT Liposome gel formulation (**Table 6.6**).

DTE (%) indices for RIV-HT gel, RIV-HT Liposome gel and CHT@RIV-HT Liposome gel was observed to be 281.28 %, 419.38 % and 651.44 %. While DTP (%) indices were observed to be 64.44 %, 76.15 % and 84.64 % respectively. The DTE (%) and DTP (%) values computed for RIV-HT Liposome gel and CHT@RIV-HT Liposome gel signify direct nose-to-brain uptake of both formulations. Comparatively higher DTE (%) and DTP (%) values for CHT@RIV-HT Liposome gel than RIV-HT Liposome gel is by virtue of mucoadhesion and delayed mucociliary clearance time. The chitosan coating improved absorption and direct brain uptake to the brain through targeting pathways.

The higher DTP value for RIV-HT Liposome and CHT@RIV-HT Liposome may be due to reduced particle size attributing improved olfactory-mediated drug transport to the brain. The presence of *in-situ* gel-loaded formulations improved RIV-HT nasal residence time. The rapid gelation prevented leakage or spread of formulation from the olfactory region to the respiratory epithelium within the nasal cavity. This probably enhances the amount of RIV-HT available for direct nose-to-brain uptake rather than systemic absorption *via* respiratory epithelium.

Overall, it can be stated that CHT@RIV-HT Liposome gel formulation helped to overcome drawbacks associated with oral therapy and plain RIV-HT intranasal therapy. It improved the

concentration of RIV-HT in brain with lesser systemic exposure and associated peripheral side-effects. This may allow dose reduction of RIV-HT. Further, it has been observed that CHT@RIV-HT Liposome gel improved brain MRT levels for a long time. Thus, it may reduce the dosing frequency of RIV-HT.

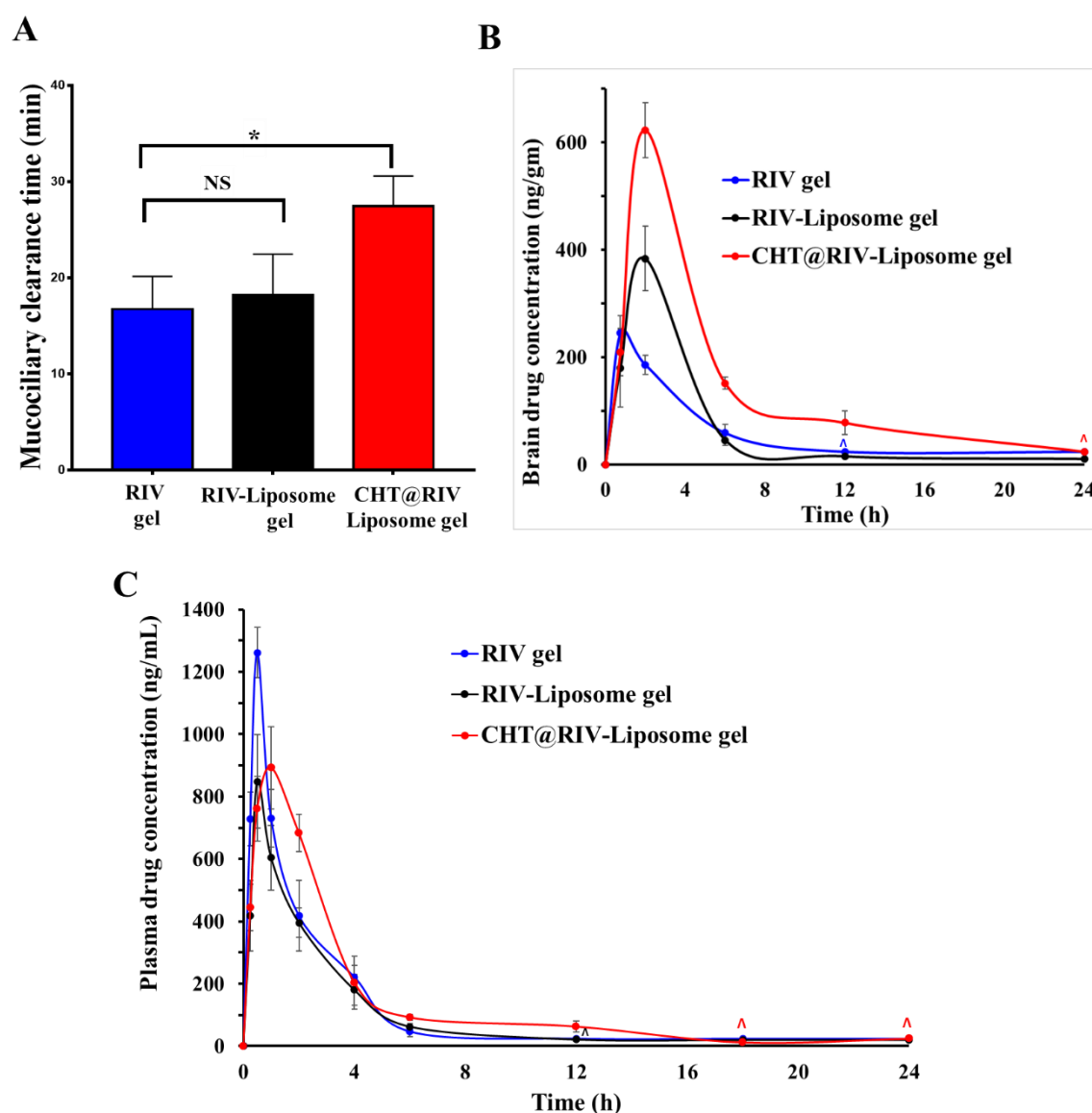


Fig. 6.6. (A) demonstrates significantly increased mucociliary clearance time of CHT@RIV-Liposome gel formulation (* signify $p < 0.05$ and NS signify no significant difference). (B) Brain profile of RIV formulations demonstrate significantly improved brain concentrations and mean residence time of RIV in CHR@RIV-Liposome gel formulation. (C) Represents plasma profile of RIV formulations in which RIV gel showed higher plasma concentrations and RIV-

Liposome gel and CHT@RIV-Liposome gel formulations showed comparatively reduced plasma concentration of RIV. ‘^’ represents data points that were analyzed but are present below the quantifiable limit.

Table 6.6. Brain and plasma PK parameters after intranasal administration of RIV-HT gel, RIV-HT Liposome gel and CHT@RIV-HT Liposome gel

Matrix	PK parameters	RIV-HT gel	RIV-HT Liposome gel	CHT@RIV-HT Liposome gel
Brain	C _{max} (ng/g)	277.38 ± 0.20	380.33 ± 78.40	622.85 ± 51.84
	T _{max} (h)	0.66 ± 0.08	2.00	2.00
	T _{1/2} (h)	1.32 ± 0.26	2.76 ± 0.01	5.24 ± 0.17
	MRT (h)	2.02 ± 0.45	3.38 ± 0.42	7.23 ± 0.13
	AUC _{0-t} (ng/g*h)	934.91 ± 49.86	1254.54 ± 338.66	2991.24 ± 55.65
Plasma	C _{max} (ng/mL)	1261.21 ± 80.83	848.83 ± 150.68	917.39 ± 49.22
	T _{max} (h)	0.50	0.50	0.83 ± 0.16
	T _{1/2} (h)	1.28 ± 0.09	2.54 ± 0.10	3.38 ± 0.17
	MRT (h)	1.94 ± 0.16	3.02 ± 0.16	7.63 ± 0.23
	AUC _{0-t} (ng/ml*h)	2126.85 ± 362.04	2363.14 ± 358.88	3264.66 ± 447.26
	DTE (%)	281.28	419.38	651.44
	DTP (%)	64.44	76.15	84.64

Data is expressed as mean ± standard error of mean (n = 3)

6.3.9 Histopathological examination

Histopathological examination of nasal epithelium and brain tissue was performed to ensure the safety of developed formulations upon intranasal administration in rats. The nasal and brain tissue sections of RIV-HT Liposome gel and CHT@RIV-HT Liposome gel showed similar

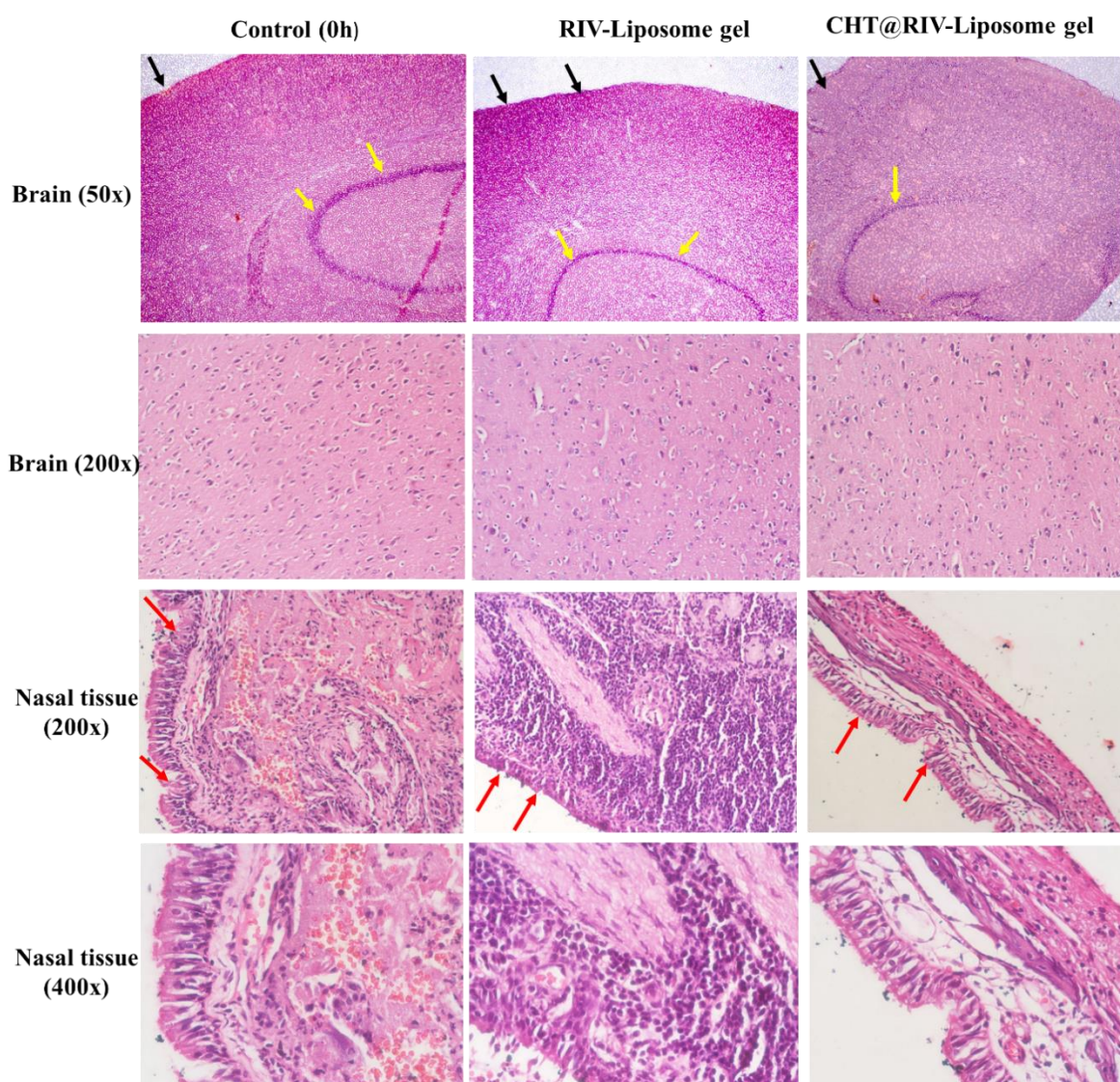


Fig. 6.7. Histopathological evaluation of nasal and brain tissue after intranasal administration of RIV-HT Liposome gel and CHT@RIV-HT Liposome gel formulations were compared with control group. The microscopic images of brain showed no signs of damage/toxicity in cerebral cortex and hippocampus. Nasal tissue also showed the intact morphological structure of

pseudostratified ciliated columnar cells of RIV-HT Liposome gel and CHT@RIV-HT Liposome gel formulation as that of control group.

Arrow indications as follows- Black arrow: Cerebral cortex, Yellow arrow: Hippocampus, Red arrow: Ciliated columnar cells.

histological morphology as that of control group (**Fig.6.7**). The brain sections of RIV-HT Liposome gel and CHT@RIV-HT Liposome gel group showed normal structures of neuronal cells in cerebral cortex, with no histopathological alteration in hippocampus and striatum as that of control group (**Fig.6.7**). The sections of nasal epithelium also showed normal architecture of pseudostratified ciliated columnar, basal and sustentacular cells as that of control group (**Fig.6.7**). The histological examination of formulation treated groups showed no signs of damage or toxicity with presence of intact morphological structures of rat nasal epithelium and brain tissues. Thus, the result demonstrate safety of developed RIV-HT Liposome gel and RIV-HT Liposome gel formulation for intranasal administration.

6.4 Conclusion

The present work explored the effect of chitosan coating in improving therapeutic efficacy for nose-to-brain delivery of RIV-HT. The optimized CHT@RIV-HT Liposome gel demonstrated enhanced stability for atleast 3 months. *In-vitro* release study demonstrated sustained drug release from CHT@RIV-HT Liposome gel. Moreover, chitosan coating greatly impacted the ability to cross mucosal barrier compared to RIV-HT Liposome gel and RIV-HT gel formulations. The PK studies of CHT@RIV-HT Liposome gel exhibited 2.25, 3.58 and 3.20-fold improvement in C_{max} , MRT and AUC_{0-t} concentrations in brain than that of pure RIV-HT gel formulation. CHT@RIV-HT Liposome gel showed 1.64, 2.38 and 2.14-fold improved C_{max} , AUC_{0-t} and MRT concentrations in brain, demonstrating improved therapeutic effect in comparison to RIV-HT Liposome gel. Overall, CHT@RIV-HT Liposome gel is effective in

managing AD and could be a potential carrier system for nose-to-brain delivery compared with currently approved oral therapy.

References

- [1] N. Subhash Hinge, K. Himanshu, M. Monohar Pandey, Rivastigmine-DHA ion-pair complex improved loading in hybrid nanoparticles for better amyloid inhibition and nose-to-brain targeting in Alzheimer's, *Eur. J. Pharm. Biopharm.* 190 (2023) 131–149. <https://doi.org/10.1016/j.ejpb.2023.06.007>.
- [2] N.S. Hinge, H. Kathuria, M.M. Pandey, Engineering of structural and functional properties of nanotherapeutics and nanodiagnostics for intranasal brain targeting in Alzheimer's, *Appl. Mater. Today.* 26 (2022) 101303. <https://doi.org/10.1016/J.APMT.2021.101303>.
- [3] Alzheimer's: Facts, Figures & Stats, BrightFocus Foundation, <https://www.brightfocus.org/alzheimers/article/alzheimers-disease-facts-figures> (accessed March 18, 2023).
- [4] Alzheimer's Disease Statistics, Alzheimer's News Today, <https://alzheimersnewstoday.com/alzheimers-disease-statistics/> (accessed June 6, 2022).
- [5] M. Bhandari, J. Shah, B. Gorain, A.B. Nair, S. Jacob, S.M.B. Asdaq, S. Fattepur, A.S. Alamri, W.F. Alsanie, M. Alhomrani, S. Nagaraja, M.K. Anwer, Optimized rivastigmine nanoparticles coated with Eudragit for intranasal application to brain delivery: Evaluation and nasal ciliotoxicity studies, *Materials (Basel)*. 14 (2021) 6291. <https://doi.org/10.3390/ma14216291>.
- [6] P. Wavikar, R. Pai, P. Vavia, Nose to brain delivery of rivastigmine by in situ gelling cationic nanostructured lipid carriers: Enhanced brain distribution and pharmacodynamics, *J. Pharm. Sci.* 106 (2017) 3613–3622. <https://doi.org/10.1016/J.XPHS.2017.08.024>.

-
- [7] F.M. Elsenosy, G.A. Abdelbary, A.H. Elshafeey, I. Elsayed, A.R. Fares, Brain targeting of Duloxetine HCl via intranasal delivery of loaded cubosomal gel: In vitro characterization, ex vivo permeation, and in vivo biodistribution studies, *Int. J. Nanomedicine*. 15 (2020) 9517. <https://doi.org/10.2147/IJN.S277352>.
- [8] A.S. Torkey, M.S. Freag, M.M.A. Nasra, O.Y. Abdallah, Novel skin penetrating berberine oleate complex capitalizing on hydrophobic ion pairing approach, *Int. J. Pharm.* 549 (2018) 76–86. <https://doi.org/10.1016/j.ijpharm.2018.07.051>.
- [9] P.R. Wavikar, P.R. Vavia, Rivastigmine-loaded in situ gelling nanostructured lipid carriers for nose to brain delivery, *J. Liposome Res.* 25 (2015) 141–149. <https://doi.org/10.3109/08982104.2014.954129>.
- [10] D. Gadhave, S. Tupe, A. Tagalpallewar, B. Gorain, H. Choudhury, C. Kokare, Nose-to-brain delivery of amisulpride-loaded lipid-based poloxamer-gellan gum nanoemulgel: In vitro and in vivo pharmacological studies, *Int. J. Pharm.* 607 (2021) 121050. <https://doi.org/10.1016/J.IJPHARM.2021.121050>.
- [11] S. Cunha, M. Swedrowska, Y. Bellahnid, Z. Xu, J.M. Sousa Lobo, B. Forbes, A.C. Silva, Thermosensitive in situ hydrogels of rivastigmine-loaded lipid-based nanosystems for nose-to-brain delivery: characterisation, biocompatibility, and drug deposition studies, *Int. J. Pharm.* 620 (2022) 121720. <https://doi.org/10.1016/J.IJPHARM.2022.121720>.
- [12] C.T. Uppuluri, P.R. Ravi, A. V. Dalvi, Design, optimization and pharmacokinetic evaluation of Piribedil loaded solid lipid nanoparticles dispersed in nasal in situ gelling system for effective management of Parkinson's disease, *Int. J. Pharm.* 606 (2021) 120881. <https://doi.org/10.1016/J.IJPHARM.2021.120881>.
- [13] N. Hinge, H. Kathuria, M.P.-A.M. Today, U. 2022, Engineering of structural and functional properties of nanotherapeutics and nanodiagnostics for intranasal brain

- targeting in Alzheimer's, *Appl. Mater. Today*. 26 (2022) 101303. <https://www.sciencedirect.com/science/article/pii/S2352940721003668> (accessed February 15, 2022).
- [14] L. Salade, N. Wauthoz, M. Vermeersch, K. Amighi, J. Goole, Chitosan-coated liposome dry-powder formulations loaded with ghrelin for nose-to-brain delivery, *Eur. J. Pharm. Biopharm.* 129 (2018) 257–266. <https://doi.org/10.1016/J.EJPB.2018.06.011>.
- [15] X. Xu, M.A. Khan, D.J. Burgess, A quality by design (QbD) case study on liposomes containing hydrophilic API: II. Screening of critical variables, and establishment of design space at laboratory scale, *Int. J. Pharm.* 423 (2012) 543–553. <https://doi.org/10.1016/J.IJPB.2011.11.036>.
- [16] C. Weber, M. Voigt, J. Simon, A.K. Danner, H. Frey, V. Mailänder, M. Helm, S. Morsbach, K. Landfester, Functionalization of Liposomes with Hydrophilic Polymers Results in Macrophage Uptake Independent of the Protein Corona, *Biomacromolecules*. 20 (2019) 2989–2999. https://doi.org/10.1021/ACS.BIOMAC.9B00539/SUPPL_FILE/BM9B00539_SI_002.XLSX.
- [17] D.A. Kuznetsova, G.A. Gaynanova, L.A. Vasileva, G. V. Sibgatullina, D. V. Samigullin, A.S. Sapunova, A.D. Voloshina, I. V. Galkina, K.A. Petrov, L.Y. Zakharova, Mitochondria-targeted cationic liposomes modified with alkyltriphenylphosphonium bromides loaded with hydrophilic drugs: preparation, cytotoxicity and colocalization assay, *J. Mater. Chem. B*. 7 (2019) 7351–7362. <https://doi.org/10.1039/C9TB01853K>.
- [18] J.O. Eloy, M. Claro de Souza, R. Petrilli, J.P.A. Barcellos, R.J. Lee, J.M. Marchetti, Liposomes as carriers of hydrophilic small molecule drugs: Strategies to enhance encapsulation and delivery, *Colloids Surfaces B Biointerfaces*. 123 (2014) 345–363.

- <https://doi.org/10.1016/J.COLSURFB.2014.09.029>.
- [19] L. Ramezanzade, S.F. Hosseini, B. Akbari-Adergani, A. Yaghmur, Cross-linked chitosan-coated liposomes for encapsulation of fish-derived peptide, *LWT*. 150 (2021) 112057. <https://doi.org/10.1016/J.LWT.2021.112057>.
- [20] S. Nageeb El-Helaly, A.A. Elbary, M.A. Kassem, M.A. El-Nabarawi, Electrosteric stealth Rivastigmine loaded liposomes for brain targeting: preparation, characterization, ex vivo, bio-distribution and in vivo pharmacokinetic studies, *Drug Deliv.* 24 (2017) 692–700. <https://doi.org/10.1080/10717544.2017.1309476>.
- [21] C. Sebaaly, S. Haydar, H. Greige-Gerges, Eugenol encapsulation into conventional liposomes and chitosan-coated liposomes: A comparative study, *J. Drug Deliv. Sci. Technol.* 67 (2022). <https://doi.org/10.1016/J.JDDST.2021.102942>.
- [22] M. Zhao, S.H. Lee, J.G. Song, H.Y. Kim, H.K. Han, Enhanced oral absorption of sorafenib via the layer-by-layer deposition of a pH-sensitive polymer and glycol chitosan on the liposome, *Int. J. Pharm.* 544 (2018) 14–20. <https://doi.org/10.1016/J.IJPHARM.2018.04.020>.
- [23] E.H. Lee, S.J. Lim, M.K. Lee, Chitosan-coated liposomes to stabilize and enhance transdermal delivery of indocyanine green for photodynamic therapy of melanoma, *Carbohydr. Polym.* 224 (2019) 115143. <https://doi.org/10.1016/J.CARBPOL.2019.115143>.
- [24] J. Zhuang, Q. Ping, Y. Song, J. Qi, Z. Cui, International Journal of Nanomedicine Dovepress Effects of chitosan coating on physical properties and pharmacokinetic behavior of mitoxantrone liposomes, 2010. <https://www.dovepress.com/>.
- [25] N.S. Hinge, M.M. Pandey, Sensitive RP-HPLC method of rivastigmine for applicative

- quantification of nanostructured lipid carriers, *Microchem. J.* 188 (2023) 108341. <https://doi.org/10.1016/J.MICROC.2022.108341>.
- [26] J. Ma, C. Wang, Y. Sun, L. Pang, S. Zhu, Y. Liu, L. Zhu, S. Zhang, L. Wang, L. Du, Comparative study of oral and intranasal puerarin for prevention of brain injury induced by acute high-altitude hypoxia, *Int. J. Pharm.* 591 (2020) 120002. <https://doi.org/10.1016/j.ijpharm.2020.120002>.
- [27] S. Salatin, J. Barar, M. Barzegar-Jalali, K. Adibkia, M. Jelvehgari, Thermosensitive in situ nanocomposite of rivastigmine hydrogen tartrate as an intranasal delivery system: Development, characterization, ex vivo permeation and cellular studies, *Colloids Surf. B. Biointerfaces.* 159 (2017) 629–638. <https://doi.org/10.1016/j.colsurfb.2017.08.031>.
- [28] K. Florence, L. Manisha, B.A. Kumar, K. Ankur, M.A. Kumar, M. Ambikanandan, Intranasal clobazam delivery in the treatment of status epilepticus, *J. Pharm. Sci.* 100 (2011) 692–703. <https://doi.org/10.1002/JPS.22307>.
- [29] M. Phetdee, A. Polnok, J. Viyoch, Development of chitosan-coated liposomes for sustained delivery of tamarind fruit pulp's extract to the skin, *Int. J. Cosmet. Sci.* 30 (2008) 285–295. <https://doi.org/10.1111/J.1468-2494.2008.00447.X>.
- [30] A.C.C. Vieira, L.L. Chaves, S. Pinheiro, S. Pinto, M. Pinheiro, S.C. Lima, D. Ferreira, B. Sarmiento, S. Reis, Mucoadhesive chitosan-coated solid lipid nanoparticles for better management of tuberculosis, *Int. J. Pharm.* 536 (2018) 478–485. <https://doi.org/10.1016/J.IJPHARM.2017.11.071>.
- [31] L. Malgarim Cordenonsi, A. Faccendini, M. Catanzaro, M.C. Bonferoni, S. Rossi, L. Malavasi, R. Platchek Raffin, E.E. Scherman Schapoval, C. Lanni, G. Sandri, F. Ferrari, The role of chitosan as coating material for nanostructured lipid carriers for skin delivery of fucoxanthin, *Int. J. Pharm.* 567 (2019) 118487.

- <https://doi.org/10.1016/J.IJPHARM.2019.118487>.
- [32] N. Dhas, T. Mehta, Cationic biopolymer functionalized nanoparticles encapsulating lutein to attenuate oxidative stress in effective treatment of Alzheimer's disease: A non-invasive approach, *Int. J. Pharm.* 586 (2020) 119553. <https://doi.org/10.1016/j.ijpharm.2020.119553>.
- [33] H. Hamedinasab, A.H. Rezayan, M. Mellat, M. Mashreghi, M.R. Jaafari, Development of chitosan-coated liposome for pulmonary delivery of N-acetylcysteine, *Int. J. Biol. Macromol.* 156 (2020) 1455–1463. <https://doi.org/10.1016/j.ijbiomac.2019.11.190>.
- [34] C.T. Uppuluri, P.R. Ravi, A. V. Dalvi, S.S. Shaikh, S.R. Kale, Piribedil loaded thermo-responsive nasal in situ gelling system for enhanced delivery to the brain: formulation optimization, physical characterization, and in vitro and in vivo evaluation, *Drug Deliv. Transl. Res.* 11 (2021) 909–926. <https://doi.org/10.1007/s13346-020-00800-w>.
- [35] M.S.A. Tan, P. Pandey, J.R. Falconer, D.J. Siskind, A. Balmanno, H.S. Parekh, Clozapine-Encapsulated Binary Mixed Micelles in Thermosensitive Sol–Gels for Intranasal Administration, *Gels*. 8 (2022). <https://doi.org/10.3390/GELS8010038>.
- [36] A.T. Chatzitaki, S. Jesus, C. Karavasili, D. Andreadis, D.G. Fatouros, O. Borges, Chitosan-coated PLGA nanoparticles for the nasal delivery of ropinirole hydrochloride: In vitro and ex vivo evaluation of efficacy and safety, *Int. J. Pharm.* 589 (2020) 119776. <https://doi.org/10.1016/j.ijpharm.2020.119776>.
- [37] S. Al Harthi, S.E. Alavi, M.A. Radwan, M.M. El Khatib, I.A. AlSarrah, Nasal delivery of donepezil HCl-loaded hydrogels for the treatment of Alzheimer's disease, *Sci. Rep.* 9 (2019) 1–20. <https://doi.org/10.1038/s41598-019-46032-y>.
- [38] M.M. Mady, M.M. Darwish, Effect of chitosan coating on the characteristics of DPPC

- liposomes, *J. Adv. Res.* 1 (2010) 187–191. <https://doi.org/10.1016/J.JARE.2010.05.008>.
- [39] A.T. Chatzitaki, S. Jesus, C. Karavasili, D. Andreadis, D.G. Fatouros, O. Borges, Chitosan-coated PLGA nanoparticles for the nasal delivery of ropinirole hydrochloride: In vitro and ex vivo evaluation of efficacy and safety, *Int. J. Pharm.* 589 (2020) 119776. <https://doi.org/10.1016/j.ijpharm.2020.119776>.
- [40] R. Ana, M. Mendes, J. Sousa, A. Pais, A. Falcão, A. Fortuna, C. Vitorino, Rethinking carbamazepine oral delivery using polymer-lipid hybrid nanoparticles, *Int. J. Pharm.* 554 (2019) 352–365. <https://doi.org/10.1016/J.IJPHARM.2018.11.028>.
- [41] N. Dhas, T. Mehta, Intranasal delivery of chitosan decorated PLGA core /shell nanoparticles containing flavonoid to reduce oxidative stress in the treatment of Alzheimer's disease, *J. Drug Deliv. Sci. Technol.* 61 (2021) 102242. <https://doi.org/10.1016/j.jddst.2020.102242>.
- [42] N. Dhas, T. Mehta, Cationic biopolymer functionalized nanoparticles encapsulating lutein to attenuate oxidative stress in effective treatment of Alzheimer's disease: A non-invasive approach., *Int. J. Pharm.* 586 (2020) 119553. <https://doi.org/10.1016/j.ijpharm.2020.119553>.

CHAPTER 7

FUTURE SCOPE OF WORK

Nose-to-brain delivery has been well-known for delivering actives directly to the brain. In the present research work, we have developed nanocarrier-based intranasal delivery systems for the treatment of AD. The formulation approach involved the development of thermoresponsive gel-loaded lipid-polymer hybrid nanoparticles and hydrogel-loaded ion-pair complex-based nanodispersion system. Another formulation approach involved the development of thermoresponsive gel-loaded liposome and chitosan-coated liposome-based delivery system. Amongst developed formulations, cationic lipid polymer hybrid nanoparticles showed efficient nose-to-brain delivery, improved brain targeting, and extended therapeutic action. There are several facets of the developed formulations and nano-platform that could be investigated in the future.

The pharmacodynamic study of RIV:DHA loaded cationic LPH gel (RIV:DHA LPH(+ve) gel) can be performed for evaluation of therapeutic efficacy in Alzheimer-induced rat model. The therapeutic efficacy of RIV:DHA LPH(+ve) gel could be compared with RIV-HT gel. As rivastigmine is associated with the problem of hepatotoxicity, biochemical estimation evaluating liver function test could be performed to assess hepatotoxicity induced with the developed formulation.

DHA has been extensively explored in nose-to-brain for improving brain concentration. Several reports suggest anti-Alzheimer activity with DHA. It has also been reported to reduce symptoms of Alzheimer's disease. Pharmacodynamic study of RIV:DHA ion-pair complex could be compared with pure rivastigmine to evaluate the effects of DHA in Alzheimer's therapeutics. Immunohistochemistry and amyloid β_{1-42} biochemical estimation can assess the role of DHA in treating Alzheimer's.

RIV:DHA ion-pair complex can be loaded into chitosan-coated liposome gel for evaluation of pharmacokinetic behavior as compared to CHT@RIV-HT Liposome gel. Pharmacodynamic

study and biochemical estimation could be performed for evaluation of therapeutic efficacy of RIV: DHA-loaded chitosan-coated liposome gel and RIV-HT Liposome gel. Anti-amylogenic activity of both formulations could be evaluated with immunohistochemistry and biochemical estimation of amyloid β_{1-42} .

Ion pair complex using other anti-Alzheimer drugs such as donepezil could be prepared using DHA. As donepezil also exhibits higher water solubility, the chemical structure of the drug makes it feasible to develop an ion-pair complex. However ion-pair complex could be prepared with other essential fatty acids such as linoleic acid.

Surface modification of lipid polymer hybrid nanoparticles may improve therapeutic efficacy due to active targeting. Surface modification with polyethylene glycol or targeting moieties could be further explored for intranasal delivery.

The cationic lipid-polymer hybrid system can also be explored for intranasal delivery in the treatment of other brain disorders, such as Parkinson's disease, epilepsy and seizures, etc. The developed cationic lipid-polymer hybrid nanoparticles could be efficiently utilized in nose-to-brain delivery for delivering hydrophobic small molecules.

Appendix 1

List of Publications

1. **Hinge N.S.**, Kathuria H., Pandey M.M., Engineering of structural and functional properties of nanotherapeutics and nanodiagnostics for intranasal brain targeting in Alzheimer's, *Applied Materials Today*. 26 (2022) 101303.
2. **Hinge N.S.**, Pandey M.M., Sensitive RP-HPLC method of rivastigmine for applicative quantification of nanostructured lipid carriers, *Microchemical Journal*. 188 (2023) 108341.
3. **Hinge N.S.**, Himanshu K., Pandey M.M., Rivastigmine-DHA ion-pair complex improved loading in hybrid nanoparticles for better amyloid inhibition and nose-to-brain targeting in Alzheimer's, *Eur. J. Pharm. Biopharm.* 190 (2023) 131–149.
4. **Hinge N.S.**, Kathuria H., Pandey M.M., Chitosan-coated liposomes loaded into *in-situ* gel system improved nose-to-brain targeting of rivastigmine in Alzheimer's disease (Ready for communication).
5. **Hinge N.S.**, Kathuria H., Pandey M.M., Rivastigmine ion pair complex based nanodispersion improved nose-to-brain in Alzheimer's therapeutics (Manuscript under preparation).

Book Chapter (other than thesis work)

1. **Hinge N.S.**, Pandey M.M., Singhvi G., Gupta G., Mehta M, Satija S., Gulati M., Dureja H., Dua K. Nanomedicine advances in cancer therapy. *Advanced 3D-Printed Systems and Nanosystems for Drug Delivery and Tissue Engineering 2020 Jan 1* (pp. 219-253). Elsevier

Appendix 2

Biography of Prof. Murali Monohar Pandey

Prof. Murali Monohar Pandey is currently working as Associate professor in Department of Pharmacy, BITS Pilani, Pilani Campus. He pursued Bachelor of Pharmacy and Master's in technology (Biotechnology) from Jadavpur University, Kolkata. He completed his Ph.D. from BITS Pilani, Pilani campus. He has 17 years of extensive teaching experience and is associated with BITS Pilani since 2007. He has guided more than 40 B. Pharm. and 35 M. Pharm. students in various research-oriented projects. He has supervised 1 Ph.D. student. He also guided 3 M. Pharma and 4 B. Pharma student for their dissertation/thesis works. He is a member of the Academic Counselling Cell, BITS Pilani. He has many publications in reputed international and national peer-reviewed journals. He has attended many international scientific conferences. He has successfully completed several government research projects and industrially sponsored projects as well.

Biography of Ms. Nikita Subhash Hinge

Presently, Ms Nikita Hinge is pursuing Ph.D. degree from BITS Pilani, Pilani campus. She received Master and Bachelor of Pharmacy from BITS Pilani (Pilani campus) and Mumbai Educational Trust (Nashik). She has qualified national level entrance exams including GPAT (AIR 516), BITSAT (Rank 2nd) and Maharashtra CET (Rank 82). She has published articles in several Internationally peer-reviewed journals.